Author:	Timothy Mark Godden
Thesis title:	Coherent optical control of the spin of a single hole in a quantum dot
Qualification:	PhD

Coherent optical control of the spin of a single hole in a quantum dot

Timothy Mark Godden

The
University
Of
Sheffield.

Submitted for the degree of Doctor of Philosophy

Department of Physics and Astronomy

November 2011

Coherent optical control of the spin of a single hole in a quantum dot

Timothy Mark Godden

Abstract

This thesis describes experiments on the initialisation, coherent control, and readout of a single hole spin trapped in a self assembled InGaAs semiconductor quantum dot. High fidelity initialisation of a hole spin state is achieved by the fast ionisation of a spin polarised neutral exciton under an applied electric field and in a Faraday geometry magnetic field. The preparation of a coherent superposition state is demonstrated by observing the precession of the hole spin about a Voigt geometry magnetic field. The hole spin dephasing time is deduced from the decay of the spin contrast. Coherent optical rotation of the hole spin state about the z-axis is demonstrated using the geometric phase shift induced by a picosecond laser pulse. By combining the precession of the spin about the x-axis, and optical rotations about the z-axis, full quantum control of a hole spin is demonstrated over the surface of the Bloch sphere. This is an important prerequisite for the use of a hole spin as a qubit for quantum information processing applications.

Acknowledgments

It has been a real privilege to study and research as part of the Low Dimensional Structures and Devices group here at the University of Sheffield. I would like to thank the group for the fantastic time I have had. I am very fortunate to have been given the opportunity to work on and study something I am passionate about, and I will cherish this for the rest of my life. I would like to thank my supervisor Mark Fox for opening this door to me, and for his kind guidance and support throughout the journey. I would also like to thank the group leader Maurice Skolnick, whose tireless dedication to research is exemplary. I would also like to thank Stephen Boyle for teaching me in my first year of research. I could't have asked for a more patient mentor. I would like to say an enormous thankyou to Andrew Ramsay, for his tutoring, constructive criticism, incredible hard work, guidance and support, but most of all his friendship. Thanks Andrew.

There are many other people who I would like to acknowledge: the members of the LDSD group past and present, in particular; D. J. Mowbray, J. W. Cockburn, D. M. Whittaker, P. Kok, A. I. Tartakovskii, L. R. Wilson, D. N. Krizhanovskii, E. Chekhovich, I. J. Luxmoore, M. N. Makhonin, D. Sarkar, O. Tsyplyatyev, P. M. Walker, C. Atkins, R. A. Bradley, R. J. Coles, E. Daghigh Ahmadi, D. G. Davies, A. Foster, K. Guda, K. C. Larsen, N. E. Porter, J. L. Puebla Nunez, J. H. Quilter, D. Sercombe, M. Sich, N. A. Wasley, O. Couto Jr, S. Davies, S. Lam, N. Babazedah, B. D. Jones, R. Kolodka, J. Skiba-Szymanska, R. Oulton, P. Commin, the staff of the EPSRC National Centre for III-V Technologies and members of the EEE department, in particular R. Airey, G. Hill and K. Kennedy, R. Hogg, and all those who partook in the fruitful discussions on a Friday evening, I very much enjoyed your company! Thanks to P. Kemp-Russell, P. Robinson, and C. Vickers for their hard work on cryogenics and in the workshop. Thanks to all the staff from the departmental office. I would also like to say a big thankyou to Yanwen Wu and P. Brereton from the University of Cambridge for very kindly fabricating the devices used in the experiments of chapters 5 and 6, which were a crucial part of this thesis. Thanks to our collaborators E. M. Gauger, A. Nazir, B. W. Lovett. Thanks to M. Atature and the people of ITAP for the wonderful workshop in Turunc, Turkey. Finally, thanks to the Quantum Information Processing Interdisciplinary Research Collaboration and the Engineering and Physical Sciences Research Council for funding.

Thankyou to my family and friends in particular: my Mum, Dad, my late Grandparents (especially Ken), all my sisters, and finally my loving girlfriend Roxie for all her support. Cheers guys.

Tim Godden
Sheffield, November 2011.

Publications

A. J. Ramsay, S. J. Boyle, **T. M. Godden**, R. S. Kolodka, A. F. A. Khatab, J. B. B. Oliveira, J. Skiba-Szymanska, H. -Y. Liu, M. Hopkinson, A. M. Fox and M. S. Skolnick. "Towards coherent optical control of a single hole spin: Rabi rotation of a trion conditional on the spin state of the hole". *Solid State Communications* **149** 1458 (2009)

A. J. Ramsay, **T. M. Godden**, S. J. Boyle, E. M. Gauger, A. Nazir, B. W. Lovett, A. M. Fox and M. S Skolnick. "Phonon-induced Rabi frequency renormalization of optically driven single InGaAs/GaAs quantum dots". *Physical Review Letters* **105** 177402 (2010)

T. M. Godden, S. J. Boyle, A. J. Ramsay, A. M. Fox, and M. S. Skolnick. "Fast high fidelity hole spin initialization in a single InGaAs quantum dot". *Applied Physics Letters* **97** 061113 (2010)

A. J. Ramsay, **T. M. Godden**, S. J. Boyle, E. M. Gauger, A. Nazir, B. W. Lovett, Achanta Venu Gopal, A. M. Fox, and M. S. Skolnick. "Effect of detuning on the phonon induced dephasing of optically driven InGaAs/GaAs quantum dots". *Journal of Applied Physics* **109** 102415 (2011)

T. M. Godden, J. H. Quilter, A. J. Ramsay, Yanwen Wu, P. Brereton, S. J. Boyle, I. J. Luxmoore, J. Puebla-Nunez, A. M. Fox, and M. S. Skolnick. "Coherent optical control of the spin of a single hole in a quantum dot". *Physical Review Letters* (accepted November 2011)

Contents

1 Introduction **1**
- 1.1 Quantum information processing . . . 1
  - 1.1.1 The physical implementation of quantum computing . . . 2
  - 1.1.2 Quantum dots for quantum information processing . . . 2
- 1.2 Chapter Abstracts . . . 3

2 Background **7**
  - 2.0.1 Bits and qubits . . . 7
  - 2.0.2 Quantum logic gates . . . 8
- 2.1 Self assembled semiconductor quantum dots . . . 9
  - 2.1.1 Growth . . . 9
- 2.2 Quantum dot energy states . . . 10
  - 2.2.1 Confined states and selection rules . . . 11
  - 2.2.2 Fine structure and electron and hole exchange energy . . . 13
  - 2.2.3 Application of external fields . . . 15
  - 2.2.4 Charged excitons . . . 16
- 2.3 Coherence of carrier spins in quantum dots . . . 17
  - 2.3.1 General concepts . . . 17
  - 2.3.2 Decoherence of carrier spins in quantum dots . . . 18
  - 2.3.3 Spin relaxation T_1 via the spin orbit interaction . . . 18
  - 2.3.4 Spin dephasing T_2^* via the hyperfine interaction . . . 20
- 2.4 Coherent optical spectroscopy of two level systems . . . 22
  - 2.4.1 Rabi oscillations of excitonic qubits . . . 22
- 2.5 Coherent control of a quantum dot spin . . . 24
  - 2.5.1 Spin initialisation techniques . . . 25
  - 2.5.2 Spin readout techniques . . . 29
  - 2.5.3 Spin control techniques . . . 33
  - 2.5.4 State of the art: putting it all together . . . 39

3 Methods **47**
- 3.1 The quantum dot Schottky diode . . . 47
  - 3.1.1 Device growth and fabrication . . . 48
- 3.2 Electrical circuit and device characterisation . . . 49
- 3.3 Photocurrent detection . . . 53
- 3.4 Helium bath cryostat: Attocube system . . . 55
  - 3.4.1 Cryostat design . . . 55
  - 3.4.2 Sample mounting . . . 56
- 3.5 Optical setup . . . 59

3.5.1 Laser Source 60
3.5.2 Pulse Shaping 60
3.5.3 Coupling light into a single mode fibre 62
3.6 Single, two and three-pulse experimental setups 64
3.6.1 Single-pulse setup 65
3.6.2 Two-pulse, two-fibre setup: measurements of hole spin preparation 65
3.6.3 Two and three-pulse setup using a single fibre: measurements of the hole spin precession and optical control 68
3.6.4 Stability 69
3.6.5 Automation 71
3.6.6 Summary of optical setup 71
3.7 Measurement techniques 71
3.7.1 Photocurrent spectra 72
3.7.2 Measurement of a neutral exciton Rabi oscillation 73
3.7.3 Time-resolved photocurrent measurements 75
3.8 Summary 77

4 Fast high fidelity hole spin initialisation 79
4.1 Introduction 79
4.2 Sample details 80
4.3 Principle of operation for initialising the hole spin 80
4.4 Model of spin preparation 83
4.5 Results 87
4.5.1 Hole spin preparation without an applied magnetic field 87
4.5.2 Hole spin preparation with an applied magnetic field $B = \pm 3$ T 89
4.6 Magnetic field dependence 92
4.7 Voltage dependence 93
4.8 Summary 95

5 Hole spin precession and measurement of dephasing time 97
5.1 Introduction 97
5.2 Sample details 98
5.3 Principle of operation 98
5.3.1 Preparation of spin polarised neutral exciton 100
5.3.2 Ionisation of the neutral exciton: hole spin preparation 101
5.3.3 Precession of the hole spin 101
5.3.4 Detection 102
5.4 Results 104
5.4.1 Time dependence of X^+ amplitudes. 106
5.4.2 Magnetic field dependence of the hole spin precession 106
5.4.3 Magnetic field dependence of fidelity of hole-spin preparation . 110
5.4.4 Hole spin precession as a function of applied bias 113
5.5 Evaluation of the model of hole spin preparation 117
5.6 Oscillation in the energy of the charged exciton 119
5.7 Hole spin dephasing time T_2^* 122
5.8 Summary of measurement of hole spin precession and dephasing time 127

6 Optical rotation of a single hole spin 129

6.1 Introduction 129
6.2 Principle of the geometric phase gate 130
6.3 Results 135
6.3.1 Measurement of the electron spin precession and electron g-factor 135
6.3.2 Hole spin control: controlling the phase of the precession . . . 138
6.3.3 Controlling the angle of rotation 141
6.4 Summary of optical control of hole spin 146

7 Conclusions and future work 149
7.1 Conclusions 149
7.2 Future work 150
7.2.1 AC-Stark shift 150
7.2.2 Optical rotations about arbitrary axes 151
7.2.3 Magnetic field dependence of the hole spin dephasing time . . 152
7.2.4 Temperature dependence of the hole spin dephasing time . . . 152
7.2.5 Fidelity of spin preparation in the Voigt geometry 152
7.2.6 Preparing the hole into an energy eigenstate of the system . . 153
7.2.7 Improving the hole lifetime: voltage modulation 154
7.2.8 Quantum dot molecules 155

A Chapter 5 - Appendices 157
A.1 Single-pulse photocurrent spectra of a neutral exciton in a Voigt geometry magnetic field 157
A.2 Estimation of the bright-dark exciton mixing angle 159
A.3 Bright-dark exciton exchange energy 160
A.4 Neutral exciton effective fine-structure splitting 163
A.5 Measurements of carrier tunneling rates 166
A.5.1 Voltage dependence of carrier tunneling rates 168
A.5.2 Magnetic field dependence of electron tunneling rate 169
A.6 Model of spin preparation 170
A.6.1 Fidelity of spin preparation in a Voigt geometry magnetic-field 171
A.7 Estimate of dephasing time T_2^* 178

List of Figures

2.1 Cross-sectional STM image of a typical self assembled quantum dot . 10
2.2 Conduction and valence band states in a quantum dot 12
2.3 Faraday and Voigt geometry magnetic fields. 15
2.4 Bloch sphere representation of decoherence processes 19
2.5 Two-level system interacting with a laser field 23
2.6 Optical pumping of a spin state 25
2.7 Energy level diagram to show coherent population trapping 27
2.8 Energy level diagram of positive and negative trions in a Voigt geometry magentic field 34
2.9 Bloch sphere to illustrate the coherent precession of a spin state . . . 35
2.10 Energy level diagram to show geometric phase shift 37

3.1 Band diagram 48
3.2 Lithographic mask for device fabrication 50
3.3 Example photograph of a processed device 51
3.4 Circuit diagram 52
3.5 Current Voltage curve of Schottky diode 53
3.6 Histogram of diode IV performance 54
3.7 Attocube system helium bath cryostat 56
3.8 Photograph of packaged device and sample mounting 57
3.9 Simplified experimental setup 59
3.10 Pulse shaper 61
3.11 Pulse shaper wavelength calibration 63
3.12 Intensity profile of laser 64
3.13 Experimental setup for single pulse 66
3.14 Attocube shelf optics 67
3.15 Experimental setup: Three-pulse 70
3.16 Photocurrent spectra of apertures 73
3.17 Photocurrent spectrum of a quantum dot neutral exciton 74
3.18 Neutral exciton Rabi-Rotation at $T = 12.5K$ 75
3.19 Example measurement of time delay between laser pulses 76

4.1 Principle of operation 81
4.2 Energy level diagram 82
4.3 Rate diagram of exciton and hole decay 86
4.4 Neutral and charged exciton spectra $B = 0$T 88
4.5 Neutral and charged exciton spectra $B = 3$ T 90
4.6 Neutral exciton Zeeman energy splitting as a function of B-field . . . 91
4.7 Charged exciton spectra as a function of B 93

4.8 Fidelity as a function of magnetic field 94
4.9 Fidelity as a function of applied bias 95

5.1 Principle of operation 99
5.2 Energy level diagram of neutral and charged exciton in Voigt geometry B-field 100
5.3 Bloch sphere representation of hole spin precession 103
5.4 Example single pulse and two-pulse spectra in a magnetic field B=3T 105
5.5 PC spectra of X^+ peak oscillation in time. 107
5.6 Amplitude of X^+ peak oscillation in time. 108
5.7 Hole spin precession in magnetic field 109
5.8 determination of hole g-factor 110
5.9 Magnetic field dependence of hole spin precession contrast 111
5.10 Hole spin precession as a function of applied bias 114
5.11 Voltage dependence of hole spin precession contrast 115
5.12 Electric field dependence of in plane hole g-factor 117
5.13 Exploring the model of spin preparation 118
5.14 Exploring the model of spin preparation in the ideal case 119
5.15 oscillations in charged exciton energy splittings 120
5.16 Comparison of charged exciton energy splitting and hole spin precession 121
5.17 Amplitude of charged exciton energy splitting oscillation as a function of applied bias 122
5.18 Difference between average energy of the charged exciton as function of applied bias 123
5.19 Hole spin precession over 8.5 ns 123
5.20 Hole spin population over 8.5 ns 124
5.21 Decay of hole spin precession: measurement of T_2^* 125

6.1 Energy level diagram of hole and charged exciton system in the energy eigenstates basis 131
6.2 Energy level diagram of hole and charged exciton system in the circular basis 132
6.3 Bloch sphere to illustrate rotation of the hole spin vector about the optical axis 134
6.4 Principle of operation for preparing, controlling and measuring the hole spin state 136
6.5 Measurement of the precession of the charged exciton 137
6.6 Hole spin phase control 139
6.7 Complete linear control of the hole spin precession phase 141
6.8 Energy level diagram to illustrate control pulse detuning 142
6.9 Control over the angle of spin rotation 144
6.10 Detuning dependence of the amplitude of spin precession after control pulse 145

A.1 Neutral exciton spectra 158
A.2 Neutral exciton diamagnetic shift 159
A.3 Estimation of the bright/dark neutral exciton mixing angle 161
A.4 Energy level diagram of neutral exciton in Voigt geometry magnetic field 162

A.5 Bright/Dark exciton splitting 164
A.6 Measurement of the effective bright-bright fine-structure splitting . . 166
A.7 bright-bright neutral exciton energy splitting as a function of magnetic field 167
A.8 An example of a typical measurement to determine carrier tunneling rates 168
A.9 Electric field dependence of electron tunneling rate 169
A.10 Electric field dependence of hole tunneling rate 170
A.11 Magnetic field dependence of electron tunneling rate in the Voigt geometry 171
A.12 Rate diagram of exciton and hole decay 175

Chapter 1

Introduction

This thesis describes the coherent optical control of a single hole spin in a semiconductor quantum dot using picosecond optical laser pulses and a photocurrent detection technique. The primary motivation of the work is for applications in quantum information processing.

1.1 Quantum information processing

Moore's law states that the number density of transistors in a conventional central processing unit doubles every 18 months. As a result, the length scale for a transistor, and hence the number of electrons used to distinguish between the 'on' and 'off' states is falling. The ultimate limit is where the difference in charge of the 'on' and 'off' states is one electron, and this will be reached soon. In such a device, quantum mechanical effects will become important. The limit to classical computing was first considered by Richard Feynman with a view to simulate quantum mechanical systems [1]. Quantum mechanical effects such as parallelism have been shown to be useful for efficiently solving certain types of problems. These include finding prime factors of large numbers, search algorithms and simulation of quantum mechanical systems [2].

1.1.1 The physical implementation of quantum computing

David DiVincenzo first set out the requirements for a quantum computer [3]. The so called DiVincenzo criteria are the following: 1) “A scalable physical system with well characterised qubits”. 2) “The ability to initialize the state of the qubits to a simple fiducial state”. 3) “Long relevant decoherence times, much longer than the gate operation time”. 4) “A ‘universal’ set of quantum gates”. 5) “A qubit-specific measurement capability”. What is needed is a scalable system to realise these criteria.

1.1.2 Quantum dots for quantum information processing

A self assembled quantum dot (SAQD) might provide the means to address the DiVincenzo criteria. SAQD’s have many desirable properties: they can be easily grown using standard semiconductor reactor technology, they interact strongly with light due to the large optical dipole, they have sharp atomic like emission lines, the emission/absorption energy can be tuned using band structure engineering, and they can be scaled up and integrated with photonic structures to form on-chip devices.

An exciton confined in a SAQD is a potential qubit, and full quantum control has been demonstrated using picosecond laser pulses [4], [5], [6], [7]. However, an exciton has a short coherence time that is limited by radiative recombination. This radiative lifetime is relatively short, about a nanosecond, since the overlap of the electron and hole wavefunction is large in quantum confined systems.

Recently the interest in quantum dots for QIP applications has moved towards the use of carrier spins as qubits. Electron spin lifetimes of ms have been reported [8], and high fidelity spin initialisation demonstrated [9]. However, it is more difficult to control a carrier spin with a fast optical pulse, because of the small energy splitting between the spin states. Despite this challenge, optical spin rotation of single electron spins has been recently demonstrated with picosecond gate times, thus satisfying the DiVincenzo criterion number three [10], [11], [12]. Although the intrinsic coherence time of an electron spin is long, the extrinsic dephasing time is much smaller, just a few nanoseconds. This is due to the electron spin interaction with the bath of nuclear spins within the SAQD. This has stimulated increasing interest in the use of a hole spin in a SAQD as a potential qubit, where the p-type wavefunction, leads to a reduced hyperfine interaction [13], [14], [15]. This has been encouraged by measurements of microsecond coherence times [16].

The subject of this thesis is the fast initialisation, read-out, and full quantum control of a single hole spin confined in a self assembled quantum dot using an optical geometric phase gate. Most recently, optical control of a hole spin has been demonstrated by other groups, in both single quantum dots [17], and quantum dot molecules [18]

1.2 Chapter Abstracts

The contents of the chapters are discussed in the following abstracts.

Chapter 2: Background

The basic concepts and background information on quantum dots and coherent spectroscopy are introduced here. A discussion of the spin initialisation, control and readout techniques is given, paying particular attention to the state of the art in the field.

Chapter 3: Methods

The photocurrent spectroscopy techniques used in chapters 4-6 are described here. All experiments were performed on single InGaAs quantum dots embedded in Schottky diode structures. Optical excitation was performed using a sequence of up to three picosecond laser pulses derived from a mode-locked Ti:Sapphire laser. The laser pulses were manipulated using pulse shaping optics and have independently tunable wavelength, pulse duration, polarisation, power and phase.

A photocurrent detection technique was used to detect the quantum dot state by measuring the change in photocurrent through the device as a result of optical excitation. Schemes to measure Rabi oscillations and two/three-colour time-resolved photocurrent spectroscopy are also described.

Chapter 4: Fast high fidelity hole spin initialization

Experiments to demonstrate fast initialisation of a single hole spin trapped in an InGaAs quantum dot with a fidelity $F > 99\%$ and a 1/e time of $\sim$ 30 ps are described. The high fidelity was achieved by applying a magnetic field parallel to the growth direction. The fidelity of the hole spin, prepared by ionization of a photo-generated electron-hole pair, is shown to be limited by the precession of the exciton spin due to the anisotropic exchange interaction.

Chapter 5: Coherent precession of a single hole spin

The preparation of a partially coherent superposition of hole spin states is demonstrated by the fast (10-100 ps) dissociation of a spin-polarized electron-hole pair in a Voigt-geometry magnetic field. The spin preparation is shown to be optimal when the precession of the neutral exciton and hole spin in the Voigt geometry magnetic field are synchronized. Long dephasing times of $T_2^* = 12 - 17.5$ ns are deduced for the hole, consistent with the expected weak hyperfine coupling for holes in InAs/GaAs quantum dots, and an order of magnitude longer than for the electron.

Chapter 6: Coherent optical control of the spin of a single hole

Coherent optical control of a single hole spin confined to an InAs/GaAs quantum dot is demonstrated. A superposition of hole spin states was created by fast (10-100 ps) dissociation of a spin-polarized electron-hole pair. Full control of the hole-spin was achieved by combining coherent rotations about two axes: Larmor precession of the hole-spin about an external Voigt-geometry magnetic field, and rotation about the optical axis due to the geometric phase shift induced by a picosecond laser pulse resonant with the hole-trion transition.

Chapter 7: Conclusions and future work

A summary of the experimental results is given here. Proposals for future experiments and projects are also discussed. These include the following: 1) potential implementation of an AC-Stark shift to rotate the hole spin; 2) a rigorous test of the spin preparation model which includes schemes in which to improve the fidelity of spin initialisation; 3) proposals for picosecond spin control about arbitrary axes; 4) measurements of the hole spin dephasing time as a function of applied magnetic field and temperature, and 5) techniques to improve the effective hole lifetime using voltage modulation.

Chapter 2

Background

This introductory chapter will outline some of the basic physics used in the experimental results chapters. This will include an introduction to qubits, a brief outline of quantum dot physics and coherent spectroscopy, a discussion of spin decoherence, and a description of spin control techniques. This is followed by a review of the experimental work carried out in the field of coherent control of carrier spins in semiconductor quantum dots.

2.0.1 Bits and qubits

In a classical computer information is encoded in classical bits. A 'classical' bit can either take the value 0 or 1. Information is processed by performing a series of logical operations on the bits which returns the values 0 or 1. A qubit is different. A qubit can be constructed from any two-level system consisting of the orthogonal states $|0\rangle$ and $|1\rangle$, and rather than take the values 0 or 1, a qubit can exist in any linear superposition state described by a wavefunction $|\psi_\mathrm{I}\rangle$:

$$|\psi\rangle = c_0 |0\rangle + c_1 |1\rangle \,, \tag{2.1}$$

where c_0 and c_1 are complex amplitudes with the normalisation condition $|c_0|^2 + |c_1|^2 = 1$. The single qubit may also be written in column vector form, using the basis states $|0\rangle$ and $|1\rangle$:

$$|\psi\rangle = \begin{pmatrix} c_0 \\ c_1 \end{pmatrix}. \tag{2.2}$$

2.0.2 Quantum logic gates

Quantum logic gates are performed on single and 2-qubit states in order to control the qubit register. Single qubit gates can be written as 2×2 matrices so that they can be used to perform matrix multiplication on the initial qubit state $|\psi\rangle$. Examples of single qubit gates include the Pauli-X gate ($\hat{U}_{\mathrm{X}}$), the Pauli-Z gate ($\hat{U}_{\mathrm{Z}}$) gate and the the Hadamard gate ($\hat{U}_{\mathrm{H}}$):

$$\hat{U}_{\mathrm{X}} = \begin{pmatrix} 0 & 1 \\ 1 & 0 \end{pmatrix}, \tag{2.3}$$

$$\hat{U}_{\mathrm{Z}} = \begin{pmatrix} 1 & 0 \\ 0 & -1 \end{pmatrix}, \tag{2.4}$$

$$\hat{U}_{\mathrm{H}} = \frac{1}{\sqrt{2}} \begin{pmatrix} 1 & 1 \\ 1 & -1 \end{pmatrix}. \tag{2.5}$$

The application of the qubit gates on the wavefunction $|\psi_{\mathrm{I}}\rangle$ manipulates the coefficients c_0 and c_1. For example $\hat{U}_{\mathrm{X}}$ swaps the complex coefficients c_0 and c_1, $\hat{U}_{\mathrm{Z}}$ introduces a phase factor $e^{i\pi} = -1$ between the $|0\rangle$ and $|1\rangle$ states and $\hat{U}_{\mathrm{H}}$ converts the pure qubit states into a superposition state and vice versa. Most importantly, there is no classical analogue of the Hadamard and Pauli-Z phase gates as they act on the superposition state. In chapter 6 we will see implementation of the Pauli-Z gate on a hole spin qubit, and implementation of a non-general unitary operation which rotates the qubit about both the x and z axis by an arbitrary angle.

The manipulation of a superposition state using qubit gates has the consequence that the output for the states $|0\rangle$ and $|1\rangle$ can be calculated in parallel. This parallelism is a property of quantum processing which essentially means that a quantum computer can calculate the result for many inputs simultaneously.

2.1 Self assembled semiconductor quantum dots

In this thesis a hole spin confined in a self assembled quantum dot will be used as a qubit. This section will briefly introduce some of the background physics of quantum dots. This includes the growth, optical properties and how the energy states of excitons depend on applied electric and magnetic fields.

2.1.1 Growth

Self assembled quantum dots (SAQD from hereafter) are nano-scale islands of semiconductor surrounded by a semiconductor with a higher bandgap. Figure 2.1 shows a cross-sectional scanning tunneling microscopy image of a single InAs/GaAs SAQD [19]. The quantum dot is highlighted in the red box. Also shown are the dimensions of the quantum dot. The growth of SAQD's, such as the one shown in Fig. 2.1, is described in the following.

The starting point is a substrate of GaAs on which the semiconductor heterostructure is grown. Next, a lower bandgap semiconductor material, for example InAs, is grown slowly, atomic layer by atomic layer, on top of the GaAs to form a quantum well layer. Because of the difference in the lattice constants between the GaAs and InAs, there is high strain in the quantum well layer. After the quantum well reaches a critical thickness, it becomes energetically favorable for the InAs to release the strain by self-assembling into 'pockets' or 'islands' of material which sit on top of a 'wetting layer'. The 'islands' of InAs semiconductor material are the quantum dots. This type of growth is known as the Stranski-Krastinow growth mode. A self-assembled quantum dot is typically 15-30 nm wide (in the plane) and 1-10 nm thick (in the growth direction). Finally a GaAs capping layer is formed to encapsulate the dots within the lattice. This is shown in Fig. 2.1.

By tuning the growth conditions, such as temperature and deposition rate, it is possible to control the properties of the quantum dots such as their size, composition and surface density. This is attractive because it allows the optical properties of

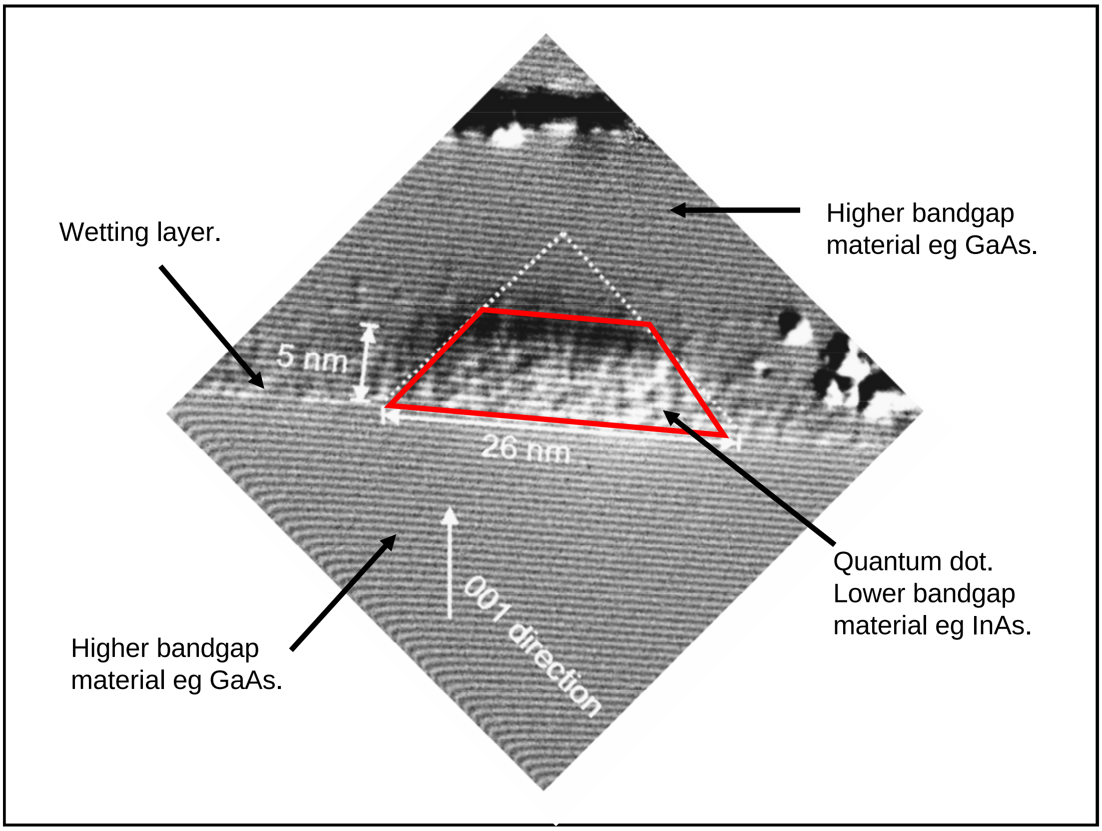

Figure 2.1: *Cross-sectional STM image of a typical self assembled quantum dot extracted from ref. [19]. A red box has been added to highlight the quantum dot. The quantum dot is made of InAs. The host material is made of GaAs.*

the quantum dots to be controlled. A good introduction to the basic principles of Stranski-Krastinow growth can be found in references [20] and [21].

This thesis describes experimental work performed on quantum dots consisting of InGaAs grown on GaAs by MBE. The dots sizes are typically 20 nm laterally and 5 nm vertically (in the growth direction). InGaAs dots of this size typically have an emission and absorption spectrum in the optical to near infra-red range.

2.2 Quantum dot energy states

This section describes the energy states of neutral and charged excitons in quantum dots. First, a simple introduction to quantum confinement will be given. This will be followed by a discussion of a simple 'lens' shape potential which is used to model the confinement in quantum dots. Next, the formation of neutral excitons will be introduced along with the optical selection rules and a discussion of fine structure. The energy states of neutral excitons in external electric and magnetic fields will then be discussed. Finally charged excitons will be introduced.

2.2.1 Confined states and selection rules

A quantum dot is a nanometer scale island of low bandgap semiconductor material which is surrounded by a higher bandgap semiconductor material. It is a physical realisation of a finite three-dimensional potential energy well, where the carriers are confined to discrete energy levels. For this reason quantum dots are often referred to as 'artificial atoms'.

The lattice mismatch in quantum dots (typically $\sim 6\%$) results in high strain, which modifies the electronic band structure through the deformation potential. The result of which is a lifting of the degeneracy of the light hole (lh) and heavy hole (hh) states in the valence band. The splitting of the light holes and heavy holes is on the order of tens of meV. For this reason, the light hole states are usually neglected when discussing the lower energy states of quantum dots. However finite mixing of the lh and hh exists in quantum dots and this will be discussed below.

Quantum dots are often modeled with a lens shape. The lens shape results in a circularly-symmetric parabolic confinement potential in the growth (xy) plane. This leads to an energy spectrum of a 2-D simple harmonic oscillator [20] with energy $E_{n,m} = (n + m + 1)\hbar\omega_0$. The confinement in the growth (z) direction has a much shorter dimension. Therefore, it is reasonable to assume there will be only one bound state in this direction with energy E_1^z. Furthermore, if there is more than one bound state in the z-direction, then the energy difference to the second level will be much larger than the energy separation associated with the lateral motion. The result of the lens model, is an atomic shell like energy spectrum, consisting of quantized orbitals with total energy $E_{n,m} = E_1^z + (n + m + 1)\hbar\omega$. The orbitals are characterised by the angular momentum about the z axis n, and are labelled with the conventional shell labels used in atomic physics, i.e. s, p, d etc.

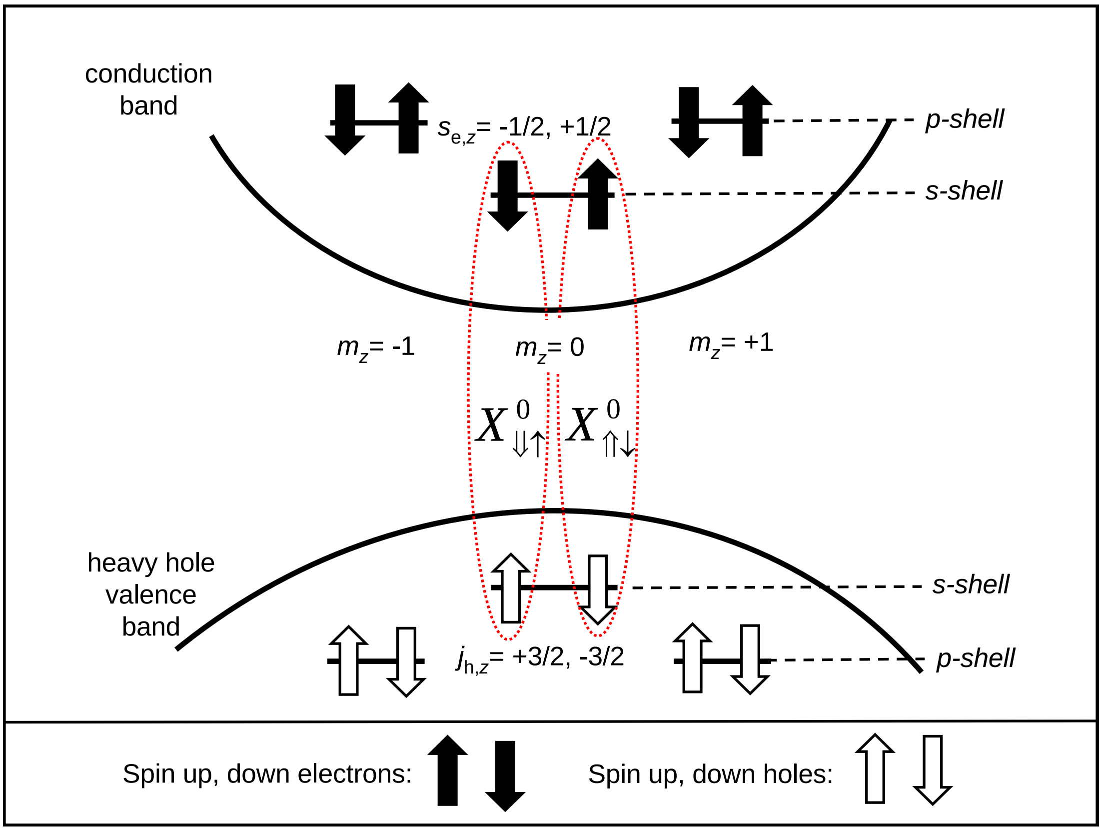

Figure 2.2: *The two-fold spin-degenerate s-shell and p-shell conduction band and valence band states in a quantum dot. The heavy hole valence band and electron conduction band states are shown for* $m_z = -1,\ 0,\ +1$. *The z-projections of the electron spin are labelled* $s_{\mathrm{e,z}}$ *for the electron and* $j_{\mathrm{h,z}}$ *for the hole. The dashed red line indicates the bound electron hole pairs or excitons:* $X^0_{\Uparrow\downarrow}$ *and* $X^0_{\Downarrow\uparrow}$

Figure 2.2 shows the s-shell and p-shell states in a quantum dot, with the two spin levels for each state identified. The electron spin angular momentum projection in the z-direction is labelled $s_{\mathrm{e,z}} = \pm 1/2(\hbar)$. The hole spin angular momentum projection in the z-direction is labelled $j_{\mathrm{h,z}} = \pm 3/2(\hbar)$. The red dashed lines in Fig. 2.2 indicate the formation of the bound electron-hole pairs, or excitons. In quantum dots, the formation of excitons results from the confinement potential, rather than the electron's and hole's mutual Coulomb interaction. However, the exciton's energy is reduced as a result of the binding of the electron and hole. The s-shell excitons are formed from the single particle electron and hole states states and have a spin $S_z = j_{\mathrm{h,z}}(\hbar) + s_{\mathrm{e,z}}(\hbar) = -2, -1, +1, +2$.

In an optical transition, the formation of exciton states with spin $S = \pm 2$ is not allowed due to the conservation of angular momentum. These states are therefore known as dark excitons. However, a small but finite light hole and heavy hole interaction results in a mixing of excitons with spin $S = \pm 1$ and $S = \pm 2$, which means the $S = \pm 2$ states can sometimes be observed [15]. The dark states have much weaker dipole moments, but the strength of the mixing can be increased by a reduction of the symmetry under the application of an external field. For example in chapter 5 we will see how a Voigt geometry magnetic field, applied in the sample plane, allows the $S = \pm 2$ states to become observable.

The exciton states with spin $S = \pm 1$ are allowed according to the selection rules for dipole transitions. These states are therefore known as bright excitons and are labelled in Fig. 2.2 as $X^0_{\Uparrow\downarrow}$ and $X^0_{\Downarrow\uparrow}$. Here, the electron and hole spin in the growth direction is denoted as 'up(down)' $\uparrow$ ($\downarrow$) and $\Uparrow$ ($\Downarrow$) respectively. A photon that is resonant with the crystal ground state $|0\rangle$ to neutral exciton state $|X^0\rangle$, and with circular polarisation σ^+, creates a spin-polarised exciton $X^0_{\Uparrow\downarrow}$. Conversely a photon that is resonant with the crystal ground state $|0\rangle$ to neutral exciton state $|X^0\rangle$, and with circular polarisation σ^-, creates a spin-polarised exciton $X^0_{\Downarrow\uparrow}$. However, as a result of the anisotropic electron-hole exchange interaction, the spin degeneracy is lifted due to the quantum dot asymmetry, and this will be explained in the following section.

2.2.2 Fine structure and electron and hole exchange energy

The neutral exciton fine-structure splitting is a result of the anisotropic electron-hole exchange interaction which originates from the asymmetry of a quantum dot. The Hamiltonian [22], [23], [24] for the electron-hole exchange interaction can be written as an effective coupling of the electron spin S and hole angular momentum J:

$$H_{\text{exc}} = -\sum_{i=x,y,z} \left(a_i J_i^{\text{h}} S_i^{\text{e}} + b_i (J_i^{\text{h}})^3 S_i^{\text{e}} \right), \tag{2.6}$$

where a_i and b_i are coupling constants, which are anisotropic due to the quantum dot asymmetry. The Hamiltonian in eqn 2.6 may be written in the basis of the eight lowest energy states consisting of excitons formed from both the heavy hole (hh) and light hole (lh) states [23]. The hh-lh splitting due to the high strain in a quantum dot, and quantum confinement, is typically much larger than the electron-hole exchange interaction energies. Therefore, the exchange interaction may be simplified to the 4×4 matrix with the basis states $|\Uparrow\downarrow\rangle$, $|\Downarrow\uparrow\rangle$, $|\Uparrow\uparrow\rangle$, $|\Downarrow\downarrow\rangle$ [23]

$$H_{\text{exc}} = \frac{\hbar}{2} \begin{pmatrix} \delta_0 & \delta_1 & 0 & 0 \\ \delta_1 & \delta_0 & 0 & 0 \\ 0 & 0 & -\delta_0 & \delta_2 \\ 0 & 0 & \delta_2 & -\delta_0, \end{pmatrix} \tag{2.7}$$

where, $\delta_0 = \frac{3}{4}a_z + \frac{27}{16}b_z$, $\delta_1 = \frac{-3}{8}(b_x - b_y)$ and $\delta_2 = \frac{-3}{8}(b_x + b_y)$ are the exchange energy splittings. For an asymmetric dot $b_x \neq b_y$ and therefore $\delta_1 \neq 0$. Typical values for the exchange energy splittings for In(GaAs) quantum dots are $\delta_0 = (100 - 500)$ μeV, $\delta_2 \sim 0$ [25], [23], and $|\delta_1| = (10 - 100)$ μeV [26]. The coupling between the bright states $|\Downarrow\uparrow\rangle$ and $|\Uparrow\downarrow\rangle$ by the off-diagonal terms δ_1 means that the energy eigenstates of the bright excitons are transformed from circular basis to the linear superpositions:

$$X^0_{\text{X}} = \frac{1}{\sqrt{2}}\left(|\Downarrow\uparrow\rangle + |\Uparrow\downarrow\rangle\right) \tag{2.8}$$

$$X^0_{\text{Y}} = \frac{1}{\sqrt{2}}\left(|\Downarrow\uparrow\rangle - |\Uparrow\downarrow\rangle\right), \tag{2.9}$$

where the X and Y states are orientated along the crystal axes [110] and [$\bar{1}$10], and are separated by the fine-structure splitting energy. $\hbar\delta_1 \equiv \hbar\delta_{\text{fs}}$.

The fine-structure splitting of the neutral exciton is often undesirable in QIP schemes. It makes it harder to conserve the transfer of information between a photon and a quantum dot exciton spin state. For example, it is difficult to produce photon entanglement from the bi-exciton radiative cascade using dots with non-zero fine structure. In chapters 4 and 5 we will see how the neutral-exciton fine structure causes a reduction in the maximum obtainable fidelity of the preparation of a hole spin state. However, there are schemes to reduce the fine structure splitting δ_1. For

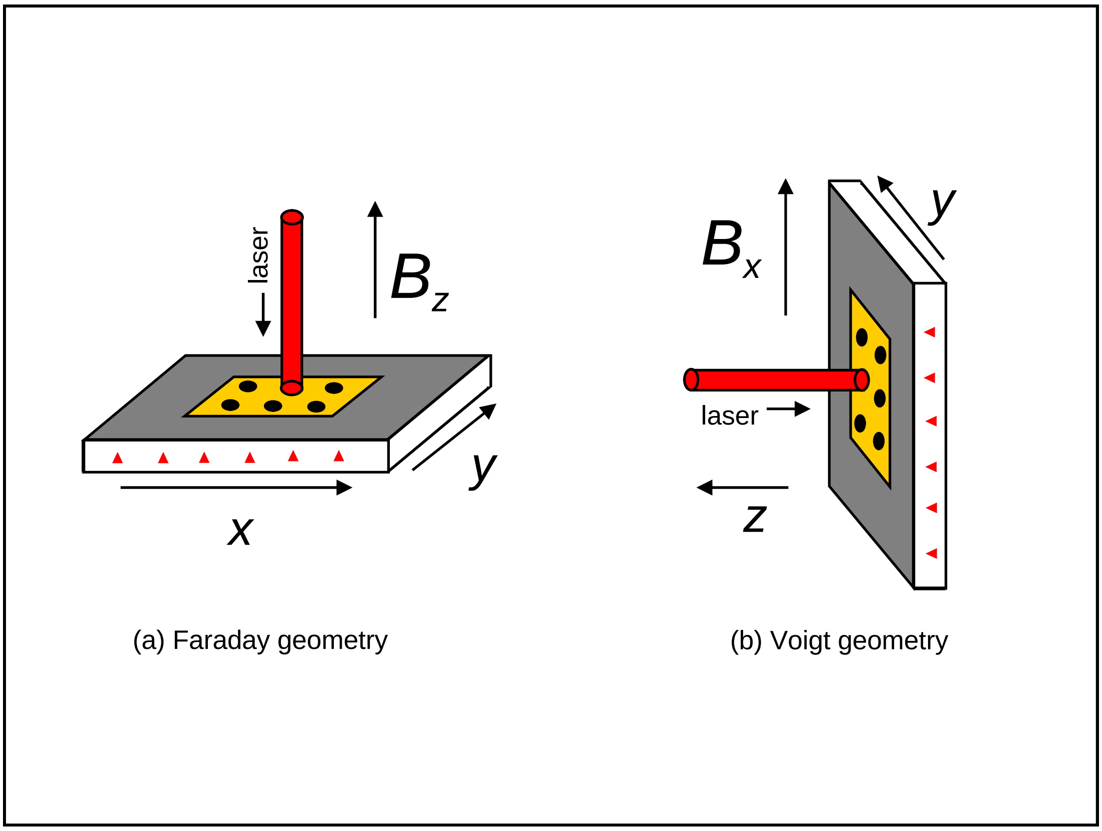

(a) Faraday geometry

(b) Voigt geometry

Figure 2.3: *The axes conventions for (a) Faraday and (b) Voigt geometry magnetic fields.*

example, many groups have recently shown schemes for tuning the fine structure to zero including techniques such as thermal annealing [27], [28], strain tuning [29] and growth on (111)B substrates [30], [31].

2.2.3 Application of external fields

The application of external magnetic and electric fields was used throughout the experiments described in this thesis. This section is a brief introduction to explain the various geometries of magnetic fields, and how the fields affect the energy levels within a quantum dot.

Magnetic fields

The application of an external magnetic field can be used to lift the degeneracy of quantum-dot spin states. The magnetic field causes a Zeeman splitting between the spin states, $\Delta E_Z = g_\alpha \mu_B B$, which is determined by the g-factor g_α. Experiments in which the magnetic field is applied along the growth direction (z) are known as Faraday geometry experiments, whereas magnetic fields applied in-plane (x or y direction) are termed Voigt geometry magnetic fields. Figure 2.3 illustrates the sample in the Faraday and Voigt geometries, along with the definition of the $x-y-z$ directions.

In chapter 4 we will see how the application of a Faraday geometry magnetic fields transforms the neutral exciton energy eigenstates from linear to circular polarisation, which improves the fidelity of the preparation of a hole spin state. In chapters 5 and 6 we will see how the application of a Voigt geometry magnetic field results in the mixing of the bright and dark neutral exciton states [23] as already discussed. Furthermore, the Voigt geometry magnetic field is an integral part of coherent control experiments since it provides an axis of rotation about which a Zeeman-split spin state precesses. This will be discussed in detail in chapter 5.

Electric fields

The energy of quantum dot excitons may also be controlled by the application of an external electric field, via the quantum confined Stark effect. The electric field causes a displacement of the electron and hole wavefunctions. The energy shift is given by $\Delta E_{\mathrm{S}} = \mu F + \alpha F^2$, where μ is the exciton electric-dipole moment and α is the polarisability in the direction of the electric field F. In order to apply a well-defined electric field in the z direction, quantum dots are often embedded in diode structures which can be used to deterministically charge [32], [33], [34] the dots and Stark shift the states [35]. Electric fields can also be applied in the quantum dot plane in order to tune the neutral exciton fine structure [36], [37].

2.2.4 Charged excitons

A neutral exciton is a bound electron-hole pair. A singly-charged exciton or trion consists of three bound charge carriers: two electrons and one hole for a negative trion or two holes and one electron for a positive trion. Trions can be photogenerated when a photon excites an additional electron hole pair in a quantum dot that already contains a charge. The resident charge in the dot can be introduced via dopants near to the quantum dot layer during growth [38], by controllable charge tuning when the dot is embedded in a diode structure [32], or by the ionisation of a neutral exciton [8] [39], [40], [41].

2.3 Coherence of carrier spins in quantum dots

One of the criteria for the physical implementation of QIP is "Long relevant decoherence times, much longer than the gate operation time" [3]. Decoherence is caused by the interaction of a quantum system with its environment. In this section the decoherence processes for electron and hole spins confined in quantum dots are considered.

2.3.1 General concepts

The coherence time of a two-level system is characterised by two timescales. The first is the relaxation of the state population T_1 which is known as longitudinal decay. The second is the decay of the phase factors in the wavefunction T_2^*, termed transverse decay. The overall coherence time of a quantum system is given by:

$$\frac{1}{T_2} = \frac{1}{2T_1} + \frac{1}{T_2^*}, \tag{2.10}$$

where T_2^* is the pure-dephasing caused by interactions which de-cohere the wavefunction without affecting the state population.

It is instructive at this point to make use of the geometric representation of the two-level system, namely the Bloch sphere. The wavefunction of the state: $|\psi\rangle = c_0 |0\rangle + c_1 |1\rangle$ can be represented by a unit vector which points to the surface of the Bloch sphere. This is illustrated by the inset in Fig. 2.4, where the co-ordinate system is also defined. An arbitrary state can be written in terms of the co-efficients of the wavefunction $x = 2\Re\langle c_0 c_1\rangle$, $y = 2\Im\langle c_0 c_1\rangle$ $z = |c_1|^2 - |c_0|^2$. Here z is the population inversion of the two-level system. The coefficients in the wavefunction, c_0 and c_1, can be defined by two angles, θ and ϕ, which give the amplitude and phase of the Bloch vector. In terms of these variables the coefficients may be written as $c_0 = \sin(\theta/2)$ and $c_1 = e^{i\phi}\cos(\theta/2)$. This fully describes the two-level quantum superposition state, and this representation is often useful for describing coherent control of the state-vector and decoherence processes.

Figure 2.4 (a) illustrates the effect of decoherence due to pure dephasing processes T_2^*. The Bloch vector is scattered from the surface of the Bloch sphere towards the center, without changing z.

Figure 2.4 (b) illustrates the effect of decoherence processes due to state relaxation (T_1). Since these effect the relative state populations, they alter z as well. This is why state relaxation T_1 is known as longitudinal decay, dephasing T_2^* is know as transverse decay, and the overall coherence time T_2 in eqn 2.10, is given by a combination of both.

2.3.2 Decoherence of carrier spins in quantum dots

There are two possible sources of spin decoherence for electrons and holes confined to InGaAs/GaAs quantum dots. The first is the coupling of the spin to its motion via the spin-orbit interaction. This leads to spin relaxation (T_1) through spin flips mediated by phonons. We will see below that this is highly suppressed in quantum dots due to quantum confinement. The second is the coupling to the ensemble of randomly fluctuating nuclear spins within the quantum dot. This is the dominant source of decoherence and is mediated by the hyperfine interaction. These effects are discussed in the following.

2.3.3 Spin relaxation T_1 via the spin orbit interaction

An electron moving in the presence of an electric field $\hat{E}$ experiences a Lorentz effective magnetic field $\hat{B}_{\text{eff}} \propto \hat{E} \times \hat{p}$, where $\hat{p}$ is the momentum of the electron. In a

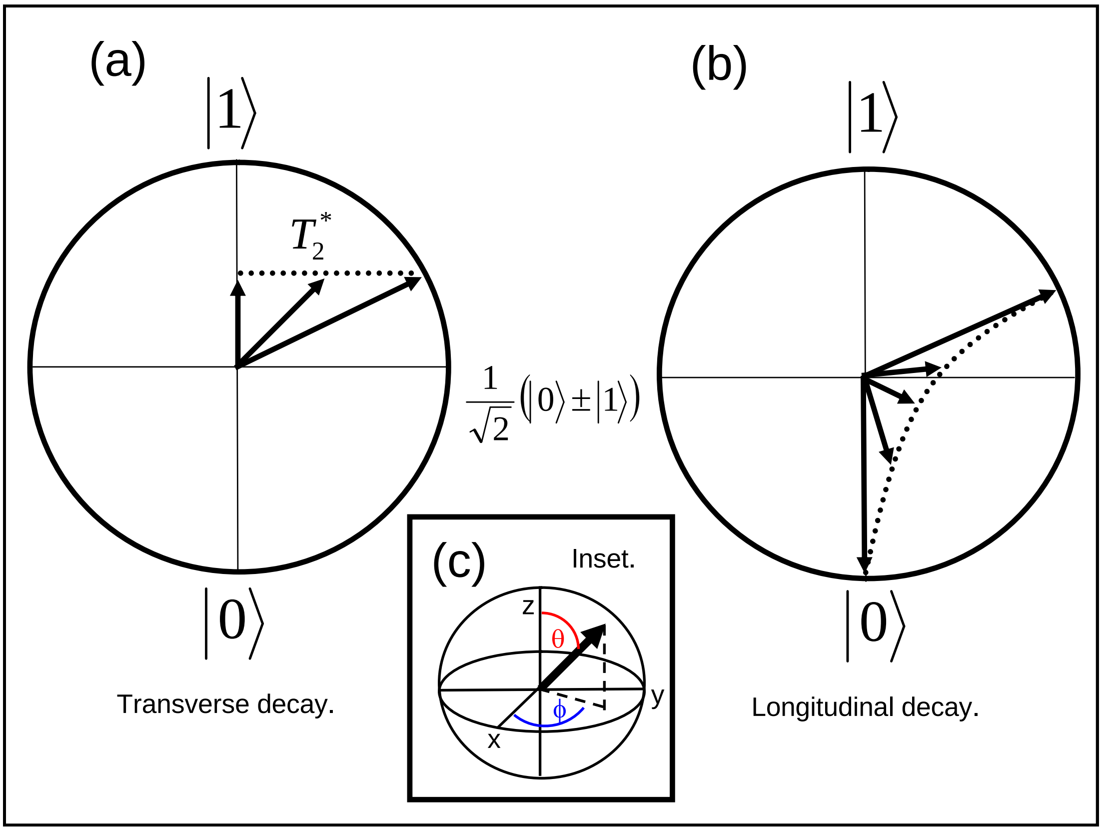

Figure 2.4: *Bloch sphere representation of decoherence processes. (a) Transverse (T_2^*) and (b) longitudinal T_1 relaxation. T_2^* processes conserve the Bloch vector length z, but T_1 do not. (c) inset: Bloch sphere angles θ and ϕ which determine the amplitude and phase of the Bloch vector.*

solid, the electric field originates from the charged atoms in the crystal lattice, and in the case of quantum confined systems, it is asymmetric. The spin-orbit interaction may be characterised by a spin-orbit length, which is a measure of the dimension in which the electron's spin is rotated by an angle π. The spin orbit length in GaAs is $\sim (1-10)$ μm [42], which is much larger than the quantum dot. Therefore, the quantum confinement suppresses the spin-orbit interaction. This has been confirmed by measurements of long electron spin relaxation times. For example $T_1^{\mathrm{e}} \sim$ tens ms has been reported in reference [8]. The hole spin relaxation time was predicted to be smaller due to finite heavy hole-light hole mixing [42]. However, hole spins in quantum dots also exhibit long spin relaxation times, due to the large energy splitting between light and heavy holes. This was confirmed by measurements of $T_1^{\mathrm{h}} \sim$ hundreds μs in reference [39] and $T_1^{\mathrm{h}} \sim 1$ ms in ref. [43].

2.3.4 Spin dephasing T_2^* via the hyperfine interaction

The confinement of an electron spin in a quantum dot suppresses the spin-orbit interaction and leads to long spin relaxation times. However, this is offset by dephasing of the electron spin state caused by the interaction with the ensemble of nuclear spins. The hyperfine interaction can be thought as an effective magnetic field which acts on the spin state. This effective magnetic field is known as the Overhauser field and fluctuates randomly in time due to the random orientation of the nuclear spins. We now consider the decoherence of an electron spin due to the randomly fluctuating Overhauser field. The Hamiltonian for an electron spin S interacting with a nuclear spin I_k may be written as [13]:

$$H_{\mathrm{hf}} \sim \delta(r_k)S.I + \frac{(n_{\mathrm{k}}.S)(n_k.I - S.I)}{r_k^3(1 + d/r_k)} + L_{\mathrm{k}}.I_k, \tag{2.11}$$

where $\mathbf{r_k}$ is the electron position operator relative to the nucleus k, $\mathbf{n_k} = \mathbf{r_k}/r_k.S$, d is the size of the nucleus and L_k is the orbital angular momentum operator. The first term in eqn 2.11 is known as the contact hyperfine interaction. It depends on the probability density of the electron wavefunction at the nuclear site. The second term is known as the dipole-dipole interaction. It describes the interaction of the electrons spin magnetic moment with the nuclear spin magnetic moment. It is a ‘long-range’ interaction, and is a function of the relative separation of the spins. The third term describes the spin-orbit interaction which couples the electron’s orbital motion to the nuclear spin. Electrons have *s*-type orbitals. Therefore the spin-orbit term is zero for the case of electrons. The randomly fluctuating Overhauser field results in the randomisation of the phase factors in the wavefunction and hence spin decoherence

The hyperfine interaction also leads to spin relaxation due to ‘flip-flop’ processes, where the spin of an electron is flipped, via exchange with a nuclear spin. This spin flip-flop rate is given by $w_s \sim |A_{\mathrm{hf}}|^2 / \Delta E_{\mathrm{e}}^2$, where A_{hf} is the hyperfine coupling constant for the electron or hole, and ΔE_{e} is the Zeeman splitting between the spin states [44]. The flip-flop processes pump nuclear spin polarisation and have been shown to lead to interesting effects such as dynamic nuclear polarisation [45] [44] [46], [47], [48], [49], nuclear spin feedback [50], [51], the ability to control nuclear spins states coherently using optically detected nuclear magnetic resonance [52], and the direct measurements of hyperfine constants [53], [54], [15]. The electron spin flip-flop processes can be suppressed by increasing ΔE_{e} by the application of a magnetic field [9] and is weaker for heavy-holes due to conservation of angular momentum.

The most significant term for electrons in eqn 2.11 is the contact hyperfine interaction. The electron has an *s*-type orbital wavefunction and therefore a high probability density at the nuclear site. This interaction leads to electron spin dephasing on a timescale of a few ns as measured by several groups [38], [11], [12], [55], [56]. The fast electron spin dephasing thus limits its usefulness as a qubit. However, the coherence can be recovered, by use of spin echo techniques, which re-focus the electron spin [57], [58] to recover the $\sim \mu$s coherence time.

A hole has a *p*-type orbital wavefunction. Therefore the contact term is zero since $|\psi(0)|^2 = 0$. This has stimulated interest in the use of hole spins as potential qubits, encouraged by measurements of μs coherence times in coherent population trapping experiments [16]. Theoretical predictions suggest that the dipole-dipole interaction of the hole spin simplifies to an Ising form: $H_{\mathrm{hf}} = \sum_k A_k^h s_z I_k^z$ [13]. Here A_k^h is the coupling constant for holes, s_z is the hole pseudospin 1/2 operator and I_k^z is the component of a nuclear spin k in the z-direction. The Ising form means that the effective magnetic field only acts in the z-direction. Calculations suggest that hole hyperfine coupling constant A^{h} should be approximately 10% of that of the electron [14]. This has been confirmed experimentally [54], [15]. The anisotropic nature of the hole hyperfine interaction may lead to a reduced decoherence in the presence of an in-plane magnetic field [13], but measurments of A^{h} in this experimental geometry are not currently available.

Recently measurement of $T_2^* = 2.3$ ns and $T_2^* = 20$ ns have been reported for holes in an in-plane magnetic field in references [38] and [59] respectively. In both cases the authors attribute the dephasing to in-plane hole g-factors that are sensitive to charge fluctuations in their p-type devices [60]. In reference [38], spin echo techniques are used to recover $\sim \mu$s coherence time for the hole. A detailed discussion of this can be found in chapter 4, where a measurement of $T_2^* \sim 15$ ns is reported.

2.4 Coherent optical spectroscopy of two level systems

A two-level system may be controlled coherently with an optical field, provided that the interaction timescale is faster than the coherence time T_2. Control over the complex amplitude and phase of the wavefunction is often achieved by using an intense laser field with well defined and uniform phase. In this section the Rabi oscillation of two-level system is introduced, the schemes to initialise spin qubits are reviewed, and the state of the art in experiments to implement spin control are discussed.

2.4.1 Rabi oscillations of excitonic qubits

A two-level system interacting with a coherent laser field will undergo Rabi oscillations, if the interaction time is less than the coherence time. Consider the two-level system in Fig. 2.5. The crystal ground state $|0\rangle$ has energy $\hbar\omega_0$. The excited state $|1\rangle$ is the bound electron-hole pair or exciton of energy $\hbar\omega_1$. The optical transition therefore has energy $\hbar\omega_{01} = \hbar\omega_1 - \hbar\omega_0$. A laser with energy $\hbar\omega_l$ and detuning $\hbar\delta_l = \hbar\omega_l - \hbar\omega_{01}$ interacts with the system. By solving the Schrödinger equation it can be shown that the state populations oscillate at the effective Rabi frequency $\Omega_{\text{eff}} = \sqrt{\Omega_{\text{R}}^2 + \delta_l^2}$ [6]

$$|c_1|^2 = \frac{\Omega_{\text{R}}^2}{\Omega_{\text{eff}}^2} \sin^2\left(\frac{\Omega_{\text{eff}} t}{2}\right), \tag{2.12}$$

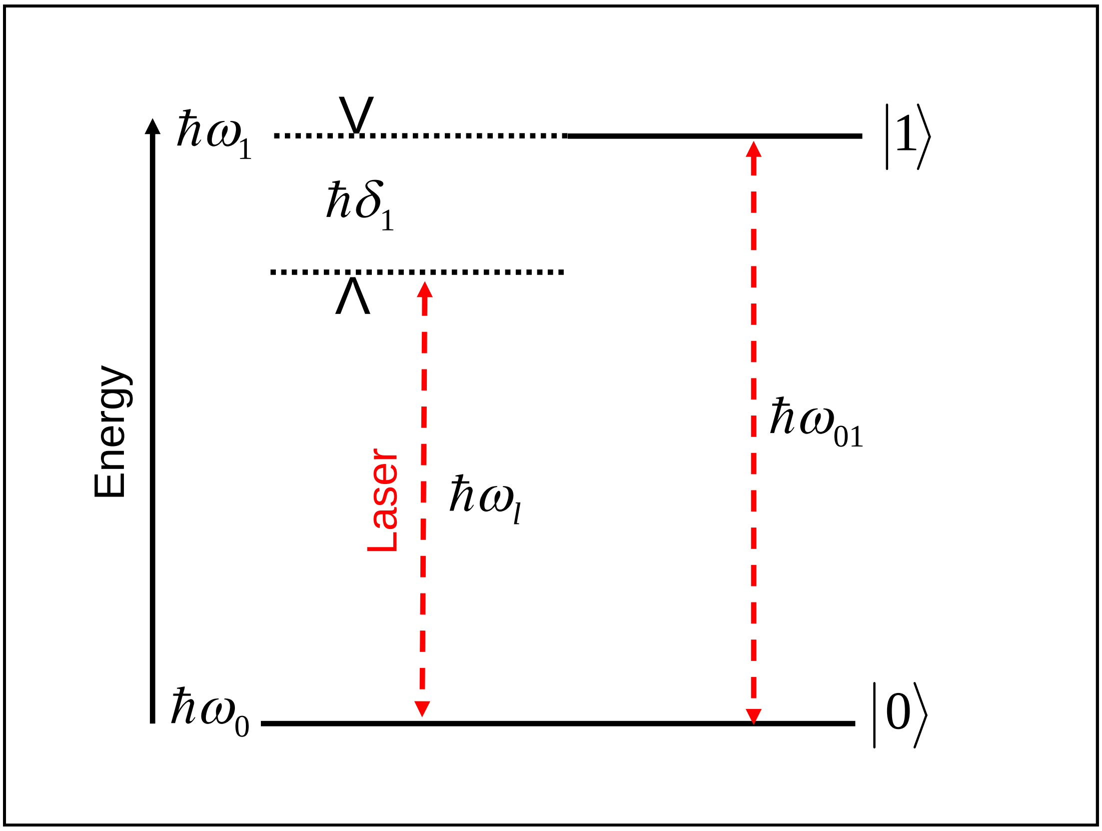

Figure 2.5: *Two-level system interacting with a laser field. $|0\rangle$ is the crystal ground state of the quantum dot. The excited state $|1\rangle$ is the neutral exciton. An optical transition of energy $\hbar\omega_{01}$ between the states may be driven by a laser with an energy $\hbar\omega_l$ and detuning δ_l.*

where c_1 is the complex amplitude state $|1\rangle$ and the Rabi frequency on resonance is Ω_{R}. It is defined as

$$\Omega_{\mathrm{R}} = \left|\frac{\bar{\mu}_{01}.\bar{E}_0}{\hbar}\right|, \tag{2.13}$$

where $\bar{\mu}_{01}$ is the dipole moment of the transition and $\bar{E}_0$ is the electric field strength of the laser. Pulsed excitation is often used to drive Rabi oscillations so that time-resolved spectroscopy can be performed. A convenient quantity used to describe pulsed excitation is the pulse area Θ, which is defined by the time integral of the Rabi-frequency:

$$\Theta = \int_{t=-\infty}^{t=+\infty} \Omega_{\mathrm{R}}(t)\mathrm{d}t, \tag{2.14}$$

where $\Omega_{\mathrm{R}}(t)$ is the time-dependent Rabi frequency, which, in the case of a Gaussian laser pulse, has a Gaussian envelope. The state of the two-level system may be considered diagrammatically using the Bloch-sphere representation (see for example Fig. 2.4. The laser pulse rotates the Bloch vector by an angle determined by the pulse area. For this reason the Rabi oscillation is often referred to as a Rabi-rotation of the state of the system, described by the matrix:

$$\hat{U}(\Theta) = \begin{pmatrix} \cos(\Theta/2) & -i\sin(\Theta/2) \\ -i\sin(\Theta/2) & \cos(\Theta/2). \end{pmatrix} \tag{2.15}$$

The wavefunction can therefore be controlled by varying the pulse area. For example, a resonant laser pulse with pulse area $\Theta = \pi/2$ acting on the state $|0\rangle$ results in the superposition state $\frac{1}{\sqrt{2}}(|0\rangle + i\,|1\rangle)$. This is equivalent to a rotation of the Bloch vector by an angle $\phi = \pi/2$. The state of the two-level system can be fully controlled by using sequences of laser pulses to observe effects such as Ramsey interference, and full control over excitonic qubits has been achieved [61], [4], [5] [62].

The interaction of the excitonic qubit with its environment leads to decoherence which manifests itself in the form of intensity damping of the Rabi-rotations. The damping of neutral exciton Rabi-rotations is caused by the interaction with a bath of longitudinal acoustic phonons [63],[64].

2.5 Coherent control of a quantum dot spin

Excitonic qubits have coherence times limited by radiative recombination, which, at best, is on the order of a ns. An electron or hole spin trapped in a quantum dot has the potential for a much longer coherence time as discussed in section 2.3. In this section techniques for initialising, controlling and reading out a single spin in a quantum dot are discussed. Furthermore a simple introduction to the various schemes used to control a single spin coherently will be given.

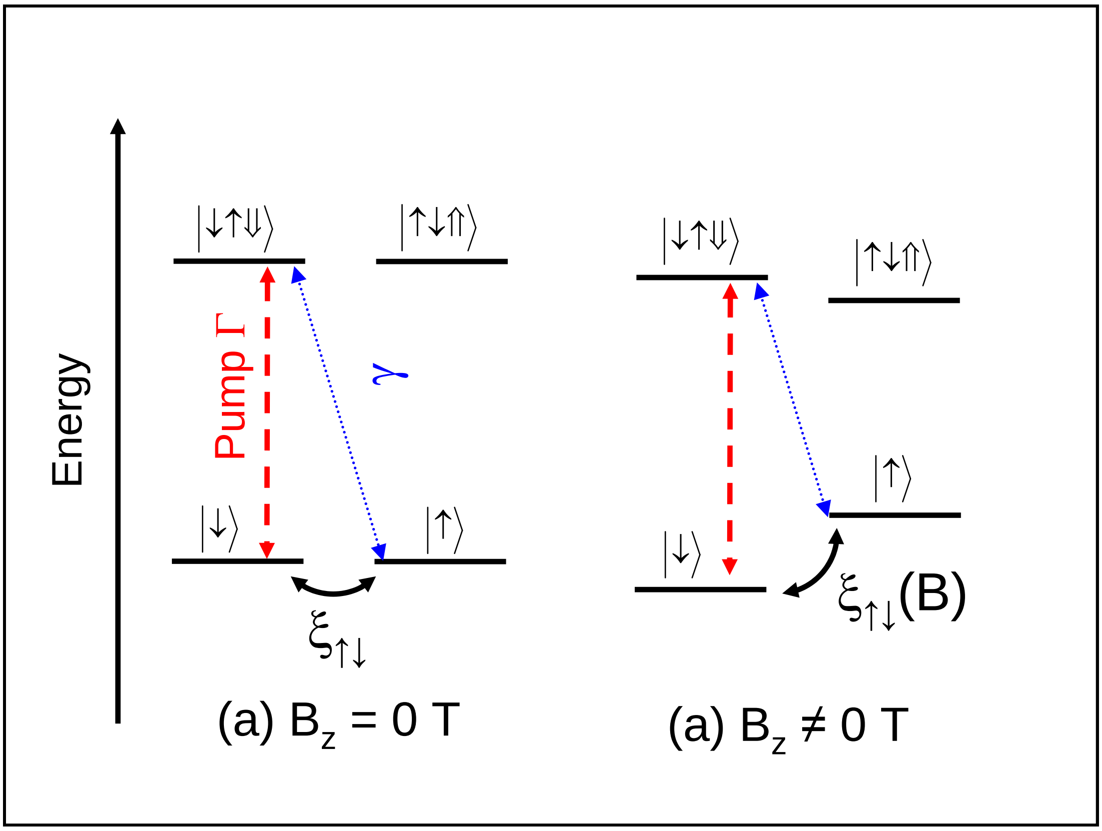

Figure 2.6: *(a) Energy level diagram electron spin states up* $|\uparrow\rangle$ *and down* $|\downarrow\rangle$*, and charged exciton states* $|\uparrow\downarrow\Uparrow\rangle$ *and* $|\downarrow\uparrow\Downarrow\rangle$ *at* $B = 0$ T *(b) equivalent diagram with an applied magnetic field* B_z*. A pump laser resonant with the* $|\downarrow\rangle \longleftrightarrow -|\downarrow\uparrow\Downarrow\rangle$ *transition excites the system into the* $|\downarrow\uparrow\Downarrow\rangle$ *state with a rate* Γ*.* γ *is the spontaneous Raman scattering rate and* $\xi_{\uparrow\downarrow}$ *is the nuclear spin 'flip-flop' rate.*

2.5.1 Spin initialisation techniques

Optical pumping

One technique for preparing a spin state in a quantum dot is optical shelving or optical pumping using a CW laser. First the quantum dot is loaded with a single charge carrier. This is usually achieved by introducing dopants near to the quantum dot layer during growth [38], or by embedding the dots in a diode and tuning the Fermi-level of the contact relative to the energy level of the quantum dot [32], [60]. The optical pumping is achieved by exciting a transition to the charged exciton state, followed by relaxation via spontaneous emission. This will be explained by following the energy level diagram in Fig. 2.6

Fig 2.6(a) is an energy level diagram consisting of the electron spin levels and the charged exciton levels which form the ground and excited states respectively. Figure 2.6(a) shows the states without an applied magnetic field. The transitions are circularly polarised and a σ^- CW pump laser is resonant with the $|\downarrow\rangle \longleftrightarrow |\downarrow\uparrow\Downarrow\rangle$ transition. This excites population of the $|\downarrow\uparrow\Downarrow\rangle$ state. The finite heavy-hole light-hole mixing results in a small but finite probability that the $|\downarrow\uparrow\Downarrow\rangle$ state decays by emission of a σ^+ photon to the $|\uparrow\rangle$ state via spontaneous Raman scattering [9]. The degeneracy of the electron spin states results in fast spin relaxation between the states $|\uparrow\rangle$ and $|\downarrow\rangle$, where $\xi_{\uparrow\downarrow}$ is the nuclear spin 'flip-flop' rate and γ is the spontaneous Raman scattering rate. Therefore, without an applied magnetic field, spin pumping will not occur. However, when a magnetic field is applied in the Faraday configuration, the electron and nuclear Zeeman energy splittings are incommensurate i.e. the spin flip rate $\xi(\mathrm{B})$ decreases with increasing magnetic field. This is illustrated in Fig. 2.6(b). After several cycles of excitation and emission and under the condition $\Gamma \gg \gamma \gg \xi_{\uparrow\downarrow}(\mathrm{B})$, the electron is shelved into the $|\uparrow\rangle$ state. Atatüre *et al.* first demonstrated high fidelity ($F \gg 99.9\%$) optical shelving of an electron spin in reference [9] by the application of a Faraday-geometry magnetic field. Furthermore Gerardot *et al.* [43] showed that the spin pumping technique works for hole spins at zero magnetic field. This is due to the fact that the nuclear spin 'flip-flop' rate ξ is much smaller for holes than for electrons. Using this fact, Gerardot *et al.* demonstrated high fidelity hole-spin preparation $F > 99.9\%$

The drawback to the optical pumping technique is that it is limited by the rate γ. γ is inherently small because the 'cross' transitions in Fig. 2.6 are only weakly allowed . This means that the time to initialise the electron spin is several μs. This problem was partially addressed in refs [65] [66]. There, Emary *et al.* and Xu *et al.* showed that the application of a Voigt-geometry magnetic field allows for faster spin intialisation because the 'cross' transitions are allowed in this configuration. This results in spin preparation times closer to the $\sim$ 1ns radiative recombination time.

In most optical-pumping schemes to initialise spins, the spin readout is performed by using the pump laser to drive a transition between the intialised spin

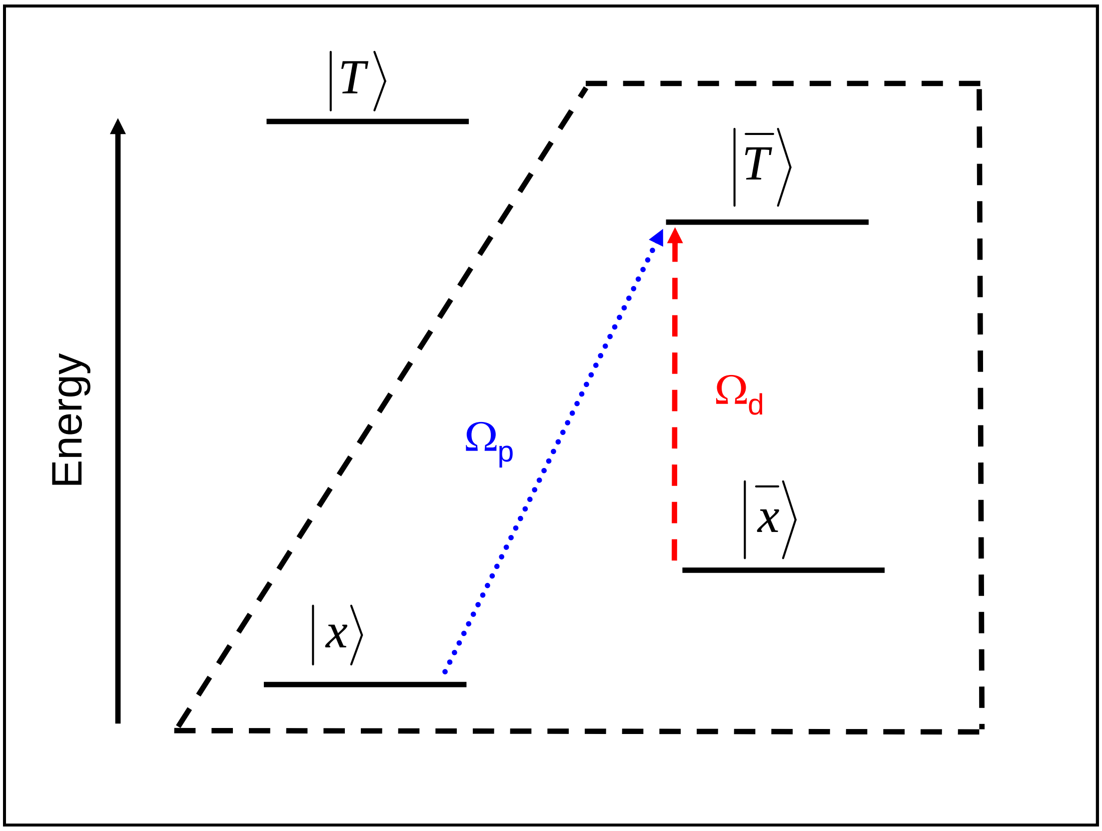

Figure 2.7: *Energy level diagram to show how coherent population trapping works. The diagram shows the electron spins eigenstates* $|x\rangle$ *and* $|\bar{x}\rangle$ *and the charged exciton eigenstates* $|T\rangle$ *and* $|\bar{T}\rangle$ *in a Voigt geometry magnetic field. Two laser fields, namely the driving laser and the probe laser, with respective Rabi-frequencies* Ω_d *and* Ω_p*, drive the system into a 'dark' state. This makes the transition 'invisible' to the probe under the two-photon resonance condition.*

and a trion. This has a drawback in that it is a destructive measurement of the spin state. One way to circumvent this is to use a quantum dot molecule (a pair of tunnel coupled quantum dots). This was the approach adapted by Kim *et al.* [67]. There the authors prepare the spin in one of the quantum dots and readout the spin via a transition in the other. This has been extended by the work of Vamivakas *et al.* who demonstrate the ability to non-destructively measure the spin state of an electron in a tunnel-coupled quantum dot in real time [68].

Coherent population trapping

A potential drawback to spin initialisation by optical pumping is that, in general, the spin can only be prepared in an eigenstate of the system, as opposed to any arbitrary state. This potential limitation of the optical pumping technique was overcome in the experiments of Xu *et al.* [69]. These experiments make use of the phenomenon of coherent population trapping (CPT) which is related to the physics of electromagnetically-induced transparency [70]. Figure 2.7 is an energy level diagram to help show how CPT is implemented. The figure shows the electron spin states $|x\rangle$ and $|\bar{x}\rangle$ and charged exciton states $|T\rangle$ and $\left|\bar{T}\right\rangle$ of a quantum dot in a Voigt-geometry field. The Zeeman energy splitting allows the four-level system to be reduced to a three-level lambda system. This is indicated by the dashed lines in Fig. 2.7. A driving laser field with Rabi-frequency Ω_{d} is resonant with the $|\bar{x}\rangle \longleftrightarrow \left|\bar{T}\right\rangle$ transition. A probe laser field with Rabi-frequency Ω_{p} is scanned through the $|x\rangle \longleftrightarrow -|T\rangle$ transition. When the probe is on resonance, the two-photon absorption condition is met, i.e. the frequency difference of the two lasers is equal to the electron Zeeman energy splitting. Under this condition a ‘dark-state’ with no trion component is formed. The dark-state is a coherent superposition of the electron spin states: $\psi = (\Omega_{\mathrm{d}} |x\rangle - \Omega_{\mathrm{p}} |\bar{x}\rangle /)\sqrt{\Omega_{\mathrm{d}}^2 + \Omega_{\mathrm{p}}^2}$ [69]. Therefore by the variation of the relative intensities of the driving and probe fields, any arbitrary coherent superposition of the eigenstates of the electron spin may be prepared.

CPT has also been demonstrated for a hole spin by Brunner *et al.*, as opposed to an electron spin [16]. In these experiments the absorption of the probe laser shows high visibility dips in the two-photon resonance condition. The visibility of the dips is a measure of the hole spin coherence. The authors report coherence times $T_2 > 100$ ns with 90% confidence. In these experiments it is likely that the dark state of the hole lies along the magnetic field direction. In this case the hole spin is less sensitive to the hyperfine interaction due to its anisotropic nature. These long coherence times demonstrate the hole spins potential as a qubit.

Ionisation of a spin-polarised electron-hole pair

Another approach to initialise a single spin in a quantum dot is to use the fast dissociation of a photo-generated, spin-polarised electron-hole pair. This approach was first used by Kroutvar *et al.* in their experiments that demonstrate electron spin memory in an ensemble of quantum dots [8]. The quantum dots were embedded in a Schottky diode structure. Kroutvar *et al.* used circular polarisation to excite spin-polarised electron-hole pairs. The large electric field ensured that the holes (in this case) tunneled from the dots much faster than the radiative recombination time to leave spin-polarised electrons. The relaxation time of the electron spins was then probed by injecting holes into the device in forward bias. Similar techniques were employed by Heiss *et al.* in experiments to measure the hole spin relaxation time [39], [71]. The exciton ionisation technique has also been used to initialise electron spins in single quantum dots by the work of Young *et al.* [40], and hole spins in single quantum dots by the experiments of Ramsay *et al.* [41], [5] and Heiss *et al.* [72]. The exciton ionisation technique for initialising a single hole spin in a quantum dot was used throughout the experiments described in this thesis in chapters 4, 5 and 6.

2.5.2 Spin readout techniques

Before discussing the techniques used to control a single spin coherently, some of the experimental techniques for spin readout or measurement will be briefly introduced. In general a spin is read out by making use of the selection rules of the spin to charge exciton transitions. See, for example, Fig. 2.8. This is used in combination with the Zeeman energy splittings of the states. Many groups use all-optical detection techniques to read out a spin state. These will be briefly discussed and compared to the electrical read out detection used in the experiments described in chapters 4, 5 and 6.

Resonance fluorescence

Resonance fluorescence refers to the measurement of photoluminescence from a resonantly-excited two-level system. The technique is inherently difficult because the excitation photons have the same energy as the emitted photons. Therefore techniques are required which isolate the emitted photons from the scattered laser light. One way to circumvent this is to use cross polarised excitation and detection [11]. Another technique, is the use of orthogonal excitation and detection paths [73], [74]. In refs [73], [74], the quantum dots were located in an optical cavity. The excitation laser path was in a direction parallel to the quantum dot plane, and the cavity preferentially emitted normal to the plane. For co-linear excitation and collection paths, it is possible to use a combination of spectral filtering, polarisation optics and lock-in detection of time-gated single-photon-counting modules (SPC), in order to isolate the quantum dot emission. These are the techniques employed by Press *et al.* in their pioneering work that first demonstrated full coherent control over a single electron spin state in a quantum dot [11]. More recently, similar techniques have been employed in experiments with hole spins [38]. In both sets of experiments, the spin readout used the same laser that optically pumped the spin state. The idea is that if the spin state has not been initialised in the correct state, then a click is recorded on the SPC which corresponds to relaxation from the charged exciton state.

Differential transmission/absorption

In differential transmission, a weak probe laser, with selected polarisation, is used to excite a spin to trion transition resonantly. A small change in the transmitted laser intensity is recorded on resonance as an absorption spectrum [9]. The relative change in transmission is typically small, on the order $\sim 10^{-3}$, which results in a small signal to background ratio. However, techniques such as Stark-shift-modulation spectroscopy can be used with lock-in detection to improve the signal to background ratio [59]. In experiments where the substrate is opaque at the relevant wavelength, a similar technique may be used by detecting the reflected light rather the transmitted light [16].

Kerr and Faraday rotation

Kerr and Faraday rotation measurments use the rotation of the linear polarisation of a probe laser by a small angle as a result of the interaction with the magnetic dipole of a spin-polarised electron. The rotation of the probe laser's linear polarisation is measured in transmission and reflection geometries for Faraday and Kerr rotation measurements respectively. The effect arises from the different phase velocities of the $\sigma^{\pm}$ components of the probe beam. Kerr rotation spectroscopy can be used as non-destructive measurement of a spin state. This has been shown in ref [75], where the probe laser is non-resonant. Kerr rotation spectroscopy has also been used to observe the coherent precession of a single electron spin [55], and to demonstrate optical control of a single electron spin [56]. The small change ($\sim$ mrad) in linear polarisation angles means that modulation and lock-in detection is required. This is often done in the form of a balanced bridge circuit, triggered by the modulation of the probe beam [24].

Electrical readout

Strong electric fields can be applied by embedding a quantum dot in a diode structure. In the regime where the carrier tunneling rates are much faster than the radiative recombination rates, electrical detection can be used to infer the state of the quantum dot. Resonant excitation of neutral and charged exciton species in the dot allows for a change in photocurrent to be measured [76]. In a charged dot, the absorption of the photons is conditional on the spin state of the resident charge. This is a result of the Pauli exclusion principle. Such effects allow for a direct mapping of the charge state to the spin [8], [39], [41]. Photocurrent detection is particularly attractive since it enables measurements with high signal to noise ratios in a relatively short space of time. Many groups have therefore used photocurrent detection for the coherent spectroscopy of quantum dots [61], [4], particularly for the coherent control of exciton spin states [62], [77], [78], [79].

Comparison of optical detection with photocurrent detection

Photocurrent detection was used throughout all the measurements described in this thesis and a comparison between this technique and others is now given. The potential disadvantages of photocurrent detection are the following:

- The large electric field applied to the quantum dot leads to short lifetimes for the carrier spin states. This is because the carriers must tunnel from the dot in order to generate a photocurrent. However, techniques such as voltage modulation [62], [80] may be used to improve the balance between achieving high detection efficiency and long lifetime.
- The diode devices required to measure the photocurrent signal of one electron per pulse need to be of high electrical quality.
- Photocurrent detection requires a large population of the trion states for spin readout and therefore constitutes a destructive measurement of the spin.
- A further drawback to electrical detection is the photocurrent background, attributed to absorption of scattered laser light by neighbouring quantum dots [41], [61]. The background is proportional to the incident laser power and therefore presents a possible challenge for high pulse area measurements in multiple-pulse, coherent-control experiments.

The potential advantages of photocurrent detection are the following:

- It offers the advantage of very high detection efficiency, since all the carriers that tunnel from the dot contribute to the photocurrent signal. For all-optical detection, most of the photoluminescence signal is lost at the semiconductor-air interface. Although the photon extraction efficiency can be improved by using solid immersion lenses (SIL) [81] and/or optical cavities, it is still limited by the efficiency of single-photon detectors.
- Photocurrent detection has the advantage of high-speed data collection. Spectral measurments over $\sim$ meV with $\sim$ 100 data points can be taken in

the space of minutes. Optical detection, on the other hand, often requires long integration times to achieve high enough signal to noise, even if the signal extraction is improved by making use of solid immersion lenses, optical cavities or sensitive detectors.

- The signal-to-noise ratio can be extremely high in photocurrent detection schemes, provided that the electrical device is of high enough quality. For example it is possible to achieve $\sim$ 10 pA signal with a $\sim$ 100 fA noise level.

- Photocurrent detection has the added simplicity that no collection optics are required, nor high-specification equipment such as single photon counting modules or spectrometers.

- Electrical detection has the prospect of integration with photonic structures within a functioning on-chip device with the possibility of electrical control [62].

2.5.3 Spin control techniques

One challenge posed by the use of spin states as qubits, as opposed to exciton states, is that resonant control of the spin states, using fast optical laser pulses, is not possible, because of the small energy splitting between the spin states. Directly controlling the spin state resonantly is only possible using microwave excitation, through electron spin resonance techniques, which are inherently slow. In this section, the methods used to overcome this challenge are introduced. The proposals and experimental reports will be discussed in terms of two approaches to optical rotations of a spin, namely the geometric phase shift, and the AC-Stark shift via stimulated Raman transitions. These concepts are combined with a review of the state of the art in the field.

Most theoretical proposals and experimental reports for the optical control of electron or hole spins make use of Voigt geometry magnetic fields. The magnetic field is used for rotations of a spin about the x axis and an optical pulse is used for

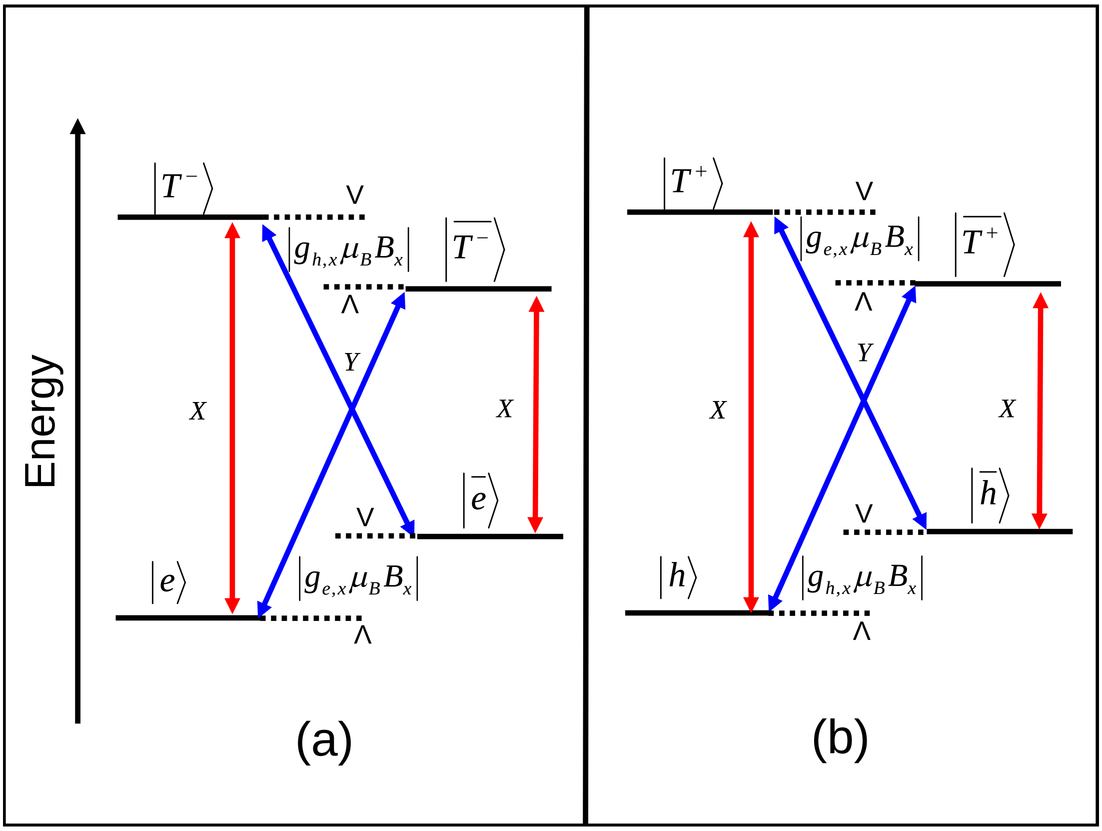

Figure 2.8: *Energy level diagram of negative (a) and positive (b) trions in a Voigt geometry magnetic field. The spin energy eigenstates of (a) the electron $|e\rangle$ and $|\bar{e}\rangle$ and (b) the hole $|h\rangle$ and $\left|\bar{h}\right\rangle$ are aligned along the magnetic field (x) direction. All four transitions from the spin eigenstates to the charged trion states $|T^{\pm}\rangle$ are allowed. The transitions have linearly polarised selection rules labelled with the polarisation X or Y.*

rotations about the z-axis. This will be explained shortly.

Figure 2.8 is an energy level digram of a charged quantum dot system in the Voigt geometry. Figure 2.8 (a) applies to a negatively-charged quantum dot. The spin eigenstates of the electron $|e\rangle$ and $|\bar{e}\rangle$ are aligned along the magnetic field (x) direction. All four optical transitions to the charged exciton states $|T^-\rangle$ and $\left|\bar{T}^-\right\rangle$ are allowed and have linear polarisations labelled X and Y. The electron spin states are split by the electron Zeeman energy splitting $\Delta E_{\mathrm{e,x}} = g_{\mathrm{e,x}}\mu_{\mathrm{B}}B_x$. The charged exciton states are split by the hole Zeeman energy splitting $\Delta E_{\mathrm{h,x}} = g_{\mathrm{h,x}}\mu_{\mathrm{B}}B_x$. Here $g_{\mathrm{e,x}}$ and $g_{\mathrm{h,x}}$ are the in-plane electron and hole g-factors respectively. Figure 2.8(b) is the positively-charged quantum dot energy level diagram which is analogous to Fig. 2.8(a).

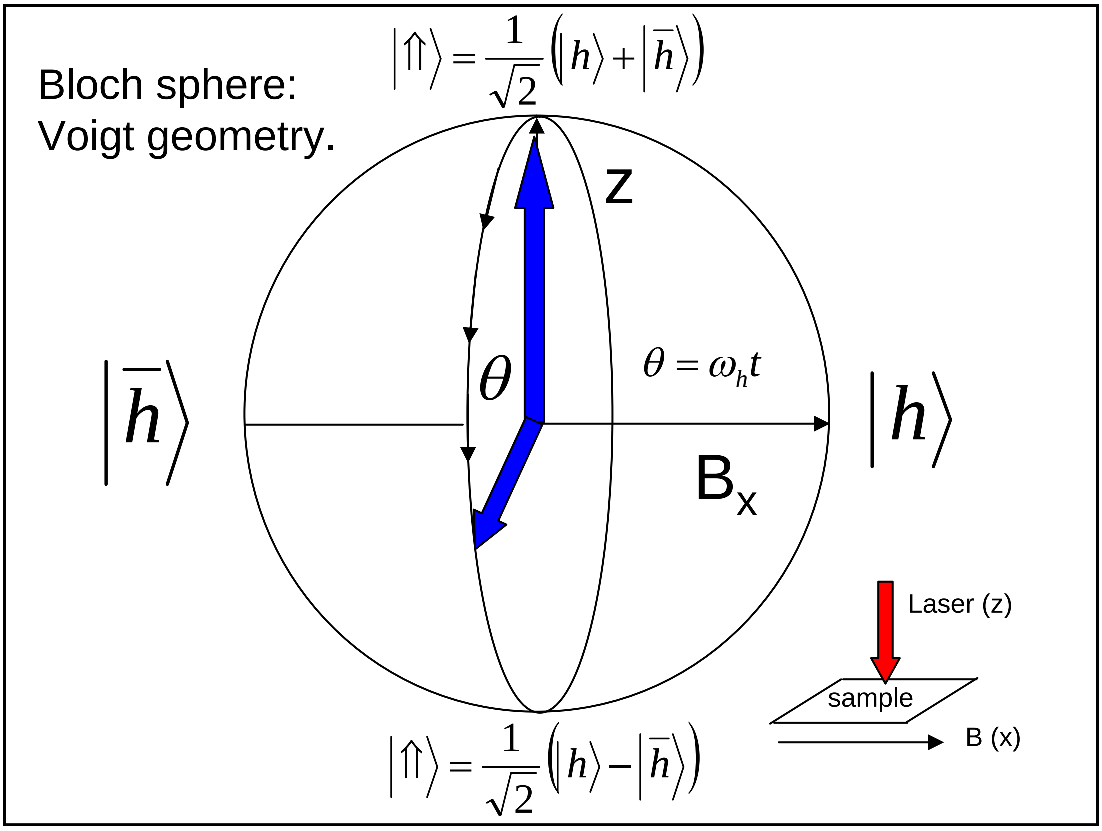

Figure 2.9: *The energy eigenstates of the hole spin* $|h\rangle$ *and* $\left|\bar{h}\right\rangle$ *lie parallel and anti-parallel to the Voigt geometry magnetic field in the x-direction. The eigenstates are split by the Zeeman energy splitting* $\hbar\omega_{\mathrm{h}}$*. A hole spin up* $|\Uparrow\rangle$ *is a superposition of these states, and if prepared (solid blue arrow), will precess about the magnetic field by an angle* $\theta = \omega_{\mathrm{h}} t$*. Inset: sample geometry*

Spin precession about an applied magnetic field

Having considered the energy-level diagram for the system, we move to consider how coherent spin control it is implemented. First we consider spin precession about an applied magnetic field. It is instructive at this point to make use of the diagrammatic representation of the spin state based the Bloch sphere. Figure 2.9 is a Bloch sphere to illustrate the rotation of a hole spin due to its precession about the Voigt geometry magnetic field. For this discussion the same arguments apply to the electron spin. As previously discussed, the energy eigenstates of the hole spin lie along the magnetic field direction. If a hole spin is initialised in an energy eigenstate, the state remains stationary and no precession will be observed. If however, a coherent superposition of the eigenstates is prepared, namely $|\Uparrow\rangle = 1/\sqrt{2}(|h\rangle + \left|\bar{h}\right\rangle)$

or $|\Downarrow\rangle = 1/\sqrt{2}(|h\rangle - |\bar{h}\rangle)$, the spin states accumulate a relative phase and the Bloch vector will precess about the magnetic field at a frequency $\omega_{\mathrm{h}} = g_{\mathrm{h,x}}\mu_{\mathrm{B}}B_x/\hbar$. The magnetic field therefore rotates the Bloch vector. The precession of electron spins in both quantum dot ensembles [50], [82], [83], [84] and single quantum dots has been measured by several groups [11], [55], [56]. More recently, the precession of a single hole spin has been reported [38], [85] and this is the subject of chapter 5 of this thesis.

Spin rotations about the optical axis

Complete control of a spin state over the full surface of the Bloch sphere requires rotation about two orthogonal axis. One of these axes of rotation is provided by the spin precession about an applied magnetic field in the x-direction. Rotations about the optical axis (z) have been proposed [86], [87], [88] and implemented [55], [56], [11], [89], [12], [38], [59] by making use of the non-linear process of stimulated Raman scattering. Optical control via stimulated Raman scattering will be described shortly. Furthermore optical control will also be discussed in terms of the geometric phase and AC-Stark shift interpretations. Stimulated Raman scattering, geometric phase and AC Stark shifts are essentially three different interpretations of the same physics in regimes of different pulse intensity and detuning. These will be explained in turn below. The results described in chapter 6 of this thesis make use the geometric phase shift.

Stimulated Raman scattering

An optical pulse, named a control pulse, with an energy width much greater than the Zeeman splitting between the electron or hole spin states is used for spin rotations. In general the pulse is detuned from the trion transition to avoid dephasing as a result of real population of the trion state. Consider the charged dot in the energy eigenstates basis as shown in Fig 2.8(a). Each trion $|T^-\rangle$ and $|\bar{T}^-\rangle$ forms a Λ type system. A broadband circularly polarised control pulse simultaneously couples all

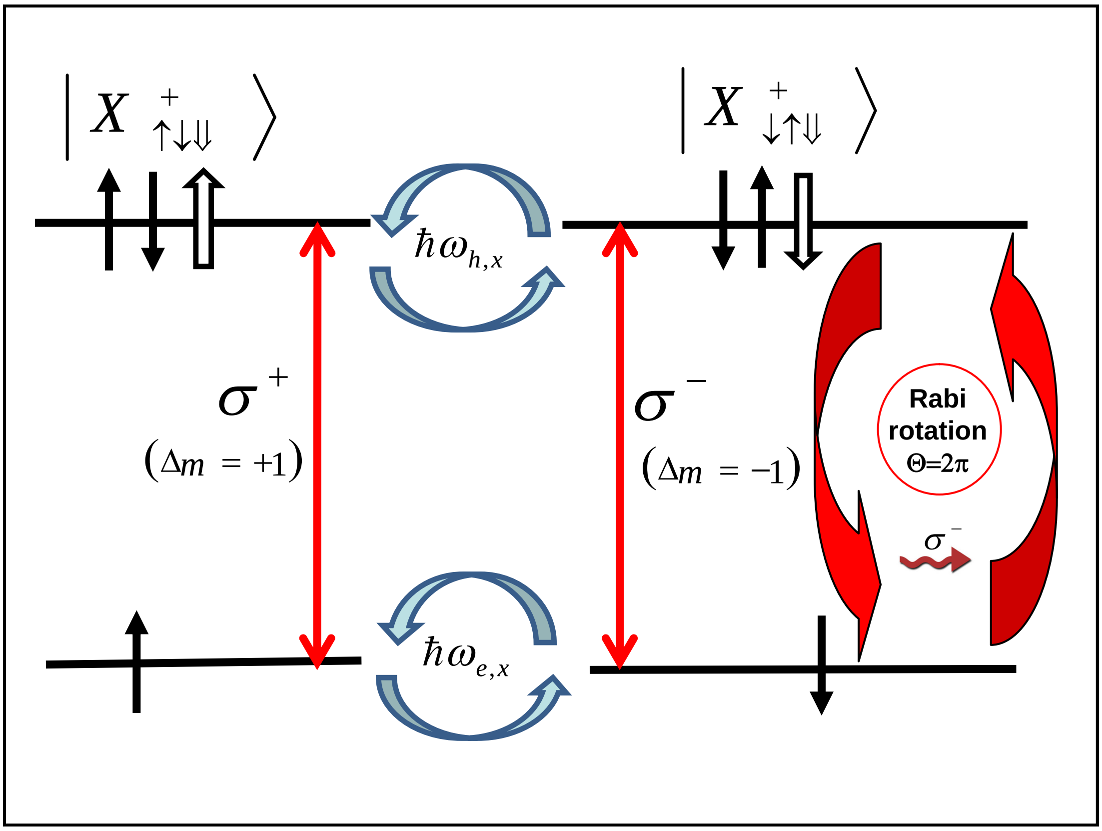

Figure 2.10: *Energy level diagram of the charged exciton* $|X^-\rangle$ *in the circular basis to show the geometric phase shift. A* σ^- *control pulse, with* FWHM $\gg \hbar\omega_{\mathrm{e,x}}$, $\hbar\omega_{\mathrm{h,x}}$, *drives a* 2π *Rabi-rotation between the electron spin state* $\downarrow$ *and charged exciton state*

four linearly polarised optical transitions. No direct optical transitions between the spin states $|e\rangle$ and $|\bar{e}\rangle$ are allowed. However, the spin states are coupled via the trion transitions, and since the phase between the x and y components of the $\sigma^{\pm}$ control pulse is well defined, the control pulse drives spin Rabi oscillations between the $|e\rangle$ and $|\bar{e}\rangle$ states. This description is equivalent to stimulated Raman transition.

Geometric phase shift

The geometric phase shift of optical spin rotation applies when a control pulse is close to or resonant with the trion transition. In the proposals of Economou *et al.*, a $\sigma^{\pm}$ control pulse with pulse area $\Theta = 2\pi$ drives a Rabi rotation between one of the electron spin states $|\uparrow\rangle$ or $|\downarrow\rangle$ and one of the charged exciton states [87]. The Rabi rotation between the spin state and charged exciton state is selected by the polarisation of the control pulse, as shown in Fig. 2.10. In this Figure, the spin and trion states are viewed in the circular basis, which is possible because the control pulse is fast compared to the Zeeman energy couplings between the spin states and the trion states. A control pulse, with pulse area 2π, imparts a phase shift on the selected spin state, relative to the unselected spin state. The phase shift depends on the detuning Δ and the Rabi frequency of the laser pulse $\Omega(t)$, and is given by eqn 2.16 [88]:

$$\Delta\phi = \frac{1}{2}\int_{-\infty}^{\infty} \mathrm{d}\tau \left(|\Delta| - \sqrt{\Delta^2 + \Omega(\mathrm{t})^2} \right), \tag{2.16}$$

where $\Omega(t)$ is the time dependent Rabi-frequency of the control pulse.

Consider the effect of the laser pulse, on a hole spin superposition state. Before the arrival of the pulse at time t_{C}, the wavefunction of the hole spin state may be expressed as:

$$|\psi(t < t_{\mathrm{C}})\rangle = h_{\Uparrow} |\Uparrow\rangle + h_{\Downarrow} |\Downarrow\rangle . \tag{2.17}$$

Under resonant excitation and in the ideal case of weak trion dephasing, a circularly-polarised laser pulse drives a Rabi-rotation between the selected hole spin and trion states. The wavefunction of the hole state after the arrival of the pulse may be expressed by making use of eqn 2.15:

$$|\psi(t > t_{\mathrm{C}})\rangle = h_{\Uparrow} |\Uparrow\rangle + h_{\Downarrow} \left[\cos(\frac{\Theta}{2}) |\Downarrow\rangle + i \sin(\frac{\Theta}{2}) |\downarrow\Uparrow\Downarrow\rangle \right], \tag{2.18}$$

where Θ is the pulse area. When $\Theta = 2\pi$, the state of the dot is returned to the hole spin subspace after having acquired a phase shift of π [87], [88]. Therefore the control pulse transforms the wavefunction in eqn 2.17 to:

$$|\psi(t > t_{\mathrm{C}})\rangle = h_{\Uparrow} |\Uparrow\rangle - h_{\Downarrow} |\Downarrow\rangle , \tag{2.19}$$

where we observe a change of sign in the superposition. This phase is equivalent to a rotation of the Bloch vector by an angle which depends on the detuning of the control pulse Δ. This was the approach that was used in the experiments described in chapter 5 of this thesis. Geometric optical control has also been demonstrated for single electrons spins by the work of Kim *et al.* in reference [89].

AC Stark shift

The AC stark shift interpretation of spin rotation applies in the regime of large detuning Δ and high pulse intensity. For large detuning, the amount of trion population is small. Therefore, the spin control is better explained in terms of an AC Stark shift of the selected spin state, rather than a Rabi rotation. For the duration of the laser pulse, one of the spin states eg $|\uparrow\rangle$ is shifted in energy by the electric field of the control pulse. The perturbed spin state is selected by the polarisation of the control pulse, in a similar manner to that described Fig. 2.10. The additional energy splitting between the spin states due to the AC Stark shift can be thought of as an effective magnetic field in the direction of the optical axis. The spin then 'precesses' about this effective magnetic field. By expanding eqn 2.16 for large detuning in terms of $\Omega(t)^2/\Delta^2$ to first order, it can shown that the phase shift induced by a control pulse of duration τ and intensity I, may be written as [24]:

$$\Delta\phi \propto \frac{\mu^2 I}{2\Delta}\tau, \tag{2.20}$$

where μ is the dipole moment of the transition, and the substitution $\Omega = \mu E/\hbar$ has been made. The description of the phase shift, in terms of an effective magnetic field, induced by a high intensity laser field, with large detuning, is the picture that Berezovsky *et al.* use in their experiments which demonstrated electron spin rotations by angles of up to π [56].

2.5.4 State of the art: putting it all together

This section describes four key experimental reports on the field of coherent control of single carrier spins in self assembled semiconductor quantum dots, that form the main references for this thesis. In chronological order these are : the work of Press *et al.*, at Stanford University, entitled "Complete quantum control of a single quantum dot spin using ultrafast optical pulses" [11]; the work of Danny Kim *et* *al.*, at Naval Research Laboratory (NRL), Washington, entitled "Ultrafast optical control of entanglement between two quantum-dot spins" [12]; the work of Kristiaan De Greve *et al.*, at Stanford entitled, "Ultrafast coherent control and suppressed nuclear feedback of a single quantum dot hole qubit" [17] and finally the work of A. Greilich *et al.*, at NRL, entitled "Optical control of one and two hole spins in interacting quantum dots" [18]. These four works, along with the results of chapters 5 and 6 in this thesis, represent the state of the art in the field at this moment in time.

"Complete quantum control of a single quantum dot spin using ultrafast optical pulses" [11]

David Press and co-workers were the first to demonstrate complete quantum control of a single electron spin in a self-assembled quantum dot [11]. In this work, high fidelity spin preparation, ultrafast coherent optical control and optical spin readout were all combined in one experiment. The experiments were performed on a single InGaAs quantum in a Voigt geometry magnetic field. The quantum dot contained a single electron, probabilistically charged from an n-type Si doping layer located 20nm from the quantum dot layer. The energy level diagram for such a system is shown in Fig. 2.8(a).

Spin initialization into an energy eigenstate of the electron spin was performed by driving the lowest energy transition in Fig 2.8(a) with a narrow band CW laser. The same laser was used for spin readout, which is advantageous because of its simplicity. Spin Rabi oscillations were demonstrated by using a broadband optical laser pulse with variable power, detuned from the trion transition to avoid state population. This constitutes rotation about the optical axis via stimulated Raman transitions.

Rotations about a second axis were provided by the coherent precession of the electron spin about the magnetic field. This was demonstrated by using a sequence of $\pi/2$ rotation pulses separated by a variable time delay: a Ramsey interference experiment. The spin was initially in an energy eigenstate of the system. The first $\pi/2$ pulse rotated the spin to an axis perpendicular to the magnetic field direction, where it began to precess. The second $\pi/2$ pulse then either rotated it back to the original spin state, or into the opposite eigenstate, depending on the phase. By varying both the phase and pulse area of the rotation pulses, the ability to control the electron spin to any arbitrary position on the Bloch sphere was demonstrated. These pioneering experiments were the first to show full quantum control of a single electron spin by using ultrafast laser pulses.

"Ultrafast optical control of entanglement between two quantum-dot spins" [12]

The experiments of Press *et al.* constitute the optical manipulation of a single spin qubit. The next challenge was to address the scalability of the spin qubit. This was addressed by the work or Danny Kim *et al.* with their coherent control experiments in coupled quantum dots [12]. In the experiments of Danny Kim *et al.* both single and 2-qubit gate phase gates were demonstrated by using optical control of the lowest energy electron spin states in a tunnel-coupled quantum dot molecule. A quantum dot molecule consists of a pair of vertically-stacked quantum dots, separated by a thin ($\sim$ 9 nm) tunnel barrier. The dots were embedded in a Schottky diode structure so that they could be deterministically charged with one electron per dot. Furthermore, the dots were deliberately grown to be a different size, such that the optical transition energies in each dot could be isolated spectrally. The tunnel barrier between the dots was carefully selected so that the exchange energy splitting was large enough to perform 2-qubit operations with a narrow band laser pulse, but small enough to perform single qubit operations with an ultrafast laser pulse. This will be explained shortly.

In the absence of an applied magnetic field, the spin eigenstates of the two-electron (2e) system consist of three degenerate triplet states: $T_0 = 1/\sqrt{2}(|\uparrow\downarrow\rangle + |\downarrow\uparrow\rangle)$, $T_- = |\downarrow\downarrow\rangle$ and $T_+ = |\uparrow\uparrow\rangle$, and the spin singlet state $S = 1/\sqrt{2}(|\uparrow\downarrow\rangle - |\downarrow\uparrow\rangle)$, which are separated in energy by a bias-dependent exchange energy splitting $\Delta_{\mathrm{ee}}(V_{\mathrm{bias}})$. The states T_0 and S couple to the same optically-active excited state X^{2-} and thus form a Λ system suitable for optical pumping. A circularly polarised CW laser resonant with the triplet to X^{2-} transition was used to shelve the spin in the singlet state, which is an entangled state of the electron spin. This was an interesting and novel effect in itself.

After demonstrating spin initialisation into an entangled state [67], Kim *et al.* next showed the ability to control the entanglement by using a pair of single-qubit gates. The single-qubit gates consisted of a pair of circularly-polarised broadband laser pulses separated by a variable time delay. The bandwidth of the pulses was chosen to be much greater than the exchange energy splitting but much smaller than the energy separation of the excitons for each dot. This was so that the laser pulses only acted on one electron in one of the dots. Each of the laser pulses rotated one of the electron spins about the optical axis via a stimulated Raman transition. A pair of $\pi/2$ pulses were used to measure the Ramsay interference. The first pulse rotated the Bloch vector into a superposition of singlet and triplet states, and the second either drove it back to the singlet or up to the triplet, dependent on the phase. Ramsey fringes were observed, with a period determined by Δ_{ee}. By varying the pulse area and phase, Kim *et al.* demonstrated control over the entangled superposition state: $\alpha\left|\uparrow\downarrow\right\rangle + \beta\left|\downarrow\uparrow\right\rangle$. Furthermore, the application of an in-plane magnetic field allowed Raman transitions to the T_+ and T_- states, enabling complete control of the full 2e system: $\alpha\left|\uparrow\downarrow\right\rangle + \beta\left|\downarrow\uparrow\right\rangle + \chi\left|\uparrow\uparrow\right\rangle + \delta\left|\downarrow\downarrow\right\rangle$

Two-qubit phase gates were also demonstrated by using a spectrally-narrow pulse, with a bandwidth much smaller than Δ_{ee}. In this situation, the laser pulse was slow compared to the exchange dynamics. This laser pulse with pulse area $\Theta = 2\pi$ was used to control the phase of the precession of the singlet-triplet superposition state. By driving a 2π Rabi rotation between only the singlet state and the excited state, the singlet state acquires a phase shift relative to the triplet state. This is analogous to the geometric phase shift discussed previously in section 2.5.3. The results of Kim *et al.* constitute real progress in demonstrating the scalability of a quantum dot system. However, a fast dephasing time $T_2^* <$ ns was measured, and although attributed to electric field fluctuations, this indicated that the hole spin might be advantageous.

"Ultrafast coherent control and suppressed nuclear feedback of a single quantum dot hole qubit" [17]

In addition to the work reported in chapter 6 of this thesis, two reports on the coherent optical control of a single hole spin in a self-assembled quantum dot have been published very recently (August and September 2011). The first was a demonstration of optical control of a single hole spin by De Greve and Press *et al.* in the group of Y. Yamamoto at Stanford University [17]. The experiments made use of samples containing either deterministically-chargeable or probabilistically-charged quantum dots, loaded with a single hole. The authors made use of the same approach to initialise, optically control, and readout the hole spin as was used for the electron spin (Press *et al.* [11]). Spin Rabi oscillations and Ramsey fringes were observed, demonstrating complete control of the hole spin over the surface of the Bloch sphere.

In addition De Greve *et al.* compared the Ramsey fringes of the electron and hole spin. For the electron spin, asymmetric fringes and hysteresis were observed. The authors attributed this to a strong nuclear spin feedback loop which affects the electron spin via the hyperfine interaction. This is because the nuclear polarisation was significantly altered during each cycle of the experiment. No such behaviour was observed for the hole spin, and the authors suggest a lower limit of a factor of 30 reduction in any nuclear spin feedback mechanism.

A dephasing time $T_2^* = 2.3$ ns was extracted from a fit to the decay of the Ramsey fringes. The authors suggest that electric field fluctuations due to charge noise were the main source of decoherence in their experiments. A further discussion of this can be found in chapter 5 section 5.7. In addition to the coherent optical control experiments, De Greve *et al.* used spin echo techniques to measure the hole spin intrinsic decoherence time T_2. This was done by using a π refocusing pulse to remove time-ensemble average dephasing. From these experiments De Greve *et al.* measured a decoherence time of $T_2^* = 1.1\ \mu$s.

“Optical control of one and two hole spins in interacting quantum dots” [18]

The second experimental report on the optical control of a hole spin was published very soon after the work of the Yamamoto group. Greilich *et al.* from NRL not only demonstrated coherent optical control of a single hole spin, but control over two interacting spins in a quantum dot molecule [12]. By deterministically charging the quantum dot molecule, Greilich *et al.* were able to move from a regime of optical control of one of the hole spins to both of the hole spins. Deterministic charging allowed for voltage control of the number of holes in each dot. This was denoted (0,1), (1,1), (1,2) or (2,1), where the number in brackets denotes the number of holes in the (‘red’, ‘blue’) dots.

In the first experiments, the authors showed spin Rabi oscillations and Ramsey interference fringes for a single hole spin in one of the quantum dots in a magnetic field. For these experiments, the blue dot had a pair of anti-parallel holes spins and the dot of interest (red) had a single spin, i.e. the charge configuration was (1,2). Spectral isolation of the transitions in each dot was used to achieve control over only one of the spins. By varying the time delay and power of two optical pulses, the entire surface of the Bloch sphere was explored.

The control of interacting holes spins was demonstrated in two different regimes. The first regime, namely the weak-coupling regime, used samples where the exchange splitting was smaller than the linewidth of the control laser pulse. The quantum dot was charged into the (1,1) state and the control laser performed spin rotations on the red dot, regardless of the spin state of the hole in the blue dot. In this regime the control laser did not directly control the spin in the blue dot, but it was indirectly coupled via the exchange interaction. This manifested itself in a beating of the Ramsey fringes at the exchange energy splitting, which could be tuned by using the applied bias.

In the final set of experiments, the authors used samples where the exchange interaction was large $\sim 80\ \mu$eV. In this regime, the energy eigenstates were expressed in the singlet and triplet basis, which is analogous to the experiments performed on coupled electrons spin by the same group [12]. By using Ramsey interferometry, Greilich *et al.* demonstrated spin rotations from the singlet to triplet states, enabling coherent control over the entanglement between the hole spins. For these experiments, the control laser rotated the spin state about the optical axis, and the singlet-triplet exchange energy provided the axis for the 'precession' of the state. The experiments were the first to demonstrate the controlled interaction of hole spins in a quantum dot molecule. This scalability is essential because it forms the basis for two-qubit phase gates.

These four papers show that the coherent optical control of single spins is a highly topical area of research. In some respects the field is in its infancy, but some of the experimental reports show the real potential of what can be achieved, both from the perspective of fundamental physics, and for applications in quantum information processing. This is especially true for a single hole spin in an optically-active quantum dot.

Chapter 3

Methods

This chapter describes the experimental methods used to perform photocurrent spectroscopy on a single InGaAs quantum dot in a Schottky diode. The basic principle behind the experiments is as follows. A picosecond laser pulse resonant with an optical transition in a quantum dot excites charge carriers. Under an applied bias to the Schottky diode, the carriers tunnel from the dot. This can be measured as a change in photocurrent through the diode. To measure the dynamics of the quantum state in the dot, up to three separate laser pulse trains were used, each with independently controllable wavelength, polarisation, power and phase. The experimental methods used to achieve this will be described in this chapter along with details of the Schottky diode sample and the experimental measurement techniques.

3.1 The quantum dot Schottky diode

Figure 3.1 is a schematic diagram of the quantum dot Schottky diode. The basic principle of the quantum dot Schottky diode is as follows: under an applied reverse bias, and at low temperature, no current flows unless a photo-excited electron-hole pair has been generated. The quantum dots are embedded in the intrinsic region of the diode and form the active element. Photons that are resonant with transitions in the quantum dots excite electron and hole pairs. The charge carriers then tunnel

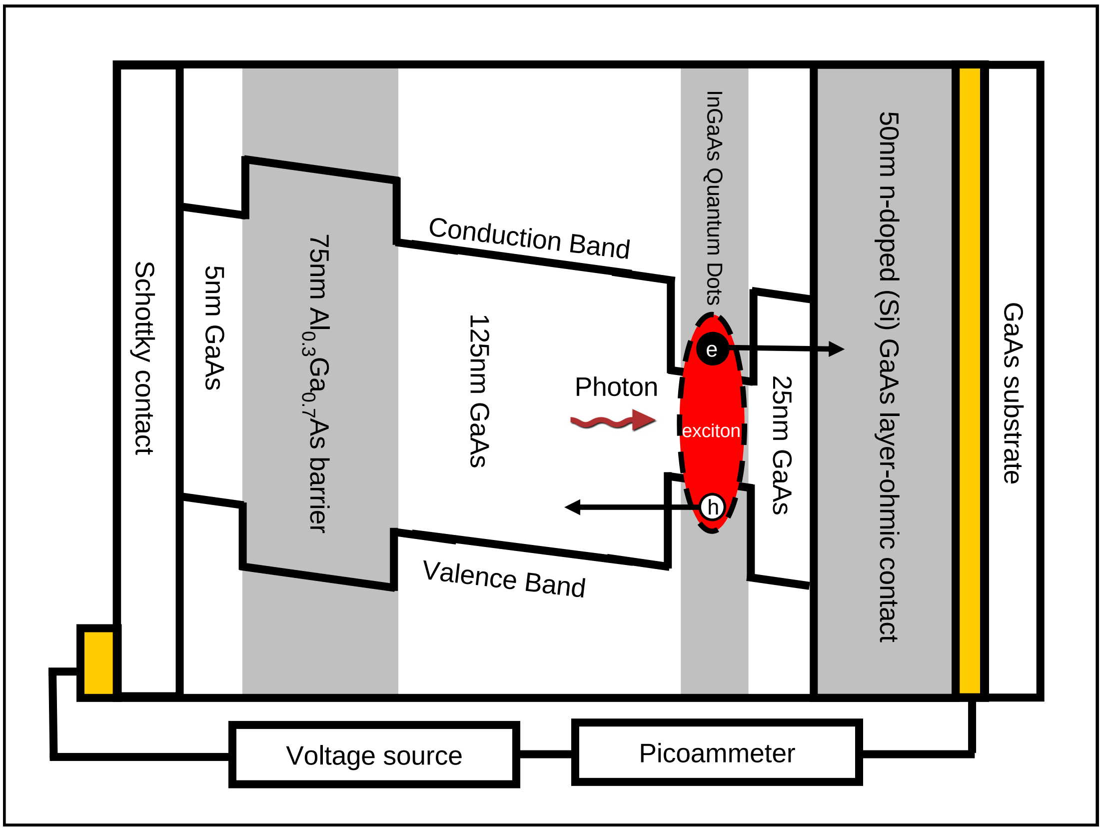

Figure 3.1: *Schematic diagram of the layer structure and band structure of a quantum-dot Schottky diode device. A resonant photon incident on the sample creates an exciton (e-h pair) in the Quantum Dot. Under the applied bias the carriers tunnel from the dot.*

from the dot under the applied bias and can be read out as a photocurrent. The quantum state of the dots can be prepared, controlled and read out using laser pulses with selected polarisation, power and time delay. By exploiting the atom-like nature of the quantum-dot energy states, the states of the carriers in the dot can be inferred according to the selection rules, and can be read out by photocurrent measurements.

3.1.1 Device growth and fabrication

The sample growth and fabrication was carried out at the National Centre for III-V Semiconductor Technology in Sheffield. Fabrication of the devices used in the experiments in chapters 5 and 6 was carried out by Yanwen Wu and Peter Brereton from the Cavendish Laboratory, University of Cambridge. The wafers were grown by Molecular Beam Epitaxy (MBE). The quantum dots were formed by self-assembled Stranski-Krastanov growth. Figure 3.1 shows the layer structure of the wafers which was the following: an undoped GaAs substrate with a 50-nm n-doped GaAs (Si, n=4x10^{8} cm^{-3}) layer, a 25 nm i-GaAs spacer layer, a single layer of InGaAs self-assembled dots, 125-nm of i-GaAs, followed by a 75-nm $Al_{0.3}Ga_{0.7}As$ blocking barrier and a 5-nm GaAs cap.

After growth, the wafers were cleaved and processed into Schottky diodes by using a combination of optical lithography, acid etching and metal evaporation. Figure 3.2 is a diagram showing an overlay of the mask design used to produce the diodes and Fig. 3.3 is a photograph of a fully processed device. Apertures in an aluminum shadow mask were made by electron beam lithography in order to spatially isolate individual quantum dots. The apertures also acted as markers to register the dots. A schematic diagram of the resulting layer structure and band structure for the Schottky diode device used for photocurrent spectroscopy can be found in Fig. 3.1.

After processing, the devices were mounted onto a ceramic, non-magnetic, leadless chip carrier (LCC). A wire-bonder was then used to form gold bonds from the contacts of the devices to the pins of the LCC. In order to make electrical connections from the detection circuit to the LCC, the LCC was housed in a custom-built compact socket made of ceramic. Figure 3.8 (b) shows an example of the resulting device. The overall design provided robust electrical connections and a protective environment for the samples, suitable for low temperature operation.

3.2 Electrical circuit and device characterisation

An important component of any photocurrent spectroscopy experiment is the electrical circuit. Figure 3.4 illustrates the basic circuit used for all measurements. The circuit consisted of a Keithley 230 (K230) voltage source, a Keithley 6485 pico-ammeter (K6485) and the Schottky diode. The instruments were connected via shielded coaxial cables, with a PTFE insulating layer. An important property of the device and circuit was a low leakage current and noise level under a reverse

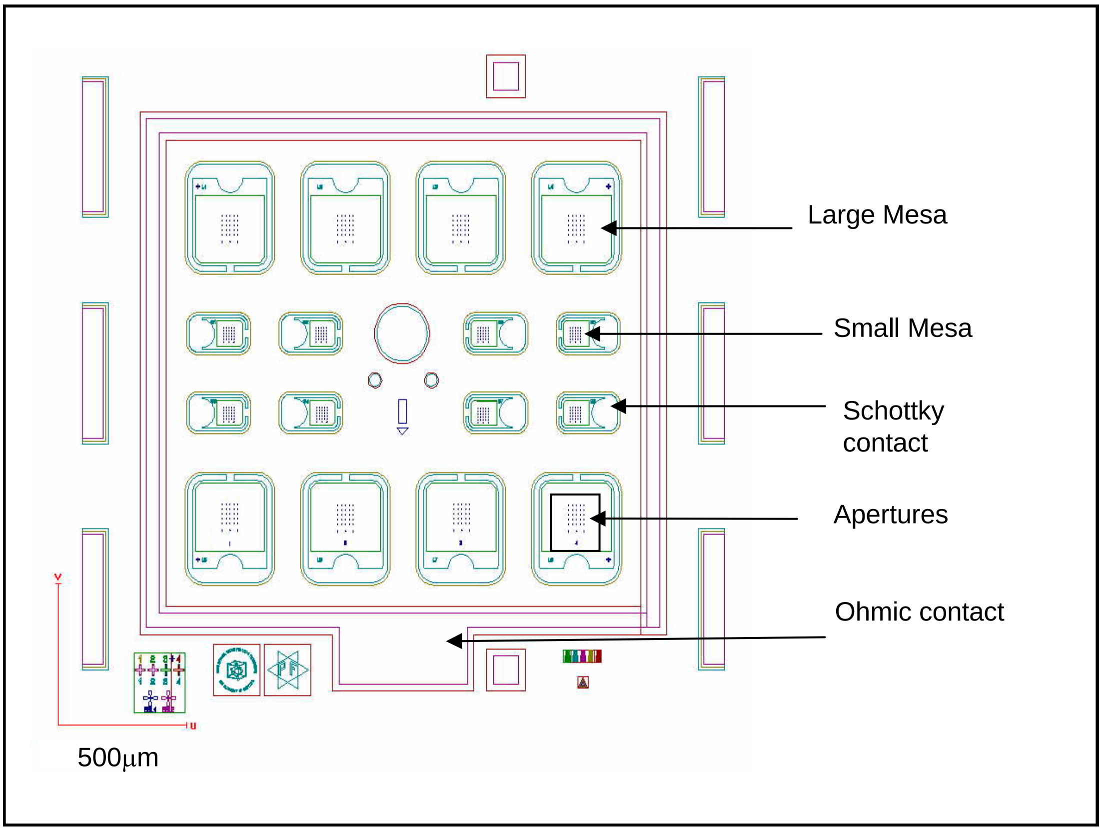

Figure 3.2: *Transparent overlay of the masks used for device fabrication. The device consisted of several independently contactable mesas (green), each with a 5×5 array of apertures. Each stage of the processing involved applying a photoresist to the sample, then masking it (with the patterns shown), before exposure to UV radiation. The mask was removed and the sample developed in a photo-developer. Finally, the sample had a metal eg, Gold or Titanium, evaporated onto it. The photoresist was then dissolved in acetone to leave the evaporated metal in the pattern of the mask.*

applied bias.

The processed diodes were tested by measuring the current as a function of applied bias to produce a current vs voltage (IV) curve. To identify the best devices, many hundreds of diodes were tested. The majority of diodes tested did not pass the IV test. Figure 3.6 shows a histogram of the performance statistics of a set of typical diodes. The diodes which did pass the IV tests were cooled to $T = 4.2$ K. Typical values for a workable diode at helium temperature were a leakage current $I < 100$ fA over the bias range $0 > V_{\mathrm{Bias}} > -3V$ with a noise $\Delta I_{\max} < 50$ fA. Figure 3.5 shows a current voltage (IV) curve at room and liquid Helium temperatures for a workable diode.

In order to minimise the circuit noise in reverse bias, several steps were taken:

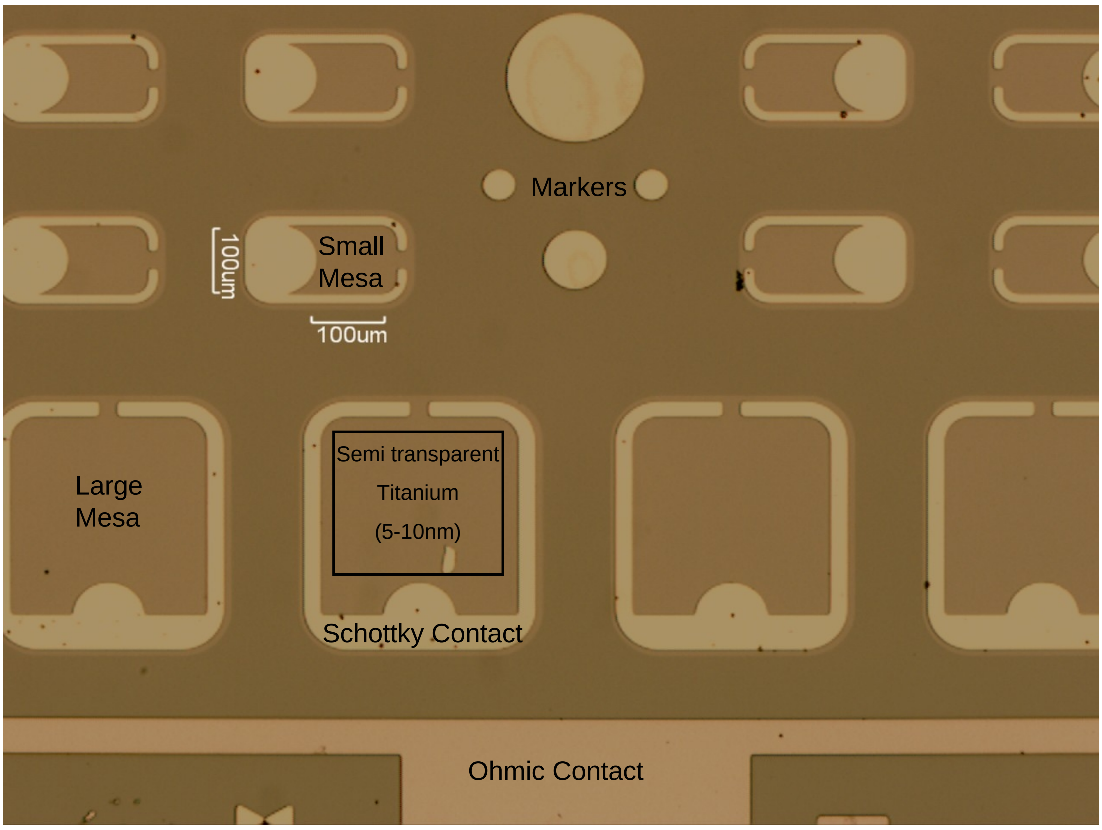

Figure 3.3: *Photograph of a fully processed Schottky diode device. Gold bonds were made from the Schottky contact and ohmic contact to the ceramic package which housed the sample. The smaller mesas were generally used, since they had smaller leakage currents due to their smaller areas. Each mesa contained an array of apertures in an aluminium shadow mask with apertures sizes ranging from 200 nm to 1 μm diameter. The reflective mask allowed for spatial isolation of individual quantum dots.*

1) The circuit was grounded in only one position to avoid ground loops. The ground was made via the K6485 chasis (grounded via mains ground). All shielding, including the outer jackets of the coaxial cables, and also the K230 ground and the cryostat dewar were connected to the K6485 grounding. Without this grounding configuration, a ground loop or antenna would pick up ambient electromagnetic fields, causing current fluctuations in the circuit.

2) The inner and outer connections of the coaxial cables were insulated via a PTFE jacket. Standard coaxial cables use a polythene insulating layer. This plastic was found to increase reverse bias noise because it is more sensitive to temperature

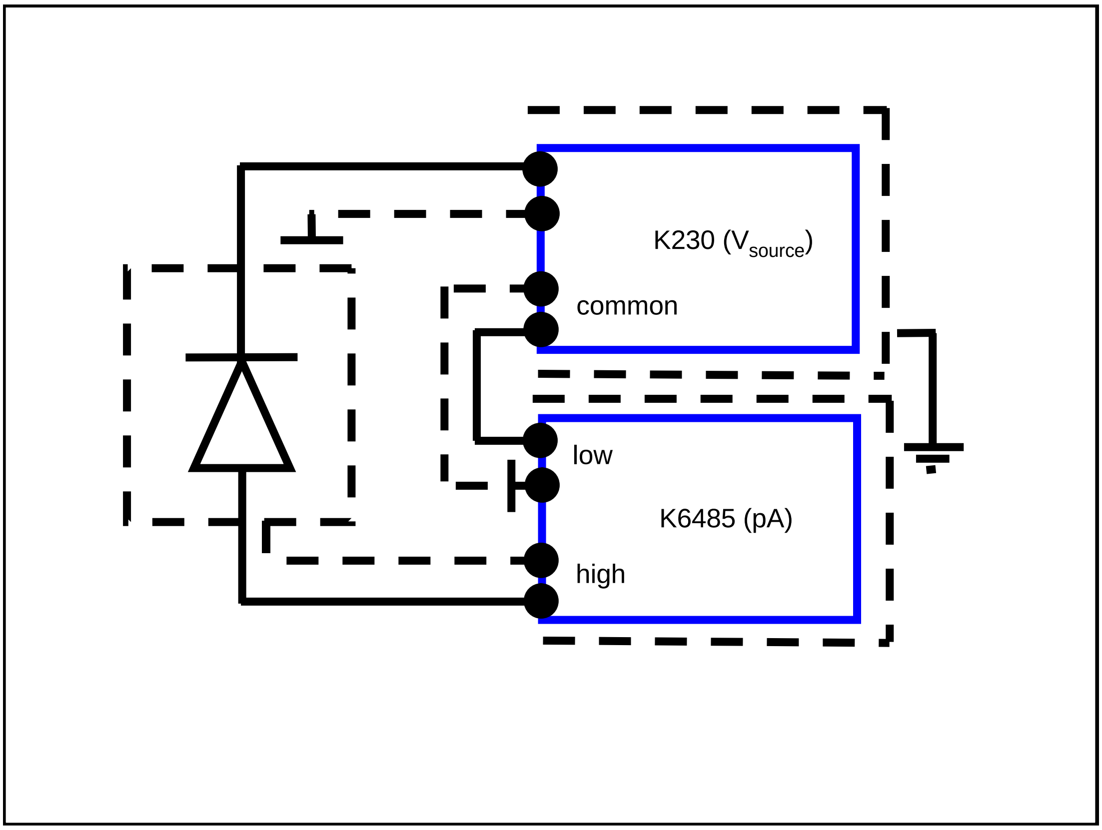

Figure 3.4: *Circuit diagram for PC spectroscopy. Solid black lines represent the electrical connections made with the inner core of co-axial cable. Dotted lines represent the shielding. K230: Voltage source. K6485: pico-ammeter (pA)*

fluctuations.

3) A thermal insulating jacket was added to the cable cladding to reduce temperature fluctuations.

4) The sockets built to encase the chip carriers were made of a ‘Macor’ ceramic material, which has excellent resistive properties, preventing any indirect leakage current. The material also has a co-efficient of thermal expansion which matches the leadless chip carriers (LCC).

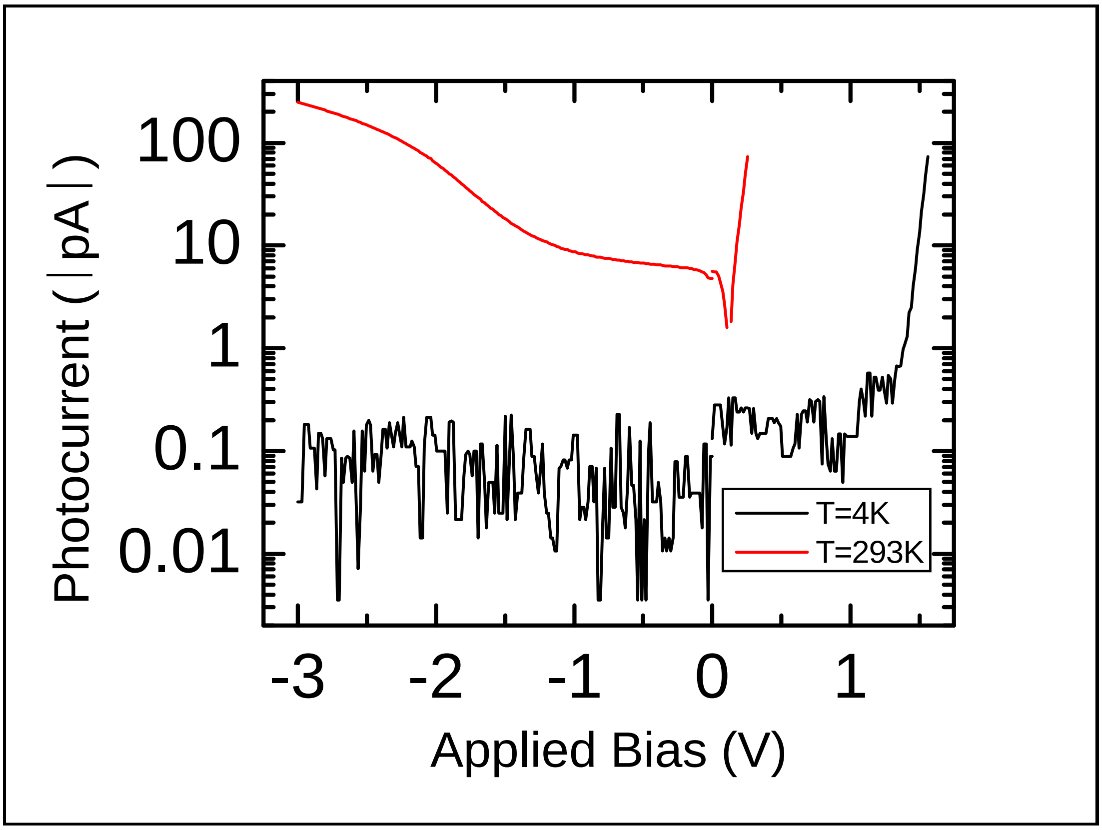

Figure 3.5: *Typical current voltage performance for a good Schottky diode at liquid helium (black) and room (red) temperature in the dark.*

3.3 Photocurrent detection

For the very best devices, negligible current flows through the diode at liquid helium temperature under an applied reverse bias in the dark. See Fig 3.5. When a photon is resonant with the crystal ground state $|0\rangle$ to the first excited state in the quantum dot $|X\rangle$, an electron is lifted across the band gap, from the valence band to the conduction band. Under the applied DC electric field, the electron and hole dissociate and tunnel out of the dot, which leads to photocurrent through the device. Due to the fact that the device only generates a single electron charge per laser pulse, it has been described as a "optically generated single electron turnstile" [76].

The amount of photocurrent signal that is generated by a train of laser pulses resonant with a pulse area $\Theta = \pi$ is determined by the photocurrent detection

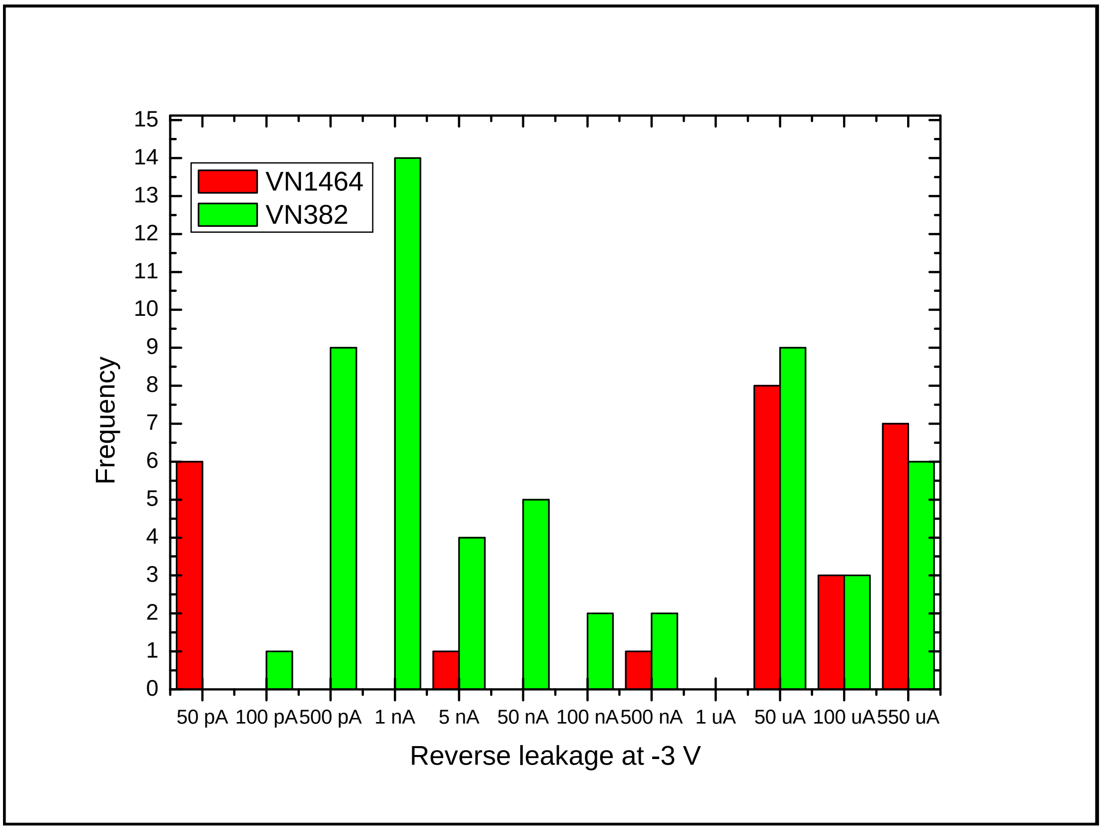

Figure 3.6: *Statistics on the number of diodes with a given reverse leakage current at room temperature under an applied bias of -3 V. Red represents the sampled labeled VN1464 and green the sample labelled VN382. Both sets of samples had the same layer structure but originate from different wafers. VN1464 had a nominally lower quantum dot density.*

efficiency. With a laser with a pulse repetition frequency of $\nu = 76$ MHz, and assuming that the π pulses fully invert the $|0\rangle \rightarrow |X\rangle$ 2-level system, the maximum measured current through the device will be $I = \eta\nu e$. Here e is the electronic charge and η is the detection efficiency. On assuming that both carriers have tunneled from the dot before the arrival of the next pulse, we expect $\eta = 1$, and hence $I = 12.18$ pA. This photocurrent can be measured with a low noise picoammeter.

The tunneling rates of the electron and hole depend on the effective mass, and vary exponentially with the applied bias [90]. For an applied bias of $\sim (-0.9{\pm}0.3)$ V, the electron tunneling time varied from tens of picoseconds to $\sim$ 100 ps. The hole tunneling times were much larger, due to the increased effective mass and additional AlGaAs barrier between the quantum dots and Schottky contacts. As an example, typical values for the tunneling times with an applied bias of -0.8 V were $(50 - 100)$ ps for the electron and $(2.5 - 4.0)$ ns for the hole. The wafers were specifically designed this way, in order to trap holes by the inclusion of the AlGaAs barrier (see Fig. 3.1). An example of the method for measuring the tunneling times can be found with reference to section A.5 Fig. A.8

3.4 Helium bath cryostat: Attocube system

3.4.1 Cryostat design

All of the measurements presented in this thesis were made with a base temperature of $T = 4.2$ K. This was achieved by using a liquid helium bath cryostat designed by Cryogen Industries of America. A helium bath cryostat is a very stable system in which to house the sample because there is no flow of Helium gas. Stable coupling between the incident laser and single quantum dot was maintained over several days. Figure 3.7 shows the design and dimensions of the cryostat. A Lakeshore superconducting magnet with magnetic fields $0 < |B| < 5$ T was also contained within the system. The basic design of the cryostat consisted of an evacuated jacket containing a bath of liquid helium. The sample was mounted inside an evacuated sleeve that sat within the helium bath, and inside the bore of the superconducting magnet.

A Thorlabs 'cage-system', which consisted of an array of 'cage-plates' connected via cage rods, was used to hold the sample and objective lens. The insert then sat within the sleeve, with a small amount of Helium exchange gas, to provide good thermal contact. The cage had several electrical pins for connecting the device, temperature sensor, heater, piezo stages etc. The whole system was then elastically suspended and acoustically insulated to de-couple it from the environment.

A stack of piezo-electric transducers designed by Attocube Systems were used to position the sample. The piezos operated under the 'slip-stick' motion control mode, in which the application of a voltage pulse moves the stages. The slip stick approach is advantageous because a constant voltage supply is not required for a

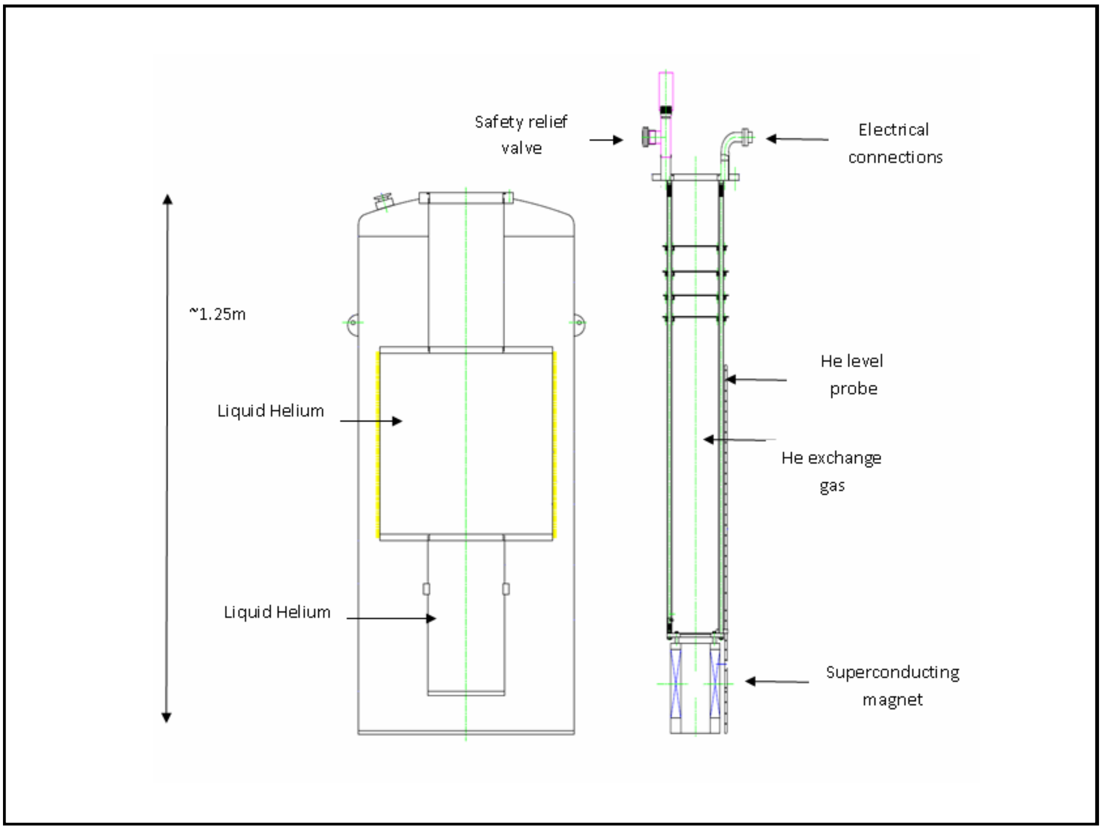

Figure 3.7: *The attocube helium bath cryostat. This diagram is extracted from the Attocube systems manual. The sample sat within an insert which contained* ~ 3 cm^3 *of helium gas (for thermal exchange). A Thorlabs 'cage system' held the objective lens and a baseplate on which the low temperature piezo-stages sat. The sample was centered in the core of the superconducting magnet.*

given stage position, therefore reducing electrical noise. The stages were operated using an ANC200 controller and the minimum step size at $T = 4$K was ~ 4 nm. This allowed for high precision control of the position of the sample in three dimensions with respect to the incident laser.

3.4.2 Sample mounting

One challenge presented by the use of the cage system was the small ($\sim 2\times2\times2$ cm^3) space available to mount the sample within the working distance of the objective lens ($f = 4.51$ mm). Two basic designs were used, one for Faraday geometry, and one for Voigt geometry. Figure 3.8 shows the design for Voigt geometry. For the Voigt geometry the direction of the laser beam was rotated by 90° using a right-angled prism mirror. The laser beam then passed through the objective lens and hit the

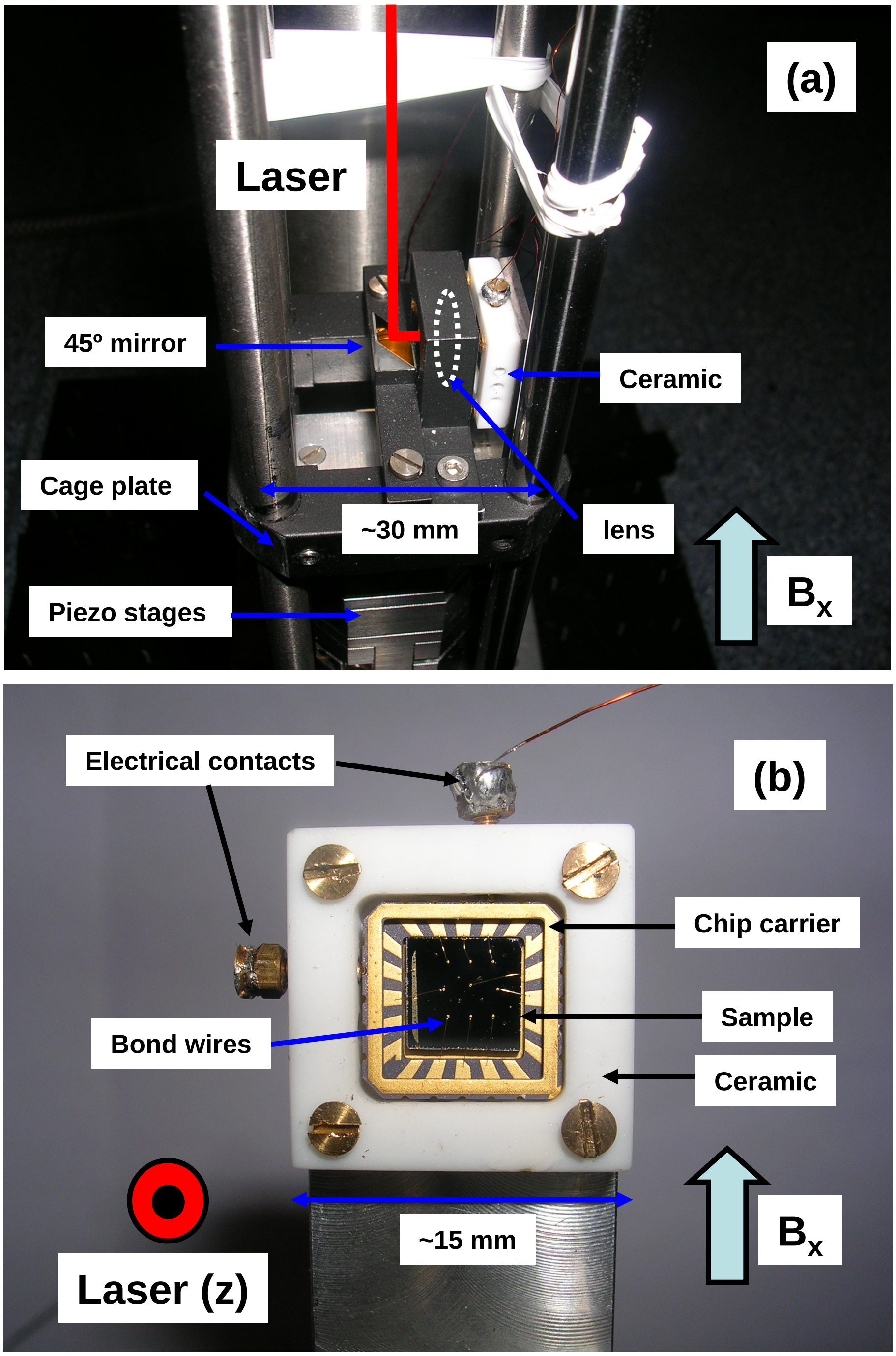

Figure 3.8: *Photograph of packaged device and sample mounting. (a) Sample mounted in the Voigt geometry within the cryostat insert stick (side on view). (b) Sample mounted within leadless chip carrier contained within a ceramic tile.*

sample, which sat on a L-shaped bracket mounted onto the piezo stages. In order to achieve the best possible coupling between the laser and the quantum dot, an objective lens with a short $f = 4.51$ mm focal length was used. The objective lens produced a spot of diameter ~ 1 μm. The lens is illustrated in Fig. 3.8(a)

A leadless chip carrier (LCC) package was chosen to fit the sample within the cage, due to its low profile ($\sim$ 2.5 mm thickness). Another benefit of the LCC was that it contained no magnetic materials. It was found that samples mounted on the more conventional TO5 header packages could not be moved by the piezo-stages under external magnetic fields because the pins/leads contained Nickel, and the maximum forces for operational stages are < 30 g. The LCC packages were mounted into custom-built Macor ceramic tile sockets. Figure 3.8 (b) illustrates the sample mounted in an LCC within a socket. In order to make the electrical connections to the LCC, brass screws in the socket 'pinched' the device into place via the LCC pins (rather like a standard mains plug socket). Solder then connected the screws to thin insulated copper wires which were connected to the rest of the circuit via the Attocube cage connector pins. The copper wires were thin, since thicker wires stiffened at low temperatures and prevented the piezo stages from moving freely (due to excess torque). For the stages to move freely, the total mass of the packaged sample, plus heater and temperature plate, and all other components had to be less than 50g. Thus aluminum brackets were chosen to fix the sockets into place.

Temperature dependent measurements

For temperature-dependent measurements, a resistive heater and temperature sensor were contained within a plate which was attached to the top of the piezo stack. The resistive heater was connected to a computer-controlled 'Aim TTi Pl303' power supply unit. A power, integral, differential or PI(D) algorithm was used to control the power supply [6]. The PI(D) control achieved stable temperatures $T = (4-70)$ K to within $\Delta T < 1$ mK. This allowed for automated temperature-dependent measurements.

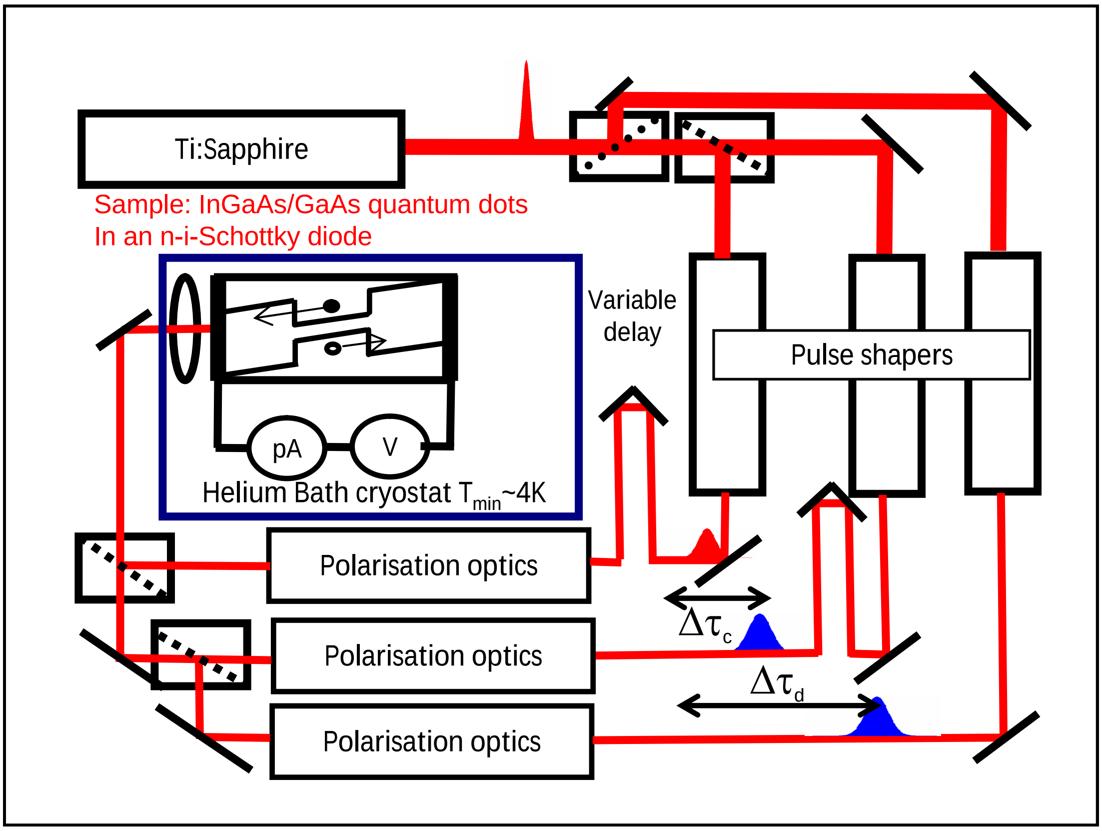

Figure 3.9: *Simplified schematic of three-pulse experimental setup. Femtosecond pulses were sourced from a Ti:Sapphire laser (top left). The beam was split into three 'arms', each incident on a pulse shaper. The first arm formed the preparation pulse, the second the control pulse (where applicable) and the third the detection pulse (where applicable). Each pulse was spectrally filtered by pulse shapers as discussed in section 3.5.2. Each pulse has its polarisation controlled. The three pulses were then re-combined before being delivered to the sample via a single-mode fibre. A breakdown of all the components is described in the following sections.*

3.5 Optical setup

This section describes the construction of the optics to provide the independently controllable laser pulse trains used to prepare, manipulate and readout the quantum dot(s) state(s). The manipulation of the laser from its source down to the objective lens within the cryostat is also discussed. The end result was a collimated beam from a single-mode fiber which carried three picosecond laser pulses, each with independently tunable wavelength, bandwidth, polarization, arrival time and power. Figure 3.9 shows a simplified diagram of the optics that illustrates the design of the three-pulse experiment.

3.5.1 Laser Source

A wavelength-tunable mode-locked Titanium:Sapphire laser (Coherent Mira 900, pumped by a Coherent Verdi V-8 laser) was used as the laser source. The laser emitted a train of laser pulses at a repetition rate of 76 MHz, corresponding to a pulse separation of ~ 13 ns. The pulses had a duration of 150 fs and hence were spectrally broad with a full width half maximum (FHWM) of ≈ 14 meV in energy, and ≈ 10 nm in wavelength. The laser wavelength was centered at ~ 950 nm. This wavelength corresponds to the crystal ground state to *s*-shell neutral exciton transitions in the quantum dots. The laser was water cooled and purged with nitrogen gas to remove any absorption by water vapor, and to maintain stable power and directionality of the output.

3.5.2 Pulse Shaping

Pulse-shaping optics were used to provide spectrally narrow ~ 0.2 meV laser pulses. This was done in order to address individual optical transisitions in a single quantum dot and to avoid unwanted coupling to neighbouring dots of similar energy. It was typical to locate several ($\sim 5-15$) quantum dots under a single aperture within the unfiltered bandwidth of the laser. In addition, the energy separation between the neutral exciton transitions, for example biexciton and charged exciton transitions, was on the order of $1-2$ meV [6]. This meant that laser pulses with energy FWHM $<< 1$ meV were required. The design of the pulse shapers followed the Fourier-Transform approach from ref. [91]. Figure 3.10 illustrates the design and layout of a single pulse shaper.

The output from the Ti:Sapphire laser was first collimated before passing it through a beam expander (5:15 f1:f2 telescope). The purpose of the beam expander was to maximise the spot size on the diffraction gratings in the pulse shapers. This was done to provide the best possible spectral resolution. The beam was split using polarising beam-splitters. Half-wave plates were used to control the fraction of light

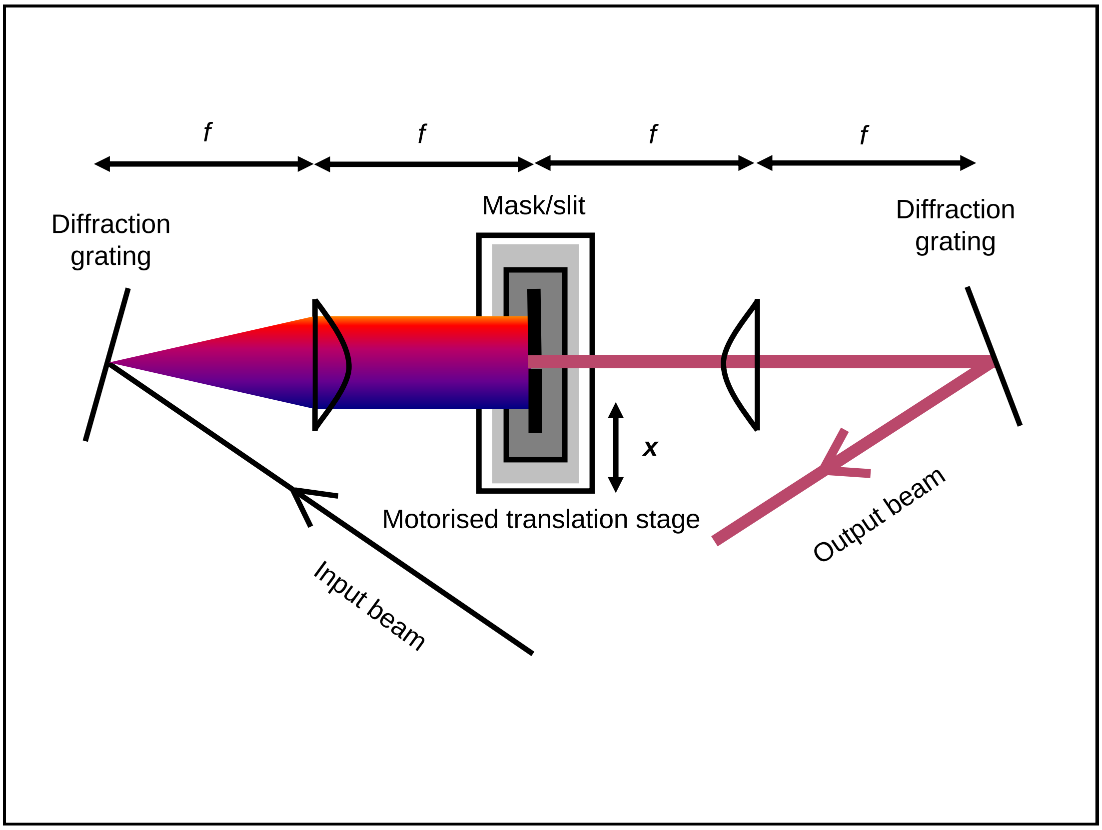

Figure 3.10: *Pulse shaper. Each pulse shaper was made up of two diffraction gratings, two lenses ($f = 50$ cm) in a 4-f arrangement, and a motorised slit in the masking plane. The focal length of the lenses determined the minimum spectral width of the output pulse. The position and width of the slits determined the output wavelength and linewidth of the output pulse.*

that entered each pulse shaper. Further half-wave plates were used to rotate the polarisation of the light to match the polarisation of the diffraction gratings.

For each pulse shaper the expanded beam was first incident on a diffraction grating with 1200 lines per mm. The grating mapped the spectral components of the pulse to an angle. The first lens was placed at the focal distance ($f = 50$ cm) and collected the diffracted light. It mapped the angle to a position at the focal plane. A motorised slit (Newport linear translation stages MFAPP, MFA-CC or M-MFN25CC, 25 mm travel) was placed at the image plane of the first lens. The slit transmitted only a small frequency component, and the lateral position of the slit determines the centre wavelength of the transmitted light. The width of the slit determined the spectral bandwidth of the transmitted light, and was chosen to produce laser pulses with $\Delta E_{\mathrm{FWHM}} = 0.2$ meV. The motorised stage allowed for automated control over the output wavelength of the pulse shaper. The second lens was placed at the focal distance $f = 50$ cm from the slit. The second lens maps the spatial position of the unmasked frequency components onto an angle. The second diffraction grating was placed at the focal plane of the second lens. It spatially recombined the frequency components of the light. The output of the second diffraction grating was a beam with a Gaussian energy spectrum, provided that the pulse shaper had a mirror symmetry about the slit. For this to be true, a pulse shaper must preserve the laser pulse characteristics in the case where no slit it present, i.e. it must be dispersionless. Such a system is known as a '4-f zero dispersion compensator' [91].

In order to check the spatial recombination of the beam after the pulse shaper, all but the highest/lowest frequency components were blocked at the masking plane and both the position and angle of the diffraction gratings were varied so that the beam had no asymmetry. The pulse shapers were tested by measuring the output pulse spectrum with a double spectrometer. Due to the fact that the beam was not ideally collimated at the input, the position of the mask was not exactly at the focal distance f. The minimum spectral width was optimised by making small adjustments to the longitudinal position of the mask. To test the recombination of the beam, spectra were taken after spatially masking all but the 'left hand side' or 'right hand side' of the output spot. This was done in order to confirm the uniformity of the wavelength across the beam profile. Finally, spectra were then taken as a function of lateral slit position in order to calibrate the pulse shapers. This provided a linear function that mapped the slit position to the wavelength of the output pulses. Figure 3.11 shows an example of a measurement of the wavelength as a function of slit position.

3.5.3 Coupling light into a single mode fibre

The laser pulses were delivered to the cryostat via single-mode fibres. The coupling efficiency into the single mode fibre was important since it was the most significant

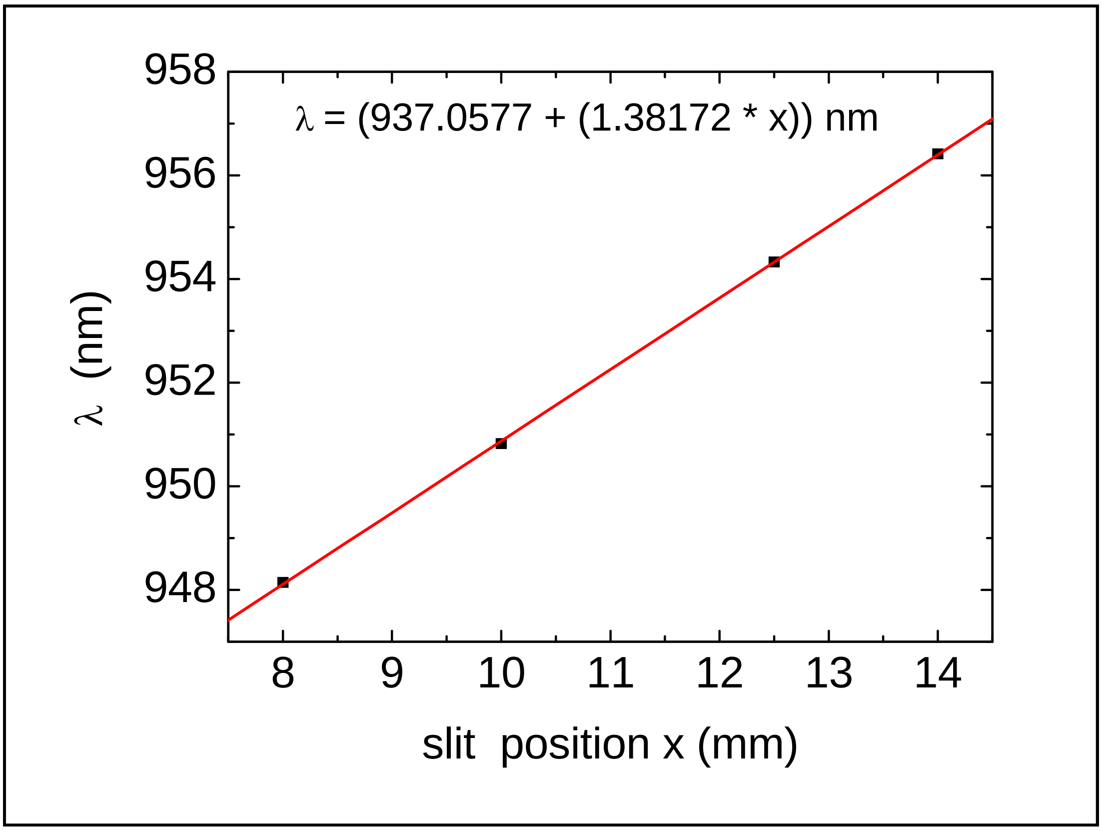

Figure 3.11: *Pulse shaper calibration. The output wavelength of the pulse shapers was measured as a function of slit position by using a double spectrometer.*

source of power loss after the pulse shapers. The pulse shapers reduced the power available from $\sim$ 800 mW to $\sim$ 800 μW. Therefore it was important to obtain the maximum possible transmission into the single-mode fibres. A high precision manual stage, with 20nm resolution, was used to couple the laser beam into the single-mode fibre (Elliot Scientific, Gold Series XYZ Flexure Stage). The single mode fibre used was designed for a wavelength operation of (830 ± 150) nm with a (730 ± 30) nm cutoff wavelength. The single-mode fibre had a 5.6 μm mode field diameter (MFD) and a 125 μm cladding. In order to achieve the maximum coupling efficiency, it was necessary to match the Gaussian mode of the input beam to the mode field diameter of the fibre. This was done by choosing a lens with the appropriate numerical aperture (NA) according to eqn 3.1, [92][93]:

$$f = \frac{\pi D w}{2\lambda}, \tag{3.1}$$

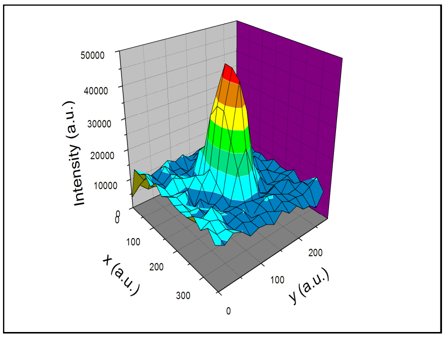

Figure 3.12: *Intensity profile of laser beam. The beam profile is assymetric due to diffraction at the slit in the pulse shapers. This reduces the maximum obtainable coupling efficiency into a single mode fibre due to mode mis-matching*

where f is the focal length of the lens, D is the Gaussian beam waist and w the mode field diameter.

By measuring the beam profile of the laser spot at the position of the microscope objective it was then possible to select a microscope objective lens with the appropriate numerical aperture. The beam profile was elliptical due to diffraction by the slit in the pulse shaper. This is shown in Fig. 3.12. Here the FWHM widths were measured as $x = 10.2$ mm and $y = 4.8$ mm. A microscope objective lens with NA $= 0.55$ and $f = 4.5$ mm was chosen. This gave a maximum measured coupling efficiency of $\sim 55\%$. This is close to maximum obtainable value of 80% [94]. The asysmmetry of the beam profile lead to a reduction in the maximum obtainable coupling efficiency into the single mode fibre. One way to circumvent this would be to use cylindrical lenses in the pulse shapers. This option was not pursued due to the added complexity in the alignment of the pulse shapers.

3.6 Single, two and three-pulse experimental setups

The experiments performed used up to three laser pulses. The experimental setup evolved as the number of pulses increased from one to three. The exact setup for a given measurement depended on the aims of the experiment and the number of pulses used. In this section the optics used for the experiments are described. For multiple pulse experiments, the pulses were labeled in accordance with their functionality: the first pulse prepared the quantum dot state and is termed the preparation pulse;

the second pulse manipulated the state and is termed the control pulse; finally, the third pulse detected the state and is termed the detection pulse.

3.6.1 Single-pulse setup

For single-pulse measurements, the laser was sent from the optical bench, via a 5m single mode fibre, to an assembly of optics which sat on a shelf on top of the cryostat. Figure 3.13 shows a schematic diagram of the experimental setup. The shelf held an assembly of optics that collimated the beam, controlled the polarisation of the output and imaged the sample. The fibre assembly was built within a cage system and consisted of a fibre connector plate, a translatable collimation lens, a linear polariser and a motorised half-wave plate. Due to the birefringence of the fibre, the linear polarisation at the input of the fibre was converted to elliptical polarisation at the output. The degree of ellipticity depended on the curvature of the bends within the fibre [95]. To minimise the effect, the optical fibre was fixed within a hose-pipe tube. This was done to fix the fibre in place and to keep the fibre bends constant. A linear polariser was placed after the collimation lens in order to correct the polarisation change within the fibre. A motorised (Newport PR50PP) rotation stage holding a half-wave plate (Newport 10RP52-2) was used to achieve control of the angle of linear polarisation. Finally, a quarter-wave plate (Newport 10RP54-2) was used to convert the linear polarisation into circular polarisation.

3.6.2 Two-pulse, two-fibre setup: measurements of hole spin preparation

The two-colour (two-pulse) experiments were carried out by using separate single mode fibres to carry the separate ‘preparation’ and ‘detection’ pulses. This experimental setup was used in the measurements of chapter 4. The reason for using two fibres was for the ease of control over the polarisation of the light. For each pulse, a separate single fibre assembly was used. See Fig. 3.13. A non-polarising beamsplitter cube was used to recombine the beams and direct the two beams to

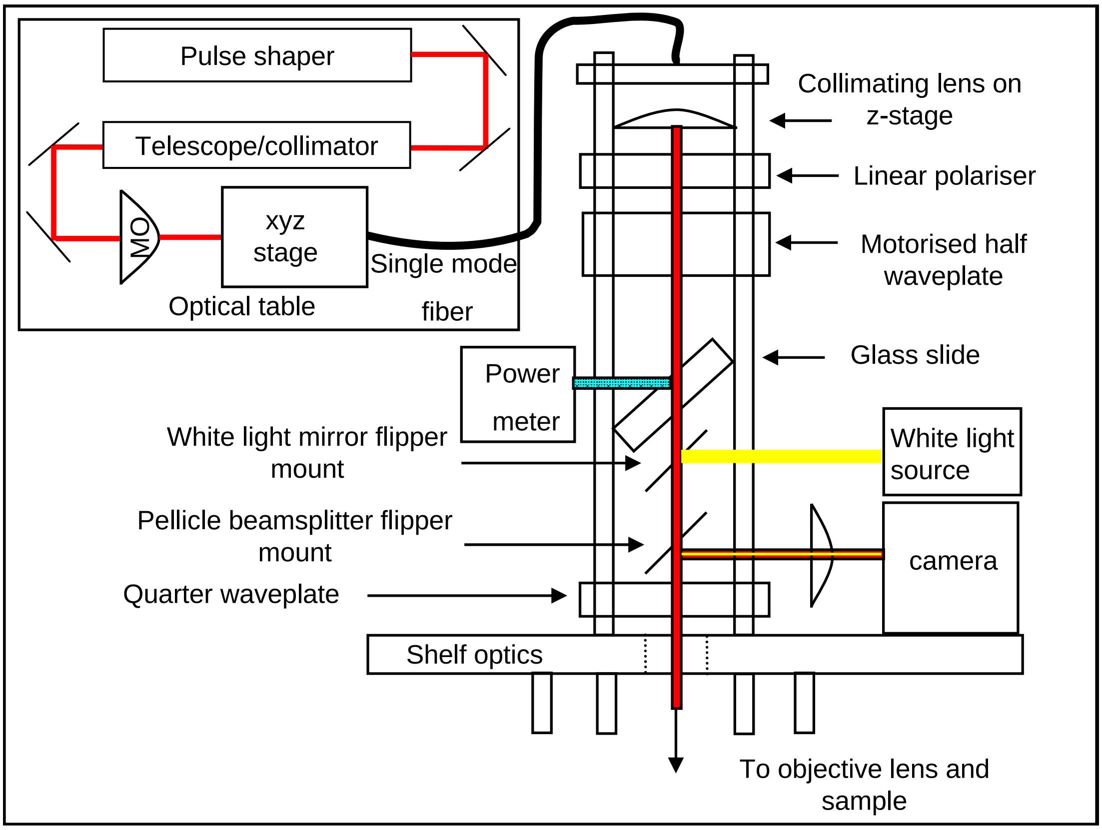

Figure 3.13: *Experimental setup for optics on top of the cryostat for single-pulse measurements. The output beam from the pulse shaper was sent via mirrors and a collimator/telescope, through a motorised neutral density filter to the 'fibre launch': a fixed microscope objective lens (MO) in front of a single-mode fibre adapator, mounted on a high precision xyz stage. A single-mode fibre sent the coupled light to the Attocube 'shelf', which held a fibre assembly and imaging optics. In order to measure the laser power, a glass slide reflected* $5-10\%$ *of the incident beam. The glass slide was chosen to be thick* $(> 5\ \mathrm{mm})$ *to prevent artifacts in the laser power spectrum*

the objective lens in the cryostat. A photograph of the shelf with the two fibre assemblies can be found in Fig. 3.14. One disadvantage of using this technique was that it was more difficult to couple both the 'preparation' and 'detection' beams to the quantum dot equally. Furthermore, the mechanical stability of the output of each beam was independent. However, automated control over the polarisation of each pulse was of crucial importance for the hole spin preparation experiments in chapter 4, making the use of two fibres essential.

A free-space delay line was constructed in order to control the relative arrival time of the preparation and detection pulses. The delay line consisted of a retro reflector (Newport UBBR2.5-1I) mounted on a linear translation stage with 15cm travel. The 15cm travel allowed for a change of path length corresponding to a 1 ns

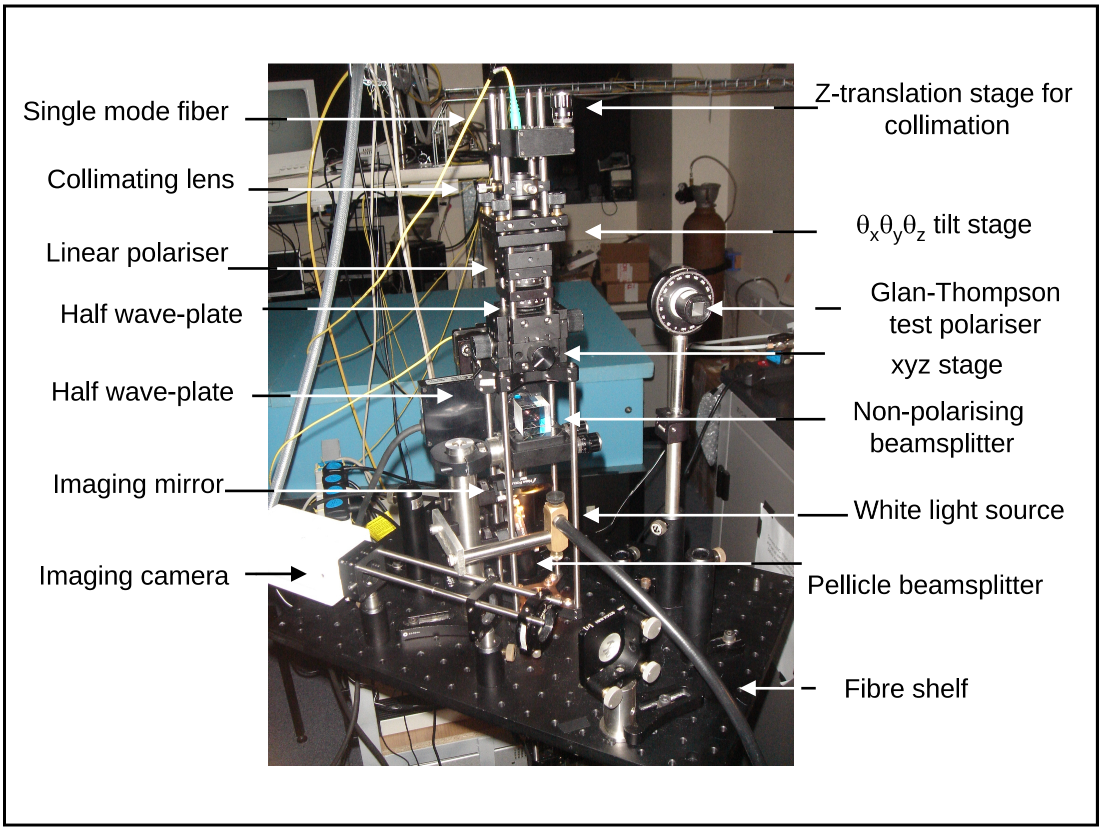

Figure 3.14: *Photograph of the 'shelf' optics which sat on top of the cryostat. The shelf optics here were arranged for a two-pulse, two-fibre assembly. Note that the second fibre assembly is hidden (into the plane of the page). To avoid the use of mirrors, each fibre assembly was mounted onto a* $x - y$ *translation stage and a tilt stage. This allowed for control over the position and angle of the beams with respect to the objective lens. For these experiments, the polarisation of each beam was controlled at the output of the fibre by using a linear-polariser and a motorised half-wave plate.*

time delay. In order to achieve minimum drift of the beam from within the delay line, care was taken to ensure that the beam direction going into the retro reflector was parallel to the axis of travel. Nonetheless, a change of coupling efficiency into the single mode fibre of 10% was measured when moving from one end of the stage to the other.

3.6.3 Two and three-pulse setup using a single fibre: measurements of the hole spin precession and optical control

As an improvement to the experimental setup, a single fibre was used to carry both the ‘preparation’ and ‘detection pulses’. This was done by recombining the beam with a 50:50 non-polarising fibre coupler/beamsplitter (Thorlabs FC830-50B). In addition to this, a section of free-space optics was introduced in each arm. The free-space sections, referred to as fibre benches, fixed the neutral density filters and half-waveplates with respect to the beam position. This was done for reasons described in section 3.6.4. Figure 3.15 contains a diagram of the so-called fibre bench which were used for power and polarisation control.

Polarisation control

The birefringence of the fibres [95] was exploited in order to achieve independent control over the polarisation of the two pulses. An in-line polarisation controller termed a ‘fibre paddle’ (Thorlabs FPC030) was used to coil and stress the fibre so that any arbitrary polarisation at the output of the fibre could be achieved. This allowed for a controlled ‘correction’ of the polarisation change due to the rest of the fibre. Fortunately, this correction was identical for orthogonal polarisations. This allowed for the motorised half-wave plates to be inserted into the ‘fibre benches’ (see Fig. 3.15). The result was the ability to have a single fibre carrying both preparation and detection pulses with arbitrary polarisations. This enabled a scale up in the number of pulses. Figure 3.15 illustrates the resulting ‘optical circuit’, which is a series of fibres and fibre beam splitters ‘mated’ together. One consequence of using such an ‘optical circuit’ was the increased power losses. This was due to ‘mating’ the fibres together and coupling losses in the free-space fibre benches. However a compromise was made to allow for scalability and improved stability.

Timing control

A variable time delay between the preparation and detection pulses of several nanoseconds was required in order to measure the hole spin precession and dephasing time T_2^*. This was achieved by replacing the 15 cm translation stage in the delay line with a stage of 30 cm travel (Newport M-IMS300CC). In addition, a double pass of the delay line was introduced by using two retro-reflectors mounted on the stage and a fixed retro-reflector mounted on the optical table. Figure 3.15 illustrates this. This increased the range of the time delay to 4 ns. Further passes of the beam through several retro-reflectors multiplies both the power losses due to changes in coupling the optical fibre, and power losses at the mirrors. Therefore it was decided not to scale up the number of passes further by using more retroflectors in the delay line to increase the available time delay. Instead, an additional length of fibre was introduced into the detection arm in order to increase the time delay between pulses beyond 4 ns. This allowed for delay times between the pulses of up to 8.5 ns.

3.6.4 Stability

A highly stable system was required to perform photocurrent spectroscopy of single quantum dots. This was particularly true in the case of multiple pulse experiments. The main source of instability in the lab was the temperature fluctuations due to the 15 minute periodic ‘on/off’ air conditioning system. These temperature fluctuations resulted in a variation of the beam direction from the laser. The pulse shapers introduced a large path length of the laser beam, which amplified the change in the beam angle and position. This caused two problems: 1) changes in coupling to the single mode fibre, and 2) changes in the position of the beam over the neutral density (ND) filter. The free-space section, referred to as the fibre bench (Thorlabs), solved the problem with the neutral density filter as it fixed the position of the beam with respect to the ND filter. A proportional, integral, or PI algorithm controlling the neutral density filter was developed to stablise the power due to changes in coupling into the single mode fibre.

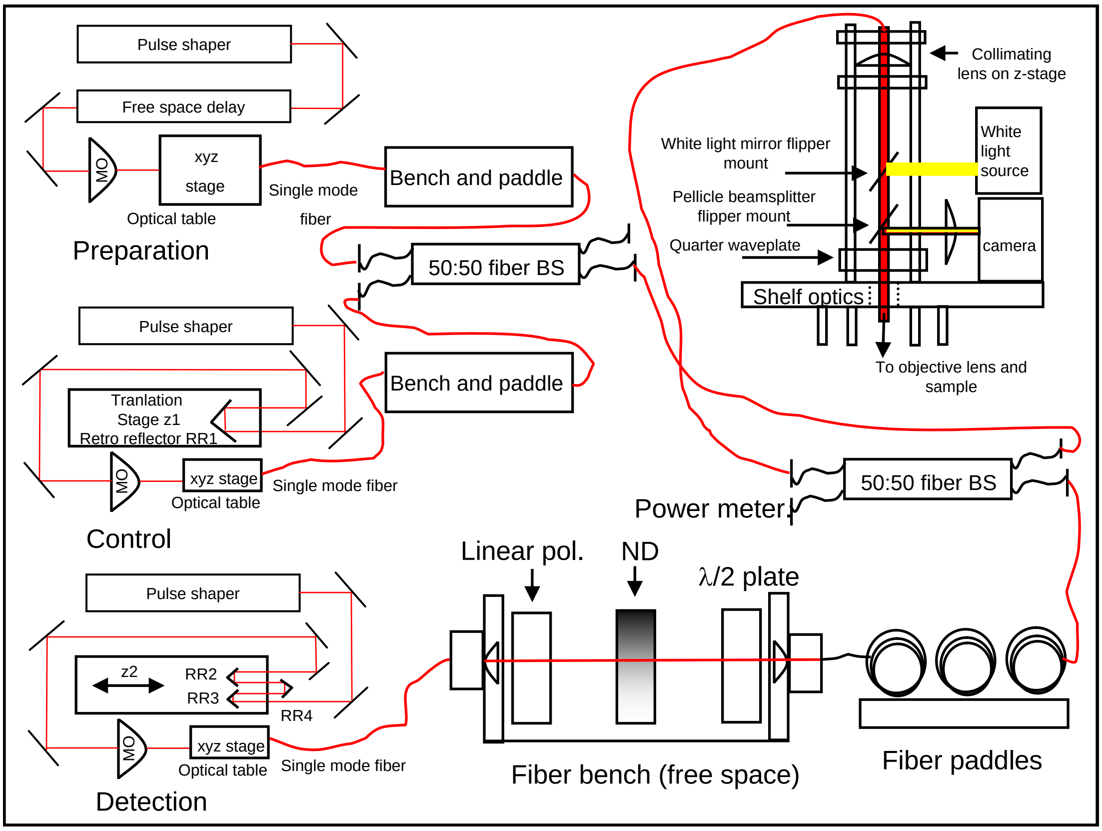

Figure 3.15: *Schematic diagram of the components used to construct an 'optical circuit' which delivered three separate laser pulse trains to the sample. The output of each pulse shaper was sent to a 'fibre bench' and 'fibre paddle' (bottom right) for power and polarisation control. The control pulse passed through a retro-reflector (RR1) delay line for up to 1ns delay with respect to the preparation pulse. The detection pulse passed through three retro-reflectors (RR2, RR3, RR4). This enabled up to 4 ns delay with respect to the preparation pulse. The pulses were re-combined in fibre beamsplitters. A single mode fibre then carried the pulses to the shelf optics. Finally, the re-combined beam was delivered to the cryostat*

A Ti:Sapphire laser only remains in stable operation when mode locked for 'constant' temperatures. Therefore the air conditioning system was required. It regulated the lab temperature to approximately within ±0.5° of 17°. A foam board insulating cover was constructed to cover the optical table fully in order to reduce the problem of beam wandering due to the temperature oscillation. This provided a fully isolated optics system and hence the level of stability in the laser power required for the experiments.

3.6.5 Automation

Many of the experiments described in this thesis required automation of the experimental setup. Measurements of time resolved photocurrent spectra required several days of continuous measurements. To carry out measurments such as this, a fully automated and remotely controlled experimental system was built. The various instruments and motor drivers were controlled using 'virtual instruments' or vi programmes written in the graphical programming language Labview. The graphical programming environment allows for easy control and link up of serial 'sub-vi's' built into a 'master' programmes which performs iterative steps to carry out an experiment. It also allows easy, real-time monitoring over the progress of an experiment.

3.6.6 Summary of optical setup

The resulting experimental setup was a single-mode fibre delivering three separate laser pulse trains at a pulse repetition of 76 MHz. Each pulse had computer controlled and independently tunable power, wavelength, polarisation and arrival time.

3.7 Measurement techniques

Several different measurement schemes were used in the experiments in this thesis. Single-pulse photocurrent spectroscopy was performed in order to characterise samples. Power-dependent photocurrent measurements were made in order to measured Rabi rotations of the neutral exciton. Two-pulse photocurrent spectroscopy was performed in order to measure the charged exciton spectra. Two and three-pulse time-resolved photocurrent spectroscopy was used in order to measure the spin dynamics of a single hole. The details of these measurement techniques are described in this section.

3.7.1 Photocurrent spectra

Single-pulse photocurrent spectra were measured in order to identify the dots most suitable for the more advanced experiments. To measure the photocurrent spectra, the laser spot was centered on an aperture within a mesa. The laser power was reduced to well below a typical π pulse power. The photocurrent was recorded as a function of the wavelength of the laser. This was done by stepping the lateral position of the slit in the pulse shaper. Measurements like this are termed 'photocurrent detuning'. Once a strong peak was identified, the laser was tuned to resonance and the photocurrent maximised by stepping the position of the sample with respect to the objective lens with the nano-positioners. The incident laser power was kept low ($\lesssim 1$ μW) so that the exciton population was not driven beyond a π Rabi rotation. An example of such a measurement for two different apertures on the same mesa can be found in Fig. 3.16. Aperture 'b3200' was selected as a candidate for single quantum dot spectroscopy. This dot was used for the measurements of the hole spin precession (chapter 4) and the hole spin control (chapter 6).

The criteria for selecting for a suitable dot for the more advanced experiments were the following: 1) any peaks within the spectrum should be spectrally isolated. 2) The dot of interest must have good coupling to the laser: the power required for a π pulse must be as low as possible, and the photocurrent signal must be as close to the maximum of 12 pA. 3) The background photocurrent I_{BG} must be as low as possible: $I_{\mathrm{BG}} <$ 2pA for a π pulse power. 4) The fine-structure splitting δ_{fs} must be as small as possible $|\delta_{\mathrm{fs}}| < 20$ μeV.

Figure 3.17 shows a typical photocurent spectrum of a 'good' quantum dot. The sample was excited with a single laser pulse of pulse area $\Theta = \pi$ and circular polarisation. The reverse bias was set to $V_{\mathrm{bias}} = -0.8$ V, where the electron and hole tunneling times were $\sim \tau_{\mathrm{e}} = 30$ ps and $\sim \tau_{\mathrm{h}} = 2.5$ ns respectively. The photocurrent was measured as a function of the laser wavelength. A clear resonance can be observed in Fig. 3.17. The resonance corresponds to the neutral exciton $|X^0\rangle$ transition. The shape and width of the resonance corresponds to the

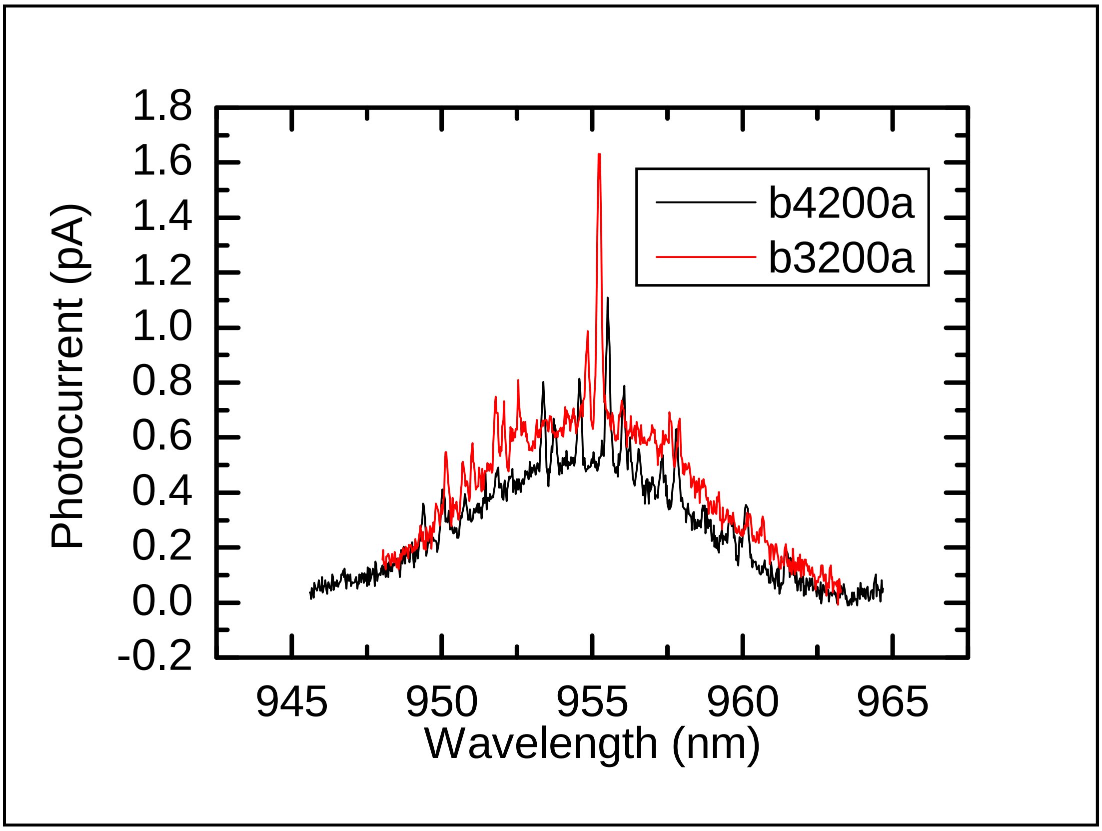

Figure 3.16: *Photocurrent spectrum of two different apertures on the same mesa of the sample labelled VN382CAM2. Aperture b4200a has several dots with poor coupling to the laser. Aperture B3200a has one very strong peak which is centered about* $\lambda = 955$ nm. *Both apertures have an undesirably large photocurrent background. Nonetheless B3200a was selected for experiments. This dot was used for measurements of the hole spin precession and control in chapters 5 and 6*

laser pulse spectrum and is fitted to a Gaussian function with an energy width FWHM ~ 0.2 meV. The amplitude is ~ 11 pA. This dot from the sample labelled 'VN382 aperture B2' was used for the hole spin preparation experiments in chapter 4.

3.7.2 Measurement of a neutral exciton Rabi oscillation

Throughout this thesis, the experiments used laser pulses with calibrated pulse areas. The calibration was done by measuring the neutral exciton Rabi rotation. First the laser pulse was set on resonance with the neutral exciton. The photocurrent was then measured as a function of the square root of the incident laser power $\sqrt{P}$ [76],[61],[77],[5],[41]. An incoherent background photocurrent, proportional

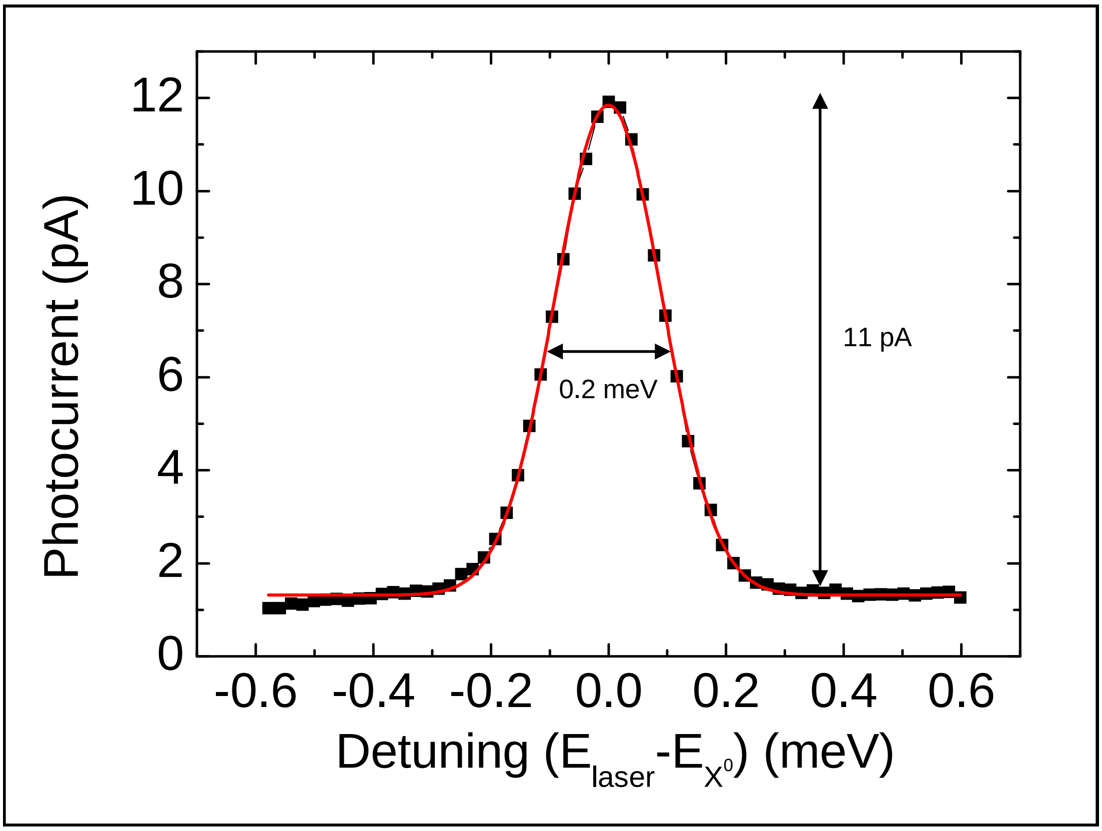

Figure 3.17: *Photocurrent spectrum of a neutral exciton in a quantum dot. The dot was excited with a single laser with pulse area* $\Theta = \pi$ *and circular polarisation. The photocurrent is plotted as a function of the detuning of the laser pulse with respect to the neutral exciton transition. Red line: Gaussian fit to the data with an energy width determine by the laser pulse* FWHM ~ 0.2 meV, *and amplitude of* ~ 11 pA.

to the incident power was subtracted for all the measurements. The background photocurrent was attributed to absorption of scattered light by other dots in the sample [61]. In order to suppress two-photon absorption and population of the bi-exciton state $|XX\rangle$, the spectral width $\Delta E_{\mathrm{FWHM}} = 0.2$ meV was set such that $\Delta E_{\mathrm{FWHM}} \ll \delta_{\mathrm{B}}$, where $\delta_{\mathrm{B}} = 2$ meV is the bi-exciton binding energy [77]. In order to suppress the population of the $|XX\rangle$ state further, circular polarisation was used for all Rabi-rotation measurements [77], [4].

Figure 3.18 shows a neutral exciton Rabi rotation at a temperature $T = 12.5$ K. Measurements similar to Fig. 3.18 were made in order to calibrate the pulse areas for multiple-pulse experiments. Oscillations in the photocurrent can be seen clearly, up to a pulse area of 14π. Beyond this pulse area, there is large scatter in the data, due to the large background. It is clear in Fig. 3.18 that the Rabi rotation is intensity

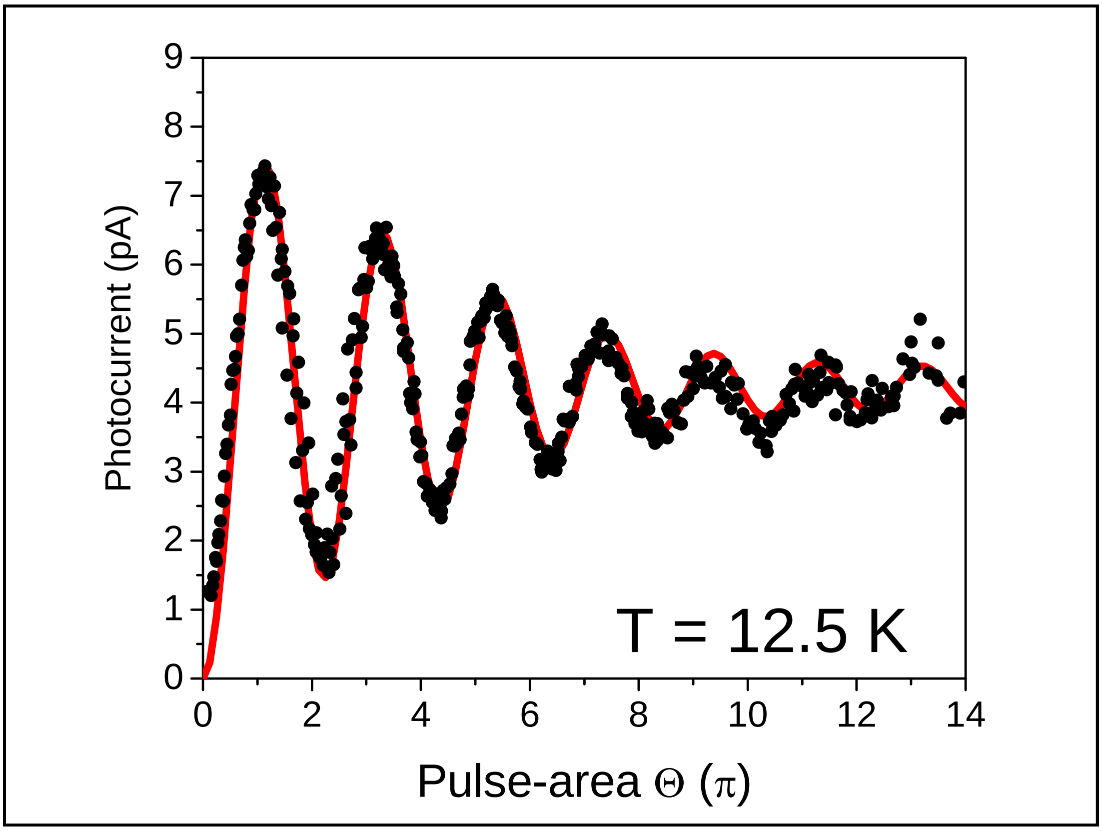

Figure 3.18: *Example measurement of a neutral exciton Rabi rotation with a temperature* $T = 12.5$ K *and applied bias* $V_B = -0.6$ V*. The fitting was done according to the model described in reference [64]*

damped. The intensity damping was studied in detail in the work of Ramsay *et al.* [63], [64] and will not be mentioned further here.

3.7.3 Time-resolved photocurrent measurements

The use of a pulsed laser source allows the measurement of the dynamics of the quantum dot hole spin state. This was achieved by varying the relative path lengths of the laser pulses which prepared, controlled and probed the hole spin state. High precision linear stages were used to vary the path length and provided sub picosecond time resolution.

Measurement of zero delay time

The first step was to ensure that the end of travel of the linear stages in each arm corresponded to a relative path length of zero. The was done by measuring the

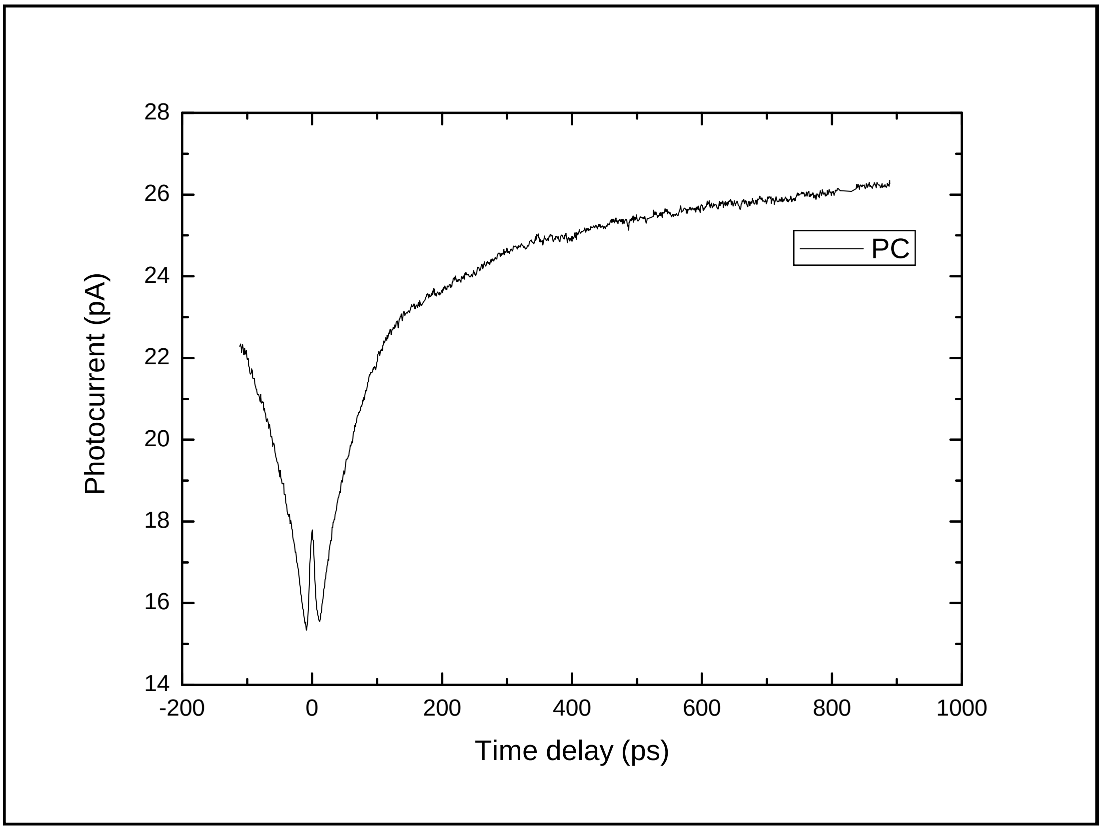

Figure 3.19: *Time resolved photocurrent measurement of how to determine 'time-zero' between two laser pulses. The photocurrent was measured as a function of the time delay between the two pulses. Both pulses were resonant with the* $|X^0\rangle$ *and had pulse area* $\Theta = \pi$. *The effective pulse area is* $\Theta = 2\pi$ *when the two* π *pulses overlap in time and this resulted in a dip in the photocurrent signal*

'inversion recovery' of the X^0 spin, to find the point at which the two/three arms in the experiments had the same path length [96]. Two laser pulses were used for these measurements. Both pulses had $\Theta = \pi$, and both were resonant with the X^0 transition. Furthermore, the pulses had either co or cross circular polarisation. The photocurrent was measured as a function of the delay time between the two pulses τ_D by stepping the position of the retro-reflector in the delay line. Figure 3.19 is an example of such a measurement. There is a dip in the photocurrent when the delay time between the laser pulses is less than the electron tunelling rate, where the pulses overlap in time, and have an effective overall pulse area $\Theta = 2\pi$. Measurements similar to Fig. 3.19 were performed for all three arms in the experiments. This allowed the relative arrival time of the laser pulses to be controlled to sub-picosecond resolution.

Measurement of fine-structure splitting

The fine-structure splitting of the neutral exciton $\delta_{\mathrm{fs}} = \hbar\omega_{\mathrm{fs}}$ could also be extracted from the inversion recovery measurements described above. This was done by fitting the difference in photocurrent (PC) for cross-polarised and co-polarised pulses, $PC_{-+} - PC_{++}$, to eqn 3.2 [96]:

$$PC_{-+} - PC_{++} = e\nu\eta f(\rho_{\uparrow\uparrow}(\tau) - \rho_{\downarrow\downarrow}(\tau)) = A\exp(-\Gamma_{\mathrm{e}}\tau)\cos(\omega_{\mathrm{fs}}\tau). \qquad (3.2)$$

Here e is the electron charge, ν is the pulse repetition frequency, η the detection efficiency and $\rho_{\uparrow\uparrow}$ and $\rho_{\downarrow\downarrow}$ are the probabilities that the exciton is in the spin up ($|X_{\Uparrow\downarrow}\rangle$) or down ($|X_{\Downarrow\uparrow}\rangle$) state respectively, and Γ_{e} is the electron tunelling rate. A physical interpretation of the measurement is the following. The circular polarisation of the first pulse creates a superposition of the linearly-polarised exciton energy eigenstates. The states accumulate a relative phase due to the fine-structure splitting δ_{fs}. Therefore the exciton state beats at the fine-structure frequency $\omega_{\mathrm{fs}} = \delta_{\mathrm{fs}}/\hbar$. This is probed by a second laser pulse, which either creates more exciton population or decreases the exciton population depending on the phase. The result of this is an oscillation in the photocurrent. More details of these type of measurements can be found in the appendix section A.4.

3.8 Summary

This chapter described the experimental methods used for performing photocurrent spectroscopy on single quantum dots embedded in Schottky diodes. First the principle of the quantum dot Schotkky diode was introduced. This was followed by a discussion of the electrical circuit used for the experiments. Next, the cryostat and sample mounting was discussed. This was followed by a discussion of the optics used for spectral filtering, and control of the polarisation, power, wavelength and arrival time or three separate laser pulses. Finally, the measurement techniques were discussed. These include measurements of a neutral exciton Rabi rotation and time resolved photocurrent spectroscopy.

Chapter 4

Fast high fidelity hole spin initialisation

4.1 Introduction

The initialisation of a spin-qubit, in this case a single hole spin, is a key ingredient of any quantum information processing protocol [3], [97]. In this chapter, experimental results demonstrating the preparation of a hole spin on a picosecond timescale are presented and the dependence of the fidelity on applied magnetic and electric fields are studied. By applying a magnetic field in the growth direction (Faraday geometry), near unit fidelity $F > 99\%$ of hole spin preparation is demonstrated. An analytical model of the spin preparation is constructed to show that the fidelity of the hole spin is limited by the precession of the exciton spin due to the anisotropic electron hole exchange interaction. The application of a Faraday geometry magnetic field improved the fidelity of spin preparation by suppressing the entanglement between electron and hole spins generated by the neutral exciton fine-structure splitting. By studying the dependence of the fidelity on the applied bias voltage, it was found that an increased electric field also improved the fidelity by reducing the time available for this spin mixing.

The results of this chapter are published in: Applied Physics

Letters: 97, 061113 (2010).

4.2 Sample details

These measurements were performed on the sample labelled VN382 aperture B2 which has been extensively studied in previous work [5], [6], [41], [77]. In the reverse bias regime, the electron tunneling rate $\Gamma_e = 30$ ps^{-1} ($V_{\text{bias}} = -0.8$ V) is much greater than the rates of hole tunneling Γ_h, radiative recombination $\Gamma_r \approx 1$ ns^{-1} and the fine-structure splitting $\delta_{\text{fs}} = 2\pi/225$ ps^{-1}. Therefore following resonant excitation of the neutral exciton transition, the electron quickly tunnels out of the quantum dot, to leave a spin-polarized hole.

4.3 Principle of operation for initialising the hole spin

Before discussing the experimental results, the principle of operation for the preparation of a single hole spin is introduced. Figure 4.1 shows a schematic diagram of the steps (a)-(e) involved in preparing and reading out the hole spin and these will be discussed in turn in the following. Each panel in Fig. 4.1 is a schematic band diagram of the quantum dot in the Schottky diode. Initially the dot is in the crystal ground state.

The first step (a) is to prepare a spin-polarised electron-hole pair using a preparation pulse with pulse area $\Theta = \pi$ and circular polarisation. Figure 4.2 (a) shows an energy level diagram of the circularly-polarised Zeeman-split neutral exciton states $X^0_{\Downarrow\uparrow}$ and $X^0_{\Uparrow\downarrow}$ in a Faraday geometry magnetic field. Here, $\Downarrow$ ($\Uparrow$) denotes the hole spin and $\uparrow$ ($\downarrow$) denotes the electron spin in the growth direction (z).

The preparation pulse was resonant with one of the Zeeman-split neutral exciton transitions. Photons with circular polarisation $\sigma^+(\sigma^-)$ carry angular momentum

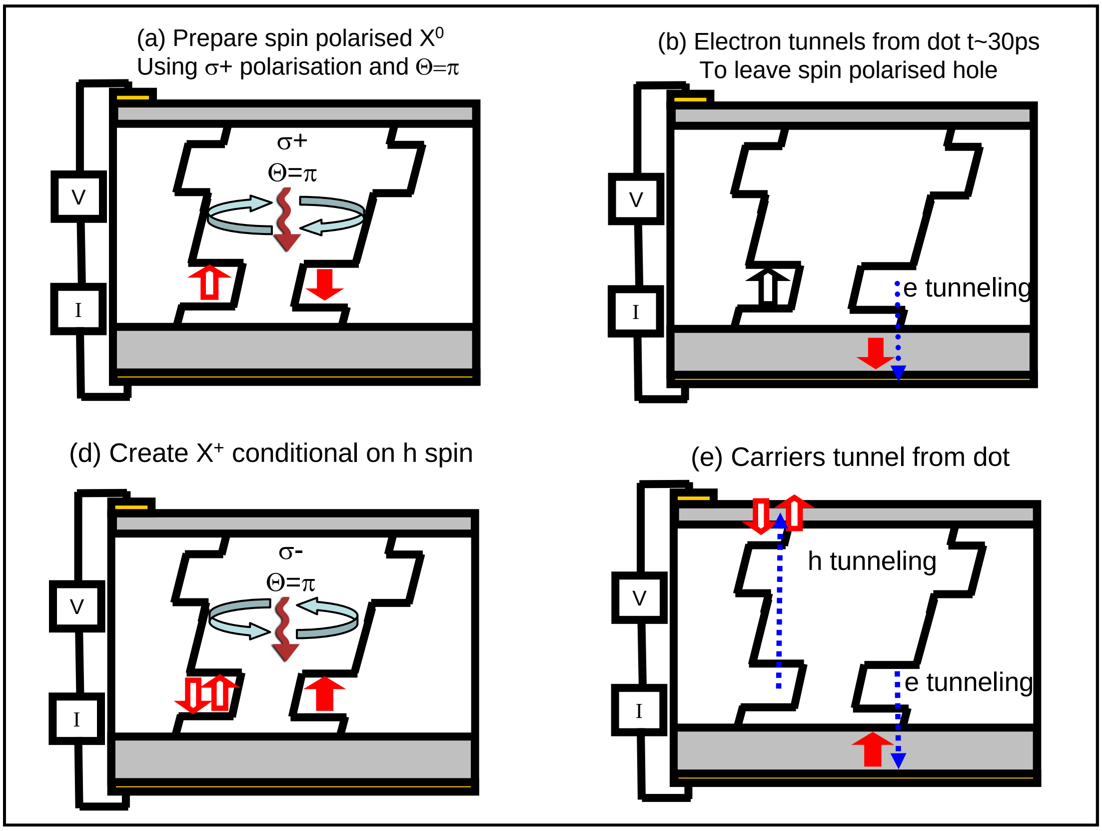

Figure 4.1: *Principle of operation for preparing and detecting the hole spin. Each panel is a schematic diagram of the Schottky diode and spin states within the quantum dot. (a) Preparation: A* $\sigma^{\pm}$ *polarised* π *pulse resonant with* X^0 *creates a spin polarised electron hole pair. (b) Ionisation: Under the applied bias the electron tunnels from the dot to leave a spin polarised hole (c) detection: A* $\sigma^{\pm}$ *polarised* π *pulse resonant with* X^+ *creates an additional electron hole pair, conditional on the spin state of the prepared hole and this can be measured as a change in photocurrent through the device after the carriers tunnel from the dot (d)*

$+1(-1)$ respectively. Due to conservation of angular momentum, the preparation pulse prepares a neutral exciton with spin $J = +1(-1)$ using circular polarisation $\sigma^{\pm}$. The exciton spin $J = m_J^{\mathrm{h}} + m_s^{\mathrm{e}}$ is the sum of the heavy-hole and electron spin projections m_J^h and m_s^e respectively. The spin projections of the hole and electron take the values $m_J^{\mathrm{h}} = \pm 3/2$ and $m_s^{\mathrm{e}} = \pm 1/2$ respectively. Therefore, a σ^+ pulse creates an exciton with spin $|\Uparrow\downarrow\rangle$ and a σ^- pulse creates an exciton with spin $|\Downarrow\uparrow\rangle$ and this is illustrates in Fig. 4.1(a) and Fig. 4.2(a). In the Faraday geometry, only bright excitons with $S = \pm 1$ are considered [23], [25] since the dark excitons are not optically active in dots with high symmetry and relatively small exchange energy. Figure 4.1(a) shows the prepared electron and hole spins in the conduction and

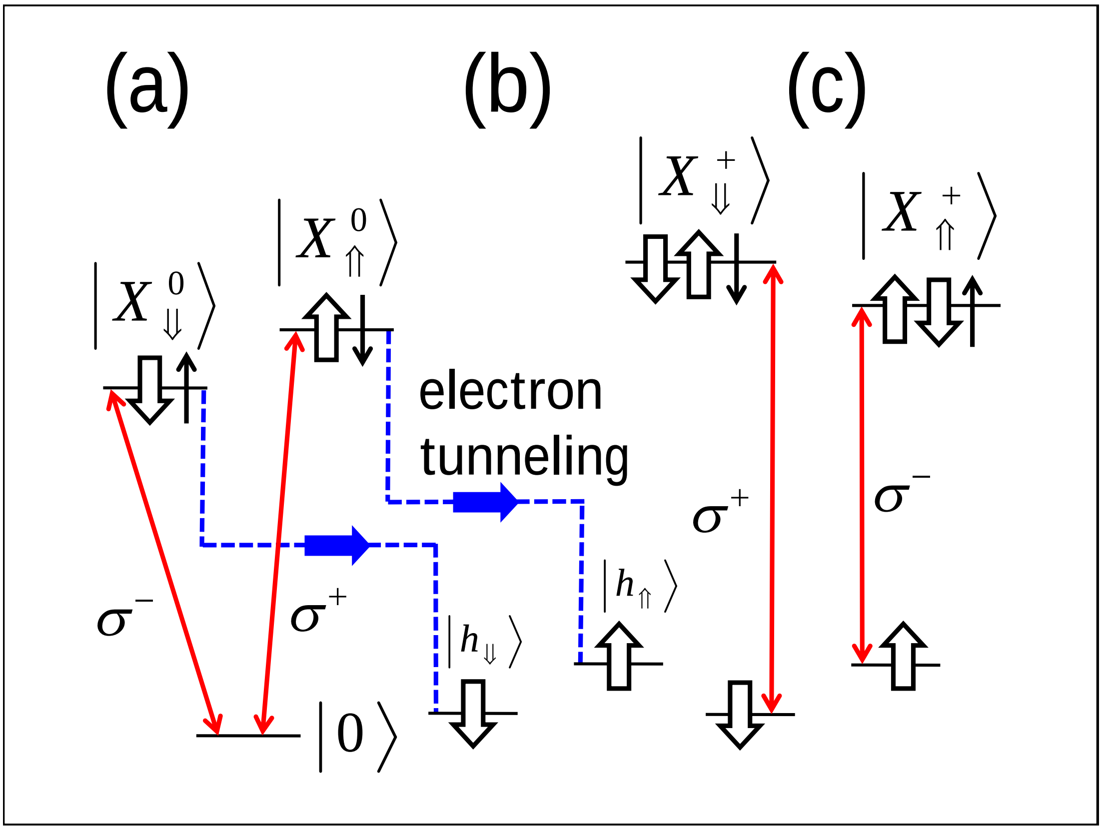

Figure 4.2: *Schematic energy level diagram in a Faraday geometry magnetic-field of (a) neutral exciton* X^0 *states* $|X_{\Downarrow\uparrow}\rangle$ *and* $|X_{\Uparrow\downarrow}\rangle$ *with* σ^- *and* σ^+ *optical selection rules respectively.(b) spin-polarised hole states* $|h_{\Downarrow}\rangle$ *and* $|h_{\Uparrow}\rangle$ *(c) Positive trion states* $|X^+_{\Downarrow}\rangle$ *and* $|X^+_{\Uparrow}\rangle$ *with optical selection rules* σ^+ *and* σ^- *respectively. Experimental procedure: (a) Preparation pulse:* $\sigma^{\pm}$ *polarised* π *pulse resonant with* X^0*. (b) Ionisation: electron tunnels out of the dot with rate* $\Gamma_e = 1/30\ \mathrm{ps}^{-1}$ *(dashed line). (c) Detection:* $\sigma^{\pm}$ *polarised* π *pulse resonant with* X^+*. If the spin has been prepared in a pure state, only the cross polarised detection pulse will be absorbed to create an additional electron hole pair due to Pauli-blocking*

valence bands respectively.

After the preparation pulse prepares the spin-polarised neutral exciton, the electron tunneled from the dot the under the applied electric field. The electron tunneling is shown in Figs 4.1(b) and 4.2(b) with blue dashed lines. The ionisation of the neutral exciton [41], [8], [72], [40], was fast compared to the neutral exciton fine-structure splitting, ensuring that a hole with a net spin was prepared.

To detect the hole spin, a second circularly-polarised pulse denoted the detection pulse, with pulse area $\Theta = \pi$, was scanned through resonance with the $h \longrightarrow X^+$ transition. Figure 4.2(b) shows the energy level diagram and selection rules for the Zeeman-split charged exciton states $X^+_{\Downarrow\Uparrow\uparrow} = X^+_{\Downarrow}$ and $X^+_{\Uparrow\Downarrow\downarrow} = X^+_{\Uparrow}$ in a Faraday geometry magnetic field. The detection pulse had either the same helicity (co-polarised) or opposite helicity (cross-polarised) as the preparation pulse. The detection pulse created an additional electron-hole pair, provided it had the opposite helicity to the preparation pulse, according to the selection rules presented in Fig. 4.2(c). Absorption of a co-polarised detection pulse was forbidden due to Pauli-blocking, since co-polarised hole spins may not occupy the same quantum state.

The amplitude of the X^+ peak is directly proportional to the hole spin projection S_z and thus the co/cross detection pulses directly map the purity of the prepared spin. Figure 4.1(d) illustrates the creation of the additional electron hole pair in the conduction and valence bands in the quantum dot. Finally the carriers tunnel from the quantum dot before the arrival of the next pulse sequence, 13ns later. This was measured as a change in photocurrent through the device as shown in Fig. 4.1(e).

4.4 Model of spin preparation

The purity of the hole spin preparation is limited by spin mixing generated by the anisotropic exchange interaction before the electron tunnels from the dot. Application of the Faraday geometry magnetic field suppresses this spin mixing since the exciton energy eigenstates become purely circular. In order to understand better the hole spin preparation purity, an analytical model was constructed.

We first consider the time evolution of the exciton spin state. At time $t = 0$ a circularly polarised laser pulse, termed the preparation pulse, with pulse area $\Theta = \pi$ and FWHM $= 0.2$ meV, is resonant with one of the neutral exciton transitions. We assume that this creates a spin-polarized electron-hole pair (exciton) with near unit probability. The fine-structure splitting $\hbar\delta_{\mathrm{fs}}$ couples the exciton states $X^0_{\Uparrow}$ and $X^0_{\Downarrow}$ and causes the exciton spin to precess. This is modeled by a 2×2 Hamiltonian with a Zeeman splitting of $\hbar\omega_z$ and a fine-structure splitting $\hbar\delta_{\mathrm{fs}}$ as seen in eqn 4.1.

$$H = \frac{\hbar}{2}\begin{bmatrix}\omega_z & \delta_{\mathrm{fs}} \\ \delta_{\mathrm{fs}} & -\omega_z\end{bmatrix}. \tag{4.1}$$

The eigenvectors $|\psi_\pm\rangle$ of the Hamiltonian H are

$$\begin{aligned}|\psi_+\rangle = &\ \sin(\theta)\,|{\Uparrow\downarrow}\rangle + \cos(\theta)\,|{\Downarrow\uparrow}\rangle \\ |\psi_-\rangle = &\ \cos(\theta)\,|{\Uparrow\downarrow}\rangle - \sin(\theta)\,|{\Downarrow\uparrow}\rangle\end{aligned} \tag{4.2}$$

where θ is a mixing angle given by $\tan(2\theta) = -\delta_{\mathrm{fs}}/\omega_z$ and $|{\Uparrow\downarrow}\rangle$ and $|{\Downarrow\uparrow}\rangle$ are the exciton spin states. The eigenvalues of H are

$$\lambda = \pm\frac{\hbar}{2}\sqrt{\omega_z^2 + \delta_{\mathrm{fs}}^2}. \tag{4.3}$$

A σ^- polarized preparation pulse creates an exciton of spin $|{\Downarrow\uparrow}\rangle$ and a σ^+ polarized preparation pulse creates an exciton of spin $|{\Uparrow\downarrow}\rangle$. The states can be expressed as linear combinations of the eigenvectors:

$$\begin{aligned}|{\Downarrow\uparrow}\rangle = &\ \sin(\theta)\,|\psi_+\rangle + \cos(\theta)\,|\psi_-\rangle\,. \\ |{\Uparrow\downarrow}\rangle = &\ \cos(\theta)\,|\psi_+\rangle - \sin(\theta)\,|\psi_-\rangle\,.\end{aligned} \tag{4.4}$$

Consider the case where the preparation pulse has σ^- polarisation. At a time t>0 the state evolves and accumulates a relative phase determined by the eigenenergy λ. The spin state $|{\Downarrow\uparrow}\rangle\Big|_{t>0}$ may then be written.

$$|\psi(t)\rangle = \sin(\theta)\,|\psi_+\rangle\, e^{i\lambda t} + \cos(\theta)\,|\psi_-\rangle\, e^{-i\lambda t} \tag{4.5}$$

We now consider the probababilty $P_{\Uparrow\downarrow}$ at at time t measuring the exciton state $|{\Uparrow\downarrow}\rangle$

by projecting $|\psi(t)\rangle$ onto the spin up basis:

$$\begin{aligned} P_{\Uparrow\downarrow} &= \left| \langle\Uparrow\downarrow|\psi(t)\rangle \right|^2 \qquad (4.6)\\ &= \sin^2(2\theta) sin^2(\lambda t) \qquad (4.7) \end{aligned}$$

Similarly the probability $P_{\Downarrow\uparrow}$ of measuring the exciton state $|\Downarrow\uparrow\rangle$ can be found by projecting onto the spin down basis.

$$P_{\Downarrow\uparrow} = \left| \langle\Downarrow\uparrow|\psi(t)\rangle \right|^2 \tag{4.8}$$

$$= 1 - (\sin^2(2\theta)\sin^2(\lambda t)) \tag{4.9}$$

From Equations 4.7 and 4.9 we can see that the total neutral exciton state population, which we define as P_+, and the difference in neutral exciton state population which we define as P_-, can be written as

$$\begin{aligned} P_+ = &\ P_{\Downarrow\uparrow} + P_{\Uparrow\downarrow} = \mathrm{e}^{-\Gamma_{\mathrm{X}}\mathrm{t}} \qquad (4.10)\\ P_- = &\ P_{\Downarrow\uparrow} - P_{\Uparrow\downarrow} = \left[1 - 2\sin^2(2\theta)\sin^2(\lambda t)\right] \mathrm{e}^{-\Gamma_{\mathrm{X}}\mathrm{t}}, \qquad (4.11) \end{aligned}$$

where a phenomenological exciton decay rate $\Gamma_{\mathrm{X}^0} = \Gamma_{\mathrm{e}} + \Gamma_{\mathrm{r}} \approx \Gamma_{\mathrm{e}}$ has been introduced to account for electron tunneling and radiative recombination at rates Γ_{e} and Γ_{r} respectively.

So far we have constructed equations for the time evolution of the neutral exciton. We must now consider how the neutral exciton states map onto the hole spin states by considering the decay paths of the neutral exciton and hole states. Figure 4.3 is a schematic diagram of the decay paths of the neutral exciton states and the hole states. The exciton spin states decay by electron tunneling to the hole spin states with a rate Γ_{e}. The exciton spin states may also decay by radiative recombination to the crystal ground with a rate Γ_{r}. The hole spin states decay by hole tunneling to the crystal ground state with a rate Γ_{h}. We neglect hole spin relaxation between the hole spin states since it is on the order of a few μs [39]. By

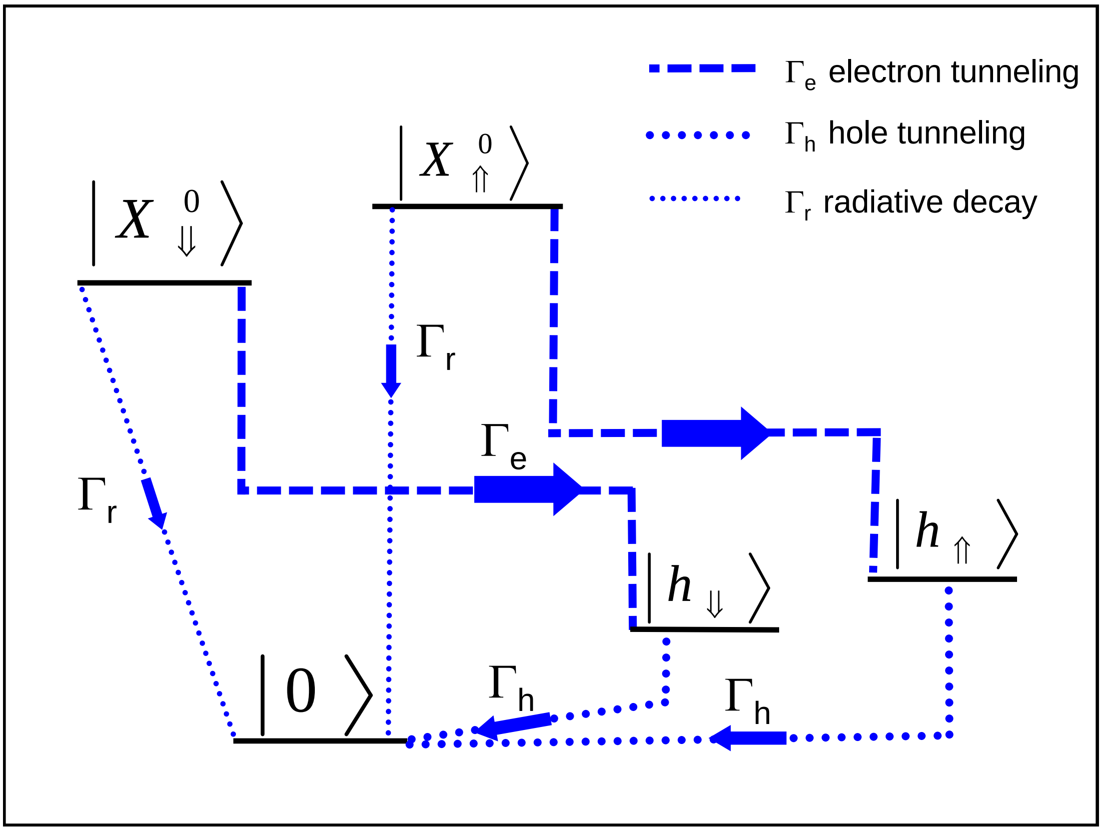

Figure 4.3: *Schematic diagram of the decay paths of the neutral exciton states* $X^0_\Downarrow$ *and* $X^0_\Uparrow$ *and hole spin states* $h_\Downarrow$ *and* $h_\Uparrow$*. After the preparation pulse prepares the exciton states, they may decay by electron tunneling with a rate* $\Gamma_\mathrm{e} \approx 30\ \mathrm{ps}^{-1}$ *or by radiative recombination, with a rate* $\Gamma_\mathrm{r} \approx 1\ \mathrm{ns}^{-1}$*. For this dot under an applied bias of* -0.8 V*, the exciton decay is dominated by electron tunneling to the hole states. The hole states decay to the crystal ground state by hole tunneling with a rate* $\Gamma_h \approx 1/2\ \mathrm{ns}^{-1}$ *at a bias of* -0.8 V*. By considering this diagram, a set of rate equations are constructed, which relate how the exciton state populations are mapped onto the hole spin state populations.*

inspection of Fig. 4.3, we can construct the following set of rate equations for the occupation of the hole spin states $|h_\Downarrow\rangle$ and $|h_\Uparrow\rangle$

$$\dot{h}_\Downarrow = \Gamma_e P_{\Downarrow\uparrow} - \Gamma_h h_\Downarrow$$

$$\dot{h}_\Uparrow = \Gamma_e P_{\Uparrow\downarrow} - \Gamma_h h_\Uparrow$$

$$\dot{h}_+ + \Gamma_\mathrm{h} h_+ = \Gamma_\mathrm{e} P_+ \tag{4.12}$$

$$\dot{h}_- + \Gamma_\mathrm{h} h_- = \Gamma_\mathrm{e} P_-, \tag{4.13}$$

where $h_{\Uparrow(\Downarrow)}$ are the hole spin up(down) state populations, and $\dot{h}_{\Uparrow(\Downarrow)}$ are the rate of change of the hole spin up(down) state populations. We define $\dot{h}_+ = \dot{h}_\Uparrow + \dot{h}_\Downarrow$ as the rate of change of the total hole spin population and $\dot{h}_- = \dot{h}_\Uparrow - \dot{h}_\Downarrow$ as the rate of change in the difference in hole spin population. We also define $h_- = h_\Uparrow - h_\Downarrow$ and $h_+ = h_\Uparrow - h_\Downarrow$ as the difference and sum of the hole spin state populations respectively. Equations 4.12 and 4.13 have the form

$$\dot{y} + \alpha y = Q \tag{4.14}$$

which has the general solution $y = e^{-I}\left[\int_0^t Qe^I dt + c\right]$ where $I = \int \alpha dt$. On solving the differential equations 4.12 and 4.13 to find h_+ and h_-, we find the hole spin contrast C and fidelity F as:

$$C = 2F - 1 = \lim_{\Gamma_X t >> 1} \left(\frac{h_-}{h_+}\right) = 1 - \left(\frac{\delta_{fs}^2}{\delta_{fs}^2 + \omega_z^2 + (\Gamma_X - \Gamma_h)^2}\right). \tag{4.15}$$

The fidelity F in eqn 4.15 is a measure of the purity of the preparation of a single hole spin. From 4.15 we can see that (i) F is limited by a competition between the fine-structure splitting and electron tunneling rate, and (ii) For large B-fields where $\omega_z^2 >> \delta_{\mathrm{fs}}^2$, $F \longrightarrow 1$ since the eigenstates are transformed from linear to circular.

4.5 Results

In order to investigate the hole spin preparation, a series of photocurrent measurements were made. To show how the fidelity of preparation improves with the application of a magnetic field, two sets of example spectral measurements are presented in this section. The first without an applied magnetic field, and the second with an applied magnetic field of $B = \pm 3$ T.

4.5.1 Hole spin preparation without an applied magnetic field

Figure 4.4(a) shows a single pulse measurements of the neutral exciton without an applied magnetic field. First, the photocurrent was measured as the preparation

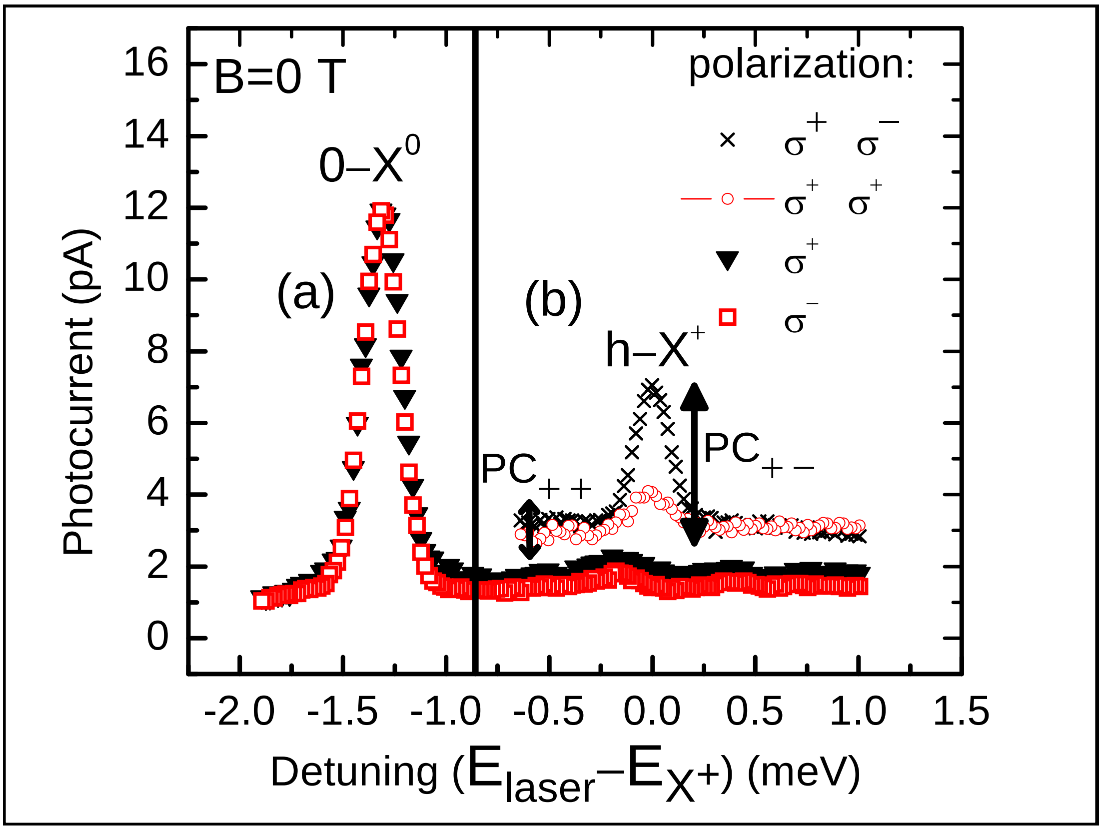

Figure 4.4: *a) Single pulse neutral exciton $0 \longrightarrow X^0$ spectra for σ^- (red squares) and σ^+ (black triangles) excitation polarisation. b) Two pulse charged exciton $h \longrightarrow X^+$ spectra using cross (black crosses) and co (red circles) polarisation. With a time delay of $\Delta\tau_D$ = 160ps, the photocurrent was measured as the detection pulse was tuned through resonance with the $h \longrightarrow X^+$. For the case of cross polarised detection, a clear peak, with amplitude PC_{+-} can be seen. In the case of co-polarised detection, a smaller peak of amplitude PC_{++} can also been seen. The charged exciton spectra have been offset for clarity*

pulse, with pulse area $\Theta = \pi$, was tuned through the $0 \rightarrow |X^0\rangle$ transition using σ^+ (black triangles) σ^- (red squared) polarisation. This was done in order to determine the optical frequency of the preparation pulse. Without a magnetic field, as in Fig. 4.4(a), the X^0 peaks occur at the same energy using σ^+ and σ^- polarisation.

With the preparation pulse resonant with the neutral exciton, the photocurrent was measured as a function of the detuning of a second pulse named the detection pulse. The detection pulse had pulse area $\Theta = \pi$ and co or cross circular polarisation with respect to the preparation pulse. With time delay of τ_D = 160 ps, an additional peak appeared in the photocurrent spectrum at $\sim +1.3$ meV detuning with respect to the X^0. This peak is shown in the case of $B = 0$ T in Fig. 4.4(b) for cross-circular polarisation (black crosses) and co-circular polarisation (red circles). The additional peak, which is present for both co and cross polarisation at $B = 0$ T is attributed to the the charged exciton X^+. This peak can be attributed to the charged exciton because of the following: 1) The peak was only present in the two pulse spectrum. 2) The signal increased exponentially with the τ_D indicating it resulted from the decay of the X^0 state. 3) The peak occurred at $\sim$ 1 meV higher energy than the X^0. Negatively charged excitons are red shifted with respect to the $|X\rangle^0$ state [34]. 4) The polarisation selection rules were consistent with the expected behaviour for the $|h\rangle \rightarrow |X^+\rangle$ transition.

The selection rules of the charged exciton transition are presented in the energy-level diagram of Fig. 4.2 (c). Absorption of the detection pulse as it is scanned through resonance with the $|h\rangle \rightarrow |X^+\rangle$ transitions is conditional on the spin of the hole. In the case of perfect spin preparation, absorption of a detection pulse co-polarized with respect to the preparation pulse is forbidden due to Pauli blocking. By contrast, absorption of a cross-polarized detection pulse is allowed, resulting in a change of photocurrent proportional to the occupation of the hole spin state, selected by the polarisation of the detection pulse. In Fig. 4.4(b) a strong X^+ peak was observed for cross polarised detection and is labelled with a photocurrent amplitude PC_{+-}. However, a weaker peak is also observed for co-polarised detection and is labelled with a photocurrent amplitude PC_{++}. The presence of this peak indicates that the hole spin was not prepared purely in the $h_\Downarrow$ state, in this case of $B = 0$ T.

4.5.2 Hole spin preparation with an applied magnetic field $B = \pm 3$ T

The neutral exciton X^0 and charged exciton X^+ spectra will now be presented in the case of an applied magnetic field $B = \pm 3$ T. The data was collected in the same manner as in the case of zero applied magnetic field. Figure 4.5(a) shows the single pulse neutral exciton spectra in an applied magnetic field $B = 3$ T

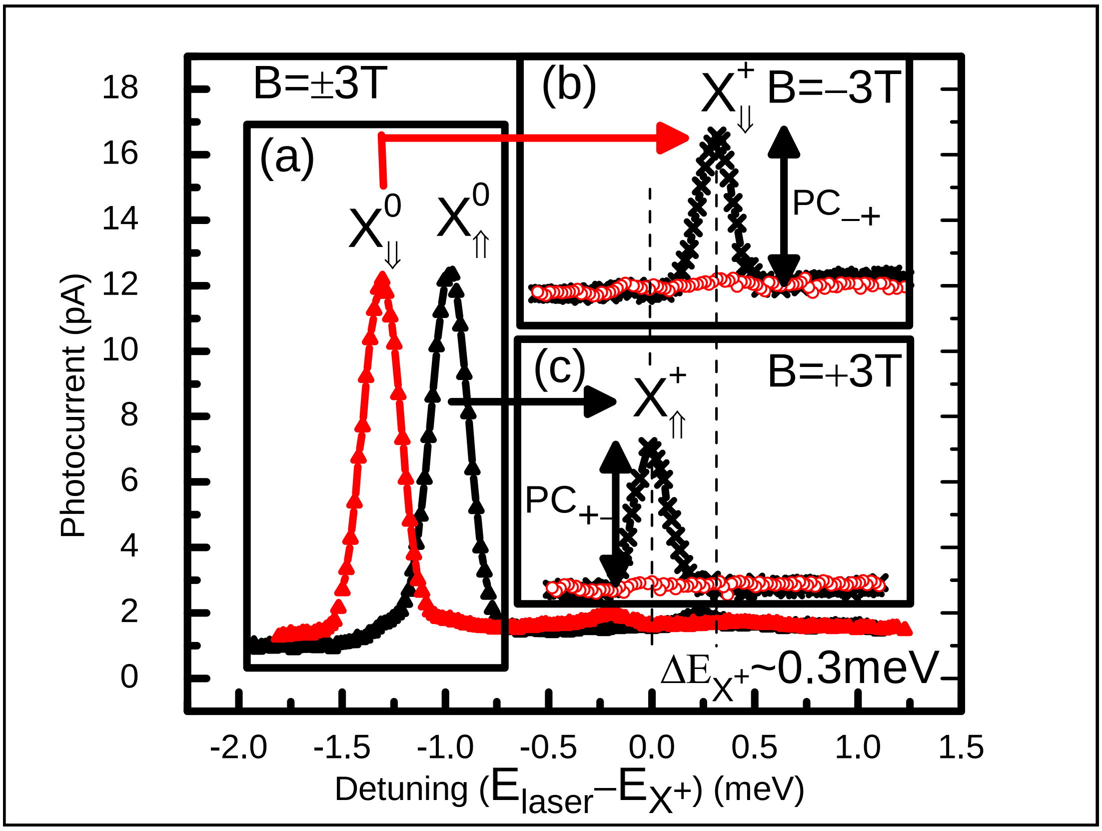

Figure 4.5: *a) Single pulse neutral exciton* $0 \longrightarrow X^0$ *spectra for* σ^- *(red triangles) and* σ^+ *(black triangles) excitation polarisation. The neutral exciton spectra are split by the Zeeman energy. (b) and (c) Two pulse charged exciton* $h \longrightarrow X^+$ *spectra using cross (black crosses) and co (red circles) polarised detection, in an applied magnetic field of* $B = +3$ T *(c) and* $B = -3$ T *(b). With a time delay of* $\Delta\tau_D = 160$ ps, *the photocurrent was measured as the detection pulse was tuned through resonance with the* $h \longrightarrow X^+$ *transitions. The red and black arrows (left to right) indicate which* X^0 *state was prepared. In both cases (b) and (c) clear peaks, with amplitudes* PC_{+-} *(c) and* PC_{-+} *(b) can be seen using cross polarised detection. In the case of co-polarisation, no peak can be seen. This indicates that the hole spin has been prepared purely in the* $h_\Uparrow$ *state for (c) and* $h_\Downarrow$ *for (b) The dotted lines in (b) and (c) indicate the expected position of the* X^+ *for the case of imperfect spin preparation. The charged exciton spectra have been offset for clarity*

using σ^- polarisation (red triangles) and σ^+ polarisation (black triangles). With an applied magnetic field, the X^0 is split into a Zeeman doublet, with well defined circular polarisation. Using σ^+ polarisation prepares the $X^0_\Uparrow$ state, and using σ^- polarisation prepares the $X^0_\Downarrow$ state. The X^0 splitting was measured as a function of applied magnetic field and the results are presented in Fig. 4.6. An out of plane g-factor for the neutral exciton, $g_{X^0} = 1.69 \pm 0.05$ was extracted from a linear fit to the data according to $\Delta E = g_{X^0}\mu_{\mathrm{B}}B_z$.

Figure 4.5(c) shows the photocurrent measurement of the charged exciton with

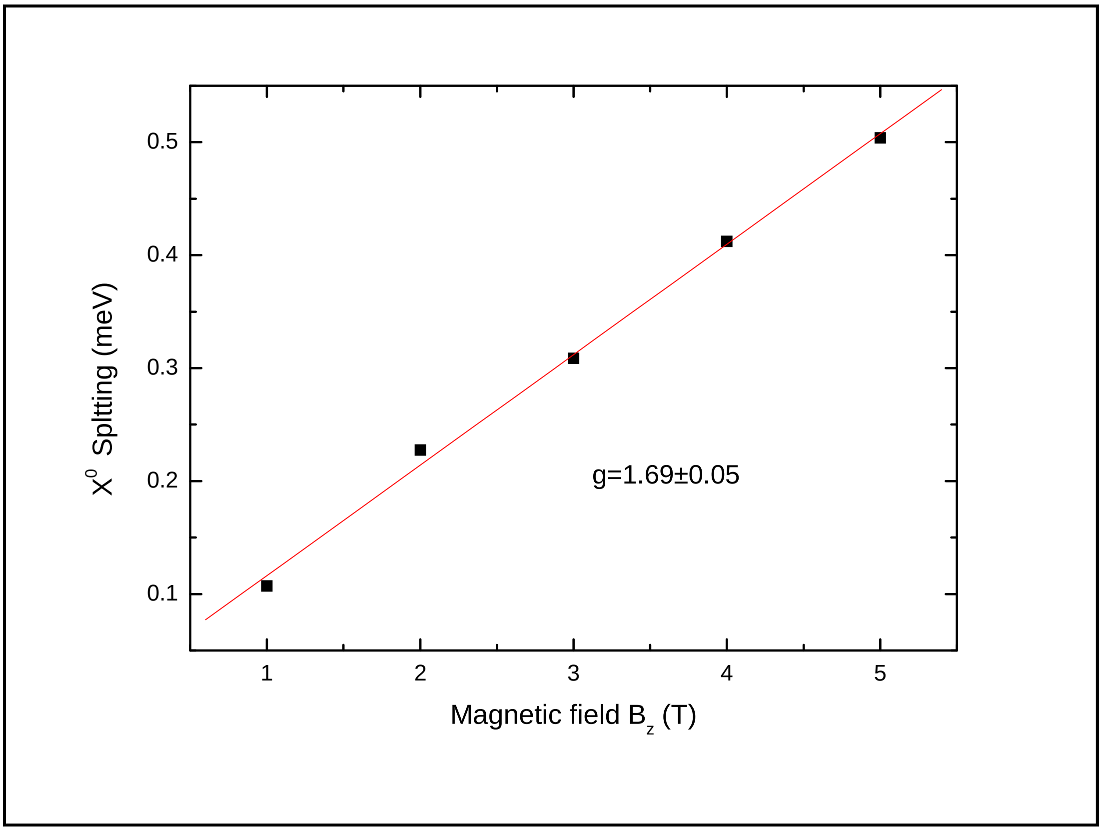

Figure 4.6: *The energy spitting of the neutral exciton as a function of applied magnetic field B_z. Gaussian fits are made to the Zeeman split neutral exciton peaks to determine the energy splitting ΔE at each magnetic field B_z. By fitting the data (red line) to $\Delta E = g\mu_\mathrm{B} B_z$, where μ_B is the Bohr-magneton, an exciton g-factor is extracted*

an applied magnetic field $B = 3$ T using both cross (black crosses) and co (red circles) polarisation. The preparation pulse with σ^+ polarisation prepared the neutral exciton state $X^0_\Uparrow$. For the case of cross polarised detection, a clear peak, with amplitude PC_{+-} can be seen in Fig. 4.5(c). This transition is allowed according to the selection rules in Fig. 4.2. In the case of co-polarised detection, no peak can be seen. This indicates that the hole spin was prepared purely in the $h_\Uparrow$ state in this case. The dotted lines in Fig. 4.5(b) indicate the expected position of the X^+ for the case of imperfect spin preparation.

To further confirm the high purity of spin preparation, the magnetic field direction was reversed and the photocurrent spectra of the X^+ are presented in Fig. 4.5(b). In this case the $X^0_\Downarrow$ state was prepared. A strong peak labelled PC_{-+} is observed using cross polarisation. Again no X^+ peak was observed for co polarised pulses, confirming the high fidelity spin preparation. From the Zeeman splitting of the charged exciton, a g-factor, $g_{X^+} = 1.69 \pm 0.05$ was obtained and $g_{X^+} = g_{X^0}$ as expected.

4.6 Magnetic field dependence

The purity of hole spin preparation is quantified by the experimental fidelity F_{PC}, defined as:

$$F_{PC} = \frac{PC_{+-}}{PC_{++} + PC_{+-}}, \tag{4.16}$$

where PC_{+-} is the amplitude of the photocurrent peak for the charged exciton using cross polarised preparation and detection and PC_{++} is the amplitude of the photocurrent peak for the charged exciton using co polarised preparation and detection.

Figure 4.7 shows an example of a series of photocurrent spectra of the X^+ as a function of magnetic field. In order to quantify the amplitude of the peaks PC_{+-} and PC_{++}, Gaussian fits were made to the data. For large magnetic fields where PC_{++} can not be resolved, an estimate of the amplitude was made. The estimate ϵ is the variance of the photocurrent noise, $\epsilon = \sigma/\sqrt{N}$, where σ is the standard deviation in the photocurrent within the FWHM of the peak position and N the number of data points within this range. The peak position was found by reversing the magnetic field direction. A set of spectral measurments for magnetic fields $(-4 \leq B_z \leq +4)$ T were made to investigate the hole spin preparation fidelity.

Figure 4.8 shows the measured fidelity as a function of applied magnetic field at a gate voltage of -0.8 V. The fidelity was observed to increase strongly as a function of B from 81% at $B = 0$ T to $\backsimeq$ 100% for $B \geq 1T$. The experimental data were fit according to eqn. 4.15 using two fitting parameters $\delta_{\mathrm{fs}} = 2\pi/(225 \pm 25)$ ps^{-1} and $(\Gamma_{\mathrm{X}} - \Gamma_{\mathrm{h}}) = 1/(28 \pm 4)$ ps^{-1}. The fitting paramaters are in good agreement with previous measurements of $\Gamma_{\mathrm{X}} = 1/30$ ps^{-1} and $\delta_{\mathrm{fs}} = 1/230$ ps^{-1} on this dot as measured by inversion recovery measurements [5], [77], [96]. The functional

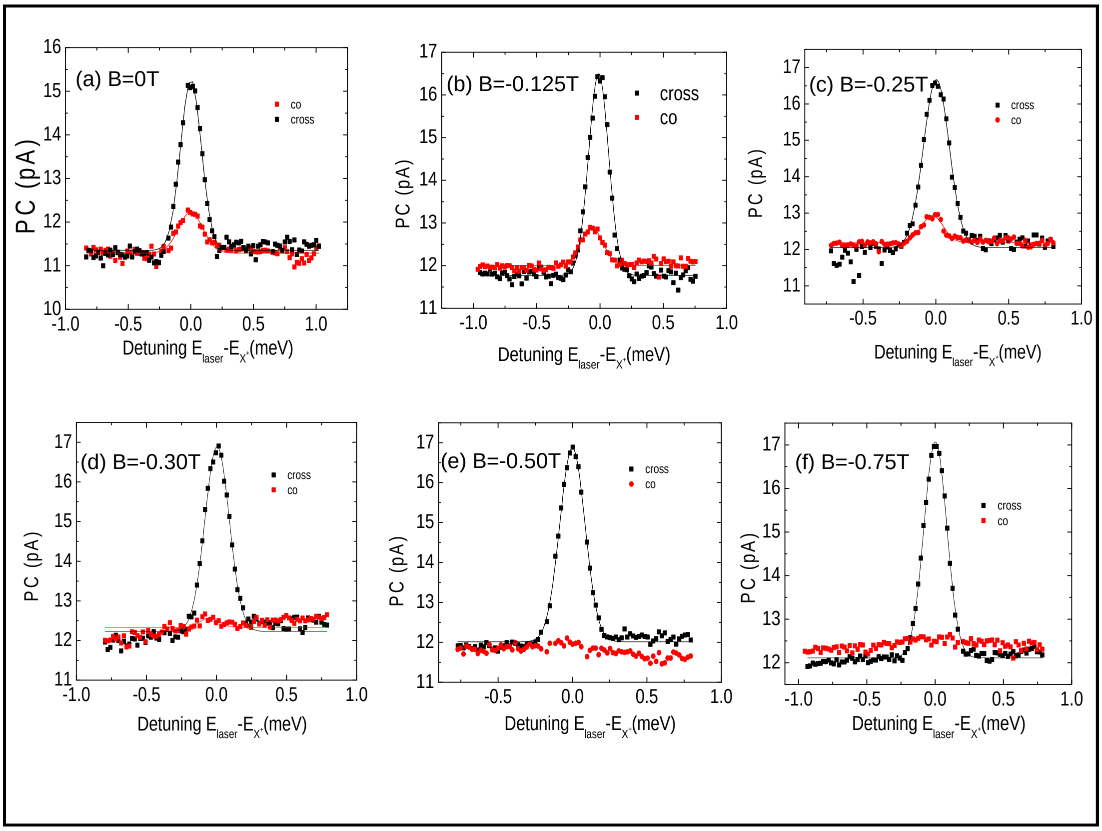

Figure 4.7: *Series of photocurrent spectra of the* X^+ *as a function of increasing magnetic field from* $B = 0$ T *(a) to* $B = -0.75$ T *(f). Black(red) are the data points for cross(co) polarised preparation an detection pulses. Black(red) solid lines are Gaussian fits to the data.*

dependence of F with magnetic field is in excellent qualitative agreement with the model.

4.7 Voltage dependence

The dependence of the fidelity on the electron tunneling rate was also investigated by measuring F_{PC} as a function of gate-voltage at $B = 0$ T. A series of photocurrent measurements of PC_{++} and PC_{+-} were made. The results are presented in Fig. 4.9. For increasing gate-voltage and hence electron tunneling rate, a rise in the measured fidelity was observed.

The red lines in Fig. 4.9 show a calculation of the range of possible values for F using known tunneling rates [5] and the fine-structure splitting determined from the fitting in Fig. 4.8. The range in values for the calculation, bound within

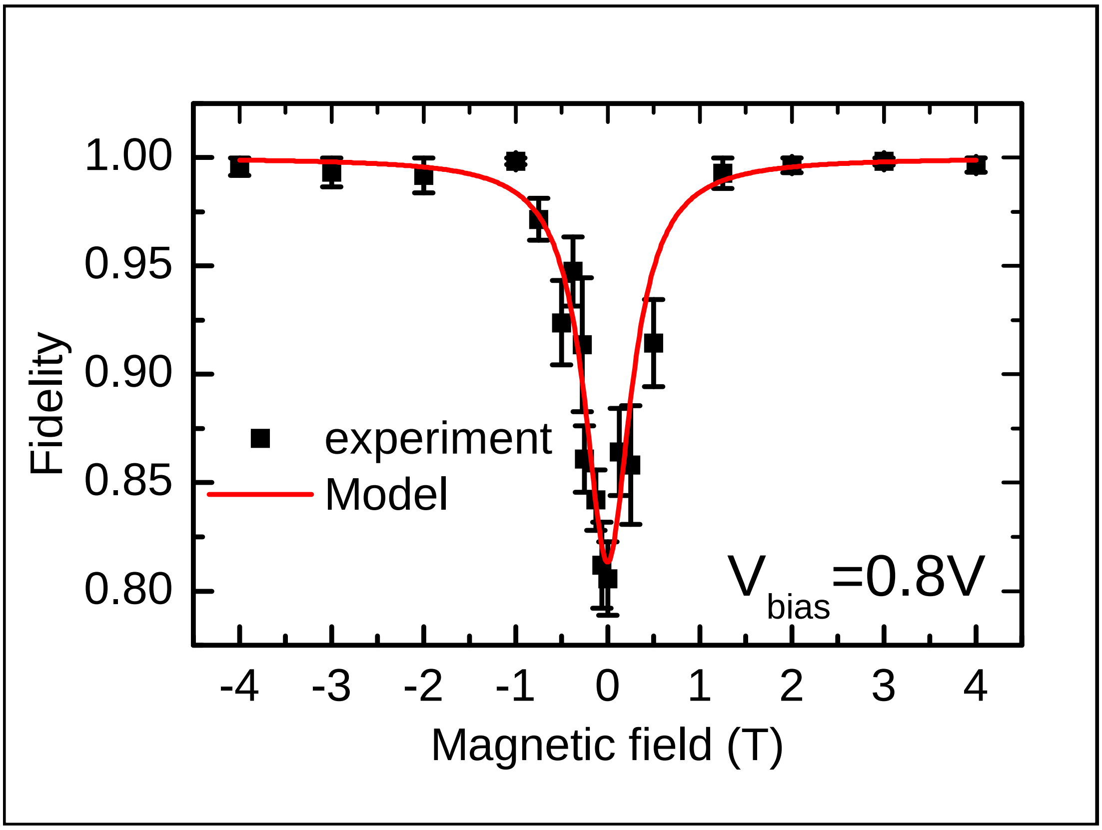

Figure 4.8: *Hole spin preparation fidelity as a function of magnetic field. The red line is a fit to eqn 4.15. Each data point was found using the photocurrent amplitudes for the* X^+ *with co and cross polarisation, and by calculating* F_{PC}. *For* $B \leq 1$ T, *errors were calculated using the least squares fitting. For* $B \geq 1$ T, *where the co-polarised peak cannot be resolved, error bounds were calculated using the variance of the photocurrent noise* $\epsilon/2$.

the solid lines of Fig. 4.9 take into account the range in values of the parameters $\Gamma_X = 1/(28 \pm 4)\text{ps}^{-1}$ and $\delta_{\text{fs}} = (2\pi/(225 \pm 25))\text{ps}^{-1}$. There is good agreement between the model and the experiment. A contributing factor to any discrepancy may be related to neglecting a small variation in the fine-structure splitting with gate-voltage [96].

The results in Fig. 4.9 indicate that increasing the gate voltage improves the spin preparation by decreasing the time available for the exciton spin to precess. However, by increasing the static gate voltage there is a trade off between improving the fidelity of the hole spin preparation and reducing the lifetime of the hole. In principle, this may be overcome through dynamic control of the tunneling rates using voltage modulation [62], [80]. Further improvements could be made by optimizing the tunnel barriers in the device to achieve faster and slower electron and hole

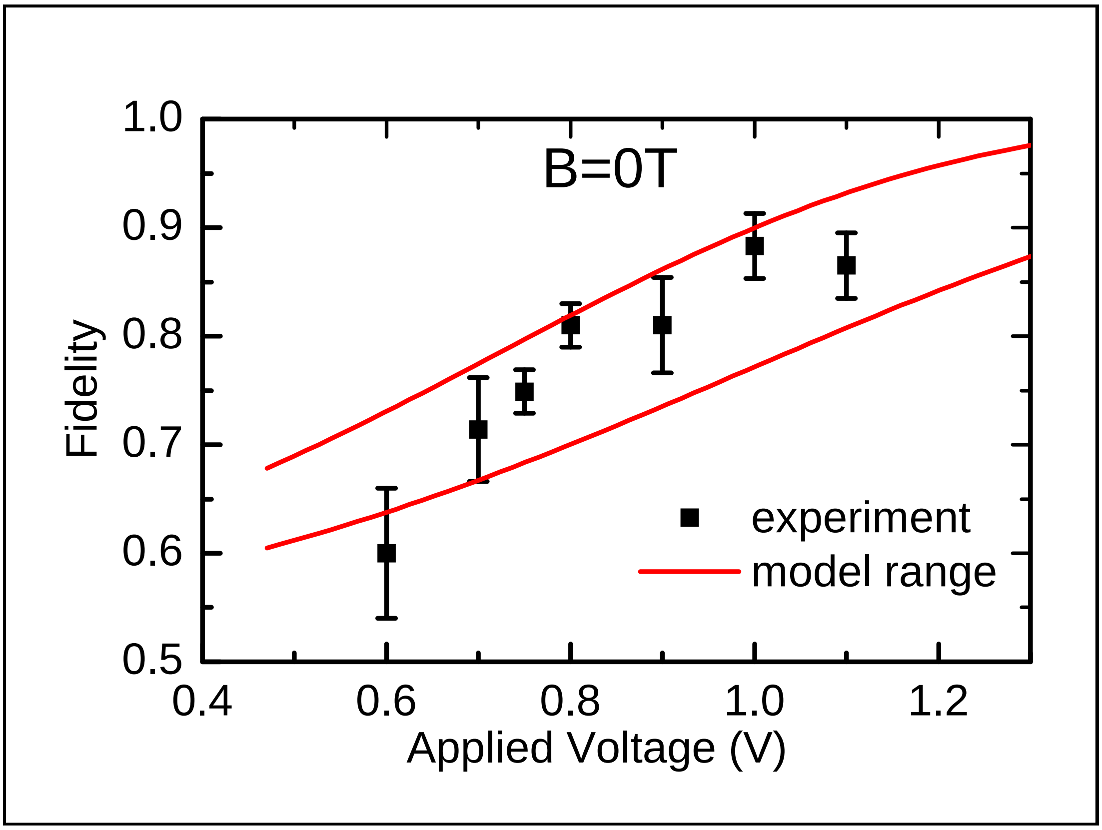

Figure 4.9: *Hole spin preparation fidelity as a function of applied reverse bias at* $B = 0$ *T. Two (red) lines indicate range of calculated values of* F *using eqn. 4.15 with* $\omega_z = 0$*. Each data point was found using the photocurrent amplitudes for the* X^+ *with co and cross polarisation by, and calculating* F_{PC}*. The errors were calculated using least squares fits.*

tunneling rates respectively.

4.8 Summary

To summarize, the fast ($1/e$ time of 30 ps), triggered, high fidelity ($F > 99\%$) initialisation of a single hole spin in a Faraday geometry magnetic field has been demonstrated by using a picosecond laser pulse and an electrical detection technique. The speed of preparation, limited by the electron tunneling rate, is compatable with gate times used in the coherent control experiments.

The purity of the hole spin preparation was limited by the mixing between the electron and hole spins, generated by the anisotropic exchange interaction before the electron tunneled from the dot. For the dot presented here, with a fine-structure splitting of $\delta_{\mathrm{fs}} = 2\pi/(225 \pm 25)\ \mathrm{ps}^{-1}$, a gate voltage of -0.8 V, and a strong 4-T magnetic field, the model predicts a fidelity of 99.9% for the hole spin preparation. By reducing δ_{fs} and the strength of spin mixing, for example by using techniques such as thermal annealing [26], strain tuning [29] and growth on (111)B substrates [30], [31], similarly high fidelities could be achieved at significantly lower magnetic fields.

Chapter 5

Hole spin precession and measurement of dephasing time

5.1 Introduction

The principal source of dephasing of an electron spin trapped on a semiconductor quantum dot is the nuclear spins of the crystal lattice [50],[98]. Since the heavy hole has a *p*-type, rather than *s*-type wavefunction, the hyperfine interaction experienced by the hole is about one tenth of that of the electron due to the suppression of the contact hyperfine interaction [13], [53], [54]. This has stimulated interest in using the hole spin as a qubit, encouraged by measurements of hundreds of μs lifetimes [39] and high visibility dips in coherence population trapping (CPT) experiments, suggesting coherence times in the microsecond regime [16]. However, as yet there is no evidence for the creation of a superposition state that survives in the absence of a driving laser, nor a direct measurement of T_2^*. This is an important prerequisite for the coherent control of a single hole spin. Important steps towards using a hole spin as a qubit include the initialisation of a single hole spin [43], [41], [99] and a demonstration of a non-general single qubit operation [41]. By comparison, there are a number of reports of the precession of a single electron spin [100] and the coherent optical control of the electron spin [11],[12], [89].

In this chapter, the observation of the precession of a single heavy-hole spin confined to an InAs/GaAs quantum dot in an in-plane magnetic field is presented, the signature of a coherent superposition of the energy-eigenstates of the hole spin. The superposition is created through the fast $(10-100$ ps) ionisation of a spin-polarised electron-hole pair, where the electron tunnels from the dot to leave a spin-polarized hole. The contrast of the spin precession is found to have a maximum value of close to one half, when the in-plane hole Zeeman energy is tuned into resonance with the effective fine-structure splitting of the bright neutral exciton. From the decay of the hole spin precession, a dephasing time $T_2^* = 12.2 - 17.8$ ns is deduced. This value is compatible with dephasing due to fluctuations in a nuclear magnetic field acting on the hole spin, and is 7-10 times longer than for an electron spin confined to an InAs/GaAs quantum dot [59].

5.2 Sample details

These measurements were performed on the sample labelled VN382 CAM2 Aperture B3200 mounted in a Voigt geometry. Importantly, in the reverse bias regime, the electron tunneling rate, $\Gamma_\mathrm{e} \approx 90\ ps^{-1}$ ($V_\mathrm{bias} = -0.8$ V), is much greater than the rates of hole tunneling $\Gamma_\mathrm{h} \sim 3\ \mathrm{ns}^{-1}$, radiative recombination $\Gamma_\mathrm{r} \approx 1\ \mathrm{ns}^{-1}$ and the fine structure splitting $\delta_1 = 2\pi/236\ \mathrm{ps}^{-1}$. Therefore, after resonant excitation the neutral exciton transition, the electron quickly tunnels out of the quantum dot, to leave a spin polarized hole. This will be explained in the following section

5.3 Principle of operation

The principle of operation for the preparation and detection of a coherent superposition state is introduced here. Figure 5.1 shows a schematic band diagram of the spin states of the quantum dot in the Schottky diode structure. This is is accompanied by the energy-level diagram in Fig. 5.2, which shows the neutral exciton (a), the hole spin states (b) and the charged exciton (c). These figures

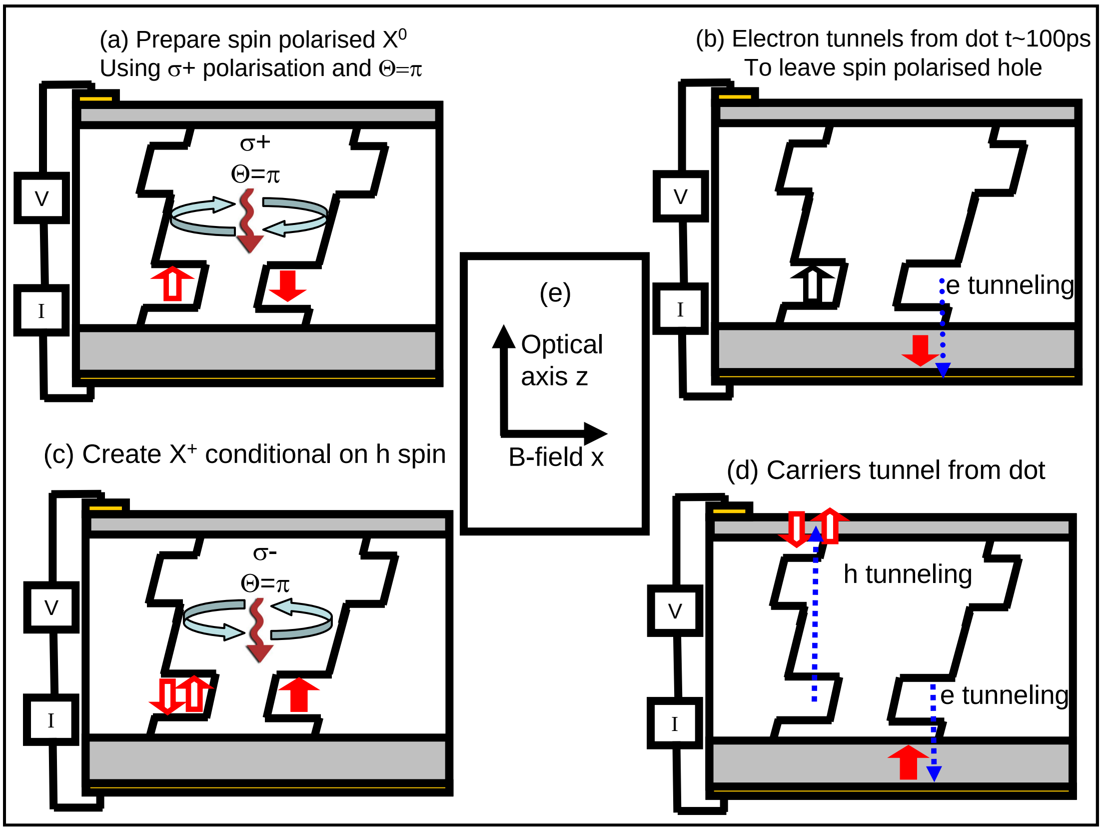

Figure 5.1: *Principle of operation for preparing and detecting the hole spin. Each panel is a schematic diagram of the Schottky diode. The electron and hole spin states within the quantum dot are denoted by solid red arrows and non-solid red arrows respectively. (a) Preparation: A* $\sigma^{\pm}$ *polarised* π *pulse resonant with* X^0 *creates a spin-polarised electron hole pair. (b) Ionisation: Under the applied bias the electron tunnels from the dot to leave a spin-polarised hole. (c) Detection: a* $\sigma^{\pm}$ *polarised* π *pulse resonant with the positively charged exciton* X^+ *creates an additional electron hole pair, conditional on the spin state of the prepared hole. This can be measured as a change in photocurrent through the device after the carriers tunnel from the dot (d)*

illustrate the steps (a)-(d) involved in preparing and reading out the hole spin and these will be explained in turn shortly. Figure 5.1 (e) shows the geometry for the experiments. The magnetic field was applied in-plane, in the x-direction, and the laser pulses propagated in the z-direction. Throughout this discussion, the hole spin states up $|\Uparrow\rangle$ and down $|\Downarrow\rangle$ and the electron spin states up $|\uparrow\rangle$ and down $|\downarrow\rangle$ are defined to be in the z-direction. Initially the dot was in the crystal ground state.

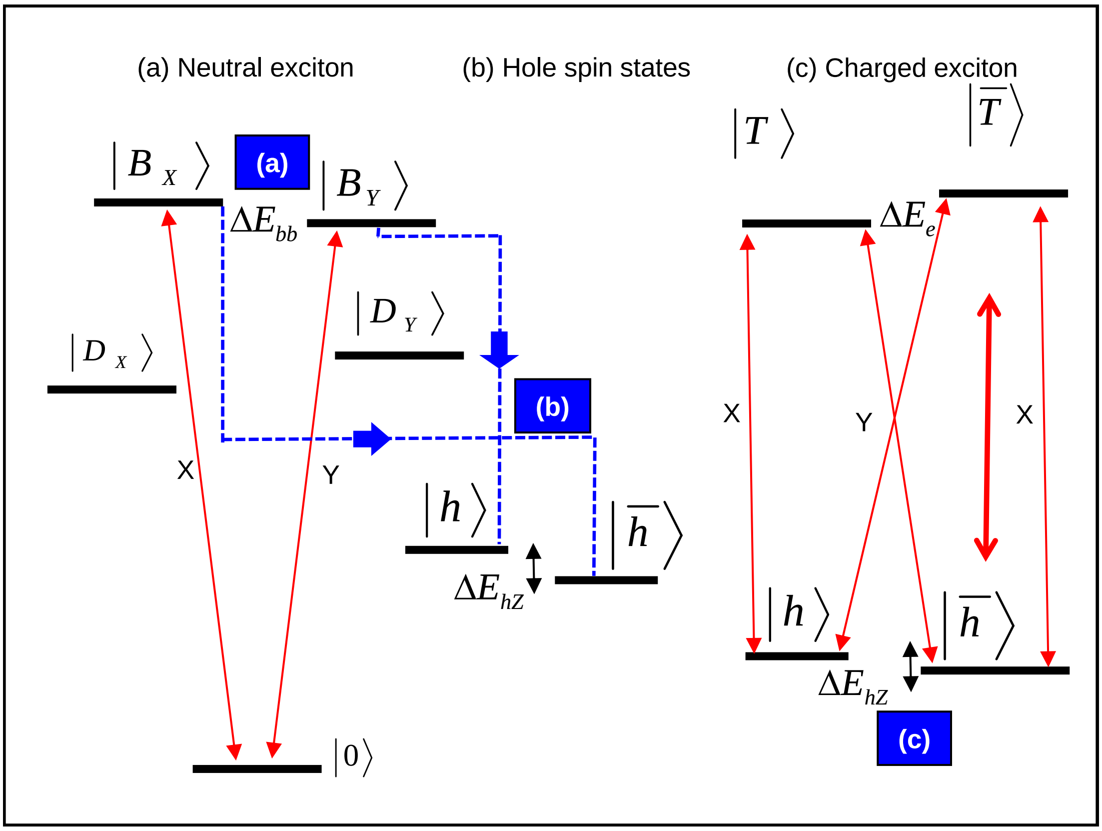

Figure 5.2: *Energy-level diagram in Voigt geometry magnetic field. (a) The neutral exciton has 4-states: two bright ($|B_\alpha\rangle, |m_J| = 1$) and two dark ($|D_\alpha\rangle, |m_J| = 2$). After preparing the neutral exciton, the electron tunnels from the dot to leave a spin polarised hole state as indicated by the dashed blue lines (b) The hole spin states are aligned parallel and anti-parallel with respect to the magnetic field: $|h\rangle, |\bar{h}\rangle$. (c) The corresponding positive trion states are $|T\rangle = |h\bar{h}e\rangle$, and $|\bar{T}\rangle = |h\bar{h}\bar{e}\rangle$. The labels X and Y indicate the polarisations of the transitions.*

5.3.1 Preparation of spin polarised neutral exciton

The first laser pulse (Fig. 5.1 (a)) was used to prepare the hole spin through ionization of a spin-polarised electron-hole pair [41], [8]. The preparation pulse had a pulse-area of π and was σ^+-circularly polarised. The polarisation of the preparation pulse σ^+ carrying angular momentum $m_J = +1$ transfers +1 unit of angular momentum to the exciton. Therefore resonant excitation of the bright neutral exciton with a π pulse and σ^+ polarisation creates an electron-hole pair $|\downarrow\Uparrow\rangle$ with high probability. Figure 5.1(a) illustrates the preparation of the spin polarised electron hole pair within the quantum dot, indicated by the spins $\Uparrow$ and $\downarrow$.

Figure 5.2 (a) shows an energy level diagram of the energy eigenstates of the neutral exciton in the Voigt geometry. There are four neutral exciton states in Fig 5.2, the bright states $|B_{x,y}\rangle$ with angular momentum $|m_J| = 1$ and the dark states $|D_{x,y}\rangle$ with angular momentum $|m_J| = 2$. The prepared exciton state $|\Uparrow\downarrow\rangle$ is a superposition of the bright exciton states $|B_{x,y}\rangle$ with some dark-exciton $|D_{x,y}\rangle$ component due to admixing by the in-plane magnetic field. The superposition evolves in time due to the energy-splitting E_{bb} between the bright exciton states, which is a combination of the in-plane Zeeman energies E_{hZ}, E_{eZ}, and the electron-hole exchange energies. More details of the neutral exciton in the Voigt geometry can be found in section A.1 and with reference to Fig. A.4.

5.3.2 Ionisation of the neutral exciton: hole spin preparation

Figures 5.1(b) and 5.2 (b) show the electron tunneling from the dot under the applied electric field. Provided that the time evolution of the neutral exciton state, due to the energy splitting E_{bb}, is slow compared to the electron tunneling rate, the resulting state is a hole with a net spin. For example, using a σ^+ preparation pulse to prepare a neutral exciton with spin $|\Uparrow\downarrow\rangle$, prepares a hole spin $|\Uparrow\rangle$, and conversely, using σ^- preparation pulse to prepare the state $|\Downarrow\uparrow\rangle$, prepares the hole spin state $|\Downarrow\rangle$. The hole tunneling rate is much slower than the electron tunneling rate, due to its increased effective mass, and due to an AlGaAs blocking barrier, as discussed in section 3.3. The factors that determine the purity of the hole spin preparation will be discussed later.

5.3.3 Precession of the hole spin

The energy eigenstates of the hole spin $|h\rangle$ and $|\bar{h}\rangle$ in Fig. 5.2 are aligned parallel and anti-parallel with respect to the magnetic-field direction. The hole spin-up $|\Uparrow\rangle$ is a superposition of these states $|\Uparrow\rangle = \frac{1}{\sqrt{2}}(|h\rangle + \left|\bar{h}\right\rangle)$, and consequently the hole spin precesses about the magnetic field, as the $|h\rangle$ and $\left|\bar{h}\right\rangle$ states accumulate a relative phase due to the in-plane hole Zeeman splitting, E_{hZ}. The wavefunction of the superposition state has the form:

$$|\psi(t)\rangle = \frac{1}{\sqrt{2}}\left(e^{\mathrm{i}\omega_\mathrm{h}\mathrm{t}/2}\left|\mathrm{h}\right\rangle + e^{-\mathrm{i}\omega_\mathrm{h}\mathrm{t}/2}\left|\bar{\mathrm{h}}\right\rangle\right), \tag{5.1}$$

where $\omega_\mathrm{h} = \Delta E_\mathrm{hZ}/\hbar = g_\mathrm{h}\mu_\mathrm{B}B/\hbar$ is the precession frequency due to the hole Zeeman energy splitting between the states, and g_h is the in-plane hole g-factor. The energy splitting between the hole spin states $|h\rangle$ and $|\bar{h}\rangle$ is shown in Fig. 5.2(b).

Figure 5.3 shows the Bloch sphere representation of the precession of the Bloch vector about the magnetic field. The blue arrow represents the Bloch vector which initially points in the z-direction, it depicts the initial hole spin state $|\Uparrow\rangle$. The Bloch vector then precesses about the x-axis (magnetic field direction) at a frequency ω_h. Therefore, the Bloch vector oscillates between hole spin up $\Uparrow$ and hole spin down $\Downarrow$, which modulates the spin z-component between maximum and minimum values of ± 1 in the ideal case of perfect spin preparation.

5.3.4 Detection

A second laser pulse, named the detection pulse, was used to measure the hole spin z-component. It arrived at a time τ_D after the preparation pulse. The detection pulse of pulse-area π and circular polarisation, was tuned into resonance with the hole to positive trion transition. It created an additional electron hole pair, conditional on the spin state of the hole, due to Pauli blocking. The detection pulse had co/cross circular-polarisation $\sigma^\pm$ w.r.t. the preparation, and selected either the hole spin up or down state to map to the trion state. Figure 5.1(c) shows the excitation of an additional electron-hole pair when cross polarised preparation and detection is used. When the additional carriers tunnel from the dot, a change in photocurrent is detected, which is proportional to the occupation of the selected hole spin state [41]. The tunneling of the additional carriers from the dot is illustrated in Fig. 5.1(d).

By writing the hole spin projections in the z-direction $|\Uparrow\rangle$ and $|\Downarrow\rangle$ in terms of the eigenstates $|h\rangle$ and $\left|\bar{h}\right\rangle$; $|\Uparrow\rangle = 1/\sqrt{2}\left(|h\rangle + |\bar{h}\rangle\right)$ and $|\Downarrow\rangle = 1/\sqrt{2}\left(|h\rangle - |\bar{h}\rangle\right)$,

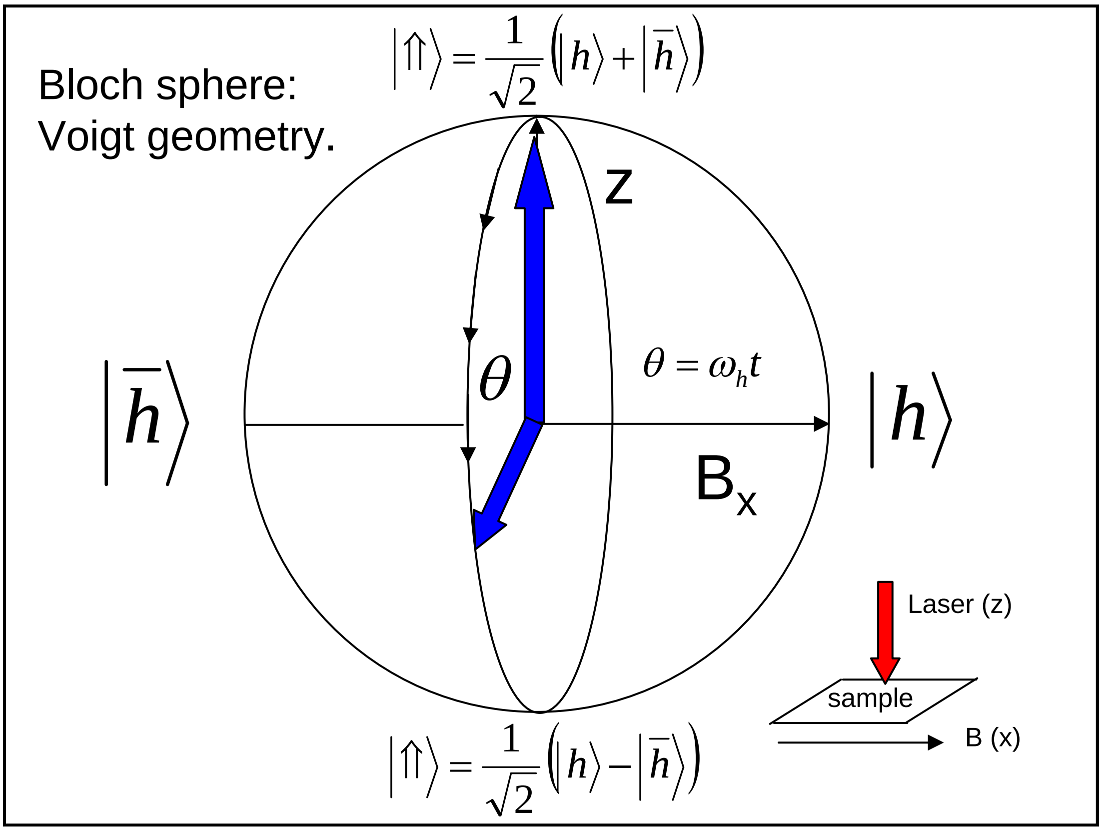

Figure 5.3: *A Bloch sphere representation of the hole spin state evolution. Using a σ^+ preparation pulse prepares a hole spin up $|\Uparrow\rangle$. The hole spin up state is represented by a Bloch vector (large blue arrow) in the z-direction. The prepared spin state $|\Uparrow\rangle$ is perpendicular to the magnetic field direction (x) and thus the spin vector precesses about the x-axis. Also shown (lower right) is the Voigt experimental geometry.*

we can calculate the time evolution of the probability of measuring a particular spin z-component by projecting eqn 5.1 onto the spin states $|\Uparrow\rangle$ and $|\Downarrow\rangle$. In the measurements, this corresponds to measuring a change in photocurrent proportional to the hole spin z projection, which is given by:

$$\Delta PC_{\text{cross}} = A\,|\langle\Uparrow|\psi(t)\rangle|^2 = A\cos^2(\omega_{\text{h}}t/2) \tag{5.2}$$

$$\Delta PC_{\text{co}} = A\,|\langle\Downarrow|\psi(t)\rangle|^2 = A\sin^2(\omega_{\text{h}}t/2) \tag{5.3}$$

$$\Delta PC_{\text{cross}} - \Delta PC_{\text{co}} = A\cos(\omega_{\text{h}}t) \tag{5.4}$$

Here A is the maximum measured photocurrent for the $h - X^+$ transition, which is determined by the carrier tunneling rates and photodiode detection efficiency. Thus by measuring the amplitude of the charged exciton spectra, using both co and cross circularly polarised preparation and detection pulses, as a function of the time delay between the pulses, it's possible to map out the hole spin z-projection in time, and observe the coherent precession of the spin about the magnetic field.

5.4 Results

The main results of this chapter will now be presented. The results show the observation of the precession of a single hole spin trapped in a quantum dot, a signature of the preparation of a coherent superposition of the hole spin state. This was achieved by measuring a series of photocurrent spectra of the charged exciton vs the inter-pulse time delay τ_{D}. An example spectral measurement, with a time delay $\tau_{\mathrm{D}} = 130$ ps, and an applied a magnetic field $B = 4.7$ T, is presented in Fig. 5.4. Figure 5.4 contains six different spectra which will be described in the following sections.

Analysis of single and two pulse spectral measurements

Figure 5.4 shows the single pulse photocurrent measurements of the neutral exciton using σ^- and σ^+ polarisation in the green and blue respectively. The photocurrent was measured as the laser was tuned through the neutral exciton resonance, which is labelled X^0_{bright} in Fig. 5.4. This was done in order to determine the frequency of the preparation pulse. The dot of interest is labelled quantum dot A, the dots labelled B and C are of sufficiently large detuning to be ignored. For all the measurements, the preparation pulse had a pulse area $\Theta = \pi$, which was calibrated using the neutral exciton Rabi-rotation, as described in the methods chapter section 3.7.2. In addition to the bright exciton peak in Fig. 5.4, a smaller shoulder peak is present at ~ -0.3 meV detuning. This peak is the contribution from the dark exciton $|M| = \pm 2$ states and is labelled $|X^0_{\mathrm{dark}}\rangle$ in Fig. 5.4. More details about dark excitons can be found in the appendix sections A.1, A.2 and A.3.

With the preparation pulse resonant with the neutral exciton, the photocurrent was measured as a function of the detuning of the detection pulse. The detection

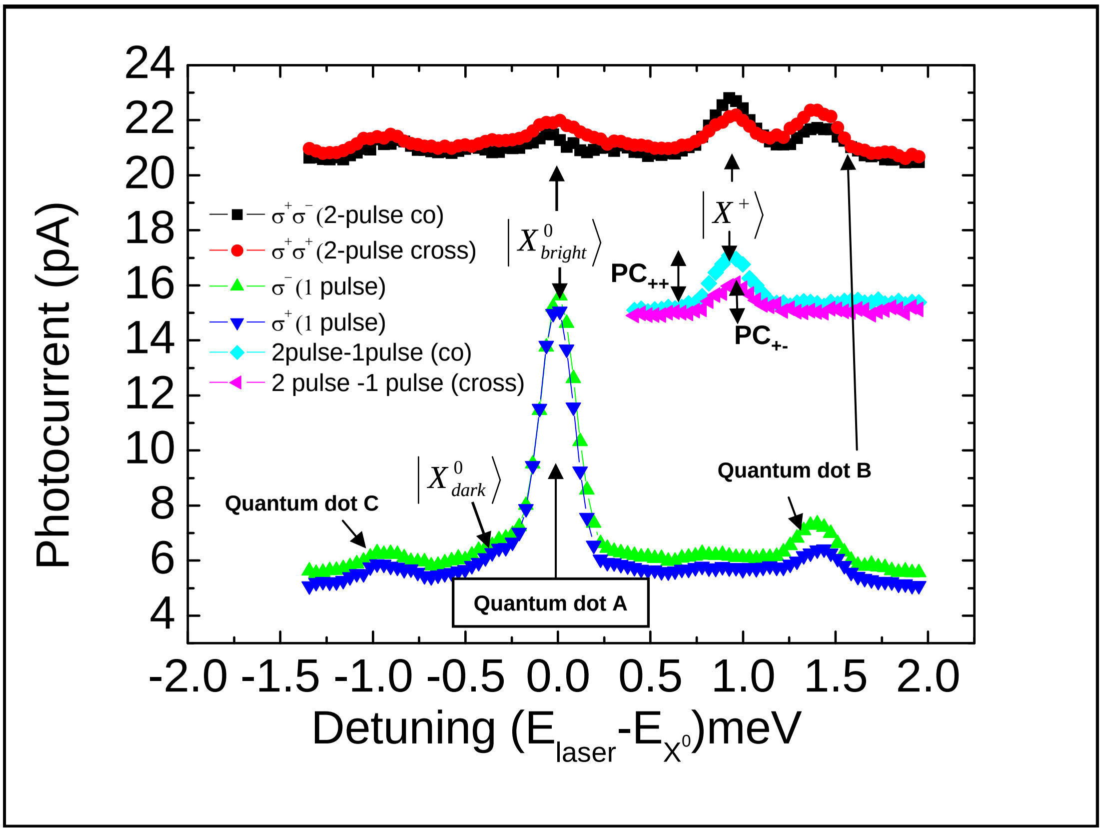

Figure 5.4: *. Photocurrent spectra of neutral and positively charged exciton. Green and blue: single π pulse spectra of the neutral exciton using σ^- and σ^+ excitation respectively. Red and Black: two pulse measurements of the charged exciton. Pink and light blue: the single pulse photocurrent spectra (green and blue) are subtracted from the two-pulse photocurrent spectra (red and black)to remove photocurrent contribution from the neighbouring quantum dots B and C. The important feature of these measurements are the photocurrent amplitudes of the X^+ peaks for co and cross circularly polarised preparation and detection.*

pulse had co or cross circular polarisation w.r.t the preparation, and pulse area $\Theta = \pi$. With a detection time delay $\tau_D = 130$ ps an additional peak was observed at $\sim +1$meV detuning with respect to the X^0 peak. This peak was not present in the single pulse measurements in Fig. 5.4 (green and blue). The additional peak is shown in the red and black in Fig. 5.4 and is labelled $|X^+\rangle$. The additional peak is attributed to the $h - X^+$ transition for reasons described in chapter 4, section 4.5.

The pink and light blue data in Fig. 5.4 are the two-pulse measurements of the X^+ with the single pulse measurements subtracted. The subtraction was done in order to remove unwanted photocurrent contribution from the preparation pulse, and from neighbouring dots. The amplitudes of the resonances for co and cross circular excitation were determined from Gaussian fitting and are labelled in Fig. 5.4 with PC$_{++}$ and PC$_{+-}$ respectively. These amplitudes are the most important features of Fig. 5.4 since they were used to determine the hole spin z-component according to:

$$
\begin{aligned}
S_{\mathrm{Z}} &= \frac{PC_{+-} - PC_{++}}{PC_{+-} + PC_{++}} && (5.5)\\
&= \frac{PC_{+-}\cos^2(\omega_h t/2) - PC_{++}\sin^2(\omega_h t/2)}{PC_{+-} + PC_{++}} && (5.6)\\
&= C\cos(\omega_h t). && (5.7)
\end{aligned}
$$

Here, C is the spin contrast, ω_{h} is the precession frequency of the hole, and τ_{D} the detection pulse time delay. A set of spectral measurements similar to those presented in Fig. 5.4 were made as a function of τ_{D} in order to map out the evolution of the hole spin. For each time delay, the amplitude of the X^+ was determined and the results are presented in the following.

5.4.1 Time dependence of X^+ amplitudes.

Figure 5.5 presents a series of two-colour spectra of the X^+ over a 190-ps time delay range, with an applied magnetic field $B = 4.7$ T. The amplitudes of the $h - X^+$ peaks for co and cross circular excitation, PC$_{++}$ and PC$_{+-}$, oscillate in anti-phase with the time-delay τ_{D}. PC$_{++}$ and PC$_{+-}$ are plotted as a function of τ_{D} in Fig. 5.6. The normalised difference in photocurrent amplitudes is proportional to the hole spin z-component as described in eqn 5.7. This is a time resolved measurement of the coherent precession of the hole spin about the magnetic field and demonstrates that the preparation pulse has created a coherent superposition of the hole spin eigenstates: $1/\sqrt{2}(|h\rangle \pm \left|\bar{h}\right\rangle)$.

5.4.2 Magnetic field dependence of the hole spin precession

A set of measurements of the trion peak amplitude oscillations were made as a function of magnetic field, in order to confirm that the photocurrent oscillation

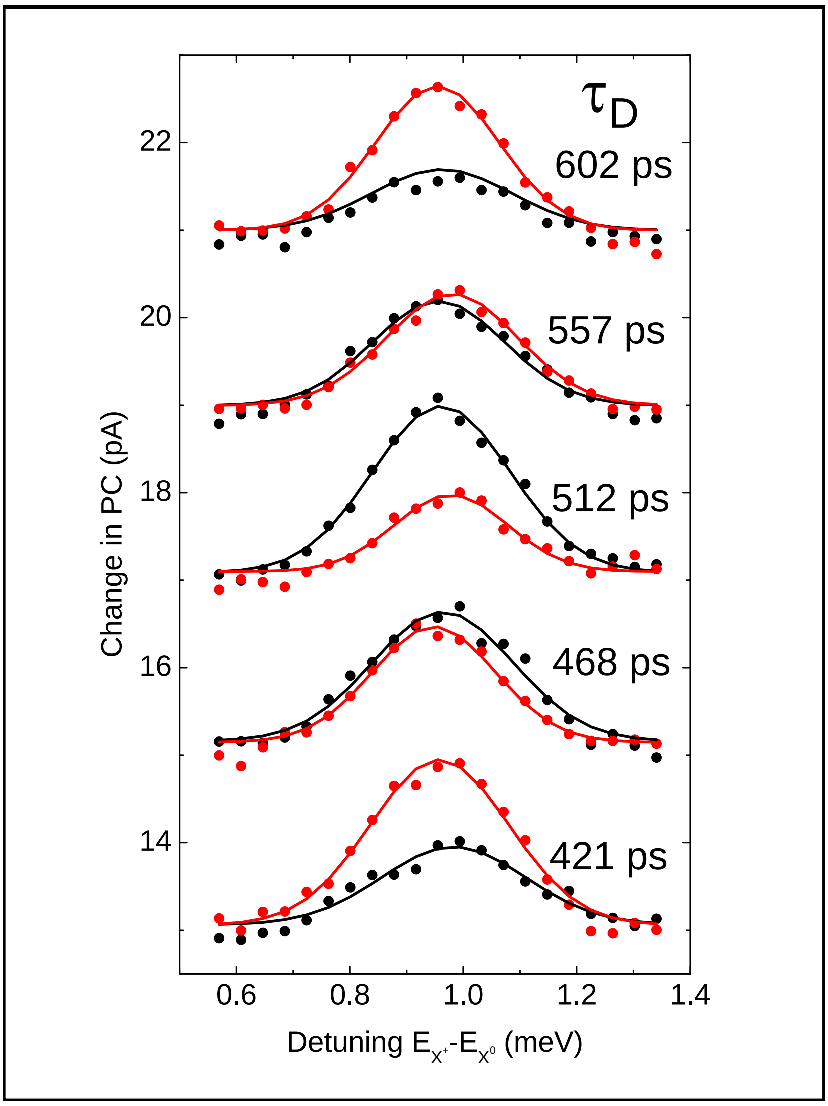

Figure 5.5: *. A example set of two-pulse measurements of the charged exciton X^+ using co and cross (red and black) circularly polarised preparation and detection pulses over one period of the hole spin precession. The data are vertically offset for clarity. Each set of measurements (red and black) is labelled with the time delay between preparation and detection τ_D. The solid red and black lines are Gaussian fits to the data.*

results from a superposition of the two Zeeman split hole spin states. The results are presented in Fig. 5.7. The left column in Fig. 5.7 is set of measurements of PC_{++} and PC_{+-} (red and black) as a function of time delay for four different magnetic fields (top to bottom). The frequency of the oscillation increases with applied magnetic field, confirming that the oscillation results from a superposition of hole spin states separated in energy by the Zeeman splitting. The pink data points, in the left column in Fig. 5.7, are the sum of the co and cross charged exciton peak

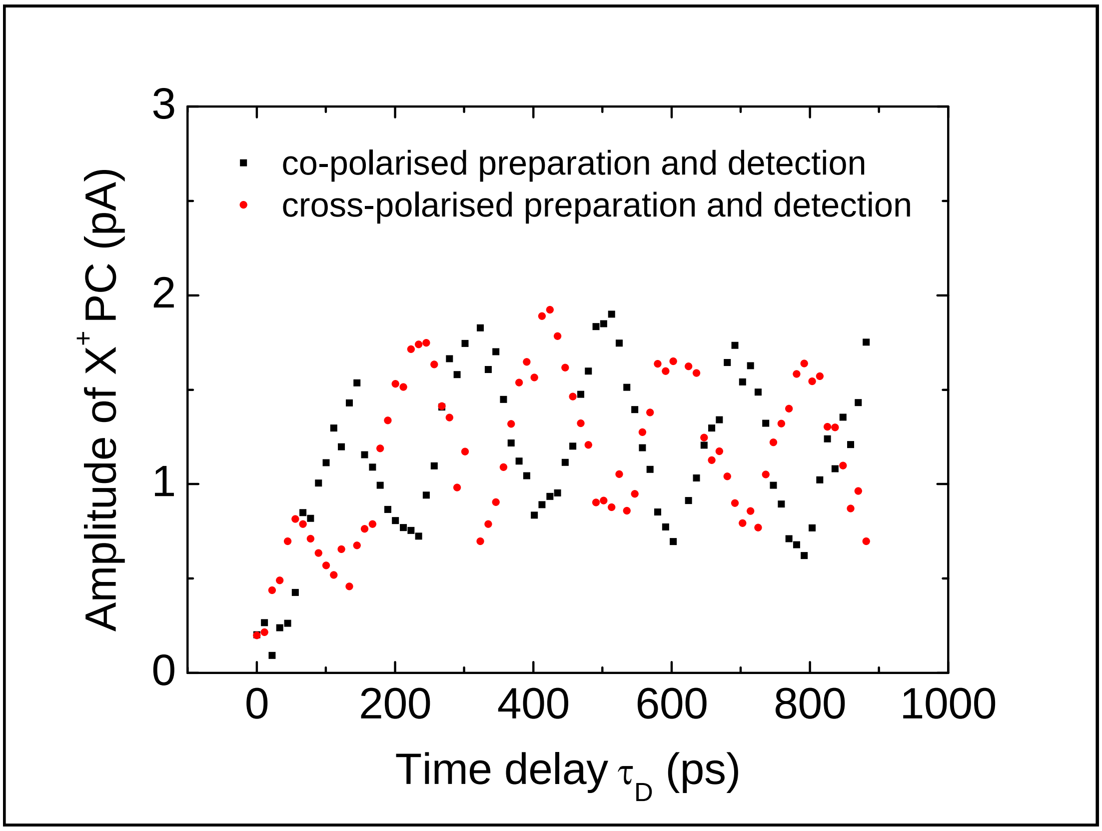

Figure 5.6: *Photocurrent amplitude of the charged exciton X^+ as a function of time delay τ_D for co polarised (black) and cross polarised (red) preparation and detection.*

amplitudes $PC_{+-} + PC_{++}$, a measure of the total hole spin population. There is an initial fast rise in the photocurrent as the electron tunnels from the dot under the applied electric field and the neutral exciton decays into the hole states. This is followed by a much slower decay, where the hole tunnels from the dot. The solid pink line is a fit to equation A.6 to extract the electron and hole tunneling rates, which is described in section A.5.

The right hand column in Fig. 5.7 is the hole spin z-component as a function of time delay for each magnetic field. The hole spin z-component oscillates between a value $\sim \pm 0.4$, depending on the magnetic field. The precession frequency is determined by the Zeeman splitting between the hole spin states $|h\rangle$ and $\left|\bar{h}\right\rangle$, which is given by $\hbar\omega_\mathrm{h} = g_\mathrm{h}\mu_\mathrm{B}B$. The solid navy lines in Fig. 5.7 are fits of the spin precession data to eqn 5.7, to extract the frequency ω_h and the amplitude or contrast C of the spin precession for each magnetic field. The frequency of the precession

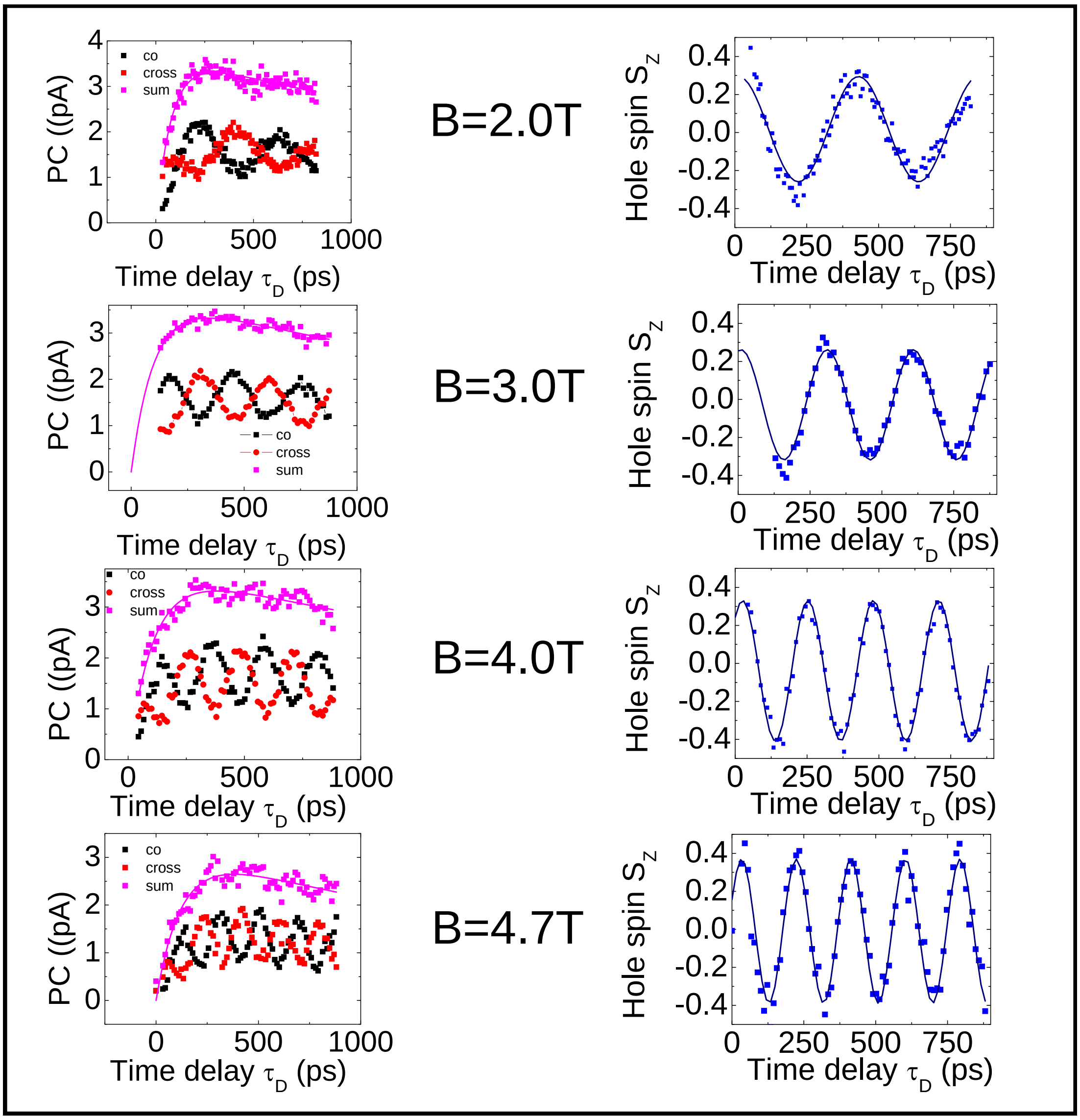

Figure 5.7: *Hole-spin precession as a function of applied magnetic field. The left column is set of measurements of the photocurrent amplitudes of the charged exciton for co and cross-polarised preparation and detection (red and black) as a function of time delay for four different magnetic-fields (top to bottom). The pink data points are the sum of the co and cross charged exciton peak amplitudes, a measure of the total hole-spin population. The solid pink line is a fit to equation A.6 to extract the electron and hole tunneling rates. The right hand column is the corresponding hole-spin z-component as a function of time-delay for each magnetic-field. The solid navy line is a fit to a cosine function to extract the frequency, phase and amplitude of the oscillation. The contrast of the oscillation or spin z-component is given by the normalised difference between cross and co-circular excitation:* $S_Z = (PC_{+-} - PC_{++})/(PC_{+-} + PC_{++})$ *as presented in the right-hand panel.*

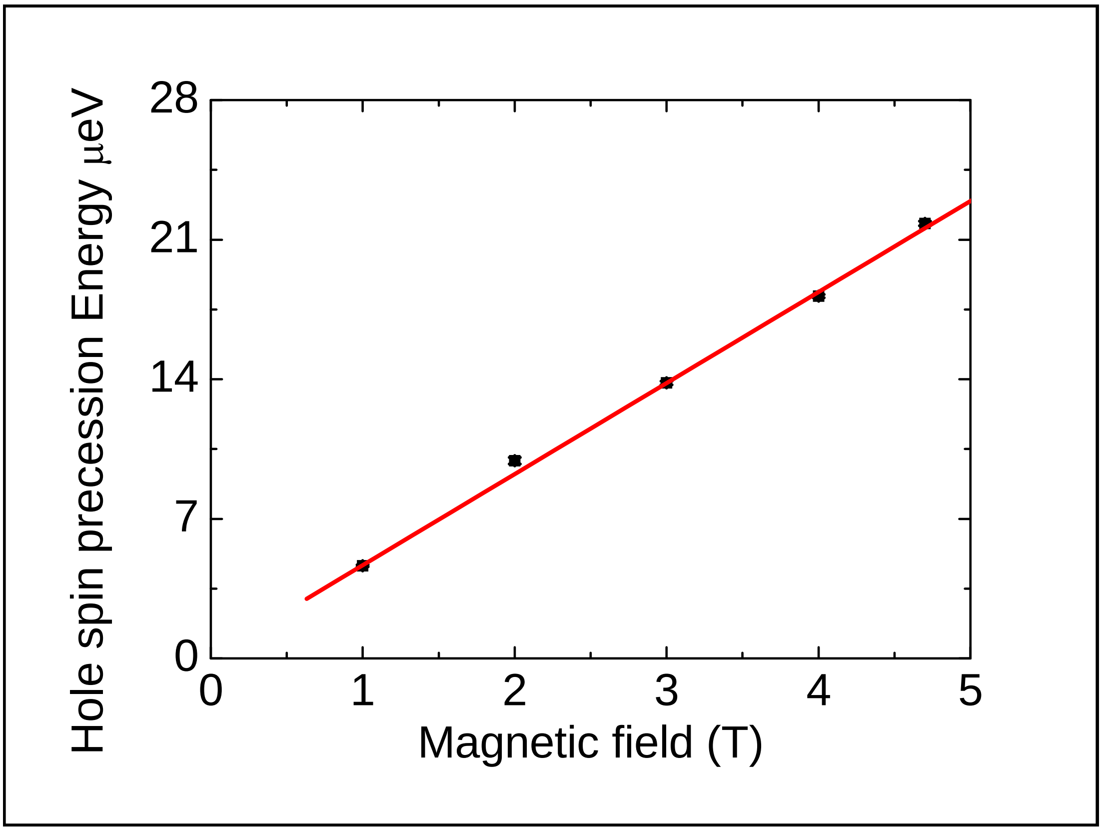

Figure 5.8: *Hole spin precession energy* $\Delta E_{rmh} = \hbar\omega_{\mathrm{h}} = g_{\mathrm{h}}\mu_{\mathrm{B}}B$ *as a function of applied magnetic field. The precession energy as determined by the frequency of the fits* ω_{h} *in fig. 5.7 is extracted from fitting the spin oscillations from fig. 5.7. The solid red line is a linear fit to the data. An in plane hole g-factor* $g_{\mathrm{h}} = 0.079 \pm 0.004$ *is extracted from the fit*

has a linear dependence on the applied magnetic field as shown in Fig. 5.8, and a fit to $\hbar\omega_{\mathrm{h}} = g_{\mathrm{h}}\mu_{\mathrm{B}}B$ gives an in-plane hole g-factor $g_{\mathrm{h}} = 0.079 \pm 0.004$ at a bias of $V_{\mathrm{bias}} = -0.8$ V. The in-plane hole g-factor is small but non-zero as expected for a dot with finite asymmetry [23].

5.4.3 Magnetic field dependence of fidelity of hole-spin preparation

The amplitudes of the oscillations in the hole spin z-component were used to quantify the contrast C of the spin preparation and provide a measure of the purity of the prepared coherent superposition state. A value of $C = 1$ indicates perfect spin preparation. The amplitude of the precession is plotted as a function of magnetic field in Fig. 5.9. In the previous chapter, we saw how the fine structure of the neutral

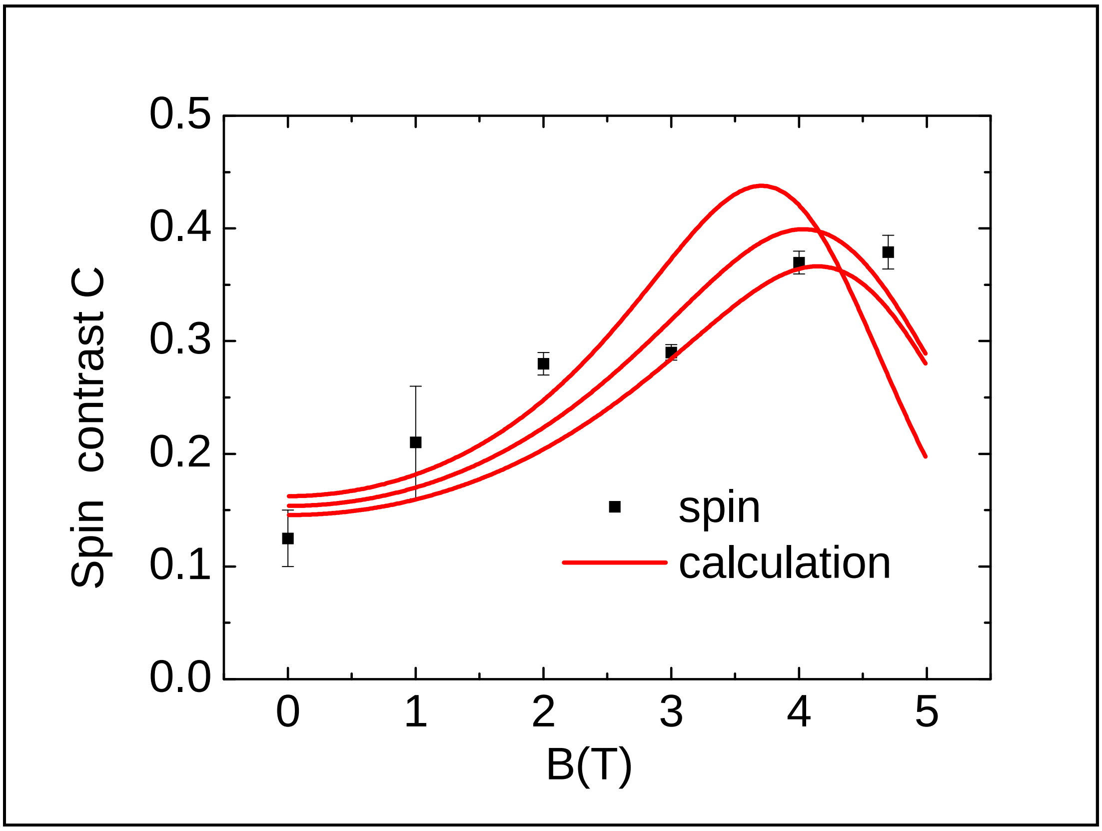

Figure 5.9: *Hole spin precession contrast as a function of applied in-plane magnetic field. The amplitudes of the oscillations in the hole spin (see for example fig. 5.7) provide a measure of the purity of the prepared coherent superposition state, which is termed the contrast. The red lines are calculations based on the model of the spin preparation described in section A.6 using the measured values of the electron and hole tunneling rates* $\Gamma_{\mathrm{e}}(B)$, Γ_{h}, *the bright-bright splitting* $\Delta\ E_{\mathrm{bb}}(B)$ *and the mixing angle* $\theta(B)$. *The varying calculations take into account the uncertainty in the measured parameters.*

exciton results in reduction of C. Intuitively, one might expect that an increasing effective fine-structure splitting in a Voigt geometry magnetic-field would result in a reduction of the contrast C. However C was found to increase with magnetic field as shown in Fig. 5.9.

The details of the model of the spin preparation fidelity can be found in section A.6, where the spin contrast is shown to be given by:

$$C = \lim_{\Gamma_e t \gg 1 \gg \Gamma_h t} \frac{h_{\Uparrow} - h_{\Downarrow}}{h_{\Uparrow} + h_{\Downarrow}} \tag{5.8}$$

$$C = \frac{1}{2}\cos(2\theta)[f(\omega_h - \omega_{bb}) + f(\omega_h + \omega_{bb})] \tag{5.9}$$

$$f(a) = \frac{(\Gamma_e - \Gamma_h)^2}{(\Gamma_e - \Gamma_h)^2 + a^2}, \tag{5.10}$$

where θ is the mixing angle between bright and dark excitons, Γ_{e} and Γ_{h} are the electron and hole tunelling rates, ω_{h} the hole spin precession frequency and $\hbar\omega_{\mathrm{bb}}$ the energy splitting or effective fine structure of the bright neutral exciton. Equation 5.9 is a Lorentzian function which is resonant when $\omega_{\mathrm{h}} = \omega_{\mathrm{bb}}$. With increasing magnetic field up to $B \sim 4$T, the hole precession energy is tuned into resonance with the bright-bright fine structure splitting, which improves the spin contrast.

The solid red lines in Fig. 5.9 are calculations from the model described in eqn 5.9 using measured values of the electron and hole tunneling rates $\Gamma_{\mathrm{e}}(B)$, Γ_{h}, the bright-bright neutral exciton splitting $\Delta E_{\mathrm{bb}}(B)$ and the mixing angle $\theta(B)$. These values were measured in experiments and the details can be found in the appendix section A. The values of the experimentally determined parameters used in the calculation are:

1) $\Gamma_{\mathrm{e}}(B) = \Gamma_{\mathrm{e}}(0) + kB^2$, where $\Gamma_{\mathrm{e}}(0) = (0.01095 \pm 0.0002)$ ps^{-1} is the tunneling rate at zero field ($\tau_{\mathrm{e}}(0) \sim 90$ ps^{-1}) and $k = (-0.00013 \pm 0.00001)$ps^{-1} T^{-2} is a curvature constant, which accounts for the helical trajectory of the electron in the magnetic field as determined experimentally (see section A.5.2).

2) The hole tunneling rate $\Gamma_{\mathrm{h}} = 1/(3 \pm 0.2)$ ns^{-1} (see section A.5.2).

3) A mixing angle given by $\tan^2\theta \approx (aB)^2$, where $a = (0.085 \pm 0.01)$ T^{-2} as determined in section A.2.

4) The bright-bright neutral exciton energy splitting, $\Delta E_{\mathrm{bb}} = \delta_1 + KB^2$, where $\delta_1 = (16.5 \pm 0.5)$ μeV and $K = (0.13 \pm 0.004)$ μeVT^{-2} as determined in section A.4.

5) The in-plane hole g-factor $g_{\mathrm{h}} = 0.079 \pm 0.004$ as determined in Fig. 5.8.

The uncertainty in θ, ΔE_{bb} and Γ_{e} give rise to a range in possible values for the calculation. From the calculations, it is clear that the contrast takes a maximum value when $\omega_{\mathrm{h}} = \omega_{\mathrm{bb}}$, which occurs at magnetic fields $B \sim 4\mathrm{T}$. The model is in reasonable quantitative agreement with the data and reproduces the increase in C with magnetic field.

An interpretation of the spin preparation is as follows. As part of an electron-hole pair, the hole experiences an additional effective magnetic field due to the electron via the exchange interaction. Since the electron has components aligned parallel and anti-parallel to the external magnetic field, the hole spin precesses with two frequency components, $\pm\omega_{bb}$. For the rotating component, if $\omega_h = \omega_{bb}$, the precession of the hole spin with or without the electron are synchronized and the hole spin is unaffected by the removal of the electron. For the counter-rotating component, the frequency mismatch between the hole spin precession with and without the electron, combined with the time-uncertainty of the electron tunneling event, randomizes the phase of the hole spin resulting in a mixed state. The net effect using a dot with $\delta_1 \sim 16.5\ \mu\mathrm{eV}$ and $\Gamma_{\mathrm{e}} \sim 1/90\ \mathrm{ps}^{-1}$ is a spin-polarized hole with a contrast of up to one half.

Higher contrasts up to $C > 0.9$ at $B \sim 2T$ could be achieved using dots where the fine-structure can be tuned to zero using techniques such as thermal annealing [27], [28], strain tuning [29] and growth on (111)B substrates [30], [31]. More details on the effect of the fine-structure splitting can be found in section 5.5 where calculations are performed to explore the effects of zero fine structure splitting and increased electron tunneling rate.

5.4.4 Hole spin precession as a function of applied bias

In order to understand better the role of the electron tunneling rate in the partial mixing of the spin, the spin preparation contrast was studied as a function of applied reverse bias voltage with a constant applied magnetic field $B = 4.7$ T.

Figure 5.10 shows an example set of measurements of the voltage dependence of the hole spin precession. The pink data points in Fig. 5.10 show how the electron and hole tunneling rates increase with applied bias. The tunneling rates are examined

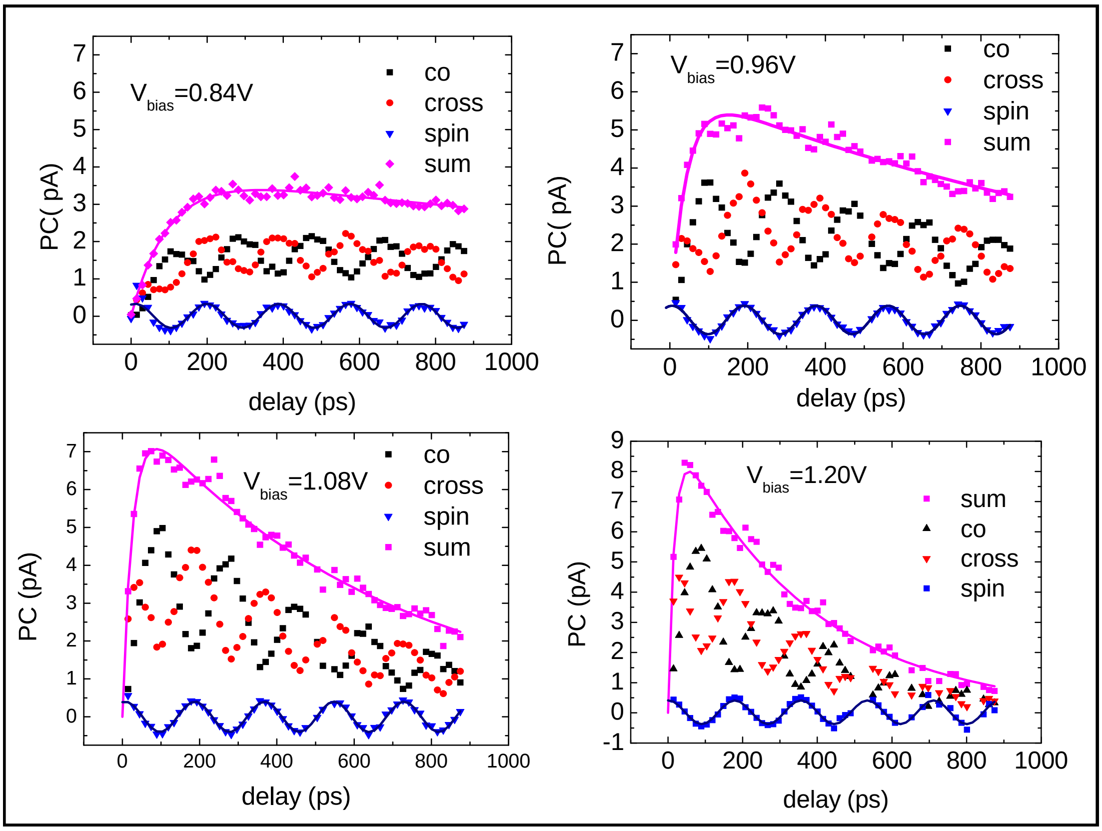

Figure 5.10: *Hole spin precession with an applied magnetic field* B = 4.7 T *for various applied bias voltage. The red and black data points are the photocurrent amplitudes of the charged exciton for co and cross excitation* PC_{+-} *and* PC_{++}*. The pink data points are the sum of the co and cross photocurrent amplitudes* $PC_{+-}+PC_{++}$ *with fits to eqn A.6 to extract the electron and hole tunneling rates. The blue data points are the spin contrast,* $(PC_{+-}-PC_{++})/(PC_{+-}+PC_{++})$*, fit (solid navy) to a cosine function to extract the spin amplitude or contrast* C *and frequency of the spin precession* ω_{h}*.*

in section A.5 and will not be mentioned further here. The red and black data points in Fig. 5.10 are the amplitudes PC_{++} and PC_{+-} for co and cross excitation which oscillate in anti-phase. The blue data points in Fig. 5.10 are the normalised difference in the the amplitudes $(PC_{++}-PC_{+-})/(PC_{++}+PC_{+-})$, proportional to S_z. Fits to eqn 5.7 were used to extract the amplitude or contrast C and frequency of the precession at each voltage.

Spin preparation contrast as a function of applied bias

Figure 5.11 shows the contrast of the hole spin precession as a function of applied bias, with a constant magnetic field $B = 4.7$ T. The contrast was found to increase with applied bias. This is because the contrast is limited by a competition

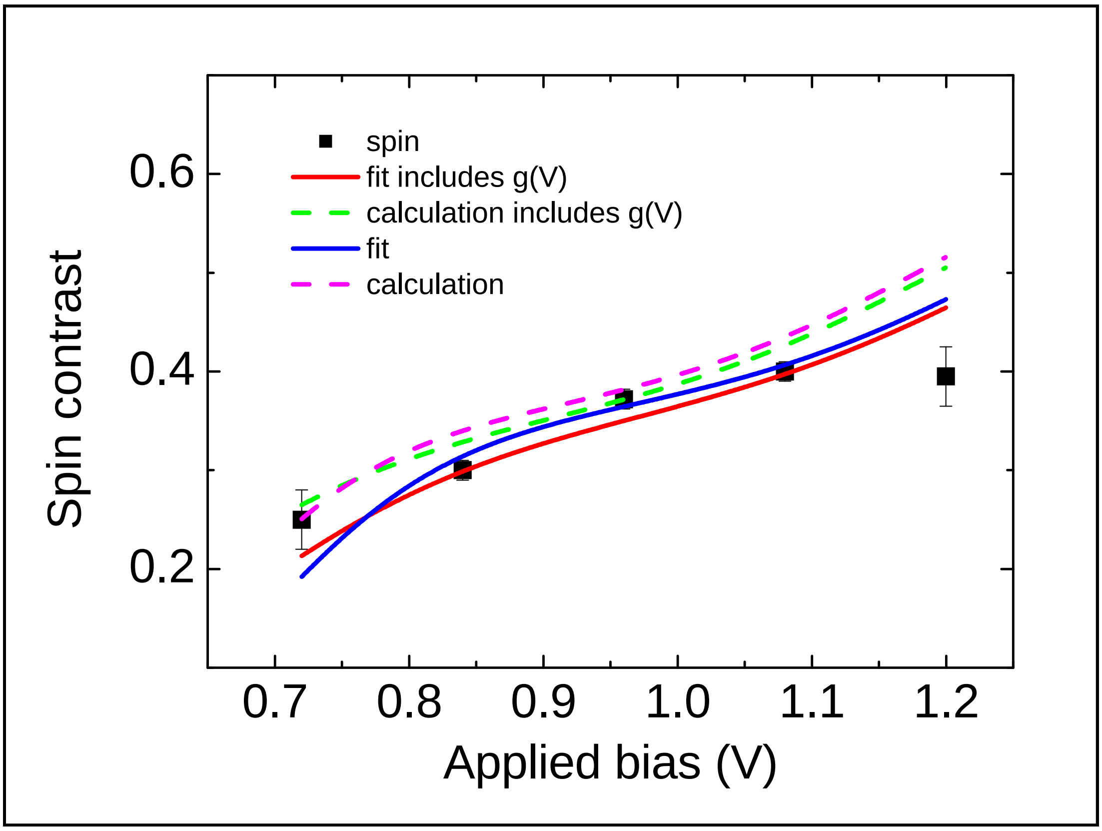

Figure 5.11: *The spin precession contrast as a function of applied bias voltage, with an applied magnetic field $B = 4.7T$. The dashed lines are calculations using eqn A.27 from the model of the spin preparation in section A.6. The solid lines are fits to the data using a fitting parameter which gives the voltage dependence of the electron tunneling rate.*

between the electron tunneling rate and frequency mismatch between the effective fine structure splitting and the hole precession energy. The dashed lines in Fig. 5.11 are calculations using eqn 5.9 from the model of the spin preparation in section A.6. The following parameters were used in the calculation: 1) The measured value of the mixing angle θ from the magnetic field dependence of the bright dark mixing (Fig. A.3), where at $B = 4.7$ T, $\cos(2\theta) = 0.72$. 2) The measured value of the bright-bright neutral exciton splitting or effective fine structure $E_{\mathrm{bb}} = 19.7$ μeV at $B = 4.7$ T and $V_{\mathrm{bias}} = -0.8$ V. 3) The hole precession energy as a function of applied bias: $\hbar\omega_h(V) = (18.4 + 4.1V_{\mathrm{bias}})$ μeV (see section 5.4.4). 4) The voltage dependence of the electron tunneling rate using the function $\Gamma_{\mathrm{e}} \propto \exp\frac{-V_0}{V_{bias}+V_{bi}}$ as measured in Fig A.9. 4) For simplicity the hole tunneling is neglected since $\Gamma_{\mathrm{e}} >\gg \Gamma_{\mathrm{h}}$ for all Voltages. The calculations are in good qualitative agreement with the measured values. The solid lines in Fig. 5.11 are fits to the experimental data using the measured constants E_{bb}, $\cos(2\theta)$ and $\hbar\omega_h(V)$, and using only one fitting parameter; the gradient m of the electron tunneling rate $\Gamma_{\mathrm{e}}(V_{\mathrm{bias}})$, where $\ln(\Gamma_{\mathrm{e}}(V_{\mathrm{bias}})) = c - m/(V_{\mathrm{bias}} + V_{\mathrm{bi}})$. The gradient extracted from the fit was 15.5, whereas the measured value is 15 ± 2.8. The experimental data is in reasonable agreement with the theory for $V_{\mathrm{bias}} < 1.1$ V. The model predicts a higher spin contrast than was measured for the data point $V_{\mathrm{bias}} = 1.2$ V. The discrepancy at $V_{\mathrm{bias}} = 1.2$ V, may be due to the fact that, at this bias, the electron tunneling rate $\Gamma_{\mathrm{e}} \sim 1/18\ \mathrm{ps}^{-1}$, becomes comparable to the preparation pulse of duration FWHM $\sim$ 12 ps.

Electric field dependence of the in-plane hole g-factor

Figure 5.12 shows the precession energy of the hole $\hbar\omega_{\mathrm{h}} = g_{\mathrm{h}}\mu_{\mathrm{B}}B$ as a function of electric field F, for a magnetic field $B = 4.7$ T. The hole spin precession frequency ω_{h} was found to increase with applied bias at a magnetic field $B = 4.7$ T. This can be understood as the tuning of the in-plane hole g-factor using the vertical electric field applied to the device. The data in Fig. 5.12 was fit to a linear function with a gradient of $\mathrm{d}(\hbar\omega_{\mathrm{h}})/\mathrm{dF} = (0.90 \pm 0.04)\ \mu\mathrm{eV/V}\mu\mathrm{m}^{-1}$. An increasing in-plane hole g-factor with electric field has also been observed recently in other Voigt geometry experiments [38], [85]. The effect is attributed to the sensitivity of the hole spin Zeeman interaction to electric fields and strain due to anisotropy of the confinement potential of p-type hole states [85]. Similar effects have also be observed in the tuning of the out of plane g-factor in neutral excitons [101]. Here the effect is attributed to a changing overlap of the hole wavefunction with the Indium-rich region of the quantum dot. Tunable exciton g-factors have also been explained by the coupling to the continuum of states in the contacts in reference [102].

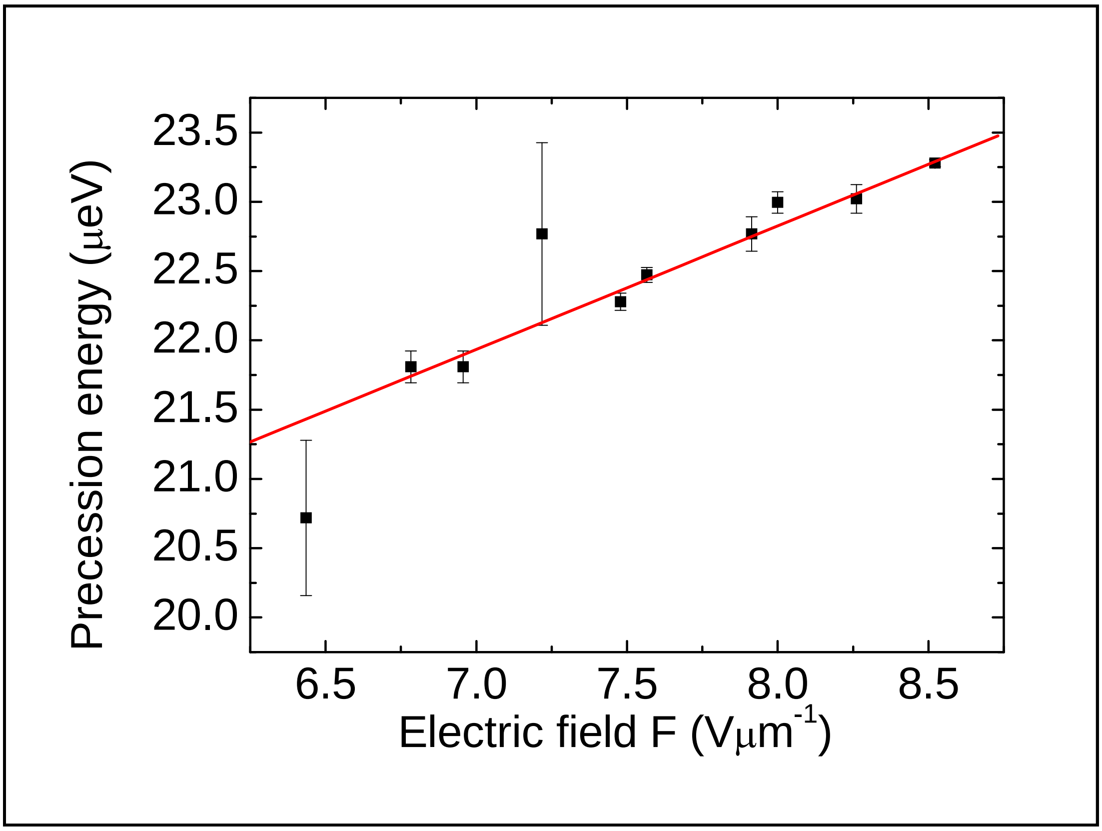

Figure 5.12: *The precession energy of the hole* $\hbar\omega_\mathrm{h} = g_\mathrm{h}\mu_\mathrm{B}B$ *as a function of applied bias for a magnetic field* $B = 4.7$ T. *This linear increase with bias indicates a tuning of the in plane hole g-factor. The data is fit to a linear function* $\hbar\omega_\mathrm{h} = (15.7 + 0.9F)\mu\mathrm{eV}$

5.5 Evaluation of the model of hole spin preparation

It is instructive to consider the effect of varying the parameters that limit the contrast of the hole spin preparation in eqn 5.9. The important parameters are the neutral exciton fine structure splitting at zero magnetic field δ_1, and the electron tunneling rate Γ_e or time $\mathrm{t_e}$. Figure 5.13 shows various calculations based on the model, using a range of values of δ_1 and $\mathrm{t_e}$. In Fig. 5.13 (a), the contrast is calculated for various values of $\delta_1 = (0 \longrightarrow 18)\ \mu\mathrm{eV}$ and a fixed value of the electron tunneling time $\mathrm{t_e} = 90$ ps (at zero B-field). As δ_1 tends to zero, the maximum value for C tends towards 1, but C_max occurs at increasingly lower B-fields. This is because C_max occurs when the exciton energy splitting is equal to the hole precession

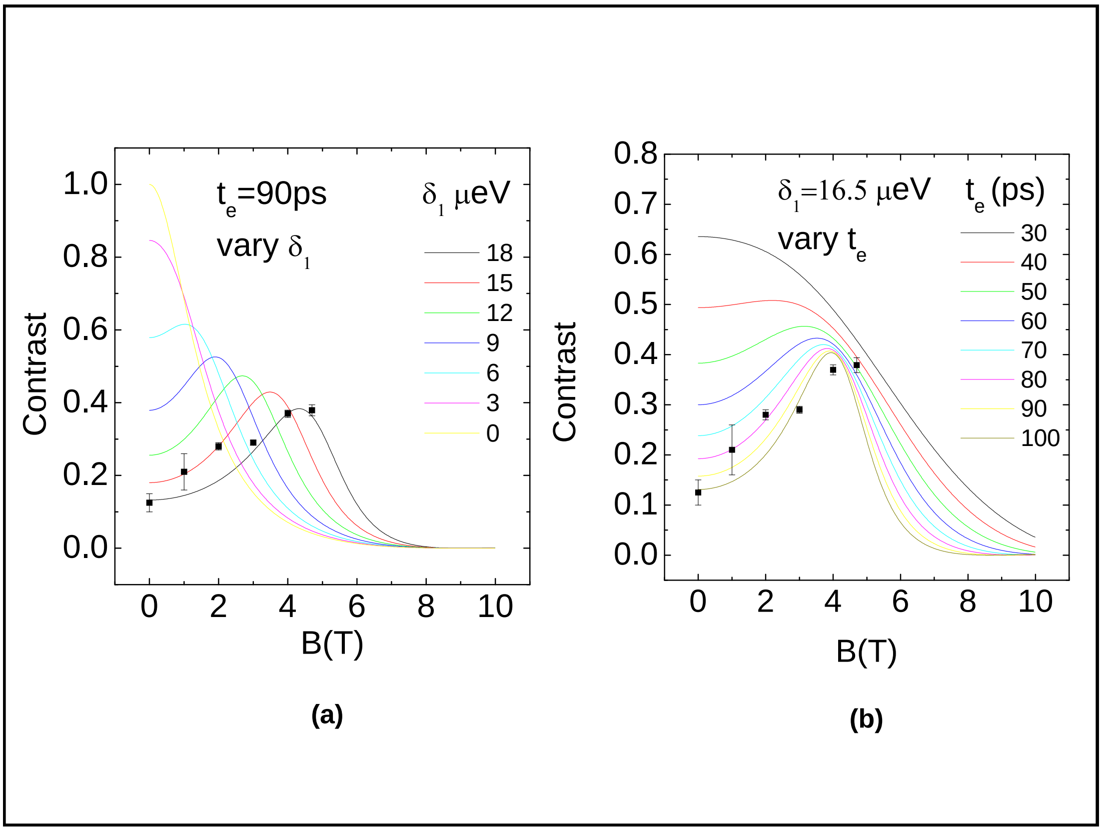

Figure 5.13: *Exploring the model of spin preparation. The figures (a) and (b) show calculations based on the model of the contrast of the hole spin preparation using eqn A.27. (a) contrast for various fine-structure splittings δ_1 and a fixed electron tunneling time $\mathrm{t_e} = 90$ ps. (b) contrast for various $\mathrm{t_e}$ with fixed δ_1*

energy ($\delta_{\mathrm{bb}} = \omega_{\mathrm{h}}$).

In Fig. 5.13 (b) the contrast is calculated for various electron tunneling times $\mathrm{t_e} = (30 \longrightarrow 100)$ ps and a fixed value of $\delta_1 = 16.5$ μeV (at zero B-field). In this case, the width of the resonance increases and also C_{max} increases with decreasing tunneling time. Therefore, it is possible to obtain high values of C over a larger range of magnetic field. This is because for faster electron tunneling there is a reduced time for spin mixing due to the exciton spin rotation. The minimum value for the tunneling time used $\mathrm{t_e} = 30$ ps is not unreasonable, since this is the value measured for the device used in the experiments of the hole spin preparation in the Faraday geometry in section 4.5. Also presented in Figs 5.13 (a) and (b) are the experimental values of C for a reference. Figure 5.14 shows calculated values of C in the ideal case of fast electron tunneling $\Gamma_{\mathrm{e}} = 1/30$ ps^{-1} and decreasing δ_1. The

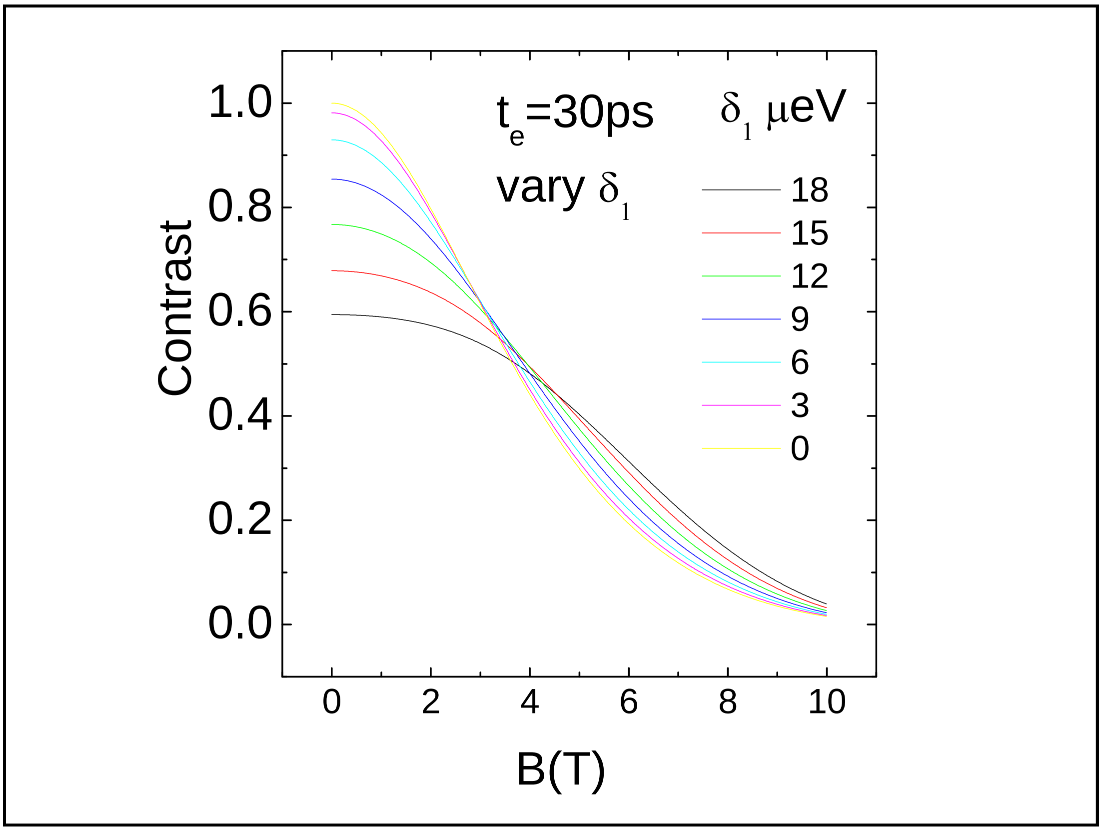

Figure 5.14: *Exploring the model of spin preparation in the ideal case of fast electron tunneling and small fine-structure splitting. The figure shows calculations based on the model of the contrast of the hole spin preparation using eqn A.27 in the ideal case of fast electron tunneling* $\mathrm{t_e} = 30$ ps *for various* δ_1

resonance shifts towards lower B-field, but with a fast electron tunneling time, the resonance is broad and it is possible to obtain values $C > 90\%$ at magnetic fields $B \sim 1.5$ T using values of δ_1 close to zero.

5.6 Oscillation in the energy of the charged exciton

In addition to the oscillation in the amplitudes of X^+, the *energy splitting* ΔE_{X^+} between the X^+ peaks measured for co and cross-circular excitation also oscillates. This can be seen by close inspection of the energy position of the peaks for co-polarised and cross-polarised excitation presented in Fig. 5.15.

Figure 5.16 shows a comparison between the hole spin precession and ΔE_{X^+}.

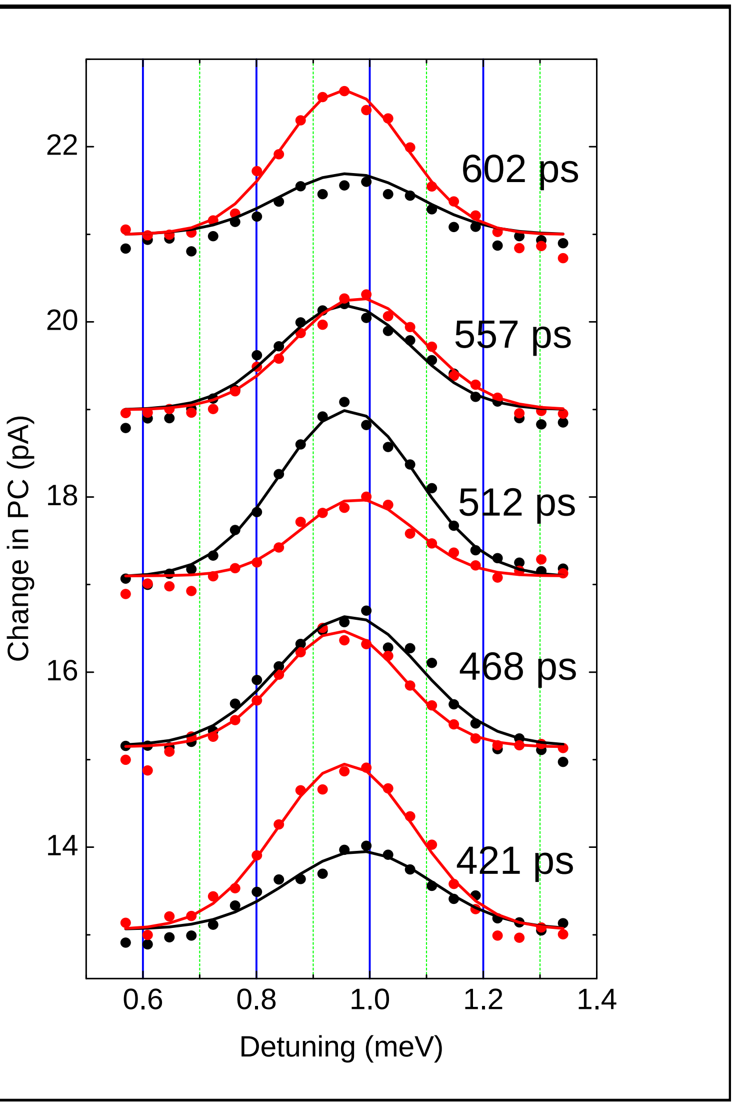

Figure 5.15: *The charged exciton photocurrent spectra for co and cross excitation (red and black) over one period of the spin precession. In addition to an oscillation in the amplitudes of the peaks, there is an oscillation in the energy splitting which can been seen with close inspection of the energies of the peaks*

The period of the oscillations is the same for the two data sets, but the maximum splitting occurs 40 ps after the maximum value for S_z. The energy-splitting ΔE_{X^+} may arise from an effective magnetic (Overhauser) field generated by polarised nuclear spins. Nuclear spin effects are important, since they determine the dephasing time of the hole spin, as discussed in section 5.7. In each cycle of the experiment, the total electron spin generated by the pulse-pair oscillates with the time delay, modulating the pumping rate of the nuclear spins, and hence the energy splitting of the charged exciton ΔE_{X^+}. The amplitude of a cosine fit to the oscillation of

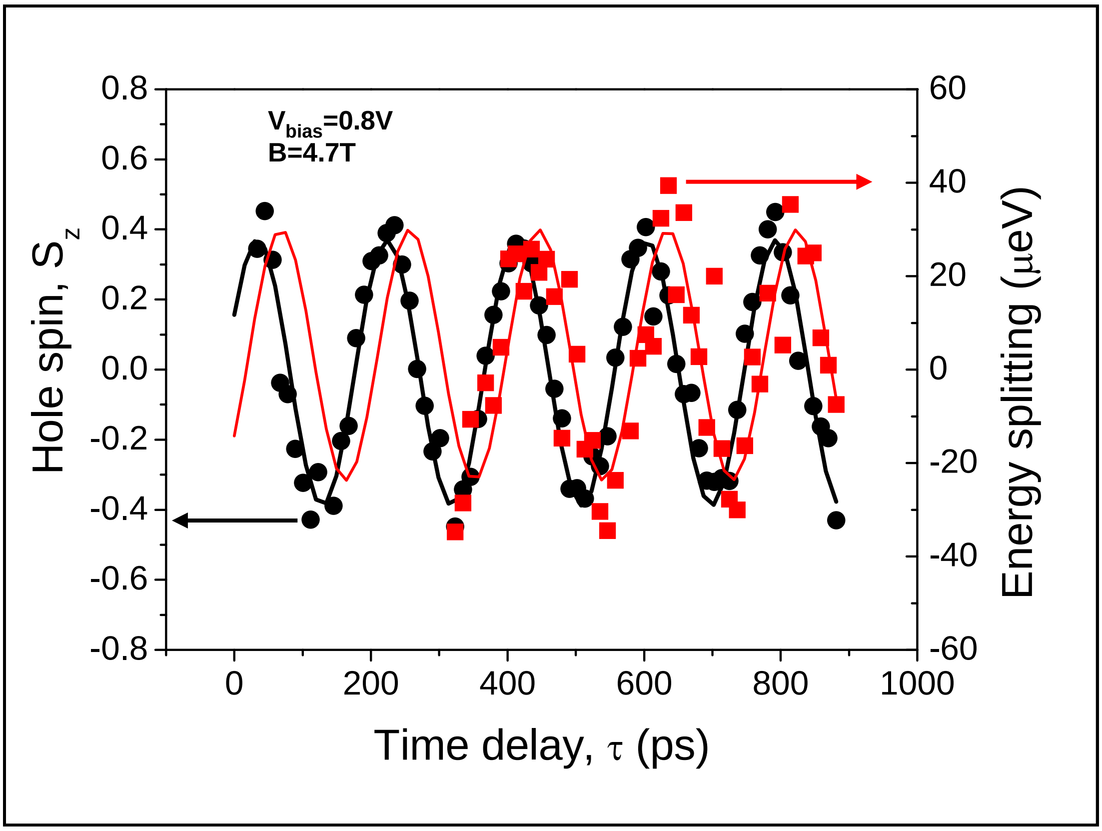

Figure 5.16: *Hole spin precession (black) and the energy splitting of the charged exciton* ΔE_{X^+} *(red) plotted vs. time delay, for a magnetic field* $B = 4.7$ T *and bias of 0.8 V. The solid lines are cosine fits to the data. The period of the oscillation is the same for both data sets. The amplitude of the fit to the energy splitting oscillation gives an indication of the maximum splitting.*

ΔE_{X^+} in Fig.5.16 was used to infer the maximum X^+ splitting $\Delta E_{X^+}^{\max}$. Figure 5.17 shows $\Delta E_{X^+}^{\max}$ as a function of applied bias. The coloured data points are repeat measurements made on different days. It is postulated that the efficiency of nuclear spin pumping, and hence Overhauser field, increases with the electron tunneling rate. An increasing Overhauser field with increasing bias has been observed before with similar devices [103], [46], [48], but never using pulsed excitation.

Figure 5.18 shows the average energy difference of the charged exciton peaks for co and cross circular excitation. The average energy is defined by the offset of cosine fits to the X^+ energy oscillations for both co and cross polarised excitation. Interestingly, the average difference decreases with increasing bias, whereas the amplitude of the oscillation increases. It is possible that as the peaks are tuned closer in energy with increasing bias, the electron-nuclear spin flip-flop process is

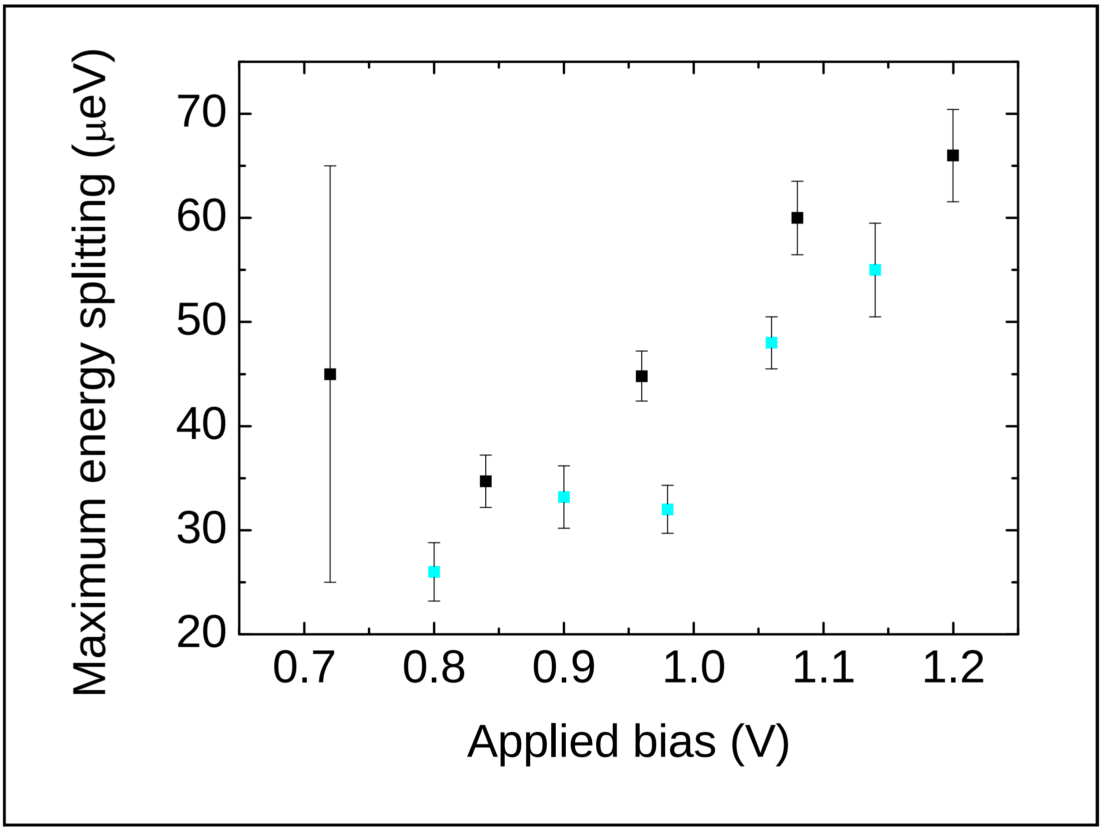

Figure 5.17: *Amplitude of charged exciton energy splitting oscillation as a function of applied bias. The maximum splitting of the charged exciton is determined by the amplitude of the fit to the oscillation in the energy splitting and is found to increase with bias.*

more efficient, since the energy cost of the flip-flop process decreases. This would explain the increase in the amplitude of the splitting oscillation with increasing bias, but further work is required to investigate these interesting effects.

5.7 Hole spin dephasing time T_2^*

The extrinsic dephasing time of a hole spin trapped in a quantum dot T_2^* is the parameter that limits its usefulness as a qubit. Furthermore, measurements of T_2^* give insight into the physics of spin coherence in quantum dots. In this section the decay of the contrast of the hole spin precession is used to measure T_2^*, and the measured value of T_2^* is consistent with dephasing due to fluctuations in the nuclear spin bath within the quantum dot.

Figure 5.19 presents a measurement of the hole spin precession over a 8.5 ns

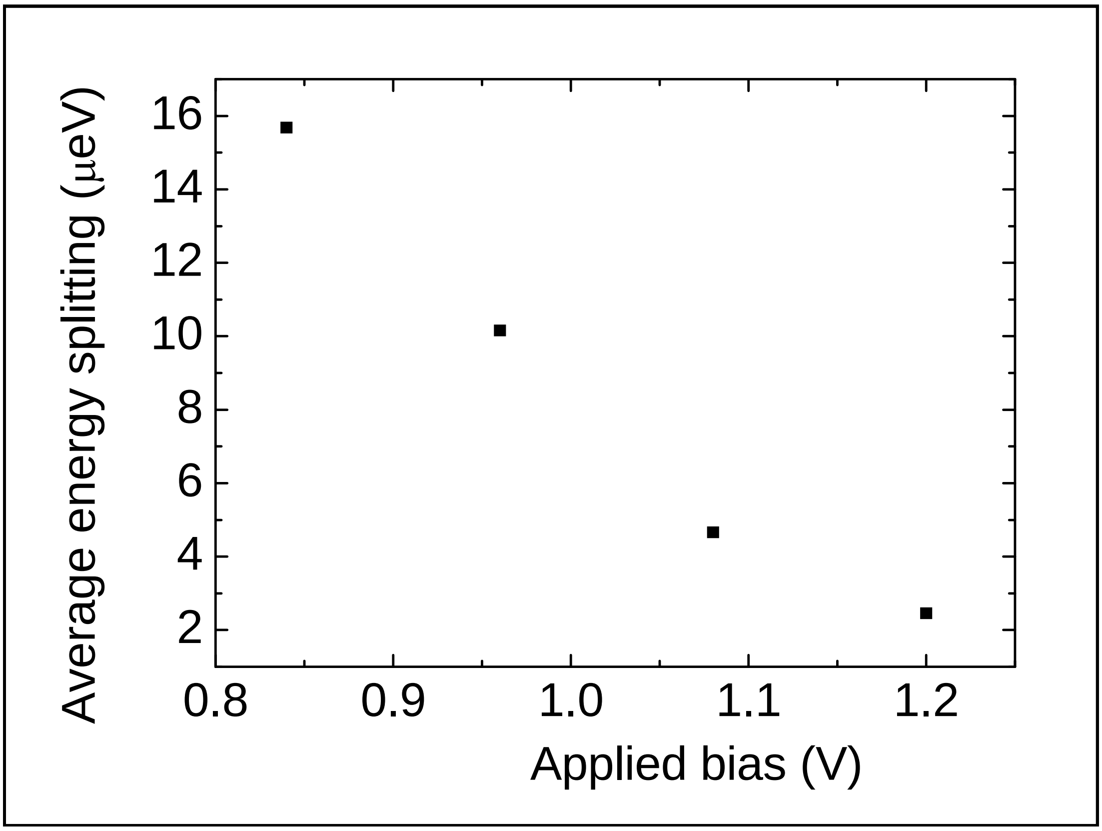

Figure 5.18: *Difference between average energy of the charged exciton for co/cross circular excitation as function of applied bias. The average energy is determined by the offset in the fits to cosine functions of the oscillation in the energy splitting.*

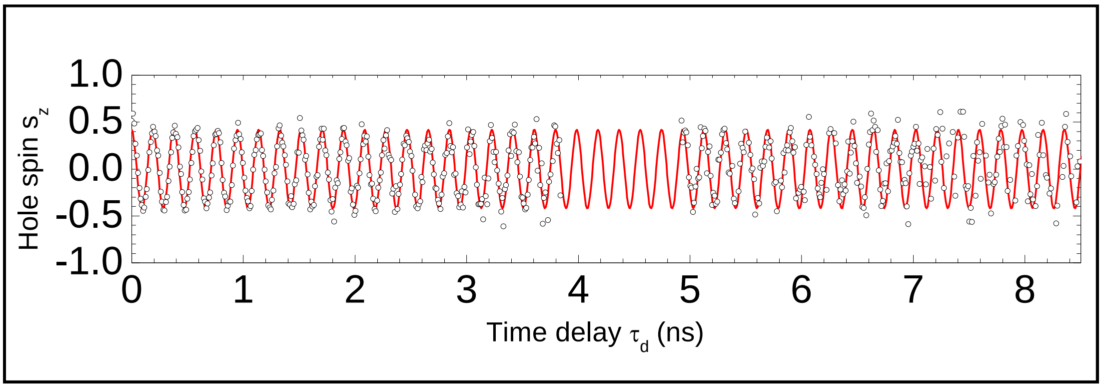

Figure 5.19: *Precession of the hole spin as a function of τ_D (white circles) with a an undamped cosine (red line) function to guide the eye. Over 40 periods of the oscillation can be clearly seen with very little decay in the amplitude.*

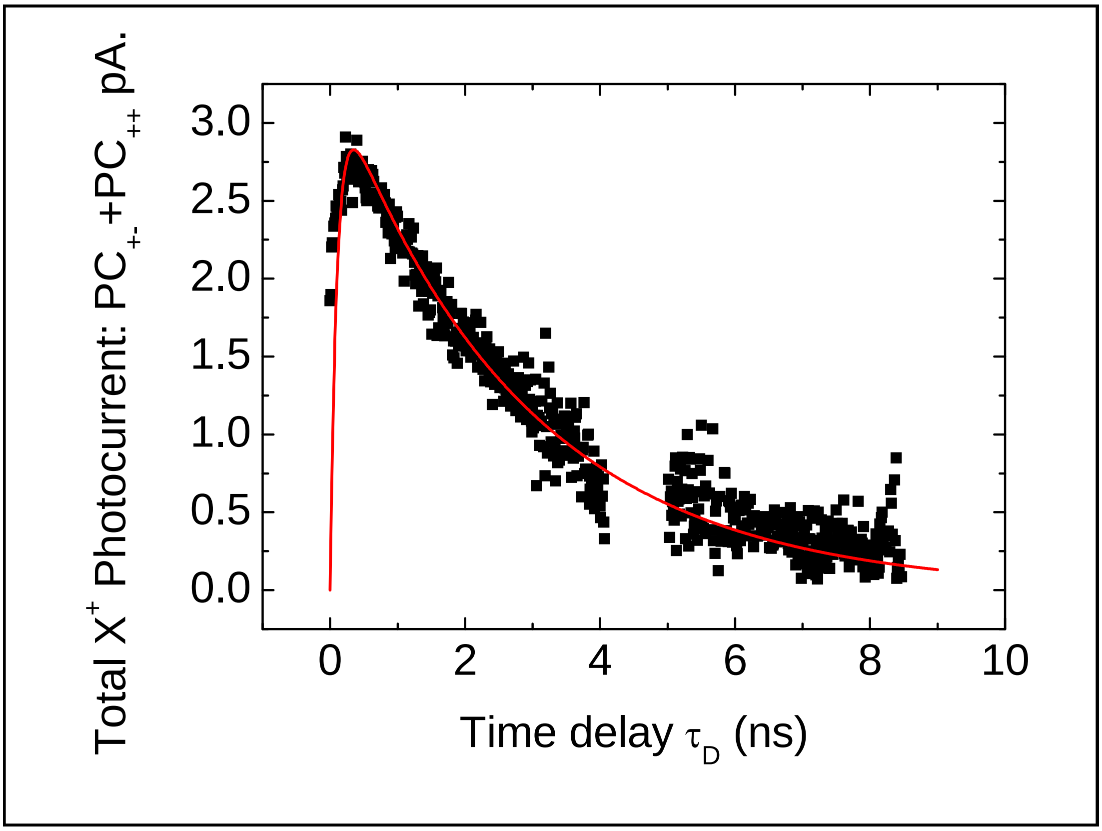

Figure 5.20: *Hole spin population over 8.5 ns. The data points are the sum of the photocurrent amplitudes of the* X^+ *for co and cross-polarised excitation* $PC_{+-} + PC_{++}$*. The red line is fit made to eqn A.6 as outlined in the appendix section A.5 and gives a hole tunneling time* $\tau_\mathrm{h} = (3.0 \pm 0.2)$ns

time delay. The data was collected and processed in the same manner as in the data of Fig. 5.7. For the gate voltage used, the hole tunneling time was about 3 ns, which is small compared to the 13 ns repetition period of the laser, ensuring the dot was empty on the arrival of the next preparation pulse.

Figure 5.20 shows the total photocurrent signal $PC_{+-} + PC_{++}$ of the charged exciton. The photocurrent signal of the trion peak becomes weak at large time delays due to hole tunelling. The total X^+ signal after 8.5 ns is reduced to $\sim$ 150 fA, which is comparable to the photocurrent noise. This results in the increased scatter of the data for large τ_D in Fig. 5.19. Nevertheless, more than 40 periods of the hole spin precession can be resolved in Fig. 5.19 at an applied magnetic field $B = 4.7$ T.

The decay in the spin contrast C was used to infer the dephasing time T_2^*. Figure 5.21 plots the amplitude of the oscillation at the time delay τ_D. This was found by

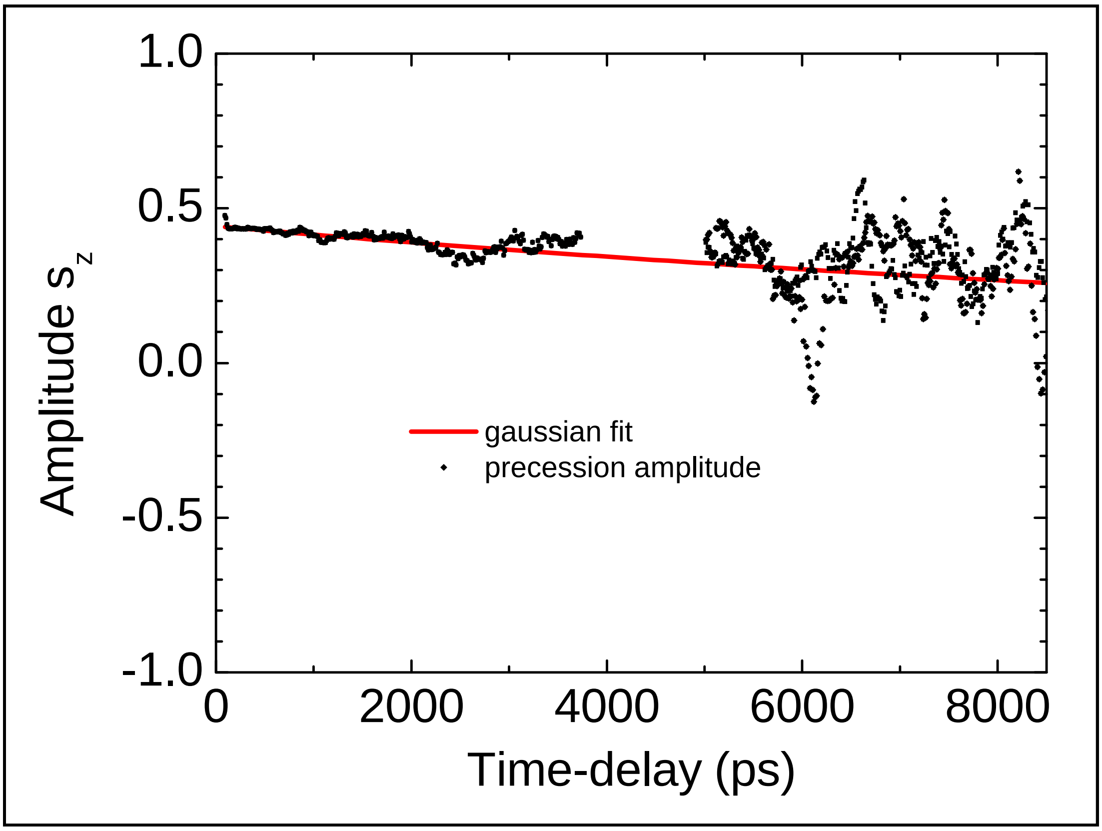

Figure 5.21: *The amplitude of the hole spin precession is plotted as a function of time. The fit is to a Gaussian decay and yields a dephasing time of* $T_2^* = 12.2 - 17.5$ ns

fitting a cosine to the data for the time range $\tau_{\mathrm{D}} \pm T/2$, where T is the period. The hole-spin contrast C decays with time delay. Since no spin-echo techniques were employed, the most likely source of dephasing is inhomogeneous broadening due to variations in the effective Overhauser field acting on the hole spin. The decay of the hole spin interacting with a nuclear spin bath in Voigt geometry magnetic field is expected to have a Gaussian-like decay, $s_z \propto \exp\left(-\tau^2/T_2^{*2}\right)$, where $T_2^* = \hbar\sqrt{2}/\sigma$ and σ is the variance of the hole-nuclear hyperfine interaction [13]. A value of $T_2^* = 12.2 - 17.5$ ns was deduced from fits to data in Fig. 5.21.

The dephasing time is 7-10 times longer than the 1.7 ns measured by Press *et al* for an electron spin confined to a single InGaAs/GaAs quantum dot [38], [11]. This is in-line with the ratio of the hyperfine interaction strengths of the electron and hole measured for InAs/GaAs quantum dots [54], [15], suggesting that the main source of dephasing is the hole-nuclear spin interaction. Furthermore the measured value of T_2^* is consistent with the theoretical estimates described in section A.7. The T_2^* is small compared to the microsecond-scale "T_2^*" measured by Brunner *et al* [16] in a coherent population trapping (CPT) experiment. The dynamics of a hole spin in a nuclear spin bath has two characteristic times, in the 10-ns ($\sim 1/\sigma$) and microsecond ($\sim E_{hZ}/\sigma^2$) regimes [13], where E_{hZ} is the hole Zeeman energy splitting. It is possible that the Brunner experiments measure the longer of these two time constants.

In Recent experiments by De Greve *et. al.* [38] and Greilich *et. al.* [85] hole spin dephasing times of $T_2^* = 2.3$ ns and $T_2^* = 20.7$ ns have been reported respectively. Both groups attribute the dephasing to in-plane hole g-factors that are sensitive to local electric field fluctuations, and both groups use deterministically chargeable p-type devices. Recent experiments by Gerardot *et. al.* [104] show that, in general, the linewidth for X^+ transitions is $\sim 3\times$ larger for p-type devices compared to n-type devices. Similar devices are used in ref. [85], and this presumably results in the strong electric field dependent in-plane g-factor reported. The gradient of the hole spin precession energy with respect to electric field F, $\mathrm{d}(\hbar\omega_\mathrm{h})/\mathrm{dF}$, reported in ref [85] is ~ 14 μeV/Vμm^{-1}. This is $\sim 15\times$ larger than the value of 0.9 μeV/Vμm^{-1} measured in the n-type devices used in these experiments (see Fig. 5.12). The result of this is that the reported 4.3 mV fluctuations in ref. [85] due to charge noise in the devices gives rise to a dephasing time which is limited by spectral diffusion of the optical transitions. This is further confirmed by the work of ref. [38], where the dephasing is again attributed to charge noise in the p-type device. In this case a relatively large in-plane hole g-factor is reported, $g_\mathrm{h} = 0.27$. Large in-plane hole g-factors are a result of significant heavy-hole light-hole mixing. The reported g-factor gradient $\sim 2\mu$eV/Vμm^{-1} is small in this case. Therefore, $T_2^* = 2.3$ ns is more likely to be dominated by the hyperfine interaction [14].

5.8 Summary of measurement of hole spin precession and dephasing time

This chapter describes the preparation of a coherent superposition state of a single hole spin by observing the spin precess in a Voigt geometry magnetic field. The method for preparing the superposition state, the ionisation of a spin polarised electron hole pair, is unique compared to other spin preparation techniques [9], [11], [16], [59], [38] in that it is created by a single picosecond laser pulse, and survives in the absence of a driving laser field. Furthermore the preparation is fast and is limited by the electron tunneling rate.

The dependence of the spin preparation contrast or fidelity on the applied magnetic and electric fields has been studied and compared to a simple model formulated from first principles. Calculations using measured parameters are able to predict well the expected spin preparation contrast as a function of applied magnetic and electric fields.

For the magnetic field dependence, the contrast is maximum $C \sim 0.4$ when the hole spin precession frequency is equal to the bright neutral exciton effective fine structure splitting. Although the contrast of the spin precession is small, in this case less than one half, it would be possible to improve it by using a quantum dot with zero fine structure splitting to values $C > 0.9$ at magnetic fields $B < 2$ T. Many groups have recently shown techniques for tuning the fine structure to zero. These include techniques such as thermal annealing [27], [28], strain tuning [29] and growth on (111)B substrates [30], [31]. For the electric field dependent studies, the contrast is shown to improve with increasing electric field. The improved contrast with increasing electric field is due to the fact that with faster electron tunneling, there is less time available for spin mixing.

The dephasing time of the hole was measured by observing the decay in amplitude of the hole spin precession contrast at long time delays, up to around 8.5 ns. The most likely source of dephasing is the fluctuations in the nuclear magnetic field coupling to the hole spin via the hyperfine interaction. By fitting the decay in amplitude of the precession contrast to a Gaussian decay, a dephasing time $T_2^* = 12.2 - 17.5$ ns was inferred, which is 7-10 times longer than the 1.7 ns measured by Press *et al* for an electron spin confined to a single InGaAs/GaAs quantum dot [38], [11]. This is in line with the ratio of the hyperfine interaction strengths of the electron and hole measured for InGaAs/GaAs quantum dots [54], [15], confirming that the main source of dephasing is the hole-nuclear spin interaction.

In conclusion, this is the first[1] observation of a the precession of a single hole spin and is an important step towards full quantum control of a hole spin state in a quantum dot. The next step to achieving full quantum control over the hole spin state, is the rotation of the spin about an axis orthogonal to the magnetic field direction, and this is the subject of the next chapter.

---

[1] During the completion of the experiments other groups were carrying out similar work [38], [59]

Chapter 6

Optical rotation of a single hole spin

6.1 Introduction

One of the DiVincenzo criteria for quantum computation using a carrier spin confined in a quantum dot is the ability to perform a single qubit operation with a gate speed much faster than the coherence time of the specified qubit [3], [97]. In the previous chapter the extrinsic dephasing time of a hole spin in a quantum dot on the order of tens of nanoseconds was reported. This means that the maximum gate time for qubit operations needs to be on the order of a few picoseconds in order to achieve thousands of quantum operations before decoherence. One approach to achieve this is to use a picosecond optical laser pulse to perform a spin rotation. Pioneering experimental work which demonstrated the rotation of a single electron spin state in a quantum dot has been reported [11], [100], [89], [56], [12]. However, there are been no such reports on the coherent optical control of a single hole spin qubit [1], which has the prospect of a longer coherence time due to the suppression of the contact hyperfine interaction [13].

This chapter describes the first experimental demonstration of the coherent

---

[1] During the completion of the experimental work, two other groups achieved similar experimental goals, [85], [38]

optical rotation of a single hole spin using a picosecond laser pulse. A geometric phase gate is demonstrated, which is equivalent to a Pauli-Z qubit gate, and more general rotations about the z-axis are also shown. Additional data will be presented that shows the ability to control the angle of rotation and the direction of the Bloch vector using the detuning and phase of a picosecond optical pulse. In conjunction with the rotation due to the Larmor precession about the external magnetic field, the experiments show the first full coherent quantum control of a single hole spin trapped in quantum dot over the surface of the Bloch-sphere. It is noted that during the completion of the experimental work, two other groups achieved similar experimental goals, [85], [38].

6.2 Principle of the geometric phase gate

The approach to rotate the hole spin was adopted from theoretical proposals based on geometric phase in references [87], [88]. To see how the phase gate works, we first consider the energy level diagram of the energy eigenstates for the system consisting of a hole spin and a charged exciton in the Voigt geometry as depicted in Fig. 6.1. The hole eigenstates $|h\rangle$ and $|\bar{h}\rangle$ are split by the Zeeman energy $\hbar\omega_{\mathrm{h}} = g_{\mathrm{h}}\mu_{\mathrm{B}}B$. The excited states consisting of the positively charged excitons $|T\rangle$ and $|\bar{T}\rangle$ are split by the electron Zeeman energy $\hbar\omega_{\mathrm{e}} = g_{\mathrm{e}}\mu_{\mathrm{B}}B$. The dipole allowed transitions between the hole and the charged exciton states are linearly polarised and labelled with the polarisations X and Y.

Figure 6.1 depicts the states in the energy eigenstates basis. In order to implement the geometric phase shift, it is necessary to use a laser pulse that drives a Rabi-rotation between selected hole spin and charged exciton states. To achieve this requires a laser pulse with a bandwidth $\Delta\omega$ much greater than the Zeeman energy splittings $\hbar\omega_{\mathrm{h}} = g_{\mathrm{h}}\mu_{\mathrm{B}}B$ and $\hbar\omega_{\mathrm{e}} = g_{\mathrm{e}}\mu_{\mathrm{B}}B$. To see how this can be implemented requires a change of basis in which we view the hole and charged exciton states.

Figure 6.2 shows an energy level diagram in the circular basis, where the hole and charged exciton states are coupled using a laser pulse with a bandwidth much

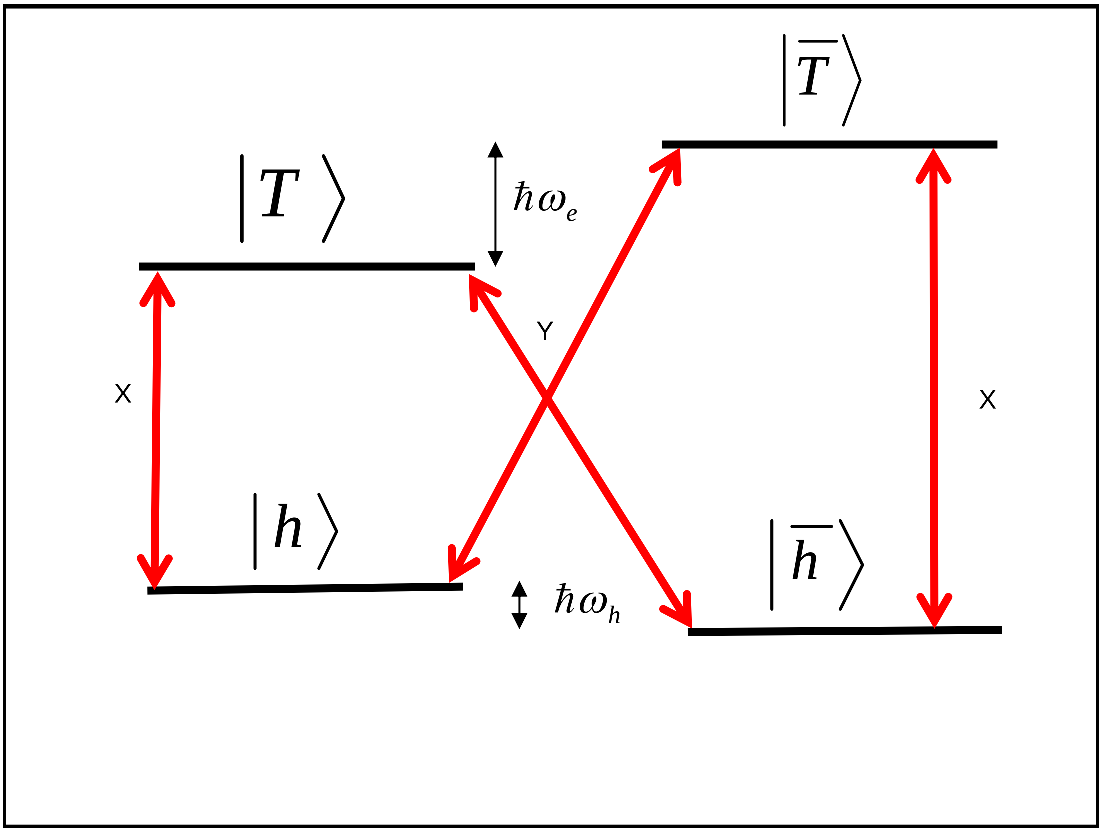

Figure 6.1: *Energy level diagram of the hole states $|h\rangle$ and $|\bar{h}\rangle$ and the charged exciton states $|T\rangle$ and $|\bar{T}\rangle$ in the energy eigenstates basis. The transitions are linearly polarised (labelled X and Y) and all four transitions are optically active.*

greater than the energy splittings in the system. In this case the spin-z states can be considered quasi-stationary since the laser pulse has a time duration much shorter than timescales of the precession of the hole and charged exciton states. The application of a picosecond circularly-polarised laser pulse drives a Rabi rotation between the hole and charged exciton spin states selected by the circular polarisation of the excitation. This leaves the other states unaffected because of the transitions must obey $\Delta m = \pm 1$. For example, a σ^- pulse resonant with the hole to charged exciton transition couples the hole spin state $|\Uparrow\rangle$ to the charged exciton state $|\Uparrow\Downarrow\uparrow\rangle$. Conversely, a σ^+ pulse resonant with the hole to charged exciton transition couples the hole spin state $|\Downarrow\rangle$ to the charged exciton state $|\Downarrow\Uparrow\downarrow\rangle$. Figure 6.2 shows the case where a 2π pulse with σ^- polarisation drives a Rabi-rotation between the state $|\Uparrow\rangle$ to $|\Uparrow\Downarrow\uparrow\rangle$ back down to the $\Uparrow$. The result of this is to impart a phase shift on $|\Uparrow\rangle$ hole spin state relative to the $|\Downarrow\rangle$ hole spin state. The phase shift depends on the

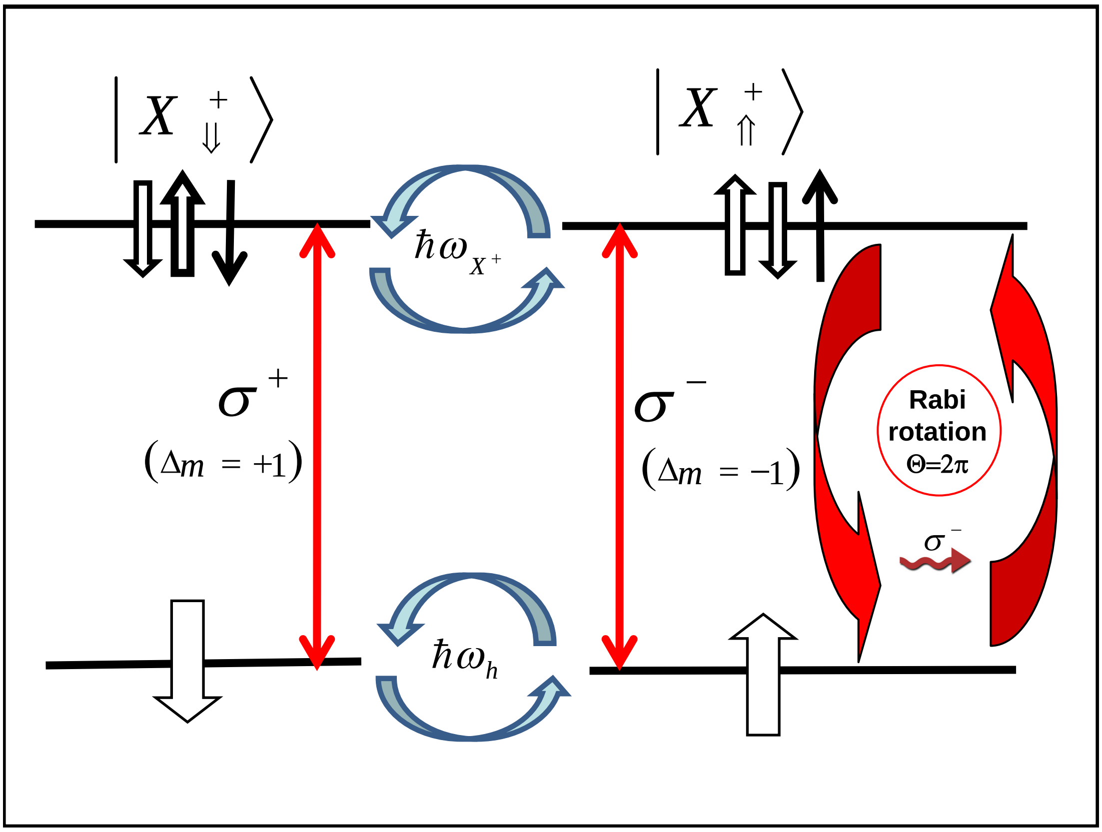

Figure 6.2: *Energy level diagram of hole and charged exciton system in the circular basis. In this picture the hole spin states* $|\Uparrow\rangle$ *and* $|\Downarrow\rangle$ *are coupled by the hole Zeeman energy splitting* $\hbar\omega_{\mathrm{h}} = g_{\mathrm{h}}\mu_{\mathrm{B}}B$ *and the charged exciton states* $|\Uparrow\Downarrow\uparrow\rangle$ *and* $|\Uparrow\Downarrow\downarrow\rangle$ *are coupled by the charged exciton Zeeman energy splitting* $\hbar\omega_{\mathrm{e}} = g_{\mathrm{e}}\mu_{\mathrm{B}}B$ *as depicted by the blue curved arrows. The curved red arrows show how a fast laser pulse with* σ^- *polarisation only couples to the* $\Uparrow$*-*$\Uparrow\Downarrow\uparrow$ *transition, driving a Rabi-rotation between these states, selected by the polarisation of the laser pulse.*

detuning Δ and the Rabi frequency Ω of the laser pulse and is given by eqn 6.1 [88]:

$$\Delta\phi_z = \frac{1}{2}\int_{-\infty}^{\infty} d\tau \left(|\Delta| - \sqrt{\Delta^2 + \Omega(t)^2}\right), \tag{6.1}$$

where the time integral is performed over the duration of the laser pulse. Consider the effect of the laser pulse, on the hole spin superposition state. Before the arrival of the pulse at time t_{C}, the wavefunction of the hole spin state may be expressed as:

$$|\psi(t < t_{\mathrm{C}})\rangle = h_{\Uparrow}\,|\Uparrow\rangle + h_{\Downarrow}\,|\Downarrow\rangle\,. \tag{6.2}$$

Under resonant excitation and in the ideal case of weak trion dephasing, a circularly-polarised laser pulse drives a Rabi-rotation between the selected hole spin and trion states. The wavefunction of the hole state after the arrival of the pulse may be expressed as:

$$|\psi(t > t_{\mathrm{C}})\rangle = h_{\Uparrow} |\Uparrow\rangle + h_{\Downarrow} \left[\cos(\frac{\Theta}{2}) |\Downarrow\rangle + i \sin(\frac{\Theta}{2}) |\downarrow\Uparrow\Downarrow\rangle\right], \tag{6.3}$$

where Θ is the pulse area. When $\Theta = 2\pi$, the state of the dot is returned to the hole spin subspace having acquired a phase shift of π [87], [88]. Therefore the control pulse transforms the wavefunction in eqn 6.2 to:

$$|\psi(t > t_{\mathrm{C}})\rangle = h_{\Uparrow} |\Uparrow\rangle - h_{\Downarrow} |\Downarrow\rangle, \tag{6.4}$$

where we observe a change of sign in the superposition. Figure 6.3 shows a Bloch sphere to illustrate the optical rotation about the z-axis, due to the control pulse. It is apparent that the result of the control pulse is a rotation about the optical (z) axis by an angle $\Delta\phi_z$ determined by the detuning of the control pulse.

Full coherent control of the hole spin state requires rotations of the spin about two orthogonal axis. Figure 6.3 shows a Bloch sphere to illustrate both the optical rotation about the z-axis, due to the control pulse, and the Larmor precession about the x-axis, due to the applied magnetic field. The lower right of the figure shows the Voigt experimental geometry. We first consider the general case for spin rotations using a resonant control pulse. The hole spin up state $|\Uparrow\rangle$ is prepared, and is depicted by the blue arrow pointing in the z-direction in Fig. 6.3. The spin state precesses about the magnetic field and is rotated by an angle $\theta = \omega_{\mathrm{h}} t$. At the time of the arrival of the control pulse, the Bloch vector points in the y-direction as depicted by the vector labelled $\mathrm{S}_{\mathrm{before}}$ in Fig. 6.3. The control pulse rotates the Bloch vector by an angle $\Delta\phi_z$ about the z-axis to the vector labelled $\mathrm{S}_{\mathrm{after}}$ in Fig. 6.3. The Bloch vector then continues to precess having acquired a phase shift of π.

A rotation of the Bloch vector using a control field is equivalent to a qubit operation. When the control pulse is resonant with the hole to charged exciton

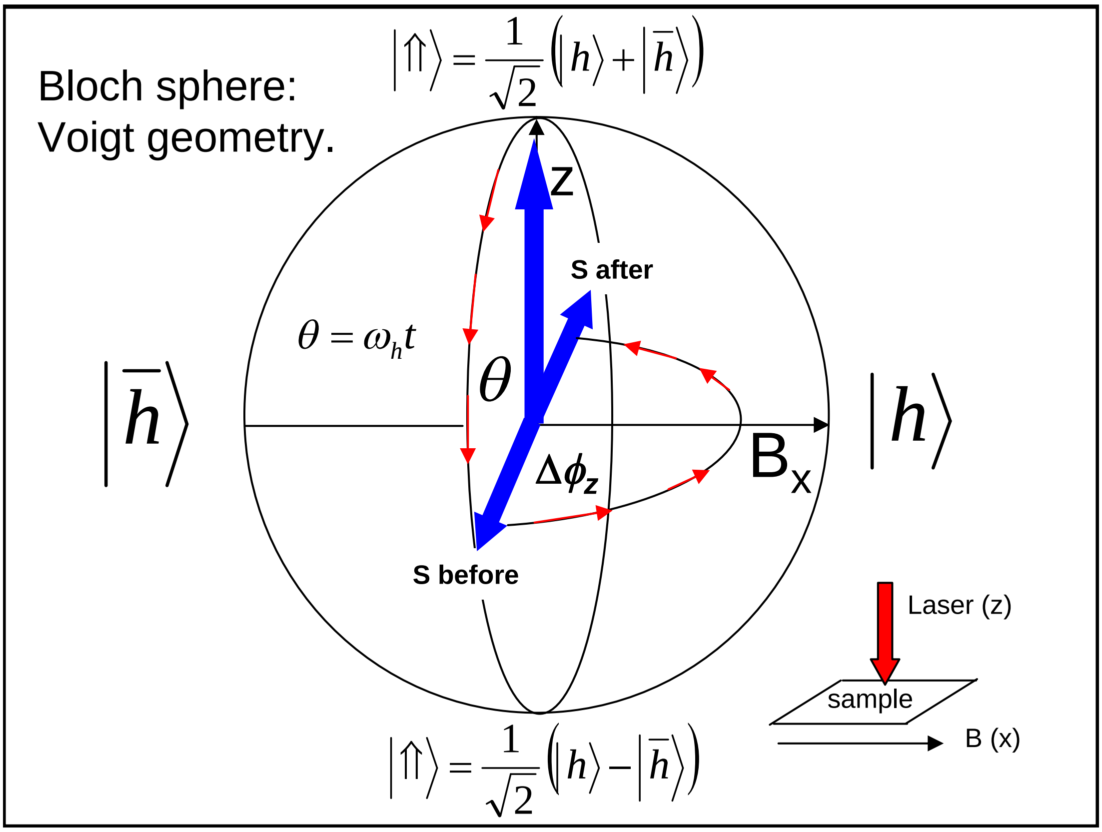

Figure 6.3: *Bloch sphere to illustrate rotation of the hole-spin vector about the optical axis. The precession of the Bloch-vector (large blue arrow) about the magnetic field direction (x) is shown by the angle $\theta = \omega_h t$. The control pulse arrives at a point when the Bloch vector is directed along the y-axis ($\mathrm{S}_{\mathrm{before}}$) and rotates the Bloch vector about the optical (z) axis to the vector $\mathrm{S}_{\mathrm{after}}$ by an angle $\Delta\phi_z$ dependent on the detuning. The path of the Bloch vector in time is indicated by small red arrows. Also shown (lower right) is the Voigt experimental geometry.*

transition and arrives at a time when the the Bloch vector point along the y-axis as shown in Fig. 6.3, the control pulse acts as a Pauli-Z gate $\hat{U}_z$ on the hole spin qubit:

$$\hat{U}_z \left|\psi_{\mathrm{I}}\right\rangle = \begin{pmatrix} 1 & 0 \\ 0 & -1 \end{pmatrix} \begin{pmatrix} h_{\Uparrow} \\ h_{\Downarrow} \end{pmatrix} = \begin{pmatrix} h_{\Uparrow} \\ -h_{\Downarrow} \end{pmatrix}$$

Furthermore the overall phase of the precession and angle of rotation can be controlled by varying the arrival time of the control pulse and its detuning. Using combinations of rotations about the x and z axes provides full control of the hole spin over the surface of the Bloch sphere.

6.3 Results

The coherent optical control of the hole spin was achieved using a three pulse experiment. The first pulse, termed the preparation pulse had circular polarisation and pulse area $\Theta = \pi$ and was resonant with the neutral exciton transition, it prepared the hole spin in a coherent superposition state at time $\tau_{\mathrm{P}} = 0$. The second pulse, termed the control pulse had circular polarisation, pulse area $\Theta = 2\pi$ and variable detuning with respect to the charged exciton transition. The control pulse also had variable time delay with respect to the preparation pulse and was used to coherently rotate the hole spin. Finally, the third pulse, termed the detection pulse, was used to detect the hole spin at times τ_{D}. The detection pulse had co or cross circular polarisation with respect to the preparation pulse and was resonant with the charged exciton transition. The photocurrent absorption of the detection pulse was proportional to the hole spin z-component and provided a time resolved measurement of the hole spin precession. Chapter 5 outlines the method to prepare and detect the hole spin state and observe the coherent procession. The experiments in this chapter followed the same procedure as described in 5.3, the only difference being the addition of the control pulse to the experiments. Fig. 6.4 is a schematic diagram listing the steps (i)-(v) involved in the experiment. The lower part of Fig. 6.4 shows the pulse sequence. The upper part of Fig. 6.4 shows schematic band diagrams of the device. This illustrates the preparation, the control and precession and also the detection of the hole spin over the course of the experiment.

6.3.1 Measurement of the electron spin precession and electron g-factor

In order to determine the magnetic field conditions for the experiments, a measurement of the electron *g*-factor was made. To measure the electron *g*-factor, a time resolved measurement of the trion precession was made under an applied magnetic field. The electron g-factor was measured using the same three-pulse

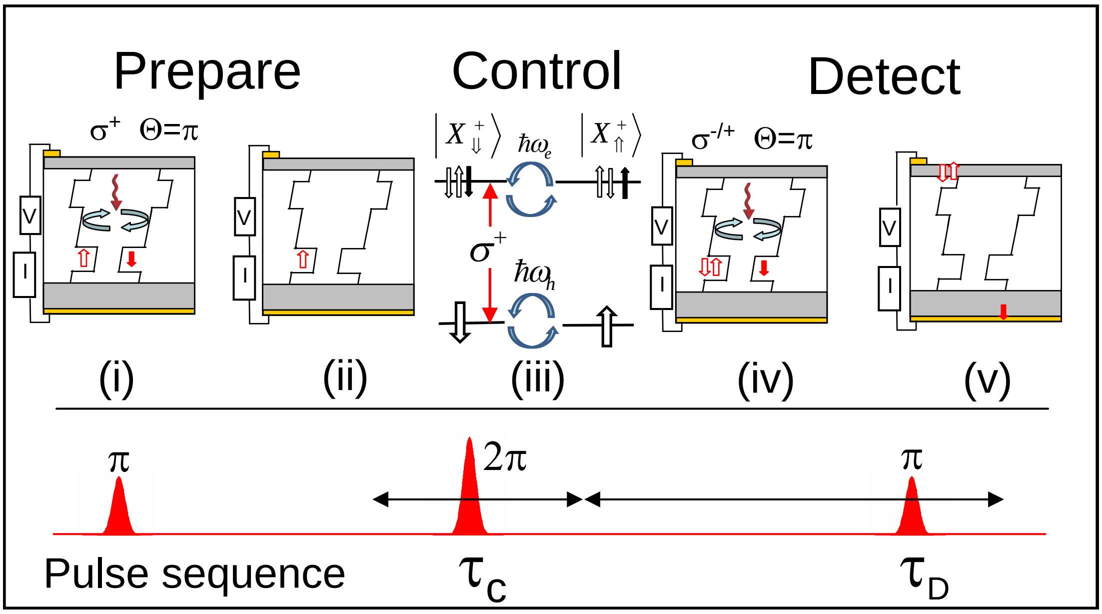

Figure 6.4: Principle of operation for preparing, controlling and measuring the hole spin state. The figures shows a series of schematic band diagrams of the device to illustrate the steps in the experiment (i) Resonant excitation of the neutral exciton transition by a laser pulse propagating along the z-axis creates a spin-polarized electron-hole pair. (ii) When the electron tunnels it leaves a spin-polarized hole that precesses about the magnetic field applied along the x-axis. (iii) Rotation of hole-spin. The hole (trion) spin-z states are coupled with in-plane Zeeman energies of $\hbar\omega_h$ ($\hbar\omega_e$) respectively. This is depicted by curved blue arrows. The σ_+-polarized control pulse couples the $|\Downarrow\rangle \leftrightarrow |\Downarrow\Uparrow\downarrow\rangle$ states only, imparting a phase-shift on $|\Downarrow\rangle$. (iv) To detect the hole-spin, a circularly polarized laser pulse resonant with the hole-trion transition is absorbed conditional on the spin-z state of the hole. (v) When the additional carriers created in step (iv) tunnel from the dot a change in photocurrent proportional to the occupation of the hole spin state selected by the helicity of the detection pulse is measured.

experimental method to control the hole spin. The only difference being that in this case the control pulse had pulse area $\Theta = \pi$ and not $\Theta = 2\pi$. The control pulse with $\Theta = \pi$ created near unit population of the charged exciton state, which precessed about the magnetic field. This type of experiment is equivalent to the measurements of the energy splitting of the neutral exciton [96] previously discussed in chapter 3 section 3.7.3, and described in detail in the appendix section A.4, except that here the energy beat of the charged exciton due to the electron Zeeman energy splitting was measured.

Figure 6.5 shows an example of the time resolved measurement of the trion precession. Two data sets are presented in 6.5. For both measurements the photocurrent was recorded as a function of the time delay between preparation

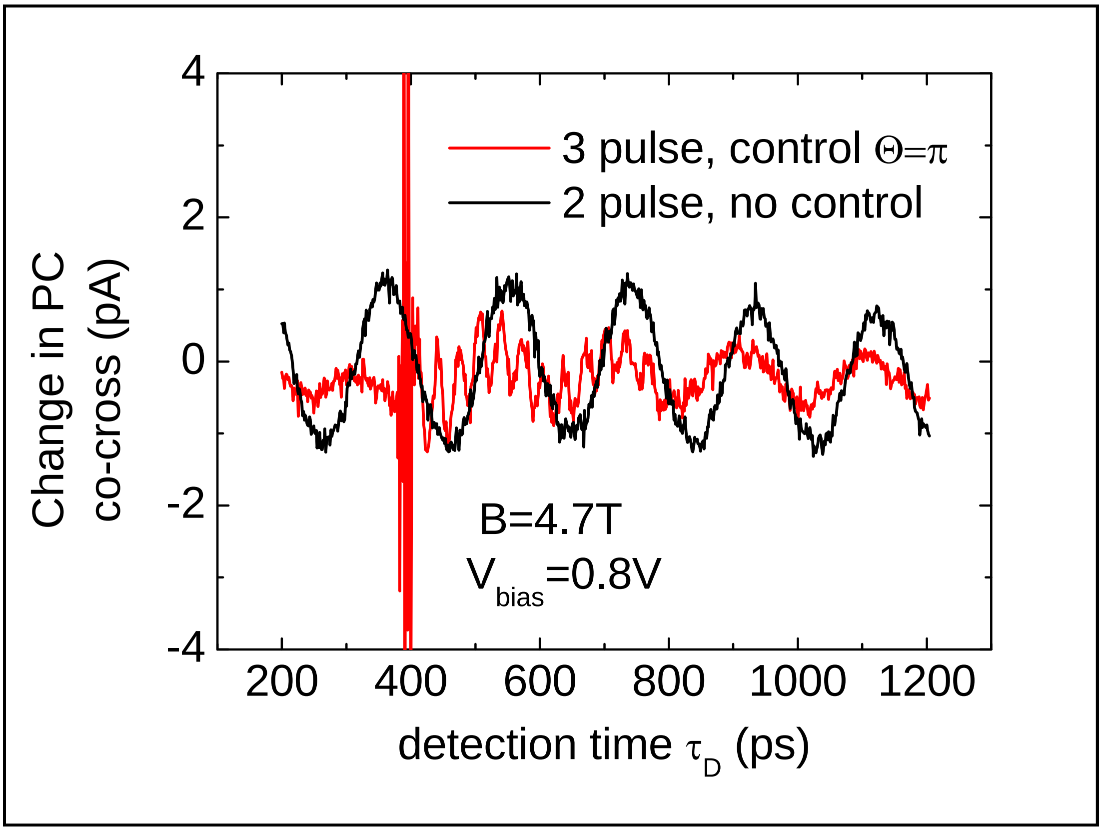

Figure 6.5: *Measurement of the precession of the charged exciton. The black curve is a two pulse measurement of the hole spin precession without a control pulse, in a magnetic field* $B = 4.7$ T*. The red curve is a three pulse measurement, where the control pulse had a pulse area* $\Theta = \pi$ *and was resonant with the hole to charged exciton transition. For the three pulse measurement (red), two oscillation frequencies can be observed (i) the hole spin precession and (ii) the faster charged exciton precession.*

and detection pulses. This was done using both co and cross circularly polarised preparation and detection and the difference in photocurrent $PC_{+-} - PC_{++}$ is plotted in Fig. 6.5 for the cases of with and without a control pulse. The data in the black in Fig. 6.5 is a two-pulse measurement of the hole spin precession. This is for the case of without any control pulse and is used as a reference. The red data in Fig. 6.5 is the three pulse measurement, where the control pulse had pulse area $\Theta = \pi$. Two oscillation frequencies can be observed. The slower oscillation is due to the hole spin precession, while the faster oscillation is a result of the electron Zeeman energy splitting. A fast Fourier transform of the data yields an oscillation period of $\tau = 33$ ps, which at a magnetic field of $B = 4.7$ T corresponds to an electron g-factor $|g_{\mathrm{e}}| = 0.47$. Using the results from the measurments of the

g-factors, a magnetic field $B = 1.128$ T was used in all experiments related to the hole spin control. At this magnetic field the Zeeman energy splittings of the hole and charged exciton are 5.1 μeV and 30 μeV. These are factors of 40 and 7 times smaller than the bandwidth of the control pulse. Therefore the splittings at this magnetic field satisfied the approximate stationary state condition which is required for the geometric phase shift.

6.3.2 Hole spin control: controlling the phase of the precession

In order to understand the effect of the control pulse on the hole spin state, a set of measurements of the hole spin precession vs the control pulse arrival time were made. For all these measurments the control pulse was tuned on resonance with the hole-trion transition. The pulse sequence is illustrated in the lower part of Fig. 6.4. The hole-spin precession was measured by scanning the detection time τ_{D}, and a series of measurements for different values of τ_{c} are presented in Fig. 6.6. The difference between the photocurrents measured for $\sigma_{\pm}$ detection pulses is plotted: $\Delta I = I_{\mathrm{cross}} - I_{\mathrm{co}}$. For reference, the hole-spin precession with a period of 770 ps was measured without the control pulse and is shown as the lowest plot in Fig. 6.6 in bold black. The main effect of the control pulse was to change the phase of the hole-spin precession as seen in Fig. 6.6. For detection times within the electron-tunneling time, a fast oscillation with a period 138-ps period was also observed. This was due to precession of a trion component created by the control pulse, as a result of the imperfect contrast of the hole-trion Rabi rotation. The effect of the control pulse is highlighted for three cases in Fig. 6.6 and these will be discussed in turn in the following. The red trace in Fig. 6.6 presents the case where the hole-spin points along the z-axis when the control pulse arrives. This is illustrated by the Bloch sphere (a) in Fig. 6.6. Since the control pulse produces a rotation about the z-axis, it is expected to have minimal effect on the hole-spin in this case. This can be seen by comparing the bold black and red-traces of Fig. 6.6.

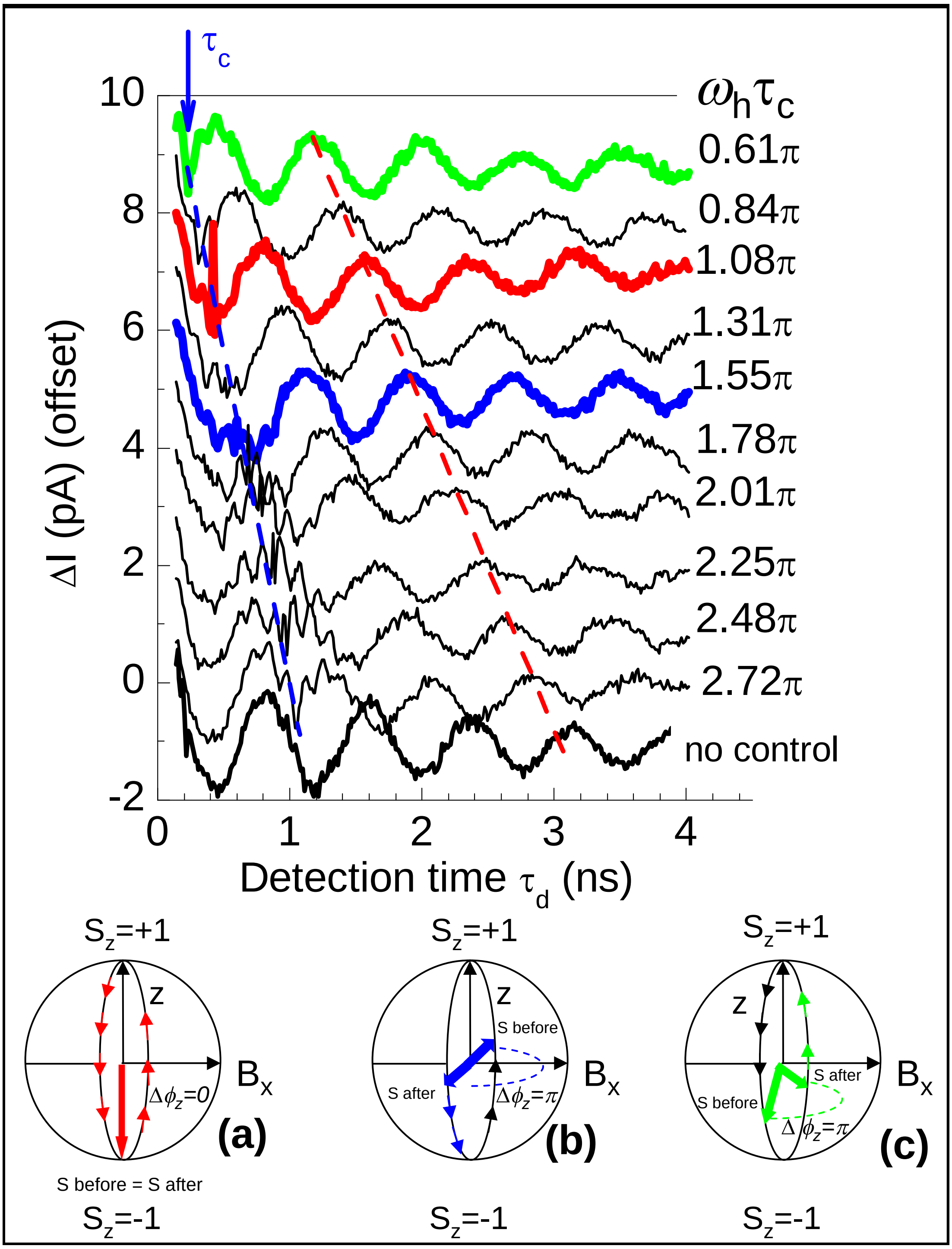

Figure 6.6: *Control over the hole spin precession phase. Plotted is* $\Delta I = PC_{\mathrm{cross}} - PC_{\mathrm{co}}$ *as a function of the detection time* τ_{d} *for various control times* τ_{c}*. Also plotted is the hole spin precession without a control pulse in the thick black as a reference. Highlighted in red green and blue are three cases with corresponding Bloch spheres to illustrate the effect of the control pulse*

The Bloch sphere (a) of Fig. 6.6 illustrates this process. It shows how the Bloch vector (large red arrow) is unaffected by the presence of the control pulse, and therefore there is no change of phase of the precession.

The blue-trace in Fig. 6.6 presents the case where, just before applying the control pulse, the hole-spin points along the y-axis. In this situation a rotation of π about the z-axis caused by the control pulse, shifts the phase of the hole-spin precession by π. This is can be seen by comparing the blue trace in Fig. 6.6 to the bold (black) and is illustrated with the Bloch sphere (b).

The green-trace in Fig. 6.6 presents the case where, just before applying the control pulse, has Bloch vector precessed by an angle of approximately 0.6π. In this situation a rotation of π about the z-axis caused by the control pulse, again shifts the phase of the hole-spin precession by π. This means the Bloch vector continues to precess from the angle $2\pi - 0.6\pi = 1.4\pi$ This is can be seen by comparing the green trace in Fig. 6.6 to the bold (black) and is illustrated with the Bloch sphere (c).

In a general case, the effect of the rotation is to reflect the hole-spin about the z-x plane. The hole-spin before applying the control pulse can be written as $\mathbf{s} = s^{(0)}(0, \sin\omega_h\tau_c, \cos\omega_h\tau_c)$. A reflection about the z-x plane maps $\mathbf{s} \rightarrow s^{(0)}(0, \cos\omega_h\tau_c, \sin\omega_h\tau_c)$, and subsequently the measured hole-spin precession evolves as $s_z = \cos(\omega_\mathrm{h}(\tau_d - 2\tau_c))$. In other words, the phase of the hole-spin is shifted by $-2\omega_h\tau_c$, as occurs in a spin-echo experiment. The expected gradient of 2 for the phase of the hole-spin precession $\omega_h\tau_s$ is confirmed in Fig. 6.7 which plots the precession start time τ_s against the control pulse arrival time τ_c. Here τ_s is defined with respect to the case of no control pulse and is found by fitting the time-traces of Fig. 6.6 to $\Delta I(\tau_\mathrm{d}) = \Delta I^{(\mathrm{c})}\cos(\omega_\mathrm{h}(\tau_\mathrm{d} - \tau_\mathrm{s}))$, for $\tau_\mathrm{d} \gtrsim \tau_\mathrm{c} + 200$ ps.

The results in Fig. 6.6 demonstrate optical rotations of the hole spin by angles of up to π when the control pulse is resonant with the $|X^+\rangle$. Furthermore, the phase of the hole spin precession can be controlled by varying the arrival time of the control pulse. In the next section, control over the angle of rotation is demonstrated.

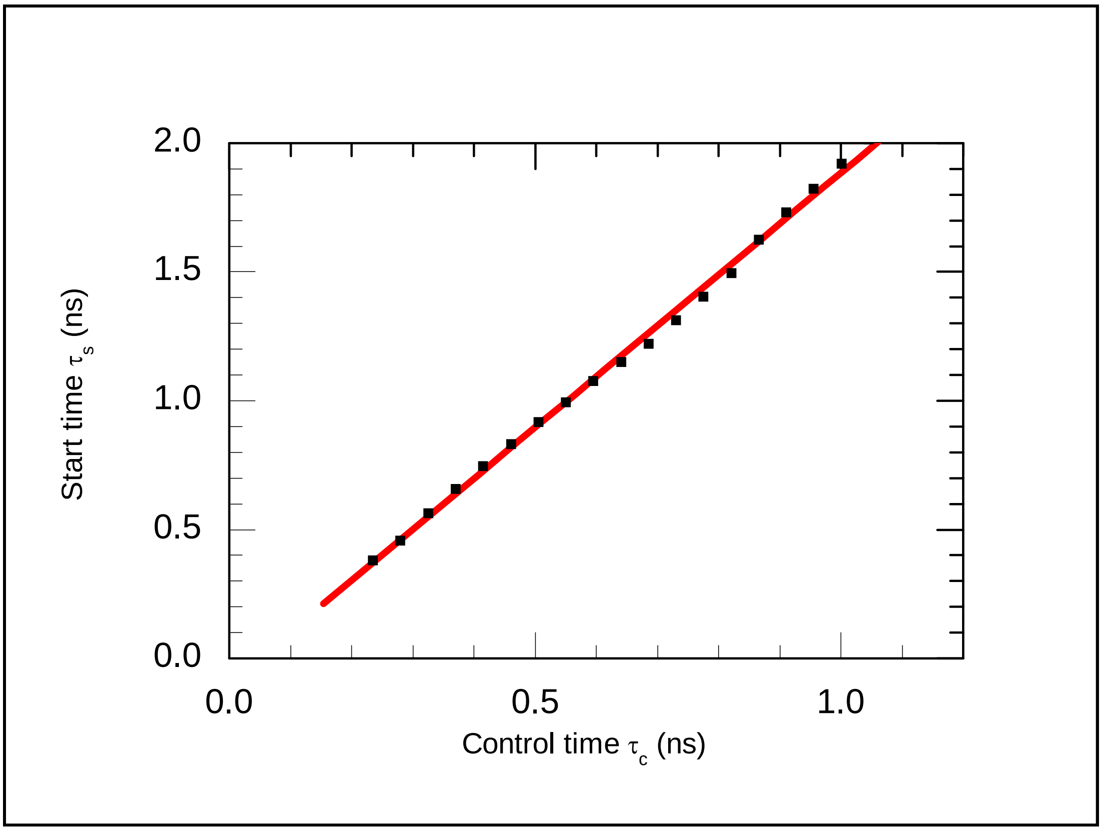

Figure 6.7: *The 'start time'* τ_s *of the spin precession after the arrival of the control pulse is plotted as a function of the control pulse arrival time* τ_c*. The start time is defined by the phase of the oscillation as determined by the cosine fits to the precession curves in Fig. 6.6. The linear fit has a gradient of* 2.00 ± 0.01

6.3.3 Controlling the angle of rotation

The final set of experiments demonstrate that the rotation angle $\Delta\phi_z$ can be controlled by the detuning of the control pulse Δ_c with respect to the charged exciton transition. This was in accordance with the theory that predicts $\tan(\Delta\phi_z/2) = \Delta\omega_\mathrm{c}/\Delta_\mathrm{c}$ [88]. Here $\Delta\omega_\mathrm{c}$ is the control pulse bandwidth for a hyperbolic-sech pulse. The detuning Δ_c is defined in the energy level diagram in Fig. 6.8. The time-delay of the control pulse was set to $\tau_c = 234$ ps. This value of τ_c was chosen so that, on arrival of the control pulse, the hole-spin pointed along the y-axis, where S_z was most sensitive to rotations about the z-axis. A series of hole-spin precessions were measured for different detunings of the control pulse Δ_c.

Figure 6.9 shows a series of measurements of the hole spin precession for different values of Δ_c with respect to the pulse bandwidth of the control pulse

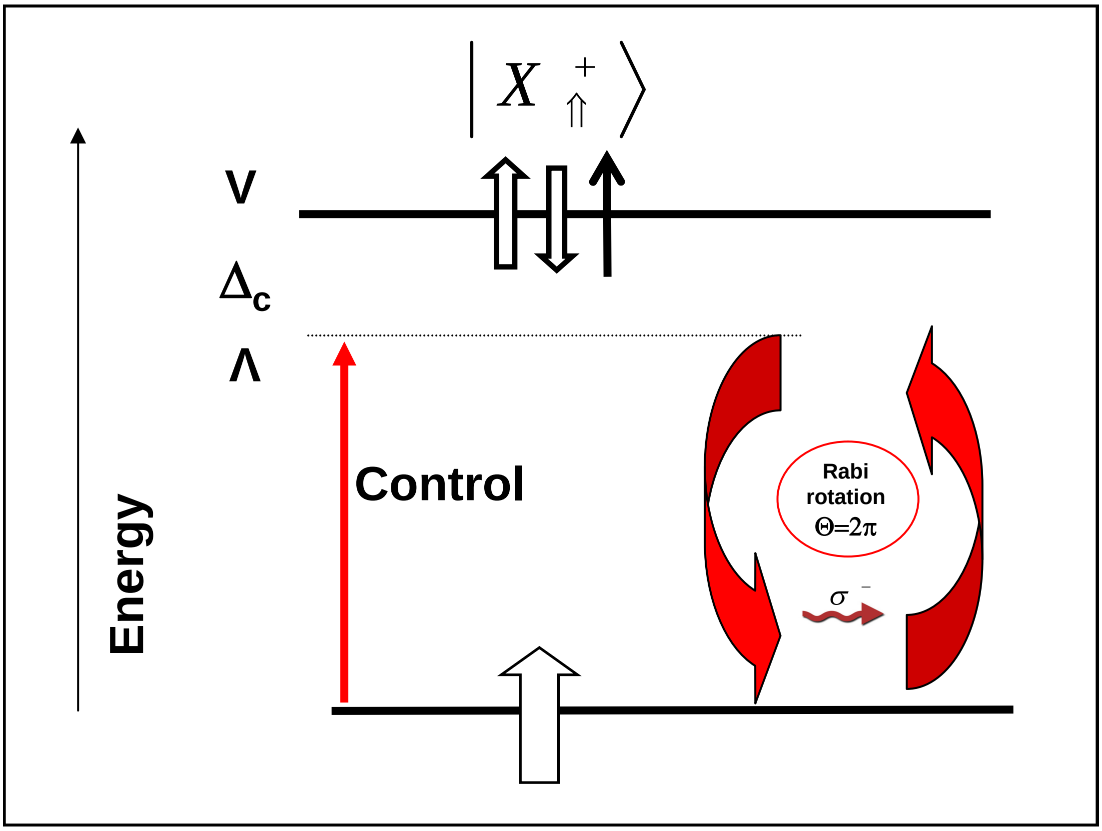

Figure 6.8: *Energy level diagram to illustrate control pulse detuning* Δ_c *with respect to the charged exciton* $|X^+\rangle$ *energy.*

$\Delta\omega_c = 0.13$ meV. Accompanying the measurements in Fig. 6.9 are a series of Bloch spheres to illustrate the effect. These will be discussed in turn in the following.

The red-trace shows the case where $\Delta_c = 0.4$ meV $>> \Delta\omega_c$. In this case, the control laser was far detuned from the hole-trion transition. The precession was relatively unaffected by the control, since the far-detuned pulse only induced a small rotation angle. This is illustrated by the Bloch sphere (a) which shows how the precession of the Bloch vector is unaffected by the control pulse for this 0.4 meV detuning.

As the control was tuned into resonance, the amplitude of the precession decreased. For a detuning of -0.14 meV, which was approximately equal to the bandwidth of the control pulse, the rotation angle $\Delta\phi_z$ was close to $\pi/2$. This left the hole-spin aligned along the x-axis. Since the Bloch vector was parallel to the magnetic field direction, the subsequent precession of the hole-spin about the magnetic field was suppressed. This is shown in the pink trace in Fig. 6.9. The spin rotation is illustrated in the Bloch sphere of Fig. 6.9(b).

Near resonance, the amplitude of the precession changed sign indicating a rotation angle of greater than $\pi/2$. This is shown in the blue trace of Fig. 6.9. The spin rotation is illustrated in the Bloch sphere (c). The amplitude of the hole-spin precession was maximal when the control was very close to resonance, as shown in the blue trace of Fig. 6.9. This indicates that the hole spin was rotated by an angle close to π.

To quantify the angle of the rotation of the hole spin due to the control pulse, the amplitudes of the spin precession were found by fitting each trace in Fig. 6.9 to cosine functions. Figure 6.10 plots of the ratio of the precession amplitudes against the detuning of the control pulse Δ_c. The ratio is normalised to the total hole population, with and without the control pulse and is defined by $R = S_z^{(c)}/S_z^{no}$.

The red-line in Fig. 6.10 is a calculation of R expected for the ideal case of no trion dephasing, namely $R = \cos(\Delta\phi_z)$, where $\tan(\Delta\phi_z/2) = \Delta\omega_c/\Delta_c$ [87]. For the pulses used here, the bandwidth of the control $\Delta\omega_c$ was 0.13 meV. There is close agreement between experiment and theory. This implies that the control-pulse rotated the hole-spin by a detuning-dependent angle $\Delta\phi_z$, with a maximum value close to π, in accordance with model of ref. [87]. The imperfect contrast in the dip of Fig. 6.10 may be due to errors in the pulse-area, or the intensity damping [64] of the hole-trion Rabi rotation. A value of $R = -1$ is expected on resonance for the case of no trion dephasing. The intensity damping of the Rabi-rotation means that the 2π control pulse creates a finite trion population, which, due to the uncertainty in the electron tunneling time, results in a scrambling of the hole spin. One way to estimate the effect is to calculate the intensity damping of the Rabi rotation for resonant excitation.

The reduction in the amplitude of the Rabi rotation is approximately 20% using a 2π pulse. The amount of charged exciton created is maximum on resonance, and reduces as the pulse is detuned. Therefore, the effect of the intensity damping

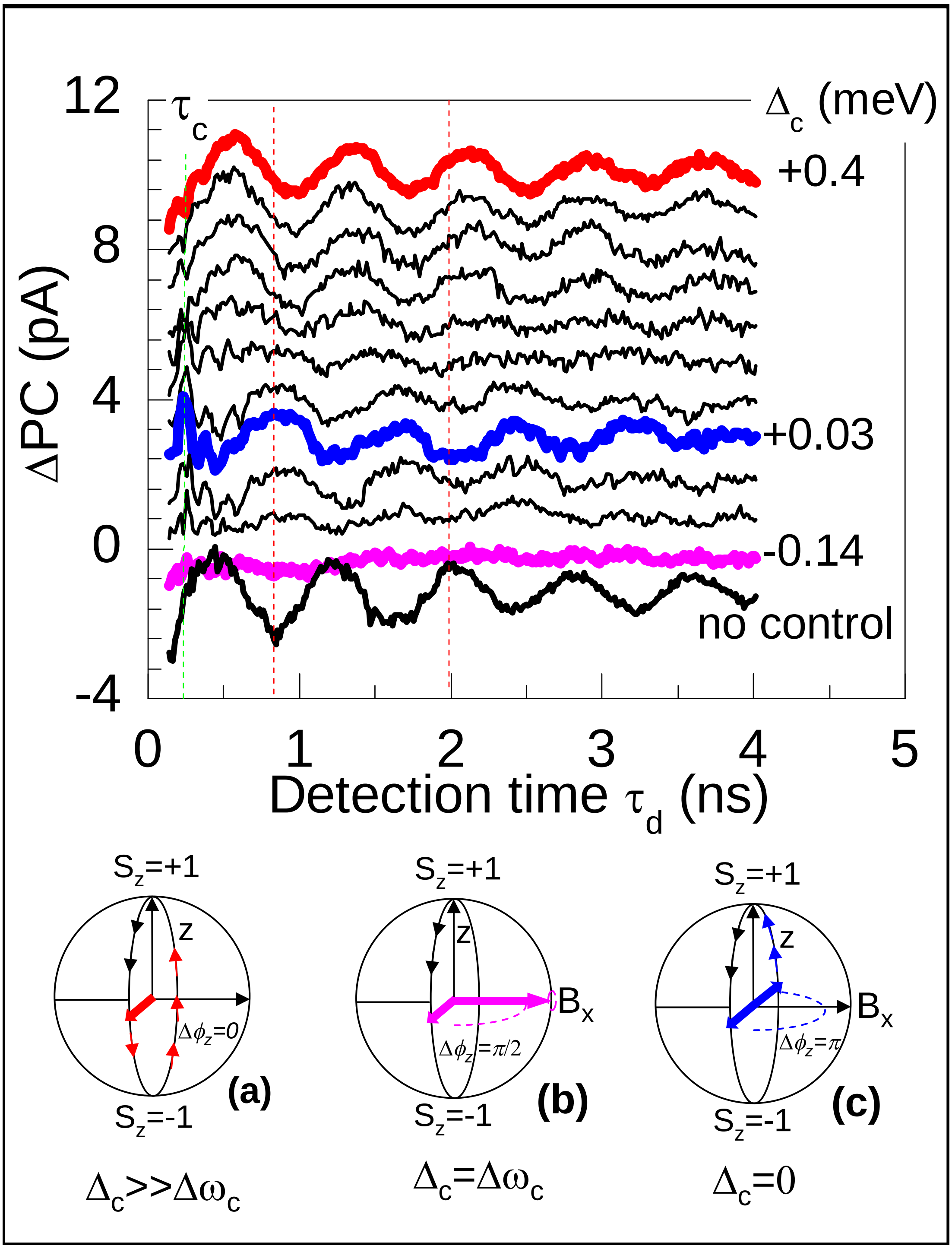

Figure 6.9: *Control over the angle of spin rotation.* $\Delta I = PC_{\text{cross}} - PC_{\text{co}}$ *is plotted as a function of the detection time* τ_{d} *for various control detunings* Δ_{c}*. The hole spin precession without control is also plotted in bold black. Highlighted in red blue and pink are three illustrative cases of* Δ_{c} *with corresponding Bloch spheres to show the effect of* Δ_{c} *w.r.t the control pulse bandwidth* $\Delta\omega_{\text{c}}$

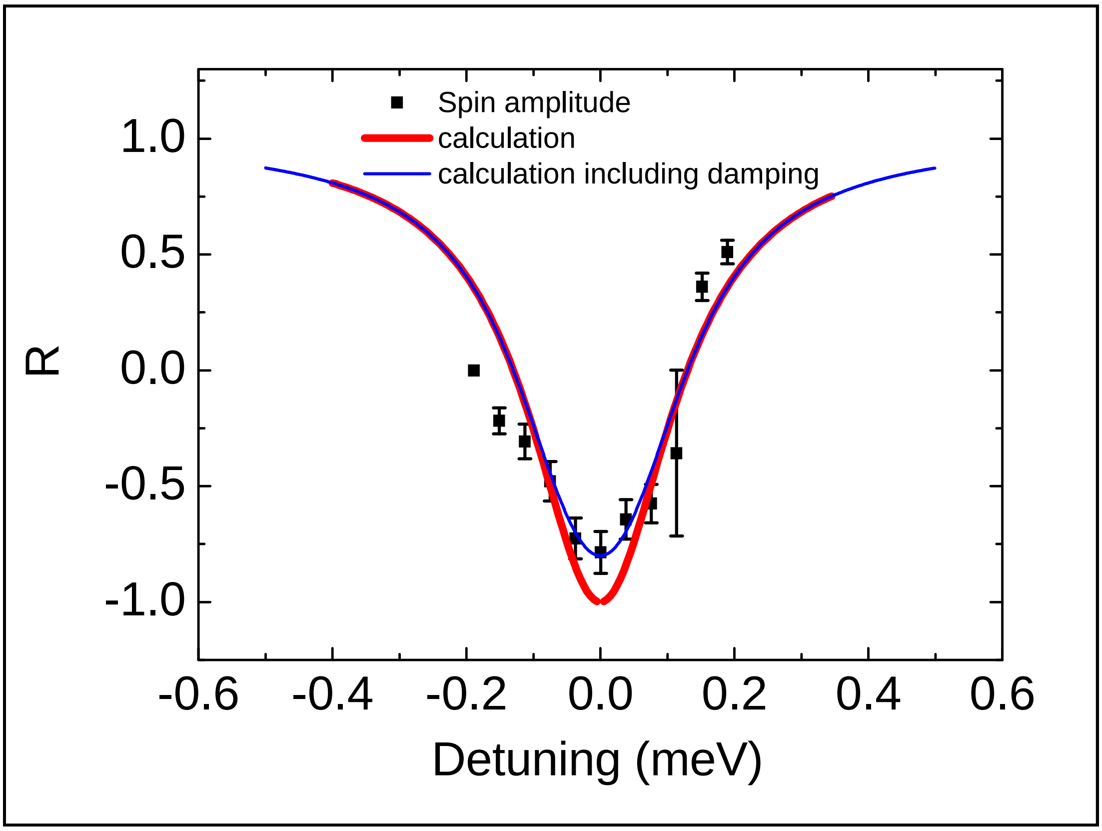

Figure 6.10: *Detuning dependence of the amplitude of spin precession after the arrival of the control pulse. The experimental data are normalised with respect to the amplitude of the precession without a control pulse. The red curve is a calculation using the theory* $R = \cos(\Delta\phi_z)$, *where* $\tan(\Delta\phi_z/2) = \Delta\omega_c/\Delta_c$ *[87]. This predicts* $R(\Delta_c = 0) = -1$. *The blue curve is a calculation which includes an estimate of the effect of dephasing due to the finite population of the trion state when the control pulse is close to resonance.*

on the reduction of the spin amplitude scales proportionally with the amount of trion created. The blue trace in 6.10 shows a calculation where the effect of the reduction in amplitude scales with the amount of charged exciton created. The trion populatation was determined from the photocurrent spectrum, which was proportional to a Gaussian G with a FWHM of the laser pulse. The calculation is given by the function $R(1-0.2G)$, where $R(\Delta_c = 0) = -1$, is the ideal case. The the factor 0.2 accounts for the intensity damping, which was 20% when $\Delta_c = 0$. This crude estimate is in reasonanble agreement with the experimental data.

6.4 Summary of optical control of hole spin

This chapter describes experiments that demonstrate the coherent optical control of a single hole spin confined to a quantum dot. The results show that a picoseconds laser pulse can be used to rotate the hole spin Bloch vector about the optical axis by an angle that depends on the detuning. Two sets of experiments were described. In the first, the phase of the precession of the hole spin state about an in-plane magnetic field was controlled by varying the arrival time of the control pulse. In the second, the angle rotation angle was varied by changing the detuning of the control pulse with respect to the charged exciton transition. The external magnetic field provided rotations about the x-axis, due to the Larmor precession of the hole spin state. By combining coherent rotations about two orthoganol axes, defined by an external magnetic field and the optical axis of a control laser, full control of the hole-spin on the Bloch sphere was achieved.

The optical rotation had a gate-time defined by the 14 ps FWHM of the control pulse, which is much smaller than the measured extrinsic dephasing time of the hole spin $T_2^* = 12.2 - 17.5$ ns. However, the rotation about the magnetic field was slower, with a 770 ps timescale defined by the in-plane hole Zeeman energy. The gate time of the rotation can not be decreased by simply increasing the strength of the applied magnetic field, and hence the precession frequency. This is because the Zeeman energy splittings of the hole and trion need to be much smaller than the bandwidth of the control pulse. A larger bandwidth control pulse could be used in principle, by designing a pulse shaper with a shorter focal length. However, this would result in a higher photocurrent background. Therefore it would be desirable to use a quantum dot with a larger in-plane hole g-factor.

Picosecond control about both axes should be possible by pursuing proposals to control the direction of the rotation axis of the control pulse [87]. For example, optical rotations about the x-axis can be achieved by using a detuned laser pulse which is linearly polarised. This drives a 2π Rabi-rotation for both linearly x-polarised transitions, so that both hole eigenstates $|h\rangle$ and $|\bar{h}\rangle$ in Fig. 6.1 accumulate a phase determined by the detuning of the laser pulse [87]. By using combinations of rotations about the z-axis and the x-axis it would be possible to achieve rotations about an arbitrary axis on a picosecond timescale.

The experimental results in this chapter have been submitted to Physical Review Letters and are under review. The submitted paper can be found on the arXiv [105].

Chapter 7

Conclusions and future work

7.1 Conclusions

This thesis described the coherent optical control of a single hole spin in a semiconductor quantum dot using picosecond optical laser pulses. Three key experimental results were presented:

- Experiments that demonstrate fast initialisation of a single hole spin trapped in an InGaAs quantum dot with a fidelity $F > 99\%$ and a 1/e time of ~ 30 ps. The high fidelity was achieved by applying a magnetic field parallel to the growth direction. The fidelity of the hole spin, prepared by ionisation of a photo-generated electron-hole pair in an electric field, was shown to be limited by the precession of the exciton spin due to the anisotropic exchange interaction.

- The preparation of a partially coherent superposition of hole spin states was demonstrated by the fast (10-100 ps) electric field induced dissociation of a spin-polarized electron-hole pair in a Voigt geometry magnetic field. The spin preparation was shown to be optimal when the precession of the neutral exciton and hole spin in the Voigt geometry magnetic field are synchronized. Long dephasing times of $T_2^* = 12 - 17.5$ ns were deduced for the hole spin, consistent with the expected weak hyperfine coupling for holes in InAs/GaAs quantum dots, and an order of magnitude longer than for the electron.

- Coherent optical control of a single hole spin confined to an InAs/GaAs quantum dot was demonstrated. A superposition of hole spin states was created by fast (10-100 ps) dissociation of a spin-polarized electron-hole pair. Full control of the hole-spin was achieved by combining coherent rotations about two axes: Larmor precession of the hole-spin about an external Voigt geometry magnetic field, and rotation about the optical axis due to the geometric phase shift induced by a picosecond laser pulse resonant with the hole-trion transition.

To summarise, the results presented in this thesis demonstrate that a hole spin trapped in a self assembled quantum dot is a potential qubit. The spin state can be initialised with high fidelity, controlled coherently to an arbitrary position on the surface of the Bloch sphere, and readout using picosecond optical laser pulses. Combined with the potential for scalability, and integration within an on chip device, the results show that the coherent optical manipulation of a hole spin state may provide a path for realising quantum information processing.

7.2 Future work

Ideas for future experiments are as follows.

7.2.1 AC-Stark shift

Optical rotation of the hole spin can be considered in two regimes. Spin rotations by angles of up to π can be achieved by using (near) resonant excitation and pulse area 2π, while spin rotations by angles beyond π require higher intensity pulses that are far detuned. The former is the geometric phase shift, which was implemented in the experiments described in chapter 6 of this thesis, and the latter is the AC-Stark shift. One of the reasons that AC stark shift approach was not taken in this thesis, was because of a lack of available power from the laser.

The maximum available power for the control pulse used in the experiments was in fact only just enough for a 2π pulse. This was mainly due to losses in power as a result of splitting and recombining the laser beams. It would be possible to achieve more power if some of the optics constructed were simplified, by making use of custom-made fiber beamsplitters. Furthermore, higher laser power could be obtained by better mode matching of the free space Gaussian beams to the modes of the fibres. This could be done by using cylindrical lenses in the pulse shapers. Alternatively, an additional mode locked Ti:Sapphire laser would also do the job.

In order to implement the AC-Stark shift, it would be necessary to find devices with lower background photocurrent. The background photocurrent is proportional to the incident laser power, but its gradient strongly depends on the dot density, the aperture size, and the reflectivity of the aluminium shadow mask. Therefore, devices with lower background signal could be fabricated by optimising these parameters. Therefore, by increasing the laser power, and by designing devices with lower background photocurrent, the AC-Stark shift experiments might be feasible.

7.2.2 Optical rotations about arbitrary axes

One of the limitations of using the precession of the hole spin as an axis of rotation, is that it is limited by the in-plane hole g-factor, and the necessity that the Zeeman energy is small compared to the control laser bandwidth. This makes the precession about the magnetic in the field in the x-direction inherently slow. In the proposals of Economou *et al*, the polarisation of the control pulse allows for optical rotations about the x-axis via the geometric phase shift [87], [88]. A linearly-polarised control pulse, drives Rabi oscillations for *both* hole spin states. Each spin state acquires a phase which depends on the detuning, and the difference in phase shift gives a rotation about the x-axis. Furthermore, the relative phase shift can also be controlled by varying the degree of ellipticity of the control pulse. Therefore, rotations about any arbitrary axes could be achieved by using combinations of rotations about the x and z axis. This would allow for rotations of the Bloch vector on a ps timescale, as opposed to the much slower spin precession, which is limited by the Zeeman energy splitting between the hole spin states.

7.2.3 Magnetic field dependence of the hole spin dephasing time

Simulations by Fischer *et al* suggest that the hole spin coherence time depends strongly on the strength of the magnetic field [13]. Despite this, De Greve *et al* showed no measurable dependence of the hole spin dephasing time with in-plane magnetic field. The authors attributed this to the fact that the hole spin dephasing time measured in their system was not limited by nuclear magnetic field fluctations [17]. However, given the anisotropic nature of the hyperfine interaction, it would be interesting to measure the decay of the spin precession as a function of applied magnetic field using the sample studied in the experiments of this thesis.

7.2.4 Temperature dependence of the hole spin dephasing time

The hole spin dephasing time is limited by the hyperfine interaction time at low temperatures. However, it would be interesting to study the effects of decoherence due to spin relaxation as a result of phonon scattering. This would indicate the relative importance of decoherence due to spin relaxation and nuclear field fluctuations. This could be implemented by measuring the decay of the hole spin precession as a function of temperature, and extrapolating to $T \sim 0$ K.

7.2.5 Fidelity of spin preparation in the Voigt geometry

The hole spin preparation fidelity in the Voigt geometry is quite poor, less than 75%. In the appendix of chapter 5, we saw how this was a result of the frequency mismatch between the neutral exciton fine structure and hole Zeeman energies, combined with the uncertainty of the electron tunneling time and finite mixing of the bright-dark neutral excitons. It would be interesting to test the model more rigorously, by comparing the spin preparation constrast for dots with different electron tunneling rates, g-factors and neutral exciton fine-structure splittings.

7.2.6 Preparing the hole into an energy eigenstate of the system

It would be interesting to investigate the use of a linearly-polarised preparation pulse to prepare the neutral exciton in an energy eigenstate of the system. The question is, how would this affect the fidelity of the spin preparation? The experimental procedure to implement this would require two control pulses, with variable time delay, which both perform rotations of angles of $\pi/2$. The linearly polarised preparation pulse would first prepare a hole in an energy eigenstate. The first control pulse would rotate the spin by an angle $\pi/2$ to a direction parallel to the optical axis, and perpendicular to the magnetic field. The spin would then begin to precess. Finally, the second control pulse would rotate the spin state, either back to the original eigenstate, or the opposite one, depending on the phase.

By making use of eqns A.8 and A.9 in section A.6, it can easily be shown that a linearly-polarised preparation pulse prepares the exciton wavefunction:

$$|\psi_0\rangle = \alpha\,|{\Uparrow}{\downarrow}\rangle + \alpha\,|{\Downarrow}{\uparrow}\rangle + \beta\,|{\Uparrow}{\uparrow}\rangle + \beta\,|{\Downarrow}{\downarrow}\rangle\,. \tag{7.1}$$

The dark exciton components are small, because they are determined by the mixing angle θ, i.e. $\beta \approx \sin(\theta)$. Therefore, for small magnetic fields, we can neglect excitons withs spin $S_z = \pm 2$, and eqn 7.1 simplifies to:

$$|\psi_0\rangle = \frac{1}{\sqrt{2}}\,|{\Uparrow}{\downarrow}\rangle + |{\Downarrow}{\uparrow}\rangle\,. \tag{7.2}$$

Eqn 7.2 is an entangled state of the electron and hole. Therefore, the preparation of this exciton state may result in a mixed hole spin state. This is because the electron and hole wavefunctions are non-separable, and therefore the electron tunneling scrambles any fixed phase relationship in the superposition. However, it would be interesting to see if this is the case. The question is, does the incoherent tunelling of the electron out of the dot collapse the wavefunction of the hole spin?

7.2.7 Improving the hole lifetime: voltage modulation

One of the main disadvantages of the photocurrent detection technique is the short hole lifetime, which ultimately limits the coherence time. The hole lifetime is typically on the order of a few ns at a moderate applied bias. The electric field cannot be simply reduced because of the necessity that the dot be empty on the arrival of the next pulse sequence. Furthermore, the detection efficiency drops off rapidly with decreasing electric field. However, a simple solution is to modulate the bias applied to the photodiode. Some preliminary work on adding an AC component to the DC bias has been carried out as part of the masters thesis of R. Coles [80]. There, Coles *et al.*, showed an improved photocurrent detection efficiency which enabled the application of a lower DC bias. The basic idea is to apply a AC electric field to the device such that the electric field is high for preparation and detection, and low for the rest of the experiment. The AC field has a sine waveform and a period equal to the repetition period of the laser source. The tunneling rates of the electron and hole are then determined by the phase and amplitude of the AC field. AC voltage modulation has been used in Schottky diodes in the work of Vasconcellos *et al.* that demonstrates coherent electrical control of exciton qubits [62]. It should be possible to obtain longer hole lifetimes, using similar techniques. Pulse picking could then be implemented in order to measure the hole spin dephasing time well beyond the 13 ns time duration between un-modulated laser pulses. This could potentially enable measurements of the intrinsic decoherence time of the hole spin, by making use of spin-echo techniques.

7.2.8 Quantum dot molecules

Universal control of quantum bits requires both single and two-qubit phase gates. Two-qubit phase gates can be implemented by making use of quantum dot molecules. Coherent control of both one and two hole spins in quantum dot molecules has been achieved in the work of Greilich *et al.* [18]. Other work on quantum dot molecular structures includes that of Vamivakas *et al.* [68]. There, Vamivakas *et al.* demonstrated non-destructive measurements of electron spins in real time [68]. It is not exactly clear whether or not a photocurrent detection would be useful for the study of quantum dot molecules, because electric fields are used to tune the quantum dots into resonance, and this may present difficulties for measurements in the photocurrent regime. Furthermore, the spin preparation technique, via exciton ionisation, may have to be reconsidered because it may be hard to load both dots with a single hole spin simultaneously. Nonetheless, it would be interesting to perform photoluminescence spectroscopy on quantum dot molecules to fully characterise the states under different bias regimes. Studies of the neutral exciton could then provide a starting point for photocurrent detection.

Appendix A

Chapter 5 - Appendices

This appendix describes the background work that was carried out for the experiments in chapter 5. For example, the model for the hole spin preparation fidelity is formulated section A.6. The model calculations in chapter 5, sections 5.4.3 and 5.4.4, use various parameters that were measured in the experiments. These include the mixing angle between bright and dark excitons $\theta(B)$, the neutral exciton effective fine structure splitting $\Delta E_{\mathrm{bb}}(B)$, and the electron and hole tunneling rates as a function of magnetic field and applied bias $\Gamma_{\mathrm{e}}(B, V_{\mathrm{bias}})$, and $\Gamma_{\mathrm{h}}(B, V_{\mathrm{bias}})$. The measurements of these parameters can be found in this section.

A.1 Single-pulse photocurrent spectra of a neutral exciton in a Voigt geometry magnetic field

Single pulse spectra of the neutral exciton X^0 were measured at each magnetic field to determine the optical frequency to be used for the preparation pulse in the two-pulse measurements of the hole spin precession. Figure A.1 shows example photocurrent spectra for single pulse measurements with and without an applied Voigt geometry magnetic field. The spectra were taken by tuning a laser pulse with circular polarisation, and pulse-area $\Theta = \pi$, through the neutral exciton resonance

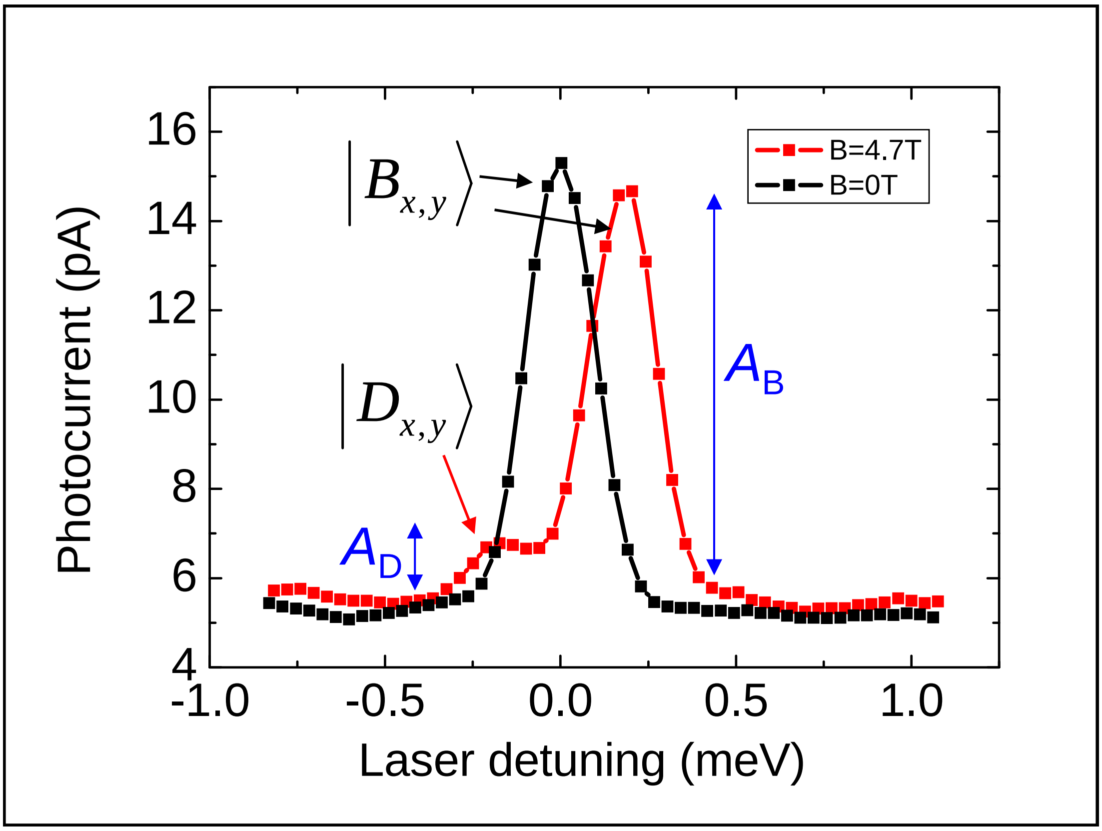

Figure A.1: *Single pulse measurement of the neutral exciton with zero applied magnetic field (black), and an applied magnetic field (red) in the Voigt geometry. A single neutral exciton peak was observed for $B = 0$ T. With the applied magnetic field, the peak was blue-shifted, due to the diamagnetic shift. Furthermore, an additional peak appeared at negative detuning and is labelled $D_{x,y}$. This is the dark exciton. The single pulse measurements were taken in order to determine the frequency to be used for the preparation pulse, and to determine the mixing angle between bright and dark excitons*

and measuring the change in photocurrent. Without an applied magnetic field, a single peak was observed; this is the bright neutral exciton labelled $|B\rangle$. With an applied magnetic field, a second peak with a smaller amplitude was present at a detuning ~ -0.34 meV from the more prominent peak. This peak was attributed to the dark exciton labelled $|D\rangle$. The pulse width was greater than than the energy splittings between $|B_{\mathrm{x}}\rangle$ and $|B_{\mathrm{y}}\rangle$ and $|D_{\mathrm{x}}\rangle$ and $|D_{\mathrm{y}}\rangle$. Therefore, it was not possible to resolve each of the four states $|M| = -2, -1, +1, +2$.

Figure A.2 shows the diamagnetic shift of the bright exciton in the applied magnetic field. The two fits to the data were made using the functions $E = S + CB + DB^2$ and $E = S + D'B^2$ in order to estimate the strength of the shift using the fitting parameters $D = (4.0 \pm 1)\ \mu\text{eVT}^{-2}$ or $D' = (5.6 \pm 0.3)\ \mu\text{eVT}^{-2}$. These

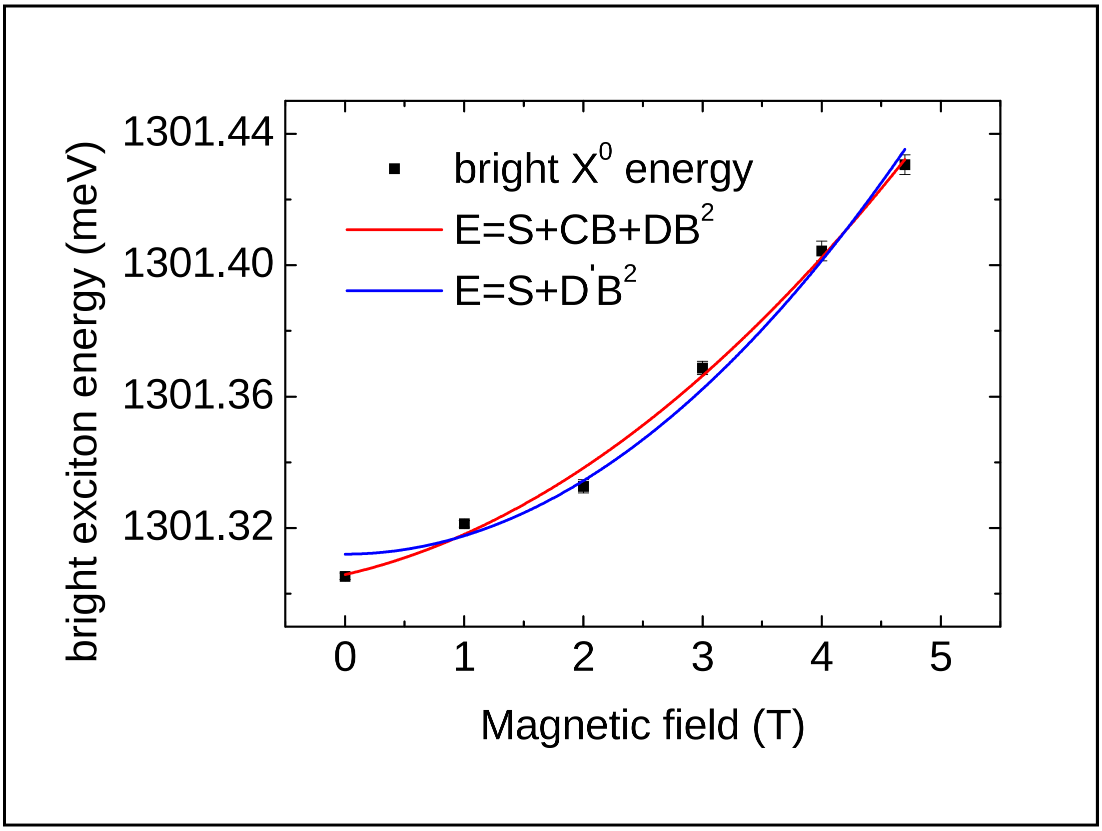

Figure A.2: *Bright neutral exciton resonance energy as a function of applied magnetic field*

values allowed for a calculation of the extent of the neutral exciton wavefunction using the function $r = \sqrt{\frac{8\mu D}{e^2}}$ [106] (assuming spherical symmetry). Here μ is the exciton effective mass $1/\mu = 1/m_{\mathrm{e}}^* + 1/m_{\mathrm{h}}^*$. The radius $r = 3.5$nm was calculated using the value $D' = 5.6$. This is in excellent agreement with the size of the wavefunction measured using the intensity damping of Rabi rotations for similar dots $\sim (3-5)$ nm [64].

A.2 Estimation of the bright-dark exciton mixing angle

A mixing angle θ can be used to characterise the strength of mixing between the bright and dark excitons in a Voigt geometry magnetic field. More details of this can be found in section A.6 with reference to eqn A.9. The ratio of the peak amplitudes for the dark and bright exciton, $A_\mathrm{D}/A_\mathrm{B}$, can be used to estimate a mixing angle between. The peak amplitudes are illustrated by the blue arrows in Fig. A.1. $A_\mathrm{D}/A_\mathrm{B}$ is plotted as a function of applied magnetic field in Fig. A.3. It was not possible to resolve the dark exciton for magnetic fields $B < 3$T, because the dark exciton signal was too weak. Furthermore, it was not possible to determine the absolute individual values of the mixing angles θ_x and θ_y, since only two of the possible four peaks were present. Therefore, an average mixing angle θ was calculated from the data in Fig. A.3. The mixing angle θ is given by:

$$\frac{A_\mathrm{D}}{A_\mathrm{B}} = \frac{\sin^2(\theta)}{\cos^2(\theta)} \approx (aB)^2, \tag{A.1}$$

which yields a value of $a = (0.085 \pm 0.01)$ T^{-1}. The ratio of the peak heights at $B = 4.7$ T is $A_\mathrm{D}/A_\mathrm{B} = 0.15$. This gives a mixing angle of 0.4 radians or 23°. This is in close agreement to values of $A_\mathrm{D}/A_\mathrm{B} = 0.15$ measured for similar dots using photoluminescence spectroscopy [23], [27], [25]. The parameter a was used to determine the bright/dark mixing strength at a particular magnetic field, and was used for calculations of the spin preparation contrast in sections 5.4.3 and 5.4.4.

A.3 Bright-dark exciton exchange energy

Figure A.4 is an energy level diagram that shows the various exchange energy splittings of the neutral exciton δ_0, δ_1 and δ_2 in a Voigt geometry magnetic field. The energy splitting between the states labelled $|B\rangle$, and $|D\rangle$ in Fig. A.1, can be used to estimate the exchange energy δ_0. δ_0 is the splitting between bright and dark excitons at zero magnetic field. For each magnetic field, a Gaussian fit was made to both the bright and dark photocurrent peaks, in order to determine the energy splitting between the states. The results are presented in Fig. A.5. The various coloured data points in Fig. A.5 are repeat measurements using $\sigma^\pm$ excitation. The red line is a calculation of the energy splitting, using the following energies extracted

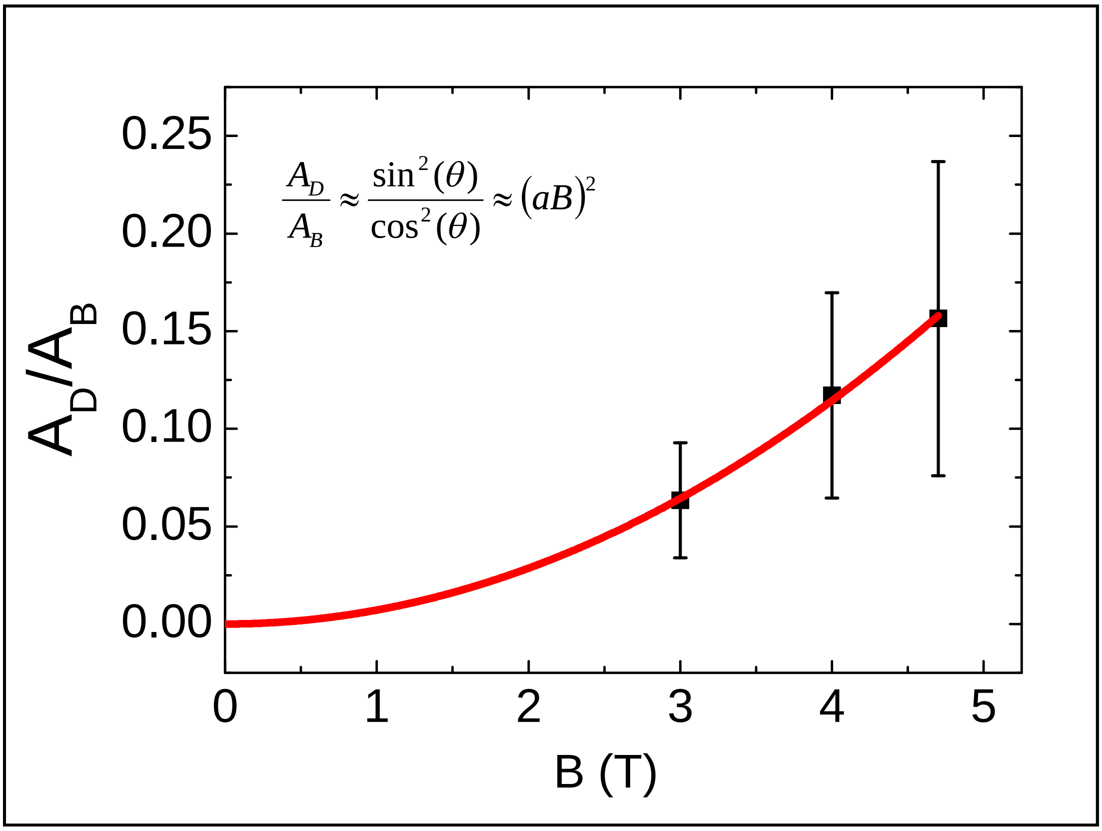

Figure A.3: *The ratio of the peak heights for the dark and bright excitons, A_{D} and A_{B}, is plotted as a function of magnetic field. This is done in order to estimate the mixing angle between the bright and dark states. The dark peak can't be resolved for magnetic fields $B < 3$ T. The solid red line is a fit to eqn A.1, which allows the mixing strength parameter a to be determined. The mixing causes a reduction in the maximum possible hole spin preparation fidelity, as discussed in section A.6*

from reference [23],

$$\begin{aligned}
&+\frac{1}{4}\left[+(\delta_1+\delta_2)+\sqrt{(2\delta_0+\delta_1-\delta_2)^2+4(g_{\mathrm{e}}-g_{\mathrm{h}})^2\mu_{\mathrm{B}}^2B^2)}\right]\\
&+\frac{1}{4}\left[-(\delta_1+\delta_2)+\sqrt{(2\delta_0-\delta_1+\delta_2)^2+4(g_{\mathrm{e}}+g_{\mathrm{h}})^2\mu_{\mathrm{B}}^2B^2)}\right]\\
&-\frac{1}{4}\left[-(\delta_1+\delta_2)+\sqrt{(2\delta_0+\delta_1-\delta_2)^2+4(g_{\mathrm{e}}-g_{\mathrm{h}})^2\mu_{\mathrm{B}}^2B^2)}\right]\\
&-\frac{1}{4}\left[+(\delta_1+\delta_2)+\sqrt{(2\delta_0-\delta_1+\delta_2)^2+4(g_{\mathrm{e}}+g_{\mathrm{h}})^2\mu_{\mathrm{B}}^2B^2)}\right],
\end{aligned} \tag{A.2}$$

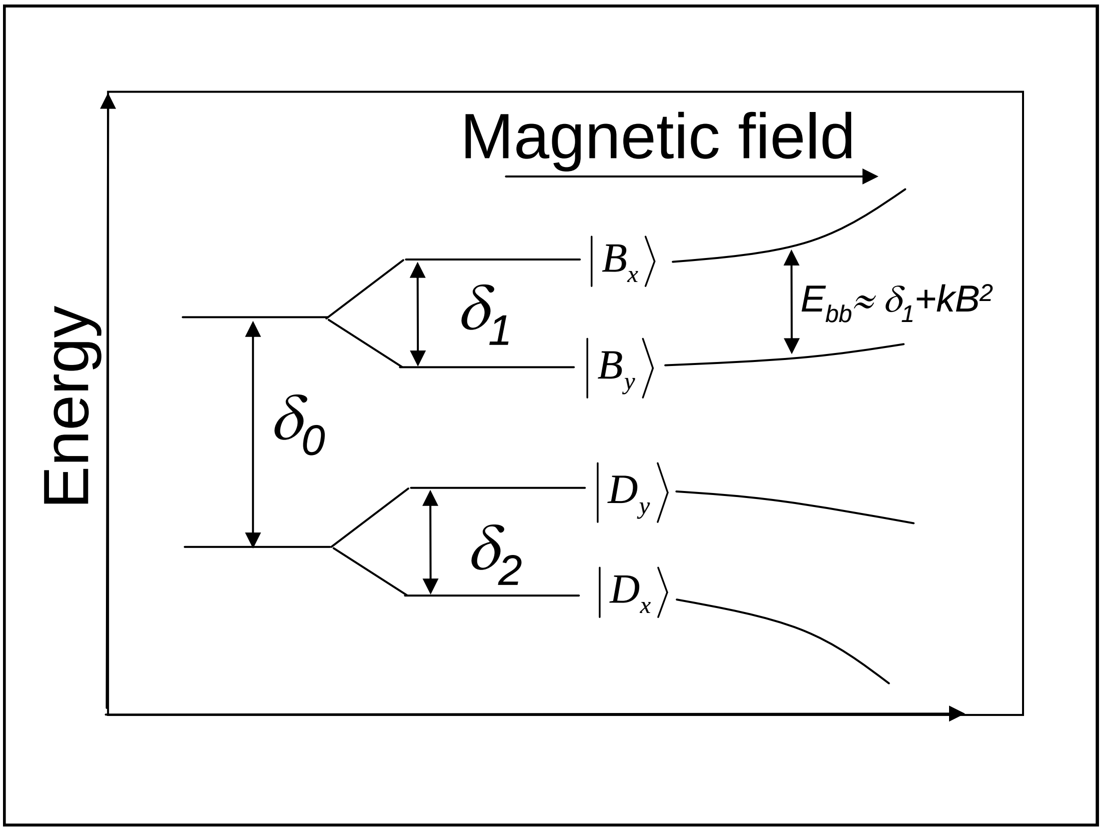

Figure A.4: *In a Voigt geometry magnetic field, the reduced rotational symmetry in plane, results in the mixing of bright exciton states with* $|M| = \pm 1$ *with the dark exciton states with* $|M| = \pm 2$*. The resulting states are labelled* $|B_\alpha\rangle$ *bright and* $|D_\alpha\rangle$ *for dark, where* $\alpha = x, y$*. The magnetic field mixes the bright state* $|B_x\rangle$ *with the dark state* $|D_x\rangle$ *and the bright state* $|B_y\rangle$ *with the dark state* $|D_y\rangle$*. The states are split by the exchange energies,* $\delta_0, \delta_1, \delta_2$*, which give rise to fine-structure splittings between the bright/dark, bright-bright and dark-dark states respectively.*

for the eigenstates [23]:

$$\begin{gathered} N_1\left[|B_y\rangle + \alpha(|D_y\rangle)\right] \\ N_1\left[|B_x\rangle + \alpha(|D_x\rangle)\right] \\ N_1\left[|D_y\rangle + \alpha(|B_y\rangle)\right] \\ N_1\left[|D_x\rangle + \alpha(|B_x\rangle)\right] \qquad \text{(A.3)} \end{gathered}$$

respectively.

The data in Fig. A.5 show little or no increase in the splitting with increasing magnetic field. This implies that the Zeeman energy splitting had a small contribution relative to the exchange energy splitting at zero magnetic field δ_0. The relatively large mixing seen in Fig. A.3 suggest that the Zeeman energy contribution is strong, which is in contradiction with the bright/dark splitting data of Fig. A.5.

One possible explanation is that the observed weak magnetic field dependence of the bright/dark splitting was due to a nuclear spin pumping effect. It is postulated that the bright exciton, which has a large dipole and large absorption, more efficiently pumps nuclear spins. This may cause a reduction or cancellation [107] of the Zeeman energy terms of eqns A.2. By contrast, the dark exciton with less absorption, pumps the nuclear spin bath at a lower rate, and the Zeeman terms are large and unaffected. This effect would give strong bright/dark mixing, without a strong bright/dark Zeeman splitting. However, due to the lack of data points, and large fitting errors in Figs A.5 and A.3, it is difficult to reach conclusions without further investigation.

The average energies of the bright and dark states were used to calculate the red line in Fig. A.5. This was done using the mean values of the energies in A.2, since was not possible to resolve all four individual states. The calculation used the following values: the bright/bright fine structure splitting at zero magnetic field measured in section A.4, $\delta_1 = 16.5\ \mu$eV, and the electron and hole in-plane g-factors $g_\mathrm{e} = 0.466 \pm 0.02$ and $g_\mathrm{h} = 0.079 \pm 0.004$, as determined by experiment (in sections 6.3.1 and 5.4.2 respectively). The dark/dark fine-structure splitting δ_2 was assumed to be negligible compared to δ_1 and δ_0 [23], [108], [109], [44]. A value of $\delta_0 \sim 0.3$ meV was obtained, in agreement with literature values [23], [44], [27].

A.4 Neutral exciton effective fine-structure splitting

The splitting between bright neutral excitons in the Voigt geometry magnetic field is estimated by [27]:

$$\Delta E_{bb} \approx \delta_1 + KB^2$$

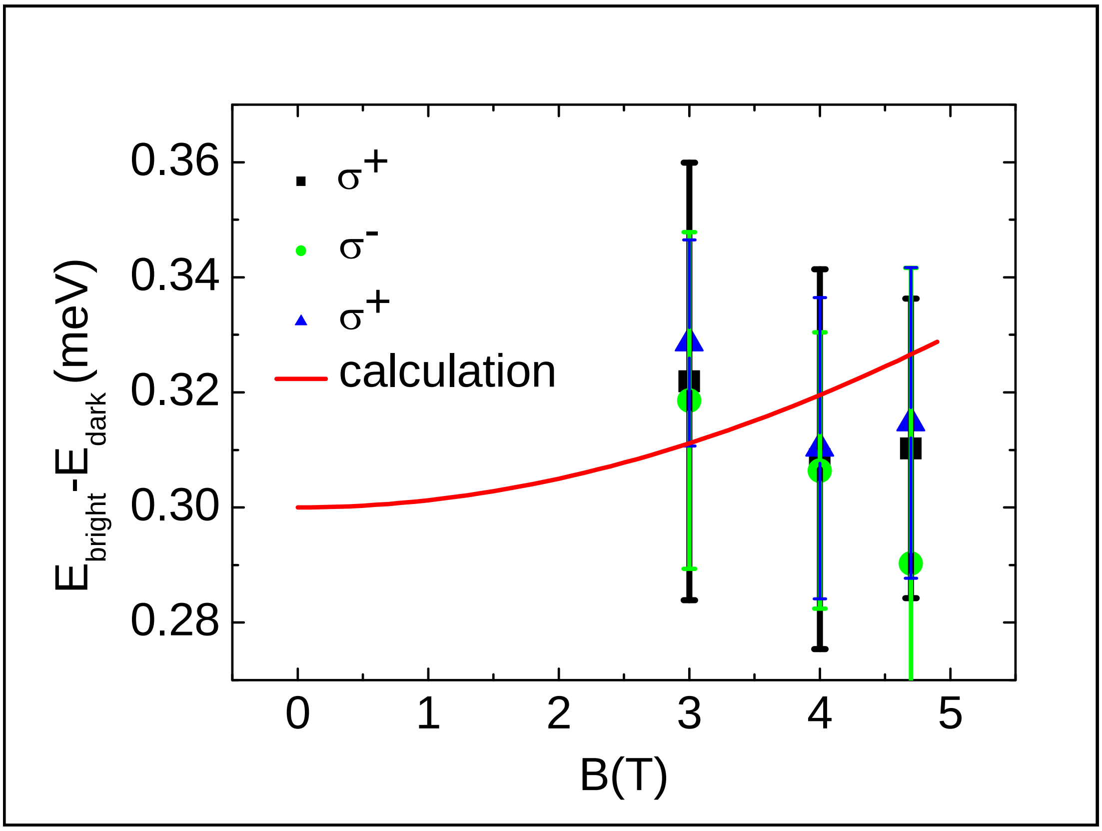

Figure A.5: *Splitting between bright and dark excitons as a function of applied magnetic field. The dark exciton peak can't be resolved for magnetic fields* $B < 3$ T*. The different coloured data points are for different polarisations and different arms in the experimental setup (repeat measurements). The spectral width of the excitation laser pulse was on a similar order to the splittings and this resulted in a large uncertainty in the the peak positions as determined by the Gaussian fitting. The solid red line is a calculation of the expected energy splitting according to eqns A.2, where a value of* $\hbar\delta_0 = 0.3$ meV *has been used for the bright-dark exchange energy at zero magnetic field.*

where

$$K = -\frac{\mu_B^2}{\delta_0(1 - (\frac{\delta_1 - \delta_2}{2\delta_0})^2)}[g_{ex}g_{hx} + \frac{\delta_1 - \delta_2}{4\delta_0}(g_{ex}^2 + g_{hx}^2)] \tag{A.4}$$

It was not possible to measure the bright-bright fine-structure splitting ΔE_{bb} directly from spectral measurements, since the spectral width of the laser pulse was large compared to ΔE_{bb}. However, it was possible to measure ΔE_{bb} using two-pulse time-resolved measurements of the neutral exciton beat in the Voigt geometry. The method for which was outlined in the methods chapter section 3.7.3. As a reminder, the basic idea is to measure the photocurrent as a function of time delay between two laser pulses, which are both resonant with the neutral exciton transition, and have co/cross circular polarisation and pulse area $\Theta = \pi$.

The effective fine-structure splitting energy of the neutral exciton ΔE_{bb} can be extracted by fitting the difference in photocurrent (PC) for cross polarised pulses and co-polarised pulses $PC_{+-} - PC_{++}$ to eqn A.5 [96]:

$$PC_{+-} - PC_{++} = e\nu\eta f(\rho_{\uparrow\uparrow}(\tau) - \rho_{\downarrow\downarrow}(\tau)) = A\exp(-\Gamma_e\tau)\cos(\Delta E_{\mathrm{bb}}\tau/\hbar) \qquad \text{(A.5)}$$

Here, e is the electron charge, ν is the pulse repetition frequency, η the detection efficiency and $\rho_{\uparrow\uparrow}$, and $\rho_{\downarrow\downarrow}$ are the probabilities that the exciton is in the spin up/down state respectively. For time delays $\Delta\tau_{\mathrm{D}} \ll \tau_{\mathrm{h}}$, the decay rate of the $|X^0\rangle$ state is $\Gamma_{X^0} \approx \Gamma_e$, where Γ_e is the electron tunneling rate.

Figure A.6 shows an example measurement of the fine-structure neutral exciton beat with an applied magnetic field $B = 4$ T. The data plotted is $PC_{+-} - PC_{++}$ fit to an exponentially decaying cosine [96] according to eqn A.5. A tunelling rate for the electron $\Gamma_{\mathrm{e}} = 1/105$ ps^{-1} was used and the extracted beat period was found to be $\tau_{bb} = 224$ ps.

The beating of the neutral exciton was measured at each magnetic field. Figure A.7 shows ΔE_{bb} as a function of the in-plane magnetic field. For some of the magnetic fields, the data was noisy and the beat period was estimated (without fitting), which results in large error bars $\sim 20\%$. Nonetheless, a clear rise in ΔE_{bb} was observed with increasing magnetic field.

The data in Fig. A.7 was fit to the function $\Delta E_{\mathrm{BB}} = \delta_1 + KB^2$, in line with the theory of eqn A.11. The fitting parameters $\delta_1 = (16.5 \pm 0.5)$ μeV and $K = (0.130 \pm 0.004)$ μeVT^{-2} were extracted from the fit. The value for K is small, but in agreement with literature values for InAs/GaAs quantum dots [27]. The energy splitting ΔE_{bb} causes a reduction in the maximum possible obtainable hole spin preparation fidelity, since it results in a partial mixing of the spin. The partial mixing is a result of the frequency mismatch between ΔE_{bb} and the hole spin precession energy $\hbar\omega_{\mathrm{h}} = g_{\mathrm{h}}\mu_{\mathrm{B}}B$, combined with the uncertainty in the electron tunneling time. This can be seen with inspection to eqn A.27 and with reference to figs 5.13 and 5.14.

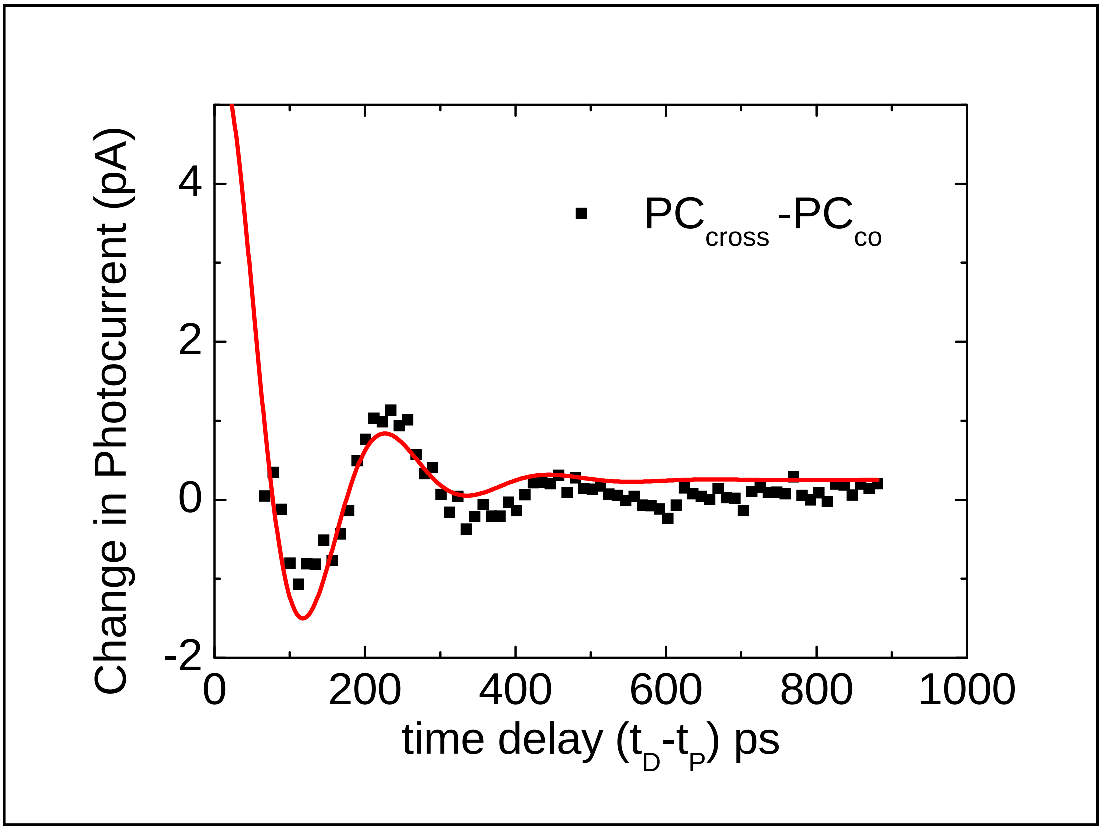

Figure A.6: *. Time-resolved measurement of the effective bright-bright fine-structure splitting ΔE_{bb} in a magnetic field $B = 4$ T. The photocurrent oscillates as a result of the beat of the exciton due to the energy splitting ΔE_{bb}. The solid red line is a fit to extract the frequency of the oscillation. The beating of the neutral exciton state results in a reduction in the maximum obtainable fidelity of the hole spin preparation.*

A.5 Measurements of carrier tunneling rates

The electron and hole tunneling rates were important parameters in the experiments. The electron tunneling rate limits the hole spin preparation fidelity and speed. The hole tunneling rate ultimately limits the coherence time of the hole spin qubit. It is possible to infer the electron and hole tunneling rates, Γ_{e} and Γ_{h}, from the two-pulse measurements of the charged exciton amplitude. Figure A.8 shows a typical measurement of the hole spin precession with an applied magnetic field $B = 4.7$ T and a gate voltage $V_{\mathrm{bias}} = -0.96V$. The preparation pulse, with pulse area $\Theta = \pi$, and circular polarisation, was resonant with the neutral exciton X^0. The detection pulse, with $\Theta = \pi$ and co or cross circular polarisation, was resonant with the charged exciton X^+. The change in photocurrent was measured as the detection

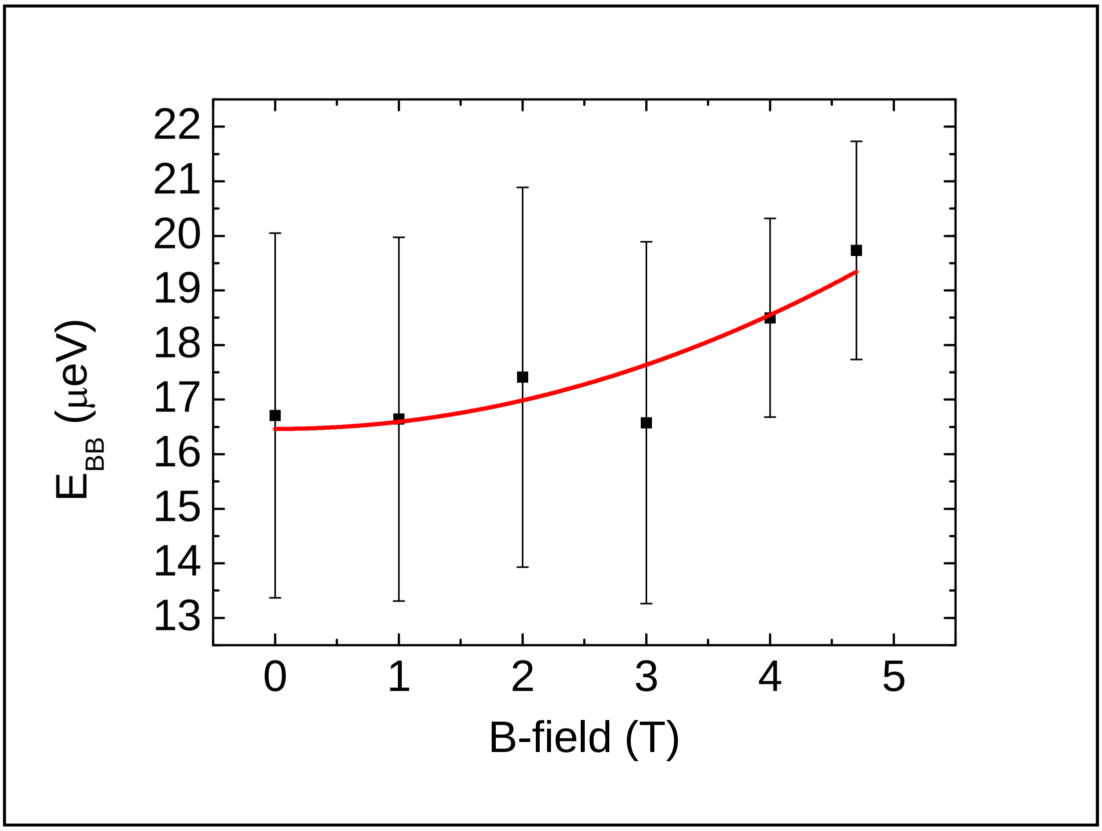

Figure A.7: *. Bright-bright energy splitting of the neutral exciton ΔE_{bb} as a function of applied magnetic field. The energy splitting at each magnetic-field is found using a two-pulse time-resolved measurement of the beat of the neutral exciton, an example of which can be found in fig. A.6. The solid red line is a fit to the function $\Delta E_{\mathrm{BB}} = \delta_1 + KB^2$ according to eqn A.11, where the fitting parameter $K = 0.13 \pm 0.03\mu\mathrm{eVT}^{-2}$ was extracted.*

pulse was tuned through resonance with the X^+. The amplitudes of the charged exciton for co-polarised (PC_{++}) and cross-polarised circular excitation (PC_{+-}) are plotted as a function of time delay in Fig. A.8. The sum of these two components $PC_{+-} + PC_{++}$ is plotted with pink data points in Fig. A.8. Initially $PC_{+-} + PC_{++}$ increases as the neutral exciton X^0 decays by electron tunneling before reaching a maximum. $PC_{+-} + PC_{++}$ then decays as the charged exciton X^+ decays by hole tunneling. Therefore, the sum $PC_{+-} + PC_{++}$ is proportional to the total hole state population. The pink data in Fig. A.8 can be used to determine the electron and hole tunneling rates $\Gamma_{\mathrm{e}} = 1/\tau_{\mathrm{e}}$ and $\Gamma_{\mathrm{h}} = 1/\tau_{\mathrm{h}}$ by fitting $PC_{+-} + PC_{++}$ to the following eqn A.6 [96], [6], [41].

$$\Delta PC_{\mathrm{total}} = A\left[(1 - e^{-\frac{\tau}{\tau_e}})e^{-\frac{\tau}{\tau_h}}\right] \tag{A.6}$$

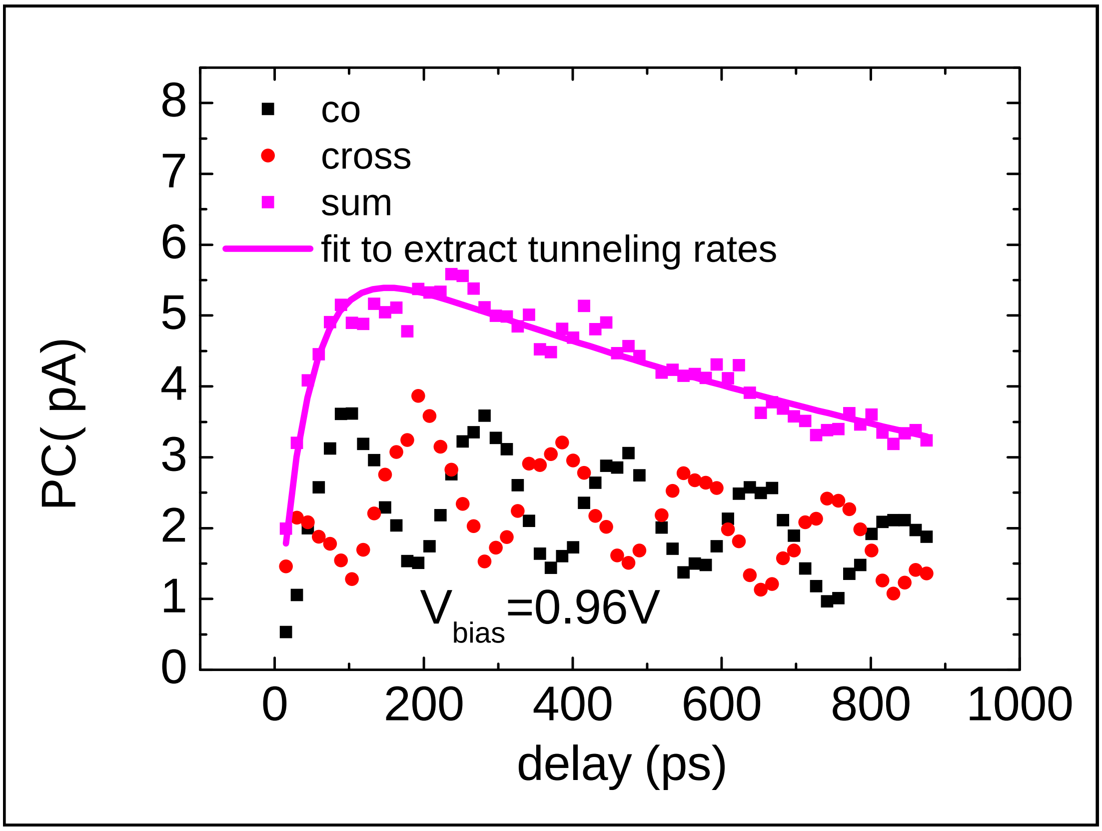

Figure A.8: *Red and black: photocurrent amplitude of X^+ for cross and co polarised preparation and detection. Pink: sum of the amplitudes (red+black). Solid pink: fit to eqn A.6*

A.5.1 Voltage dependence of carrier tunneling rates

The electron and hole tunneling rates at each voltage were found by fitting $PC_{+-} + PC_{++}$ to eqn A.6 as previously described. Figure A.9 and fig A.10 show the effect of the applied reverse bias on the tunneling rates. The built in voltage $\mathrm{V_{bi}} = 0.76$ V is taken to be half the GaAs band gap [5], [6]. The data is fit to eqn A.7 from reference [90]:

$$\Gamma_{\mathrm{e}} = \frac{\hbar\pi}{2m^*\mathrm{L}^2} \exp\left[\frac{-4}{3\hbar e\mathrm{F}}\sqrt{2m^* E_{\mathrm{I}}^3}\right] \tag{A.7}$$

Here, m^* is the effective mass, taken to be $m^* = 0.067m_{\mathrm{e}}$ for the electron, and $m_{\mathrm{h}} = 6m^*$ for the hole [90], L is the confinement potential width, $\mathrm{F} = (\mathrm{V} + \mathrm{V_{bi}})/\mathrm{d}$ the electric field, where $d = 230$nm is the distance between electrical contacts, and E_{I} is the effective ionisation energy.

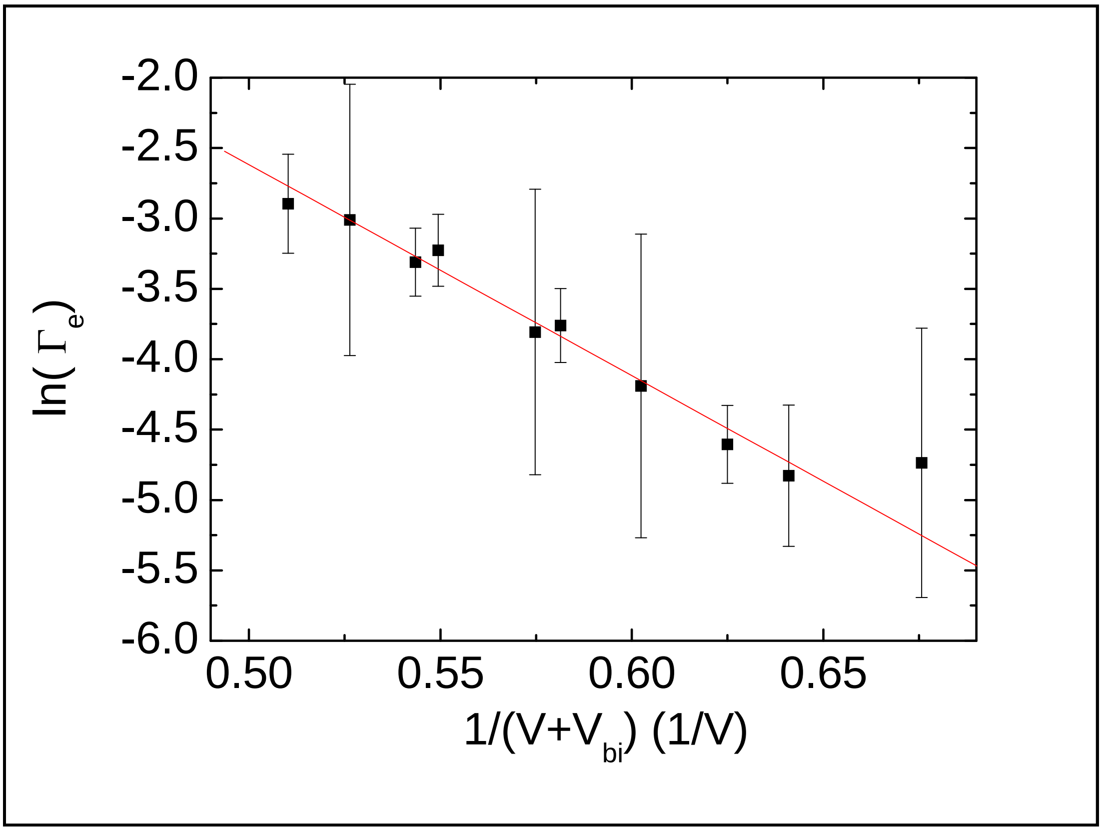

Figure A.9: *Electron tunneling rate as a function of applied reverse bias. A linear fit to the data using eqn A.7 allows for an estimate of the effective ionisation energy* $E_{\mathrm{I}} = 171 \pm 9\mathrm{meV}$ *and confinement potential width* $\mathrm{L} = 1.8 - 2.7\mathrm{nm}$ *[90]. This is consistent with the electric field dependence and values of* E_{I} *and L measured on similar devices [90], [5]. The fitting was done according to a linear function* $\ln \Gamma_{\mathrm{e}} = A + B/(V + V_{\mathrm{bi}})$*, where the constants* $A = 4.9 \pm 1.6$ *and* $B = 15.0 \pm 2.8$ *were extracted.*

A.5.2 Magnetic field dependence of electron tunneling rate

The electron and hole tunneling rates were measured as a function of applied (Voigt geometry) magnetic field. This was done using fits to eqn A.6 to the pink data in Fig. 5.7.

Figure A.11 shows the magnetic field dependence of the electron tunneling rate. The electron tunneling rate was found to increase with applied magnetic field. As the magnetic field is increased from zero to 4.7 T, the effective barrier thickness of the dot increases, due to the helical trajectory of a carrier moving parallel to the magnetic field [110]. This resulted in an increased electron tunneling time from 90-135 ps at a gate voltage of 0.8 V, as shown in Fig. A.11. The empirical fit in Fig. A.11 is of the form $\Gamma_{\mathrm{e}}(B) = \Gamma_{\mathrm{e}}(0) + kB^2$. Here $\Gamma_{\mathrm{e}}(0) = (0.01095 \pm 0.0002)\ \mathrm{ps}^{-1}$ is the

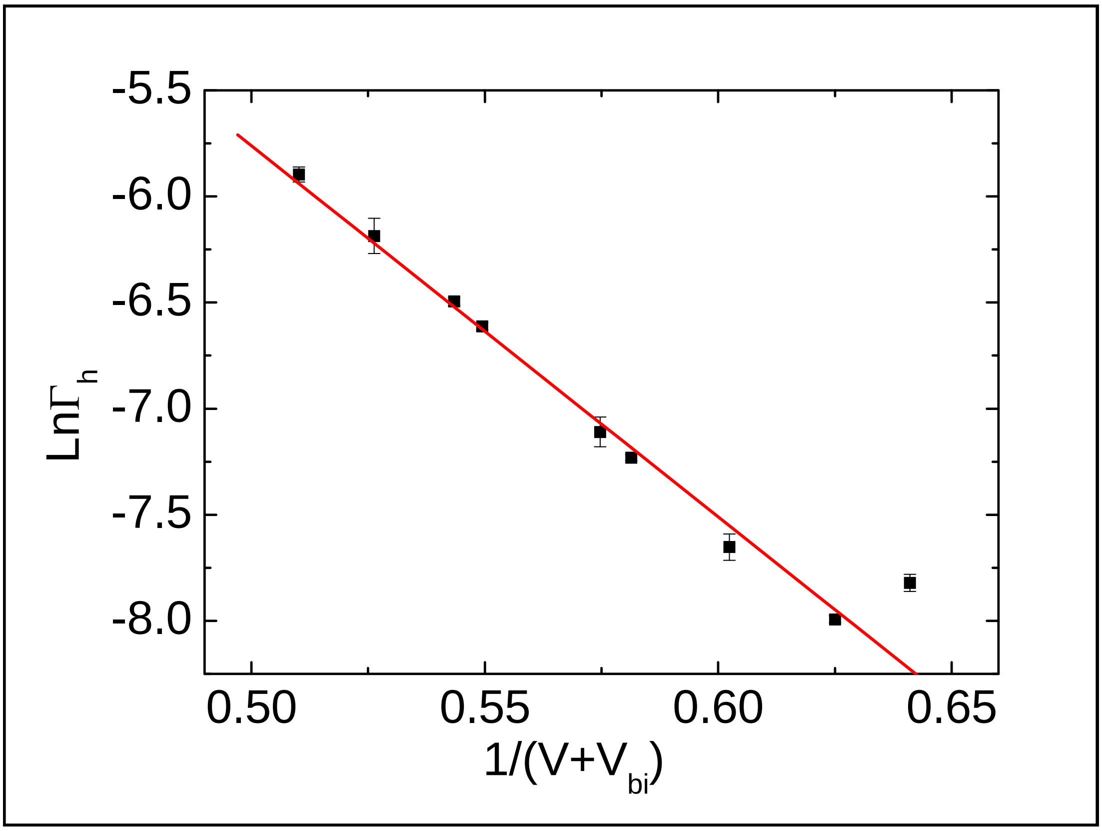

Figure A.10: *Hole tunneling rate as a function of applied reverse bias. A linear fit to the data using eqn A.7 allows for an estimate of the effective ionisation energy* $E_{\mathrm{I}} = 102 \pm 8\mathrm{meV}$ *under the applied electric field [90].*

tunneling rate at zero field, and $k = (-0.00013 \pm 0.00001)\ \mathrm{ps}^{-1}\mathrm{T}^{-2}$ is the curvature constant. This is consistent with an ionisation energy of 163 ± 12 meV [110]. The hole tunneling did not show a measurable trend with magnetic field. This might be because the extracted hole tunneling rates $\sim 1/3$ ns were much larger than the detection time delay ~ 1 ns. This resulted in an error in $\Delta\tau_{\mathrm{h}} \sim 20\%$, which may be larger than any magnetic field dependence.

A.6 Model of spin preparation

An analytical model of the spin preparation in the Voigt geometry was constructed in order to better understand what limits the spin contrast. The following model is an adaptation of the arguments presented for the Faraday geometry in chapter 4 section 4.4. To begin, we first consider the energy eigenstates of the prepared neutral

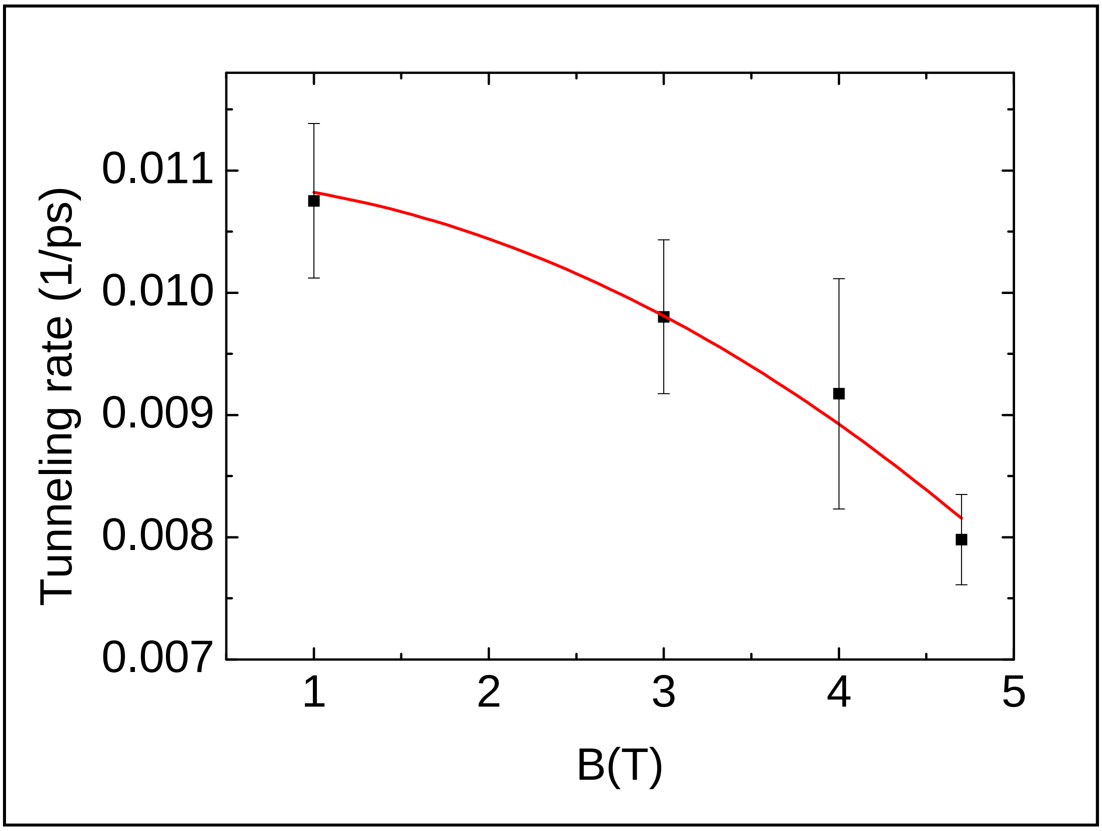

Figure A.11: *Electron tunneling rate as a function of applied magnetic field. The solid line is an empirical fit of the form* $\Gamma_{\mathrm{e}}(B) = \Gamma_{\mathrm{e}}(0) + kB^2$*, where* $\Gamma_{\mathrm{e}}(0) = (0.01095 \pm 0.0002)\ \mathrm{ps}^{-1}$ *is the tunneling rate at zero field. A curvature constant* $k = (-0.00013 \pm 0.00001)\mathrm{ps}^{-1}\mathrm{T}^{-2}$ *was extracted.*

exciton, and subsequently consider the evolution of the exciton spin state. A set of rate equations are constructed to map the decay of the neutral exciton states to the hole spin states. Finally an expression for the expected spin preparation fidelity and contrast is formulated.

A.6.1 Fidelity of spin preparation in a Voigt geometry magnetic-field

The neutral exciton states are constructed from the heavy spin states with $J_{\mathrm{h}} = \pm 3/2$ and the electron spin states of $S_{\mathrm{e}} = \pm 1/2$. From these single particle states, four exciton states, characterised by their angular momentum projections $|M| = J_{\mathrm{h}} + S_{\mathrm{e}}$, can be formed, namely $|M| = -2, -1, +1, +2$. In a Faraday geometry magnetic field, only the optically bright states are considered. Here, a photon with angular momentum $|M|\pm 1$ transfers one unit of angular momentum ($\hbar$) to create an optically bright exciton with $|M| = \pm 1$. The optically dark states with $|M| = \pm 2$ are not allowed due to conservation of angular momentum as confirmed by measurements [23]. In the Voigt geometry magnetic field, the story is different. The application of a magnetic field in the sample plane (x) direction results in a mixing of the bright and dark states and all four exciton $|M| = -2, -1, +1, +2$ states are observable [23] [25]. The mixing is a result of the reduced symmetry of the quantum dot under the application of the in-plane magnetic field and is characterised by the exchange interaction energy splittings namely δ_0, δ_1 and δ_2. Figure A.4 is a schematic energy level diagram showing the states labelled $|B_x\rangle$, $|B_y\rangle$, $|D_x\rangle$ and $|D_y\rangle$. The states are labelled B for bright and D for dark, and the subscripts indicate the polarisation x or y. The bright and dark states may be written as superpositions of the electron and hole spins in the growth direction z, $\downarrow, \uparrow$ and $\Downarrow, \Uparrow$:

$$\begin{aligned}
|B_x\rangle &= \frac{1}{\sqrt{2}}\left(|\Uparrow\downarrow\rangle + |\Downarrow\uparrow\rangle\right) \\
|B_y\rangle &= \frac{1}{\sqrt{2}}\left(|\Uparrow\downarrow\rangle - |\Downarrow\uparrow\rangle\right) \\
|D_x\rangle &= \frac{1}{\sqrt{2}}\left(|\Uparrow\uparrow\rangle + |\Downarrow\downarrow\rangle\right) \\
|D_y\rangle &= \frac{1}{\sqrt{2}}\left(|\Uparrow\uparrow\rangle - |\Downarrow\downarrow\rangle\right).
\end{aligned} \tag{A.8}$$

The diagonalised Hamiltonian for the neutral exciton in the in-plane magnetic field in the basis $\{|B_x\rangle, |D_x\rangle, |B_y\rangle, |D_y\rangle\}$ may be written [23]:

$$H^0 = \frac{1}{2}\begin{pmatrix} \delta_0 + \delta_1 & g_{\mathrm{e,x}} + g_{\mathrm{h,x}} & 0 & 0 \\ g_{\mathrm{e,x}} + g_{\mathrm{h,x}} & -\delta_0 - \delta_2 & 0 & 0 \\ 0 & 0 & \delta_0 - \delta_1 & g_{\mathrm{e,x}} - g_{\mathrm{h,x}} \\ 0 & 0 & g_{\mathrm{e,x}} - g_{\mathrm{h,x}} & -\delta_0 + \delta_2 \end{pmatrix}$$

. Here δ_0, δ_1, δ_2 are the exchange energies, which give rise to fine-structure splittings between the bright/dark, bright-bright and dark-dark states respectively, and $g_{\mathrm{e,x}}$ and $g_{\mathrm{h,x}}$ are the in-plane g-factors of the electron and heavy-hole respectively.

Figure A.4 shows the various exchange energies in this geometry. The energy eigenstates of H^0 may be written [23]

$$\begin{aligned} |\psi_x(B)\rangle &= \cos\theta_x\,|B_x\rangle + \sin\theta_x\,|D_x\rangle \\ |\psi_y(B)\rangle &= \cos\theta_y\,|B_y\rangle + \sin\theta_y\,|D_y\rangle \\ |\psi_x(D)\rangle &= -\sin\theta_x\,|B_x\rangle + \cos\theta_x\,|D_x\rangle \\ |\psi_y(D)\rangle &= -\sin\theta_y\,|B_y\rangle + \cos\theta_y\,|D_y\rangle\,, \end{aligned} \tag{A.9}$$

where the mixing between the bright and the dark states $|B_\alpha\rangle$ and $|D_\alpha\rangle$ is characterised by a mixing angle θ_α. At time t = 0, a circularly polarised laser pulse σ^+, with pulse area $\Theta = \pi$ and FWHM = 0.2 meV, creates a superposition of the mostly bright states. With a moderate magnetic field the dark and bright excitons are separated by an energy larger than the pulse width, and the pulse width is larger than the splitting between $|B_\mathrm{x}\rangle$ and $|B_\mathrm{y}\rangle$. Due to the energy splittings between the bright exciton states, the states accumulate a relative phase and for $t > 0$ the superposition state may be written:

$$|\psi(t)\rangle = \cos\phi e^{iE_{bb}t/2\hbar}|\psi_x(B)\rangle + \sin\phi e^{-iE_{bb}t/2\hbar}|\psi_y(B)\rangle, \tag{A.10}$$

where the parameter ϕ is defined by $\tan 2\phi = \frac{\cos\theta_x}{\cos\theta_y}$. ϕ is set to minimize the initial occupation of the $|\uparrow\Downarrow\rangle$ state, since we are considering the case where we use a σ^+ preparation pulse, which creates the $|\downarrow\Uparrow\rangle$ state. The precession of the mostly bright neutral exciton occurs at frequency $\omega_\mathrm{bb} = E_\mathrm{bb}/\hbar$. The energy splitting is a function of the exchange energies and the Zeeman energies [27]:

$$E_{bb} \approx \delta_1 + KB^2$$

where

$$K = -\frac{\mu_B^2}{\delta_0(1-(\frac{\delta_1-\delta_2}{2\delta_0})^2)}[g_{ex}g_{hx} + \frac{\delta_1-\delta_2}{4\delta_0}(g_{ex}^2 + g_{hx}^2)]\ , \tag{A.11}$$

as already discussed in section A.4.

The probability P of measuring a exciton with a hole spin down is found by calculating the projection onto the spin-down basis:

$$P_{\Downarrow} = \left| \langle \Downarrow | \psi(t) \rangle \right|^2 . \tag{A.12}$$

Similarly, the probability $P_{\Uparrow}$ of measuring a exciton with a hole spin up can be found by projecting onto the spin-up basis.

$$P_{\Uparrow} = \left| \langle \Uparrow | \psi(t) \rangle \right|^2 . \tag{A.13}$$

We now make the assumption that electron spin may be traced out, since its spin state is not measured, and therefore this information is erased [1] Therefore, if we write the wavefunction A.10 in the form

$$|\psi(t)\rangle = a| \Uparrow\downarrow\rangle + b| \Downarrow\uparrow\rangle + c| \Uparrow\uparrow\rangle + d| \Downarrow\downarrow\rangle, \tag{A.14}$$

then $P_{\Uparrow} = |a|^2 + |c|^2$ and $P_{\Downarrow} = |b|^2 + |d|^2$. By substituting eqn. A.8 into Eqn. A.9 and substituting the result into A.10, to find the co-efficients $|a|^2+|c|^2$ and $|b|^2+|d|^2$, we can find the probability of measuring an exciton with hole spin up $P_{\Uparrow}$:

$$P_{\Uparrow} = \left[\frac{1}{2} + \frac{\sin(2\phi)}{2} \left(\sin(\theta_{\mathrm{x}}) \sin(\theta_{\mathrm{y}}) + \cos(\theta_{\mathrm{x}}) \cos(\theta_{\mathrm{y}}) \right) \cos(\omega_{\mathrm{h}} t) \right] e^{-\Gamma_{\mathrm{X}} t}. \tag{A.15}$$

Similarly the probability of measuring a an exciton with hole spin down $P_{\Downarrow\uparrow}$ can be be written:

$$P_{\Downarrow} = \left[\frac{1}{2} - \frac{\sin(2\phi)}{2} \left(\sin(\theta_{\mathrm{x}}) \sin(\theta_{\mathrm{y}}) + \cos(\theta_{\mathrm{x}}) \cos(\theta_{\mathrm{y}}) \right) \cos(\omega_{\mathrm{h}} t) \right] e^{-\Gamma_{\mathrm{X}} t}, \tag{A.16}$$

where we have introduced a phenomenological decay of the neutral exciton $\Gamma_{\mathrm{X}} \approx \Gamma_{\mathrm{e}}$

---

[1] In the experiments it was found that preparing a superposition of the mostly dark excitons using a preparation pulse resonant with the dark peak in the photocurrent spectrum yielded the same results.

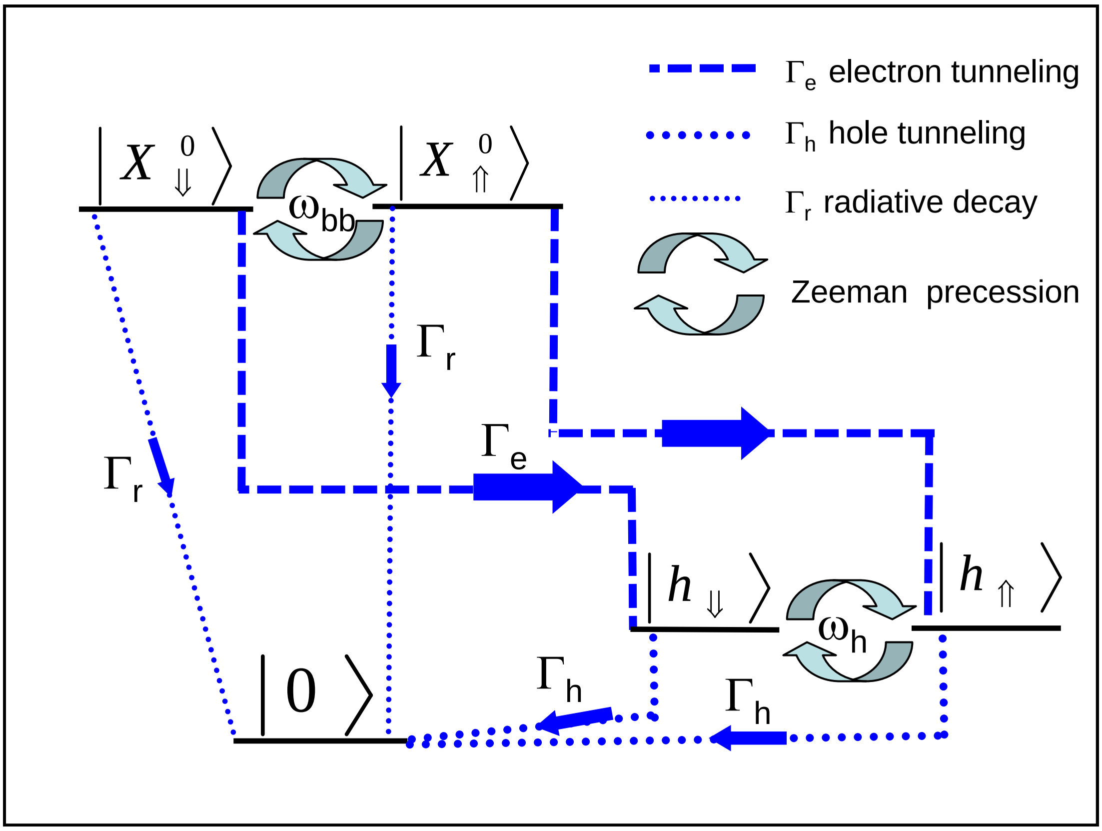

Figure A.12: *Schematic diagram of the decay paths of the neutral exciton states* $X^0_\Downarrow$ *and* $X^0_\Uparrow$ *and hole spin states* $h_\Downarrow$ *and* $h_\Uparrow$*. After the preparation pulse prepares the exciton states, they may decay by electron tunneling with a rate* $\Gamma_e \approx 1/90\ \mathrm{ps}^{-1}$ *or radiative recombination with a rate* $\Gamma_r \approx 1/\ \mathrm{ns}^{-1}$*. For this dot under an applied bias of* $-0.8\ V$ *the exciton decay is dominated by electron tunneling to the hole states. The hole states decay to the crystal ground state by hole tunneling with a rate* $\Gamma_h \approx 1/3\ \mathrm{ns}^{-1}$ *at a bias of* $-0.8\ V$*. The curved arrows represent the coherent precession of the states about the in plane magnetic field. By considering this diagram, a set of rate equations are constructed which relate how the exciton state populations are mapped onto the hole spin state populations.*

due to electron tunneling. From eqns A.15 and A.16 we can write the difference in neutral exciton state population $P_- = P_\Uparrow - P_\Downarrow$, and the total neutral exciton state population $P_+ = P_\Uparrow + P_\Downarrow$:

$$P_- = \sin(2\phi)\cos(\theta_\mathrm{x} - \theta_\mathrm{y})\cos(\omega_\mathrm{h} t)e^{-\Gamma_\mathrm{e} t} \tag{A.17}$$

$$P_+ = e^{-\Gamma_\mathrm{e} t} \tag{A.18}$$

So far we have constructed equations for the time evolution of the neutral exciton. We must now consider how the neutral exciton states map onto the hole spin states by considering the decay paths of the neutral exciton and hole states. Figure A.12

is a schematic diagram of the decay paths of the neutral exciton states and the hole states. The exciton spin states decay by electron tunneling to the hole spin states with a rate Γ_e as indicate by thick dashed blue lines in fig A.12. The exciton spin states may also decay by radiative recombination to the crystal ground with a rate Γ_r. The hole spin states decay by hole tunneling to the crystal ground state with a rate Γ_h as indicated by the thick dotted lines in fig A.12. We neglect hole spin relaxation between the hole spin states since this is on the order of 100's of μs [39]. The hole spins are coupled by the Zeeman energy splitting and precess at a frequency ω_h determined by $\Delta E = g_h \mu_{\mathrm{B}} B_{\mathrm{x}}$. With inspection of fig. A.12, we construct the following set of rate equations for the occupation of the hole spin states $|h_{\Downarrow}\rangle$ and $|h_{\Uparrow}\rangle$

$$\begin{aligned} \dot{h}_{\Uparrow} = & \ \Gamma_{\mathrm{e}} P_{\Uparrow} - \Gamma_{\mathrm{h}} h_{\Uparrow} && \text{(A.19)} \\ \dot{h}_{\Downarrow} = & \ \Gamma_{\mathrm{e}} P_{\Downarrow} - \Gamma_{\mathrm{h}} h_{\Downarrow} && \text{(A.20)} \end{aligned}$$

From these eqns we can construct rate equations for the total hole spin population and the difference in hole spin population:

$$\begin{aligned} \dot{h}_{\Uparrow} + \dot{h}_{\Downarrow} = & \ \Gamma_{\mathrm{e}}(P_{\Uparrow} + P_{\Downarrow}) - \Gamma_{\mathrm{h}}(h_{\Uparrow} + h_{\Downarrow}) && \text{(A.21)} \\ \dot{h}_{\Uparrow} - \dot{h}_{\Downarrow} = & \ \Gamma_{\mathrm{e}}(P_{\Uparrow} - P_{\Downarrow}) - \Gamma_{\mathrm{h}}(h_{\Uparrow} - h_{\Downarrow}). && \text{(A.22)} \end{aligned}$$

from which we may write

$$\begin{aligned} \dot{h}_{+} + \Gamma_h h_{+} = & \quad \Gamma_e P_{+} && \text{(A.23)} \\ \dot{h}_{-} + (\Gamma_h + i\omega_{\mathrm{h}}) h_{-} = & \quad \Gamma_e P_{-}, && \text{(A.24)} \end{aligned}$$

where we define $\dot{h}_{+} = \dot{h}_{\Uparrow} + \dot{h}_{\Downarrow}$ as the rate of change of the total hole spin population and $\dot{h}_{-} = \dot{h}_{\Uparrow} - \dot{h}_{\Downarrow}$ as the rate of change in the difference in hole spin population.

Equations A.23 and A.24 have the form

$$\dot{y} + \alpha y = \beta \tag{A.25}$$

which has the general solution $y = e^{-I}\left[\int_0^t \beta e^I dt + c\right]$ where $I = \int \alpha dt$. Solving the differential equations A.23 and A.24 to find h_+ and h_- we find the hole spin contrast C and Fidelity F where, $C = 2F - 1$, as:

$$C = \lim_{\Gamma_e t \gg 1 \gg \Gamma_h t} \frac{h_\Uparrow - h_\Downarrow}{h_\Uparrow + h_\Downarrow} \tag{A.26}$$

$$C = \frac{1}{2}\sin 2\phi \cos(2\theta)[f(\omega_h - \omega_{bb}) + f(\omega_h + \omega_{bb})] \tag{A.27}$$

$$f(a) = \frac{(\Gamma_e - \Gamma_h)^2}{(\Gamma_e - \Gamma_h)^2 + a^2}. \tag{A.28}$$

The fidelity F eqn A.27 is a measure of the purity of the preparation of a single hole spin by ionisation of a neutral exciton in a Voigt geometry magnetic field. The contrast C predicts the maximum contrast or visibility in the amplitude of the precession of the spin.

From eqn A.27 we can see that two factors determine the spin contrast. The first factor arises from the mixing of the bright and dark excitons. The second factor is a competition between electron tunelling and a frequency mismatch between the hole Zeeman energy splitting $E_\mathrm{h} = \hbar\omega_\mathrm{h}$ and the effective bright-bright fine-structure splitting E_bb. The contrast takes a maximum value when $E_\mathrm{bb} = \pm\hbar\omega_\mathrm{h}$. This can be understood as a minimal loss of coherence when the electron and hole dissociate under this resonance condition.

Figure A.4 shows the energy level diagram of the neutral exciton states. For most cases of interest $\delta_0 >> \delta_{1,2}$, which means that we can make the approximation $\theta_\mathrm{x} \approx -\theta_\mathrm{y}$. Under this assumption the mixing angle term $\cos(\theta_\mathrm{x} - \theta_\mathrm{y}) \approx \cos(2\theta)$ and therefore $\phi \approx \pi/4$. The mixing angle θ can be estimated experimentally as described in section A.2

A.7 Estimate of dephasing time T_2^*

Reference [13] considers the decoherence of a single hole-spin in an external magnetic field, due to fluctuations in a randomized ensemble of nuclear spins. The spin-component perpendicular to the applied magnetic field is found to decay as $\exp\left(-t^2/T_2^{*2}\right)$, where $T_2^* = \sqrt{2}/\sigma$, and σ is the variance in the fluctuations of the hole-nuclear interaction given in Eq. (9) of ref. [13] as:

$$(\hbar\sigma)^2 = \frac{1}{4N}\sum_j \nu_j I^j(I^j+1)|A_h^j|^2 \equiv \frac{A_{eff}^2}{4N}, \tag{A.29}$$

where N is the effective number of nuclei overlapping with the hole wavefunction, ν_j is the abundance of isotope j, I^j is the nuclear spin of isotope-j, and A_h^j is the coupling strength of the hole-nuclear interaction for isotope-j.

To calculate the effective hole-nuclear interaction strength for pure GaAs and InAs, the following values are used. $I(^{69,71}Ga) = I(^{75}As) = 3/2$ and $I(^{113,115}In) = 9/2$. The isotopes have natural abundances $2\nu(^{115}In) = 96\%, 2\nu(^{113}In) = 4\%, 2\nu(^{69}Ga) = 60\%, 2\nu(^{71}Ga) = 40\%, 2\nu(^{75}As) = 100\%$. To estimate the hole-nuclear coupling energies A_h^j, recently measured values of the ratios of the hyperfine coupling strengths of the hole and electron measured by E. A. Chekhovich *et al* were used [15]. These measurements were carried out using optically detected NMR experiments on single InAs/GaAs and GaAs dots [111],[112], [15]. The values measured are: $\bar{A}(As) = +10\%, \bar{A}(In) = -15\%, \bar{A}(Ga) = -(3-6)\%$, where $\bar{A} = A_h^j/A_e^j$. These measurements were made for the z-component of the hole-spin, with an external magnetic field aligned along the z-axis. Due to the anisotropic nature of the hole-nuclear interaction, some caution is needed in applying these numbers, but since these are the only available measurements of $\bar{A}$, these values were used. The ratio $\bar{A}$ was used along with accepted values of the electron-hyperfine coupling strengths $A_e(In) = 47$ μeV, $A_e(^{69}Ga) = 74$ μeV, $A_e(^{71}Ga) = 94$ μeV, $A_e(^{75}As) = 89$ μeV [113]. Using the numbers above, an estimate $|A_{eff}(GaAs)| = 12.6-13.9$ μeV and $|A_{eff}(InAs)| = 27.6$ μeV was made.

To estimate the effective number of nuclei of the dot $N = V_{dot}/V_0$, where V_{dot} is the effective volume enclosed by the hole wavefunction and $V_0 = a_L^3/8 = 0.0225$ nm^3 is the volume occupied by each lattice-site, a spherical carrier wavefunction of $|\psi|^2 \propto \exp(-r^2/d^2)$ with a volume of $V_{dot} = 4\pi d^3/3$ was assumed. In recent measurements on a similar dot, the size of the carrier wavefunction $d = 3.25-3.5$ nm was deduced from the intensity damping of Rabi rotation measurements of the neutral exciton transition [64]. The work of Finley *et al* [114] shows that the hole wavefunction is smaller than the electron. Therefore this value of N is more likely to provide be an upper bound on the number of nuclei. Based on the above values of d an estimate of $N = 6400 - 8000$ was made for the quantum dot, and hence $T_2^* \approx 5.4 - 13$ ns for a large In-poor and small In-rich dots respectively. This is in the same range as the measured value of $T_2^* = 15.4^{+5.5}_{-3.3}$ ns, lending support to the notion that the hole-nuclear spin interaction is the dominant source of the dephasing of the hole-spin.

Although the T_2^* measured here was large compared to an electron-spin in an InAs/GaAs quantum dot [38], it is similar to electron-spin values measured for much larger GaAs interface [55], [115] or electrically defined [116] quantum dots, where longer dephasing times are to be expected, since σ scales with the number of nuclei as $\sigma \sim N^{-1/2}$. However, InAs/GaAs dots have superior optical properties compared to GaAs dots. In particular, Rabi oscillations using charged GaAs interface dots suffer strong intensity damping, limiting their use in coherent optical control experiments [56], [117].

Bibliography

[1] R. P. Feynman, “Simulating physics with computers,” *International Journal of Theoretical Physics*, vol. 21, p. 467, 1981.

[2] D. Deutsch, “Quantum theory, the church-turing principle and the universal quantum computer,” *Proceedings of the Royal Society of London A*, vol. 400, pp. 97–117, 1985.

[3] D. P. DiVincenzo, “The physical implementation of quantum computation,” *Fortsch. Phys*, vol. 48, p. 771, 2000.

[4] S. Stufler, P. Ester, and A. Zrenner, “Ramsey fringes in an electric-field-tunable quantum dot system,” *Physical Review Letters*, vol. 96, p. 037402, 2006.

[5] R. S. Kolodka, A. J. Ramsay, J. Skiba-Szymanska, P. W. Fry, H. Y. Liu, A. M. Fox, and M. S. Skolnick, “Inversion recovery of single quantum-dot exciton based qubit,” *Physical Review B*, vol. 75, p. 193306, 2007.

[6] S. J. Boyle, *Picosecond Coherent Control of Single Self-Assembled InGaAs/GaAs Quantum Dots.* Phd thesis, University of Sheffield, 2010.

[7] E. Poem, O. Kenneth, Y. Kodriano, Y. Benny, S. Khatsevich, J. E. Avron, and D. Gershoni, “Optically induced rotation of an exciton spin in a semiconductor quantum dot,” *Physical Review Letters*, vol. 107, p. 087401, 2011.

[8] M. Kroutvar, Y. Ducommun, D. Heiss, M. Bichler, D. Schuh, G. Abstreiter,

and J. J. Finley, “Optically programmable electron spin memory using semiconductor quantum dots,” *Nature*, vol. 432, p. 81, 2004.

[9] M. Atatüre, J. Dreiser, A. Badolato, A. Högele, K. Karrai, and A. Imamoglu, “Quantum-dot spin-state preparation with near-unity fidelity,” *Science*, vol. 312, p. 551, 2006.

[10] J. Berezovsky, M. H. Mikkelsen, N. G. Stoltz, L. A. Coldren, and D. D. Awschalom, “Picosecond coherent optical manipulation of a single electron spin in a quantum dot,” *Science*, vol. 320, p. 349, 2008.

[11] D. Press, T. D. Ladd, B. Zhang, and Y. Yamamoto, “Complete quantum control of single quantum dot spin using ultrafast optical pulses,” *Nature*, vol. 456, p. 218, 2008.

[12] D. Kim, S. G. Carter, A. Greilich, A. S. Bracker, and D. Gammon, “Ultrafast optical control of entanglement between two quantum-dot spins,” *Nature Physics*, vol. 7, p. 223, 2011.

[13] J. Fischer, W. A. Coish, D. V. Bulaev, and D. Loss, “Spin decoherence of a heavy hole coupled to nuclear spins in a quantum dot,” *Physical Review B*, vol. 78, p. 155329, 2008.

[14] C. Testelin, F. Bernardot, B. Eble, and M. Chamarro, “Hole spin dephasing time associated with hyperfine interaction in quantum dots,” *Physical Review B*, vol. 79, p. 195440, 2009.

[15] E. A. Chekhovich, A. B. Krysa, M. Hopkinson, P. Senellart, A. Lemaitre, M. S. Skolnick, and A. I. Tartakovskii, “Isotope sensitive measurement of the hole-nuclear spin interaction in quantum dots,” *arXiv*, vol. arXiv:1109.0733v2, 2011.

[16] D. Brunner, B. D. Gerardot, P. A. Dalgarno, G. Wüst, K. Karrai, N. G. Stoltz, P. M. Petroff, and R. J. Warburton, “A coherent single hole spin in a semiconductor,” *Science*, vol. 325, p. 70, 2009.

[17] K. D. Greve, P. L. McMahon, D. Press, T. D. Ladd, D. Bisping, C. Schneider, M. Kamp, L. Worschech, S. Höfling, A. Forchel, and Y. Yamamoto, "Ultrafast coherent control and suppressed nuclear feedback of a single quantum dot hole qubit," *Nature Physics*, vol. 7, p. 872, 2011.

[18] A. Greilich, S. G. Carter, D. Kim, A. S. Bracker, and D. Gammon, "Optical control of one and two hole spins in interacting quantum dots," *Nature Photonics*, vol. 5, p. 702, 2011.

[19] D. M. Bruls, J. W. A. M. Vugs, P. M. Koenraad, H. W. M. Salemink, J. H. Wolter, M. Hopkinson, M. S. Skolnick, F. Long, and S. P. A. Gill, "Determination of the shape and indium distribution of low-growth-rate InAs quantum dots by cross-sectional scanning tunneling microscopy," *Applied Physics Letters*, vol. 81, p. 1708, 2002.

[20] P. Michler, *Single Quantum Dots. Fundamentals, Applications and new Concepts*, vol. 90 of *Topics in applied physics.* Springer, 2003.

[21] P. M. (Ed), *Single Semiconductor Quantum Dots.* Nanoscience and Technology, Springer, 2009.

[22] H. W. van Kesteren, E. C. Cosman, W. A. J. A. van der Poel, and C. T. Foxon, "Fine structure of excitons in type-ii gaas/alas quantum wells," *Physical Review B*, vol. 41, p. 5283, 1990.

[23] M. Bayer, G. Ortner, O. Stern, A. Kuther, A. A. Gorbunov, A. Forchel, P. Hawrylak, S. Fafard, K. Hinzer, T. L. Reinecke, S. N. Walck, J. P. Reithmaier, F. Klopf, and F. Schäfer, "Fine structure of neutral and charged excitons in self-assembled In(Ga)As/(Al)GaAs quantum dots," *Physical Review B*, vol. 65, p. 195315, 2002.

[24] O. Gywat, H. J. Krenner, and J. Berezovsky, *Spins in Optically Active Quantum Dots. Concepts and Methods.* WILEY, 2010.

[25] M. Bayer, O. Stern, A. Kuther, and A. Forchel, “Spectroscopic study of dark excitons in $\mathrm{In_xGa_{1-x}As}$ self-assembled quantum dots by a magnetic-field-induced symmetry breaking,” *Physical Review B*, vol. 61, p. 7273, 2000.

[26] R. J. Young, R. M. Stevenson, A. J. Shields, P. Atkinson, K. Cooper, D. A. Ritchie, K. M. Groom, A. I. Tartakovskii, and M. S. Skolnick, “Inversion of exciton level splitting in quantum dots,” *Physical Review B*, vol. 72, p. 113305, 2005.

[27] R. M. Stevenson, R. J. Young, P. See, D. G. Gevaux, K. Cooper, P. Atkinson, I. Farrer, D. A. Ritchie, and A. J. Shields, “Magnetic-field-induced reduction of the exciton polarization splitting in inas quantum dots,” *Physical Review B*, vol. 73, p. 033306, 2006.

[28] A. I. Tartakovskii, M. N. Makhonin, I. R. Sellers, J. Cahill, A. D. Andreev, D. M. Whittaker, J.-P. R. Wells, A. M. Fox, D. J. Mowbray, M. S. Skolnick, K. M. Groom, M. J. Steer, H. Y. Liu, and M. Hopkinson, “Effect of thermal annealing and strain engineering on the fine structure of quantum dot excitons,” *Physical Review B*, vol. 70, p. 193303, 2004.

[29] R. Singh and G. Bester, “Manipulating fine structure splitting in semiconductor quantum dots,” *Journal of Physics: Conference Series*, vol. 245, no. 012008, 2010.

[30] R. Singh and G. Bester, “Nanowire quantum dots as an ideal source of entangled photon pairs,” *Physical Review Letters*, vol. 103, p. 063601, 2009.

[31] A. Mohan, M. Felici, P. Gallo, B. Dwir, A. Rudra, J. Faist, and E. Kapon, “Polarization-entangled photons produced with high-symmetry site-controlled quantum dots,” *Nature Photonics*, vol. 4, p. 302, 2010.

[32] R. J. Warburton, C. Schä, D. Haft, F. Bickel, A. Lorke, K. Karrai,

J. M. Garcia, W. Schoenfeld, and P. M. Petroff, “Optical emission from a charge-tunable quantum ring,” *Nature*, vol. 405, p. 926, 2000.

[33] D. V. Regelman, E. Dekel, D. Gershoni, E. Ehrenfreund, A. J. Williamson, J. Shumway, A. Zunger, W. V. Schoenfeld, and P. M. Petroff, “Optical spectroscopy of single quantum dots at tunable positive, neutral, and negative charge states,” *Physical Review B*, vol. 64, p. 165301, 2001.

[34] M. Ediger, G. Bester, A. Badolato, P. M. Petroff, K. Karria, A. Zunger, and R. J. Warburton, “Peculiar many-body effects revealed in the spectroscopy of highly charged quantum dots,” *Nature Physics*, vol. 3, p. 774, 2007.

[35] J. J. Finley, M. Sabathil, P. Vogl, G. Abstreiter, R. Oulton, A. I. Tartakovskii, D. J. Mowbray, M. S. Skolnick, S. L. Liew, A. G. Cullis, and M. Hopkinson, “Quantum-confined stark shifts of charged exciton complexes in quantum dots,” *Physical Review B*, vol. 70, p. 201308, 2004.

[36] K. Kowalik, O. Krebs, A. Lemaȋtre, S. Laurent, P. Senellart, P. Voisin, , and J. A. Gaj, “Influence of an in-plane electric field on exciton fine structure in inas-gaas self-assembled quantum dots,” *Applied Physics Letters*, vol. 86, p. 041907, 2005.

[37] B. D. Gerardot, S. Seidl, P. A. Dalgarno, R. J. Warburton, D. Granados, J. M. Garcia, K. Kowalik, O. Krebs, K. Karrai, A. Badolato, , and P. M. Petrof, “Manipulating exciton fine structure in quantum dots with a lateral electric field,” *Applied Physics Letters*, vol. 90, p. 4, 2007.

[38] K. D. Greve, P. L. McMahon, D. Press, T. D. Ladd, Y. Yamamoto, D. Bisping, C. Schneider, M. Kamp, L. Worschech, A. Forchel, and S. Höfling, “Coherent control and suppressed nuclear feedback of a single quantum dot hole qubit,” *arXiv*, vol. arXiv:1106.5676v1, 2011.

[39] D. Heiss, S. Schaeck, H. Huebl, M. Bichler, G. Abstreiter, J. J. Finley, D. V.

Bulaev, and D. Loss, “Observation of extremely slow hole spin relaxation in self-assembled quantum dots,” *Physical Review B*, vol. 76, p. 241306(R), 2007.

[40] R. J. Young, S. J. Dewhurst, R. M. Stevenson1, P. Atkinson, A. J. Bennett, M. B. Ward, K. Cooper, D. A. Ritchie, and A. J. Shields, “Single electron-spin memory with a semiconductor quantum dot,” *New Journal of Physics*, vol. 9, p. 365, 2007.

[41] A. Ramsay, S. J. Boyle, R. S. Kolodka, J. B. B. Oliveira, J. Skiba-Szymanska, H. Y. Liu, M. Hopkinson, A. M. Fox, and M. S. Skolnick, “Fast optical preparation, control and readout of a single quantum dot spin,” *Physical Review Letters*, vol. 100, p. 197401, 2008.

[42] R. Hanson, L. P. Kouwenhoven, J. R. Petta, S. Tarucha, and L. M. K. Vandersypen, “Spins in few-electron quantum dots,” *Reviews of Modern Physics*, vol. 79, p. 1217, 2007.

[43] B. D. Gerardot, D. Brunner, P. A. Dalgarno, P. Öhberg, S. Seid, M. Kroner, K. Karrai, N. G. Stoltz, P. M. Petroff, and R. J. Warburton, “Optical pumping of a single hole spin in a quantum dot,” *Nature*, vol. 451, p. 441, 2007.

[44] E. A. Chekhovich, M. N. Makhonin, J. Skiba-Szymanska, A. B. Krysa, V. D. Kulakovskii, M. S. Skolnick, and A. I. Tartakovskii, “Dynamics of optically induced nuclear spin polarization in individual InP/$\mathrm{Ga_xIn_{1-x}P}$ quantum dots,” *Physical Review B*, p. 245308, 2010.

[45] Tartakovskii, A. I., Wright, T., Russell, A., Fal’ko, V. I., Van’kov, A. B., Skiba-Szymanska, J., Drouzas, I., R. S. Kolodka, Skolnick, M. S., F. P. W., A. Tahraoui, H.-Y. Liu, and M. Hopkinson, “Nuclear spin switch in semiconductor quantum dots,” *Physical Review Letters*, vol. 98, p. 026806, 2007.

[46] F. Klotz, V. Jovanov, J. Kierig, E. C. Clark, M. Bichler, G. Abstreiter, M. S. Brandt, J. J. Finley, H. Schwager, and G. Giedke, “Asymmetric optical nuclear

spin pumping in a single uncharged quantum dot," *Physical Review B*, vol. 82, p. 121307, 2010.

[47] A. S. Bracker, E. A. Stinaff, D. Gammon, M. E. Ware, J. G. Tischler, A. Shabaev, A. L. Efros, D. Park, D. Gershoni, V. L. Korenev, and I. A. Merkulov, "Optical pumping of the electronic and nuclear spin of single charge-tunable quantum dots," *Physical Review Letters*, vol. 94, p. 047402, 2005.

[48] M. N. Makhonin, A. I. Tartakovskii, A. Ebbens, M. S. Skolnick, A. Russell, V. I. Fal'ko, , and M. Hopkinson, "Nuclear spin pumping under resonant optical excitation in a quantum dot," *Applied Physics Letters*, vol. 93, p. 073113, 2008.

[49] Makhonin, M. N., Chekhovich, E. A., Senellart, P., Lemaître, A., Skolnick, M. S., and T. A. I., "Optically tunable nuclear magnetic resonance in a single quantum dot," *Physical Review B*, vol. 82, p. 161309, 2010.

[50] A. Greilich, D. R. Yakovlev, A. Shabaev, A. L. Efros, I. A. Yugova, R. Oulton, V. Stavarache, D. Reuter, A. Wieck, and M. Bayer, "Mode locking of electron spin coherences in singly charged quantum dots," *Science*, vol. 313, p. 341, 2006.

[51] X. Xu, W. Yao, B. Sun, D. G. Steel, A. S. Bracker, D. Gammon, and L. J. Sham, "Optically controlled locking of the nuclear field via coherent dark-state spectroscopy," *Nature*, vol. 459, p. 1105, 2009.

[52] M. N. Makhonin, K. V. Kavokin, P. Senellart, A. Lemaî, A. J. Ramsay, M. S. Skolnick, and A. I. Tartakovskii, "Fast control of nuclear spin polarization in an optically pumped single quantum dot," *Nature Materials online*, vol. 459, p. 10.1038/NMAT3102, 2011.

[53] E. A. Chekhovich, A. B. Krysa, M. S. Skolnick, and A. I. Tartakovskii, "Direct measurement of the hole-nuclear spin interaction in single InP/GaInP

quantum dots using photoluminescence spectroscopy," *Physical Review Letters*, vol. 106, p. 027402, 2011.

[54] P. Fallahi, S. T. Y ılmaz, and A. Imamoğlu, "Measurement of a heavy-hole hyperfine interaction in ingaas quantum dots using resonance fluorescence," *Physical Review Letters*, vol. 105, p. 257402, 2010.

[55] M. H. Mikkelsen, J. Berezovsky, N. G. Stolz, L. A. Coldren, and D. D. Awschalom, "Optically detected coherent spin dynamics of a single electron in a quantum dot," *Nature*, vol. 3, p. 770, 2007.

[56] J. B. M. H. Mikkelsen, N. G. Stoltz, L. A. Coldren, and D. D. Awschalom, "Picosecond coherent optical manipulation of a single electron spin in a quantum dot," *Science*, vol. 320, p. 349, 2008.

[57] D. Press, K. D. Greve, P. L. McMahon, T. D. Ladd, B. Friess, C. Schneider, M. Kamp, S. Höling, A. Forchel, and Y. Yamamoto, "Ultrafast optical spin echo in a single quantum dot," *Nature Photonics*, vol. 4, p. 367, 2010.

[58] F. H. L. Koppens, K. C. Nowack, and L. M. K. Vandersypen, "Spin echo of a single electron spin in a quantum dot," *Physical Review Letters*, vol. 100, p. 236802, 2008.

[59] S. G. Carter, D. Kim, A. Greilich, A. S. Bracker, and D. Gammon, "Ultrafast optical entanglement control between two quantum dot spins," in *Quant. Elec. Laser Sci. Conf. Talk QMK1, Baltimore*, 2011.

[60] B. D. Gerardot, R. J. Barbour, D. Brunner, P. A. Dalgarno, A. Badolato, N. Stoltz, P. M. Petroff, J. Houel, and R. J. Warburton, "Laser spectroscopy of individual quantum dots charged with a single hole," *arXiv*, vol. arXiv:1109.4392v1, 2011.

[61] S. Stufler, P. Ester, and A. Zrenner, "Quantum optical properties of single $\mathrm{In_xGa_{1-x}-GaAs}$ quantum dot two-level system," *Physical Review B*, vol. 72, p. 121301, 2005.

[62] S. M. de Vasconcellos, S. Gordon, M. Bichler, T. Meier, and A. Zrenner, "Coherent control of a single exciton qubit by optoelectronic manipulation," *Nature Photonics*, vol. 4, p. 545, 2010.

[63] A. J. Ramsay, A. V. Gopal, E. M. Gauger, A. Nazir, B. Lovett, A. M. Fox, and M. S. Skolnick, "Damping of exciton rabi rotations by acoustic phonons in optically excited InGaAs/GaAs quantum dots," *Physical Review Letters*, vol. 104, p. 017402, 2010.

[64] A. J. Ramsay, T. M. Godden, S. J. Boyle, E. M. Gauger, A. Nazir, B. W. Lovett, A. M. Fox, and M. S. Skolnick, "Phonon-induced rabi-frequency renormalization of optically driven single InGaAs/GaAs quantum dots," *Physical Review Letters*, vol. 105, p. 177402, 2010.

[65] C. Emary, , X. Xu, D. G. Steel, S. Saikin, and L. J. Sham, "Fast initialisation of the spin state of an electron in a quantum dot in the voigt configuration," *Physical Review Letters*, vol. 98, p. 047401, 2007.

[66] X. Xu, Y. Wu, B. Sun, Q. Huang, J. Cheng, D. G. Steel, A. S. Bracker, D. Gammon, C. Emary, and L. J. Sham, "Fast spin state initialisation in a singly charged $\mathrm{InAs-GaAs}$ quantum dot by optical cooling," *Physical Review Letters*, vol. 99, p. 097401, 2007.

[67] D. Kim, S. E. Economou, S. C. Badescu, M. Scheibner, A. S. Bracker, M. Bashkansky, T. L. Reinecke, and D. Gammon, "Optical spin initialization and nondestructive measurement in a quantum dot molecule," *Physical Review Letters*, vol. 101, p. 236804, 2008.

[68] A. N. Vamivakas, C.-Y. Lu, C. Matthiesen, Y. Zhao, S. Fält, A. Badolato, and M. Atatüre, "Observation of spin-dependent quantum jumps via quantum dot resonance fluorescence," *Nature*, vol. 467, p. 297, 2010.

[69] X. Xu, B. Sun, P. R. Berman, D. G. Steel, A. S. Bracker, D. Gammon, and

L. J. Sham, “Coherent population trapping of an electron spin in a single negatively charged quantum dot,” *Nature Physics*, vol. 44, p. 692, 2008.

[70] M. Fleischhauer, A. Imamoglu, and J. P. Marangos, “Electromagnetically induced transparency: Optics in coherent media,” *Reviews of Modern Physics*, vol. 77, p. 633, 2005.

[71] D. Heiss, V. Jovanov, F. Klotz, D. Rudolph, M. Bichler, G. Abstreiter, M. S. Brandt, and J. J. Finley, “Optically monitoring electron spin relaxation in a single quantum dot using a spin memory device,” *Phys. Rev. B*, vol. 82, p. 245316, 2010.

[72] D. Heiss, V. Jovanov, M. Bichler, G. Abstreiter, and J. J. Finley, “Charge and spin readout scheme for single self-assembled quantum dots,” *Physical Review B*, vol. 77, p. 235442, 2008.

[73] A. Muller, E. B. Flagg, P. Bianucci, X. Y. Wang, D. G. Deppe, W. Ma, J. Zhang, G. J. Salamo, M. Xiao, and C. K. Shih, “Resonance fluorescence from a coherently driven semiconductor quantum dot in a cavity,” *Physical Review Letters*, vol. 99, p. 187402, 2007.

[74] E. B. Flagg, A. Muller, J. W. Robertson, S. Founta, D. G. Deppe, M. Xiao, W. Ma, G. J. Salamo, and C. K. Shih, “Resonantly driven coherent oscillations in a solid-state quantum emitter,” *Nature Physics*, vol. 5, p. 203, 2009.

[75] J. Berezovsky, M. H. Mikkelsen, O. Gywat, N. G. Stoltz, L. A. Coldrena, and D. D. Awschalom, “Nondestructive optical measurements of a single electron spin in a quantum dot,” *Science*, vol. 314, p. 1916, 2006.

[76] A. Zrenner, E. Beham, S. Stufler, F. Findeis, M. Bichler, and G. Abstreiter, “Coherent properties of a two-level system based on a quantum-dot photodiode,” *Nature*, vol. 418, p. 612, 2002.

[77] S. J. Boyle, A. J. Ramsay, F. Bello, H. Y. Liu, M. Hopkinson, A. M. Fox, and

M. S. Skolnick, “Two-qubit conditional quantum-logic operation in a single self-assembled quantum dot,” *Physical Review B*, vol. 78, p. 075301, 2008.

[78] S. J. Boyle, A. J. Ramsay, A. M. Fox, M. S. Skolnick, A. P. Heberle, and M. Hopkinson, “Beating of exciton-dressed states in a single semiconductor InGaAs/GaAs quantum dot,” *Physical Review Letters*, vol. 102, p. 207401, 2009.

[79] Y. Wu, I. M. Piper, M. Ediger, P. Brereton, E. R. Schmidgall, P. R. Eastham, M. Hugues, M. Hopkinson, and R. T. Phillips, “Population inversion in a single ingaas quantum dot using the method of adiabatic rapid passage,” *Physical Review Letters*, vol. 106, p. 067401, 2011.

[80] R. Coles, “Voltage modulation of a quantum dot schottky diode for coherent photocurrent spectroscopy,” Master’s thesis, University of Sheffield, 2010.

[81] A. N. Vamivakas, M. Atatüre, J. Dreiser, S. T. Yilmaz, A. Badolato, A. K. Swan, B. B. Goldberg, A. Imamoğlu, , and M. S. ÜnlÜ, “Strong extinction of a far-field laserbeam by a single quantum dot,” *Nano Letters*, vol. 7, p. 9, 2007.

[82] J. A. G. R. Knobel, N. Samarth, and D. D. Awschalom, “Ultrafast manipulation of electron spin coherence,” *Science*, vol. 292, p. 2458, 2001.

[83] M. V. G. Dutt, J. Cheng, B. Li, X. Xu, X. Li, P. R. Berman, D. G. Steel, A. S. Bracker, D. Gammon, S. E. Economou, R.-B. Liu, and L. J. Sham, “Stimulated and spontaneous optical generation of electron spin coherence in charged gaas quantum dots,” *Physical Review Letters*, vol. 94, p. 227403, 2005.

[84] A. Greilich, M. Wiemann, F. G. G. Hernandez, D. R. Yakovlev, I. A. Yugova, M. Bayer, A. Shabaev, A. L. Efros, D. Reuter, and A. D. Wieck, “Robust manipulation of electron spin coherence in an ensemble of singly charged quantum dots,” *Physical Review B*, vol. 75, p. 233301, 2007.

[85] A. Greilich, S. G. Carter, D. Kim, A. S. Bracker, and D. Gammon, “Optical control of one and two hole spins in interacting quantum dots,” *arXiv*, 2011.

[86] P. Chen, C. Piermarocchi, L. J. Sham, D. Gammon, and D. G. Steel, “Theory of quantum optical control of a single spin in a quantum dot,” *Physical Review B*, vol. 69, p. 075320, 2004.

[87] S. Economou and T. L. Reinecke, “Theory of fast optical spin rotation in a quantum dot based on geometric phases and trapped states,” *Physical Review Letters*, vol. 99, p. 217401, 2007.

[88] S. E. Economou, L. J. Sham, Y. Wu, , and D. G.Steel, “Proposal for optical U(1) rotations of electron spin trapped in a quantum dot,” *Physical Review B*, vol. 74, p. 205415, Nov 2006.

[89] E. D. Kim, K. Truex, X. Xu, B. Sun, D. G. Steel, A. S. Bracker, D. Gammon, , and L. J. Sham, “Fast spin rotations by optically controlled geometric phases in a charge-tunable inas quantum dot,” *Physical Review Letters*, vol. 104, p. 167401, 2010.

[90] P. W. Fry, J. J. Finley, L. R. Wilson, A. Lemaître, D. J. Mowbray, M. S. Skolnick, M. Hopkinson, G. Hill, and J. C. Clark, “Electric-field-dependent carrier capture and escape in self-assembled inas/gaas quantum dots,” *Applied Physics Letters*, vol. 77, p. 4344, 2000.

[91] A. Weiner, “Femtosecond pulse shaping using spatial light modulators,” *Review of Scientific Instruments*, vol. 71, p. 1928, 2000.

[92] N. Corp., “Gaussian optics and single mode fiber coupling,” 2008.

[93] G. A. Brooker, *Modern Classical Optics.* Oxford Masters Series In Atomic, Optical and Laser Physics, Oxford University Press, 2003.

[94] A. J. Horton and J. Bland-Hawthorn, “Coupling light into few-mode optical fibres I: The diffraction limit,” *Optics Express*, vol. 15, p. 1443, 2007.

[95] R. Ulrich, S. C. Rashleigh, and W. Eickhoff, “Bending-induced birefringence in single-mode fibers,” *Optics Letters*, vol. 5, p. 273, 1980.

[96] A. F. A. Khatab, A. J. Ramsay, S. J. Boyle, A. M. Fox, and M. S. Skolnick, “Inversion recovery measurements of exciton fine-structure beats in a single quantum dot,” *Journal of Physics: Conference Series*, vol. 245, p. 774, 2010.

[97] D. Loss and D. P. DiVincenzo, “Quantum computation with quantum dots,” *Physical Review A*, vol. 57, no. 1, p. 120, 1998.

[98] A. V. Khaetskii, D. Loss, , and L. Glazman, “Electron spin decoherence in quantum dots due to interaction with nuclei,” *Physical Review Letters*, vol. 88, p. 186802, 2002.

[99] T. M. Godden, S. J. Boyle, A. J. Ramsay, A. M. Fox, and M. S. Skolnick, “Fast high fidelity hole spin initialization in a single ingaas quantum dot,” *Applied Physics Letters*, vol. 97, p. 061113, 2010.

[100] J. B. M. H. Mikkelsen, N. G. Stoltz, L. A. Coldren, and D. D. Awschalom, “Picosecond coherent optical manipulation of a single electron spin in a quantum dot,” *Science*, vol. 320, p. 349, 2008.

[101] F. Klotz, V. Jovanov, J. Kierig, E. C. Clark, D. Rudolph, D. Heiss, M. Bichler, G. Abstreiter, M. S. Brandt, and J. J. Finley, “Observation of an electrically tunable exciton g factor in ingaas/gaas quantum dots,” *Applied Physics Letters*, vol. 96, p. 053113, 2010.

[102] T. Nakaoka, S. Tarucha, and Y. Arakawa, “Electrical tuning of the g-factor of single self-assembled quantum dots,” *Physical Review B*, vol. 76, p. 041301, 2007.

[103] A. S. Bracker, E. A. Stinaff, D. Gammon, M. E. Ware, J. G. Tischler, A. Shabaev, A. L. Efros, D. Park, D. Gershoni, V. L. Korenev, and I. A. Merkulov, “Optical pumping of the electronic and nuclear spin of single

charge-tunable quantum dots," *Physical Review Letters*, vol. 94, p. 047402, 2005.

[104] B. D. Gerardot, R. J. Barbour, D. Brunner, P. A. Dalgarno, A. Badolato, N. Stoltz, P. M. Petroff, J. Houel, and R. J. Warburton, "Laser spectroscopy of individual quantum dots charged with a single hole," *arXiv*, vol. arXiv:1109.4392v1, 2011.

[105] T. M. Godden, J. H. Quilter, A. J. Ramsay, Y. Wu, P. Brereton, S. J. Boyle, I. J. Luxmoore, J. Puebla-Nunez, A. M. Fox, and M. S. Skolnick, "Coherent optical control of the spin of a single hole in a quantum dot," *arXiv*, vol. arXiv:1106.6282v1, 2011.

[106] A. Fox, *Optical Properties of Solids.* Oxford Masters Series In Atomic, Optical and Laser Physics, Oxford University Press, 2006.

[107] O. Krebs, P. Maletinsky, T. Amand, B. Urbaszek, A. Lemaître, P. Voisin, X. Marie, and A. Imamoglu, "Anomalous hanle effect due to optically created transverse overhauser field in single $inas/gaas$ quantum dots," *Physical Review Letters*, vol. 104, p. 056603, 2010.

[108] E. Poem, Y. Kodriano, C. Tradonsky, N. H. Lindner, B. D. Gerardot, P. M. Petroff, and D. Gershoni, "Accessing the dark exciton with light," *Nature Physics*, vol. 6, p. 993, 2010.

[109] G. Bester, S. Nair, and A. Zunger, "Pseudopotential calculation of the excitonic fine structure of million-atom self-assembled $\mathrm{In_{1-x}Ga_xAs/GaAs}$ quantum dots," *Physical Review B*, vol. 67, p. 161306, 2003.

[110] A. Patane, R. J. A. Hill, L. Eaves, P. C. Main, M. Henini, M. L. Zambrano, A. Levin, N. Mori, C. Hamaguchi, Y. V. Dubrovskii, E. E. Vdovin, D. G. Austing, S. Tarucha, and G. Hill, "Probing the quantum states of self-assembled inas dots by magnetotunneling spectroscopy," *Physical Review B*, vol. 65, p. 165308, 2002.

[111] M. N. Makhonin, E. A. Chekhovich, P. Senellart, A. Lemaitre, M. S. Skolnick, and A. I. Tartakovskii, “Optically tunable nuclear magnetic resonance in a single quantum dot,” *Physical Review B*, vol. 82, p. 161309, 2010.

[112] M. N. Makhonin, K. V. Kavokin, P. Senellart, A. Lemaitre, A. J. Ramsay, M. S. Skolnick, and A. I. Tartakovskii, “Full coherent control of nuclear spins in an optically pumped single quantum dot,” *arXiv*, vol. arXiv:1102.3636v1, 2011.

[113] D. Paget, G. Lampel, B. Sapoval, and V. I. Safarov, “Low field electron-nuclear spin coupling in gallium arsenide under optical pumping conditions,” *Phys. Rev. B*, vol. 15, p. 5780, 1977.

[114] J. J. Finley, M. Sabathil, P. Vogl, G. Abstreiter, R. Oulton, A. I. Tartakovskii, D. J. Mowbray, M. S. Skolnick, S. L. Liew, A. G. Cullis, and M. Hopkinson, “Quantum-confined stark shifts of charged exciton complexes in quantum dots,” *Physical Review B*, vol. 70, p. 201308, 2004.

[115] M. V. G. Dutt, J. Cheng, B. Li, X. Xu, X. Li, P. R. Berman, D. G. Steel, A. S. Bracker, D. Gammon, S. E. Economou, R.-B. Liu, and L. J. Sham, “Stimulated and spontaneous optical generation of electron spin coherence in charged gaas quantum dots,” *Physical Review Letters*, vol. 94, p. 227403, 2005.

[116] F. H. L. Koppens, D. Klauser, W. A. Coish, K. C. Nowack, L. P. Kouwenhoven, D. Loss, and L. M. K. Vandersypen, “Universal phase shift and nonexponential decay of driven single-spin oscillations,” *Physical Review Letters*, vol. 99, p. 106803, 2007.

[117] Y. Wu, E. D. Kim, X. Xu, J. Cheng, D. G. Steel, A. S. Bracker, D. Gammon, S. E. Economou, and L. J. Sham, “Selective optical control of electron spin coherence in singly charged $\mathrm{GaAs}-\mathrm{Al}_{0.3}\mathrm{Ga}_{0.7}\mathrm{As}$ quantum dots,” *Physical Review Letters*, vol. 99, p. 097402, 2007.